Study of the U-Am-O ternary phase diagram

Enrica Epifano

▶ To cite this version:

HAL Id: tel-01852208
https://pastel.hal.science/tel-01852208

Submitted on 1 Aug 2018

université
PARIS-SACLAY

Thèse de doctorat

ÉCOLE
POLYTECHNIQUE
UNIVERSITÉ PARIS-SACLAY

Study of the U-Am-O ternary phase diagram

Thèse de doctorat de l'Université Paris-Saclay
préparée à l'Ecole polytechnique

École doctorale n°571 Sciences chimiques : molécules, matériaux,
instrumentation et biosystèmes (2MIB)
Spécialité de doctorat: Chimie

Thèse présentée et soutenue à Paris- Saclay, le 17 Novembre 2017, par

Enrica Epifano

Composition du Jury :

Fiqiri Hodaj Professeur, Grenoble INP, SIMAP	Rapporteur
Melissa Denecke Professeur, The University of Manchester	Rapporteur
Rudy Konings Professeur, Delft University of Technology	Président du jury
Hans Seifert Professeur, Karlsruhe Institute of Technology	Examinateur
Gianguido Baldinozzi Professeur, Université Paris-Saclay - Centrale Supelec	Examinateur
Christine Guéneau Ingénieur chercheur, Université Paris-Saclay – CEA Saclay	Directeur de thèse
Philippe Martin Ingénieur chercheur, CEA Marcoule	Encadrant
Dario Manara Ingénieur chercheur, EC – JRC-Karlsruhe	Invité

DE LA RECHERCHE À L'INDUSTRIE

cea

Thèse préparée au sein du *Laboratoire de Caractérisation du Combustible*,
DEN/DMRC/SFMA/LCC, CEA Marcoule

A mio zio Nino

Thermodynamics is a funny subject. The first time you go through it, you don't understand it at all. The second time you go through it, you think you understand it, except for one or two small points. The third time you go through it, you know you don't understand it, but by that time you are so used to it, it doesn't bother you anymore.

Arnold Sommerfeld

We often think that when we have completed our study of one we know all about two, because "two" is "one and one." We forget that we still have to make a study of "and".

A. S. Eddington

Acknowledgments

This Ph.D Thesis would not have been possible without the support of the several people who helped me during these three years. I hope that few words will be sufficient to express my great gratitude for your support.

First, I want to thank the members of the jury of my PhD defence, the professors Hodaj, Denecke, Konings, Hans, Baldinozzi and doctor Manara, for having found the time to read my thesis and for their precious insights on this work.

I want now immediately pass to the two people without with this work would never have been possible: Philippe Martin and Christine Guéneau.
Philippe, thank you for the enthusiasm that you show in your work every day, no matter the technical or administrative problems. Thank you for all your precious advises and also for having dealt with my stubbornness and anxiety for three years.
Christine, you have been much more than a PhD director, you have been a role model: in every difficult moment of my PhD, a ten minutes conversation with you was sufficient to re-find my enthusiasm and my will to get back to work. Thank you for your all the suggestions and all the corrections that made me grow up during these three years.

I want also to thank all the people of the LCC lab of CEA Marcoule for their constant support. Thank you Elodie, Jean-Robert, Romain L. and Alexis, for being always ready to help in the laboratory; Caroline, for all your advises; Florent and Romain V. for all the fruitful discussions; Guathier, for all your jokes (except that about my car!) and for providing me some beautiful SEM images; Christophe for being a very present *chef de labo*, always interested and supportive to my work.
Thank you also to the LFC lab of CEA Marcoule; mainly to Sylvie Pillon and Laure Ramond, for welcoming and helping me during my first days in Atalante, and to Marc Bataille and Philippe Coste, without with I would still being struggling with the remote controls to synthesize my pellets.
Thank you to the entire SFMA service, and in particular to Meryl Brothier and Guillaume Bernard Granger for their constant interest and encouragement.
Finally, thank you to Lionel, Corinne, Pier, Lydie, Tanguy, Marie and all the other friends met in Marcoule.

Contents

List of Figures

XII

XIV

Chapter 1

Introduction and objectives

The context of this PhD thesis, related to the transmutation of americium, will be introduced. Then, the objectives of this work will be stated. Finally, the applied methodology will be briefly described and the thesis will be outlined.

1.1 Context

The management of the rising world population and the consequent energy needs is probably the major challenge of the 21st century. Fossil fuels such as coal, oil, and natural gas are still the primary source of energy, providing about 80% of the world energy supply [1]. But fossil fuels are non-renewable, and therefore they are not a valid solution for the future. Moreover, the urgency to reduce carbon dioxide emissions to mitigate their impact on climate change cannot be neglected. In this context, nuclear energy can provide a valuable alternative and can play a key role in the energy mix. However, some concerns exist with respect to the nuclear power safety and sustainability. One of the major issues is the management of the spent fuel, due to its long-term radiotoxicity, as will be discussed herein. In this respect, different routes have been followed by the various countries. For instance, Finland adopted the direct deep geological disposal of the spent fuel and the first repository for high radioactive waste is currently under construction in Olkiluoto [2]. In France, different possibilities have been explored. Indeed, the French parliament voted in 1991 the first French Waste Management Act (the so-called "Bataille's law") [3], which promoted the study of three alternative strategies for managing the spent fuel: (1) partition and transmutation (P&T); (2) deep geological disposal; (3) long-term interim storage. Since this PhD work is embedded in the frame of the research for the P&T strategy, the basic concepts of this scenario will be explained in the following.

The supply, preparation, use and ultimate disposal of the fuel for a reactor is called reactor *fuel cycle.* The parts of the fuel cycle that precede the use in the reactor are called the *front end* of the fuel cycle. In France and in most of the nuclear power plants of the world, the nuclear fuel is constituted of enriched (in ^{235}U) uranium oxide (UOX) or of uranium-plutonium mixed oxide (MOX). The front end includes the mining of uranium ore, the enrichment of uranium, the conversion of uranium fluoride in oxide, the manufacture of pellets and the fabrication of

fuel assemblies. The parts of the fuel cycle that follow the use in reactor are called the *back end* of the fuel cycle.

The fuel withdrawn from a reactor has a different chemical composition than the initial one because of the nuclear reactions. These include the fission reactions, but also the neutron captures and the consecutive decays. The elements presents in the fuel can be generally classified in: 1) not fissioned U and Pu isotopes; 2) Fission Products (FPs), produced with the fission reactions; 3) **Minor Actinides** (MAs), such as Np, Am, Cm, produced through neutron capture and subsequent β-decays. The first group represents more than the 96% of the mass of a typical UOX spent fuel, after irradiation in normal conditions (burn-up= 33 GW·d·t^{-1}) in a Pressurized Water Reactor (PWR) [4]. The FPs constitute 3.9% of the mass and the MAs represent only 0.1 wt.%.

Although FPs and MAs are present in low concentrations in the spent fuel, they represent a risk to life forms because of their radioactivity. A measure of the hazard of these elements is provided by the radiotoxicity, shown in Fig. 1.1 [5]. The reference point is the **radiotoxicity** associated with the raw material (natural uranium) used to fabricate 1 ton of enriched uranium. If no treatment is performed, the reference point is reached by the spent fuel only after about 300000 years (red curve). The radiotoxicity of the FPs (green curve) represents the highest
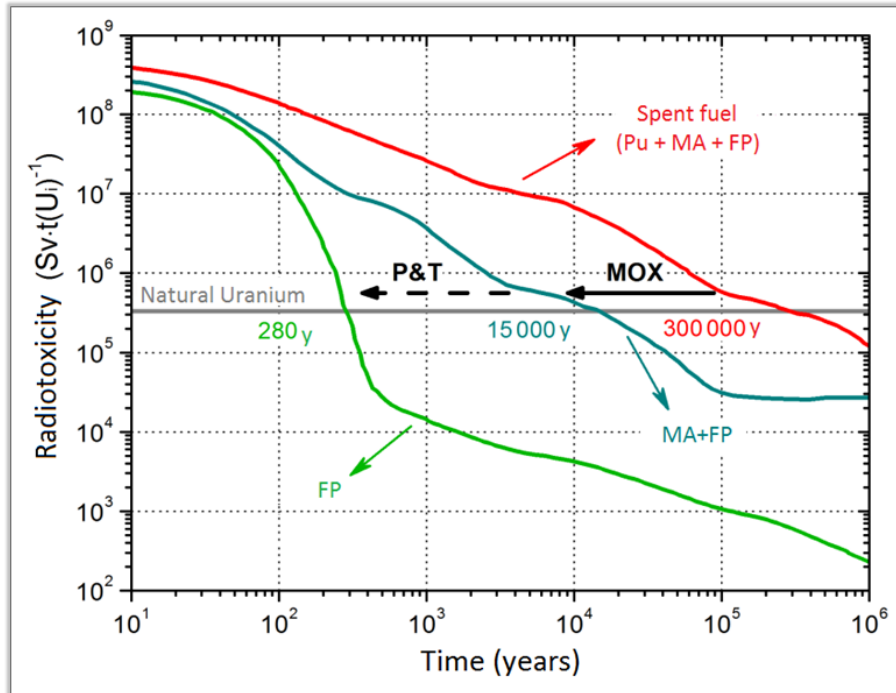
Fig. 1.1: Radiotoxicity of a spent PWR fuel and its components.

contribution during the first 100 years; subsequently, it decreases and reaches the reference level after about 300 years. After this period, the total radiotoxicity is dominated by the actinides (MAs + Pu). After the extraction of plutonium from the spent fuel (already perfomed on an industrial scale in France), the long-term radiotoxicity is caused by the minor actinides and, in particular, the americium isotopes [5] (blue curve in Fig. 1.1). For this reason, the **Partition and Transmutation strategy** (P&T) has been proposed, as a way to reduce the burden of

the long term geological disposals. Indeed, various studies have shown that the radiotoxicity inventory can be reduced by a 100 factor if all Pu and MAs are burned, which could be achieved with multi-recycling.

The first step of the P&T strategy is the re-treatment of the spent fuel, in order to extract the MAs. In France, the spent nuclear fuel is currently reprocessed on industrial scale at *La Hague* chemical plant (Digulleville, France), using the PUREX process [6]. This allows the separation of uranium and plutonium from the other components of the spent fuel (FPs and MAs). The remaining elements are now treated as wastes and vitrified. Innovative processes are currently under development, both for the extraction of all the MAs (Am, Cm and Np) or the selective separation of americium [7]. The second step consists in adding the MAs to new nuclear fuels (or transmutation targets, depending on the various strategies described below). Finally, the fission and consequent transmutation of the MAs into stable or short-live elements is performed through the irradiation in a neutron flux.

In a neutron field, the undesired neutron captures always compete with the fission reactions. In order to have an efficient fission/capture ratio for the MAs, it is preferable to use a high-energy neutron flux. This means that the current commercial light-water reactors are not suitable for the transmutation of minor actinides. Two systems are instead preferable for the purpose:

- the Accelerator Driven Systems (ADSs) [8]. These are formed by a sub-critical nuclear reactor core coupled with high-energy proton accelerator, producing neutrons by spallation.

- The Fast Neutron Reactors (FNRs) [9], which are currently developed in the frame of the Generation-IV international forum [10].

Concerning the materials in which MAs are diluted for the irradiations, two strategies can be distinguished: the homogeneous and the heterogeneous transmutation [11, 12].

The homogeneous transmutation strategies consists of diluting small quantities of MAs (≤ 5 %) in MOX fuels [13] for FNRs. The feasibility of this approach has been proven by the milestone irradiation experiment SUPERFACT, performed in the Phenix sodium fast reactor [14]. However, one major drawback of the homogeneous transmutation is the necessity to adapt the entire production chain of the fuel for the handling of minor actinides, with a considerable increase of the complexity system and hence the cost.

The heterogeneous transmutation strategy consists of adding relatively large quantities of MAs to inert matrices. The obtained transmutation targets can be irradiated both in ADSs and FNRs. Several matrices were studied, generally based on ceramics or metals [11]. For the ceramic-ceramic (CERCER) composites, matrices based on magnesium oxide or yttrium stabilized zirconia oxides were considered. For ceramic-metal (CERMET) composites, several metals were proposed (Zr, Mo, W, Nb, stainless steel).
At CEA, the P&T research focused on the heterogeneous strategy, with the use of Minor Actinide Bearing Blankets (MABBs) in sodium fast reactors [15]. In this concept, a relatively high

quantity of MAs (up to 20%) is diluted in a depleted-UO_2 matrix, forming special assemblies, located at the peripheral zone of the core. In this frame, uranium-americium oxides are very promising transmutation targets. Irradiation tests were already performed on these systems. During the MARIOS campaign (2011-2012), $U_{0.85}Am_{0.15}O_{2\pm x}$ disks were irradiated in the High Flux Reactor (Petten, Netherlands) [16], with successful results [17]. In 2014, the DIAMINO irradiation test started in the Osiris reactor (CEA Saclay, France) on $U_{0.85}Am_{0.15}O_{2\pm x}$ and $U_{0.925}Am_{0.075}O_{2\pm x}$ disks [18]. The post-irradiation examinations of these tests are still in progress.

1.2   Goals and methodology of this work

A thorough knowledge of the thermodynamic properties of advanced fuels or MABBs, to which MAs have been incorporated, is essential in order to put into practice the P&T strategy in FNRs. In a homogeneous transmutation scenario, temperatures can reach up to 2500 K, in normal operating conditions, at the centre of the fuel pin of Sodium-cooled Fast Reactors (SFRs), and about 773-1373 K on the pellet edge [19]. For the heterogeneous transmutation, temperatures up to 1450 K can be reached for the MABB [16]. The high temperature thermophysical properties, as for example the melting temperature and the thermal conductivity, are key parameters in the design of a reactor core, because they determine the safety margins and the behaviour of the fuel in the reactor. These properties are dramatically affected by the oxygen stoichiometry of the fuel, usually indicated as the **oxygen/metal** ratio (**O/M**). Indeed, the actinide dioxides do not generally form stoichiometric compounds, but solid solution with large oxygen non-stoichiometric domain. Knowing the thermodynamics of the considered actinide-oxygen system is hence a prerequisite to master the manufacture process and obtain the desired composition. To further complicate the situation, the temperature gradient in the fuel pellets causes a redistribution of the oxygen and the metals inside the pellet, meanwhile the overall composition changes with the burnup. The prediction of the formed phases and their compositions under specific temperature and oxygen potential conditions is thus crucial for the safety perspectives.

To answer to all these needs, the international TAF-ID (Thermodynamic for Advanced Fuel-International Database) project [20] has started in 2013 within the OECD/NEA, with the goal to develop a comprehensive thermodynamic database for nuclear materials. The objective of this PhD work is to contribute to this project, developing a database for the U-Am-O ternary system. The CALPHAD method has been chosen for this purpose and it is the basis of this work.

CALPHAD, which stands for CALculation of PHase Diagram, is a semiempirical method for calculating the phase diagrams from the thermodynamic functions (Gibbs energies) of a system [21]. It is based on the principle that the equilibrium state is the one with the lowest total Gibbs energy. The total Gibbs energy of a system- for a given pressure, temperature and composition- can be expressed as a linear combination of the Gibbs energy functions of all the phases present in the system. Therefore, the knowledge of the Gibbs energy expressions of all the phases, as a function of composition, temperature and pressure, is necessary and it is the aim

of a CALPHAD assessment. A schematic representation of this approach is shown in Fig. 1.2. The first step is the critical review of the experimental data available for the system and, in case they are not sufficient, an experimental campaign should be started. More specifically, the necessary data can be generally classified in three categories:

- **structure**, as crystallographic structure (space groups, atomic positions), defects, oxidation states;

- **phase diagram**, as phase identification and domain, phase boundaries, transition temperatures;

- **thermodynamics**, as formation enthalpy, standard entropy, heat capacity, chemical potentials, vapour pressures.
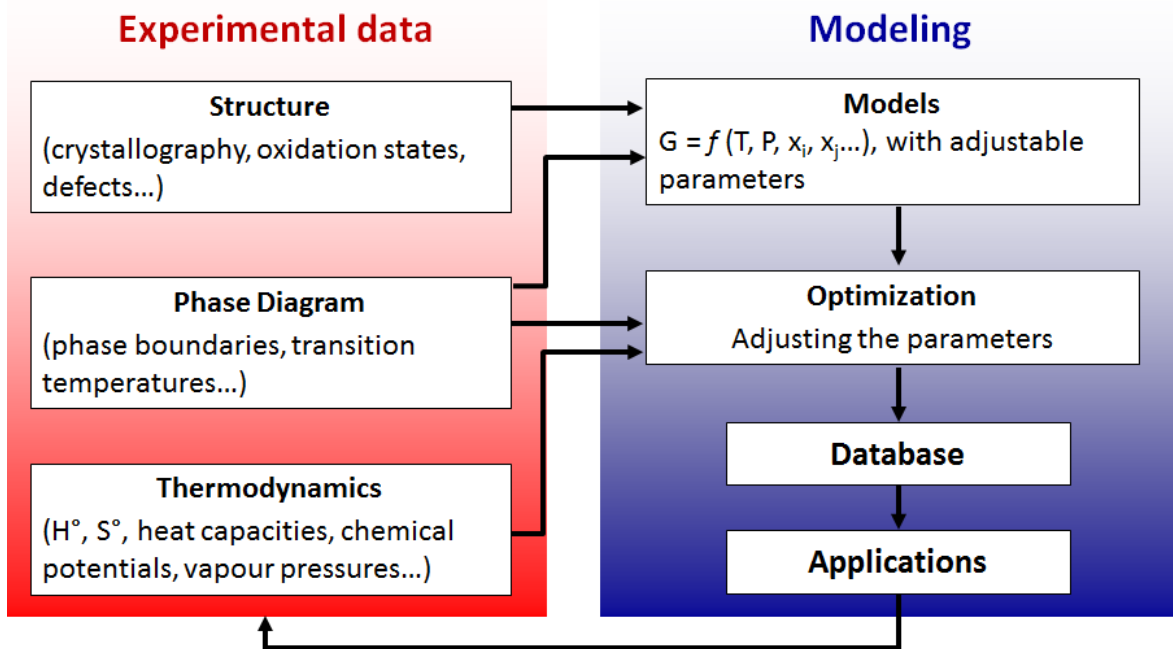
Fig. 1.2: Graphical representation of the CALPHAD method.

On the basis of the structural and phase diagram data, the thermodynamic model of the system is built. This consists of describing each phase and deriving an expression for its Gibbs energy. The selection of the model for a phase must be based on its crystallographic data and chemical bonding properties (metals, ionic solids). Complex phases, such as intermetallic or ionic solid solutions, are usually modeled using the **Compound Energy Formalism** (CEF) [22]. In the CEF, the crystal structure is considered as a sum of sublattices, generally corresponding to the crystallographic sites. Each sublattice exhibits preferential occupancy by one or more constituents. The constituents can be atoms, charged ions or vacancies. From this model, a Gibbs energy results, which is a function of temperature, pressure and composition, containing adjustable parameters.

The Gibbs energy functions of the phases are assessed by optimising the adjustable model parameters in order to achieve the best possible fit of the experimental results (phase diagram

and thermodynamic data), using a least square minimization method. Once the assessment is completed, a thermodynamic database is obtained, which can be used for several applications. Indeed, phase diagrams as well as all the thermodynamic properties can be computed. Moreover, the CALPHAD method allows predicting higher order system behavior by extrapolation from lower order systems, namely its sub-systems. For instance, in order to obtain a thermodynamic database for the U-Am-O ternary system, the associated binary sub-systems should be studied first. A first ternary database is built by extrapolation from the binaries. However, for metal-oxide systems, a pure extrapolation is not sufficient in most of the cases, because excess Gibbs energy terms derive from the interactions between the unlike atoms and, therefore, experimental data on the ternary system are also necessary. Ternary interaction parameters have to be assessed to reproduce these experimental data.

1.3 Thesis outline

Embedded in the framework of the research for MAs transmutation, this work concerns the thermodynamic investigation of the U-Am-O ternary system and it is structured according to the logic of the CALPHAD method, presented above. Therefore, the first step is a critical review of the structural, phase diagram and thermodynamic data, available for the binaries and for the mixed uranium, americium oxides, which is the object of chapter 2. This review will highlight two main issues: the uncertainty concerning the Am-O phase equilibria and the almost total lack of data for the ternary U-Am-O system. The first will be addressed in chapter 3, which is dedicated to the experimental investigation and thermodynamic modeling of the binary Am-O system. The rest of the work will be dedicated to uranium-americium mixed oxides. In chapter 4, the manufacture and characterization of $(U,Am)O_2$ samples with several compositions will be presented and important structural data, obtained by X-Ray Diffraction (XRD) and X-ray Absorption Spectroscopy (XAS), will be shown. In chapter 5, the oxygen-rich domain of the U-Am-O phase diagram will be investigated by combining high temperature XRD and XAS. In chapter 6, experimental studies of several high temperature thermodynamic properties will be shown: phase transitions by XRD, heat capacity by Drop Calorimetry (DC), melting temperature using a laser flash technique, vapour pressures by Knudsen Effusion Mass Spectrometry (KEMS). Finally, using the data collected in this work, the CALPHAD thermodynamic assessment of the U-Am-O will be presented in chapter 7.

Chapter 2

Review of the literature data

A comprehensive knowledge of the structural and thermodynamic characteristics of the nuclear fuel is essential in order to predict its in-reactor behavior. On account of the central role of uranium in the nuclear industry, numerous studies have been performed on this element and its compounds. This is especially true for the U-O system, since the uranium dioxide UO_2 is the most common nuclear fuel worldwide. On the contrary, the scientific interest for americium is relatively recent, since it derives from the management of the nuclear spent fuel from the first generation reactors. Besides, experimental investigations on americium compounds are slowed down by the high radioactivity of the isotopes of this element, which makes its handling difficult. As a result, the data reported in the literature on americium oxides or mixed U-Am oxides are rare.

In the following, a review of the phase diagram, structural and thermodynamic data of the binary U-O, Am-O, U-Am systems and the ternary U-Am-O system will be provided. Since several reviews already exist for uranium oxides [23–25], the attention will be focused on the americium oxides and the mixed Am-U oxides. Finally, the existing thermodynamic models for these systems will be described.

2.1 Phase diagrams

In this section, the state-of-the-art on the phase equilibria of the binary systems U-O, Am-O and U-Am is presented. Then, the U-Am-O ternary phase diagram is approached.

2.1.1 The U-O system

The several thermodynamic, structural and phase diagram experimental data available for the U-O system were critically reviewed by Labroche [24] and Baichi [23]. On the basis of their works, a comprehensive CALPHAD description of the U-O system was proposed by Guéneau *et al.* in 2002 [26] and later improved in 2011 [27]. The resulting computed phase diagram is showed in Fig. 2.1, where the concentration of the two elements (x-axis) is indicated with the oxygen/uranium ratio (O/U).

The oxidation state of uranium in oxide compounds ranges from 3+ to 6+, for O/U ratios
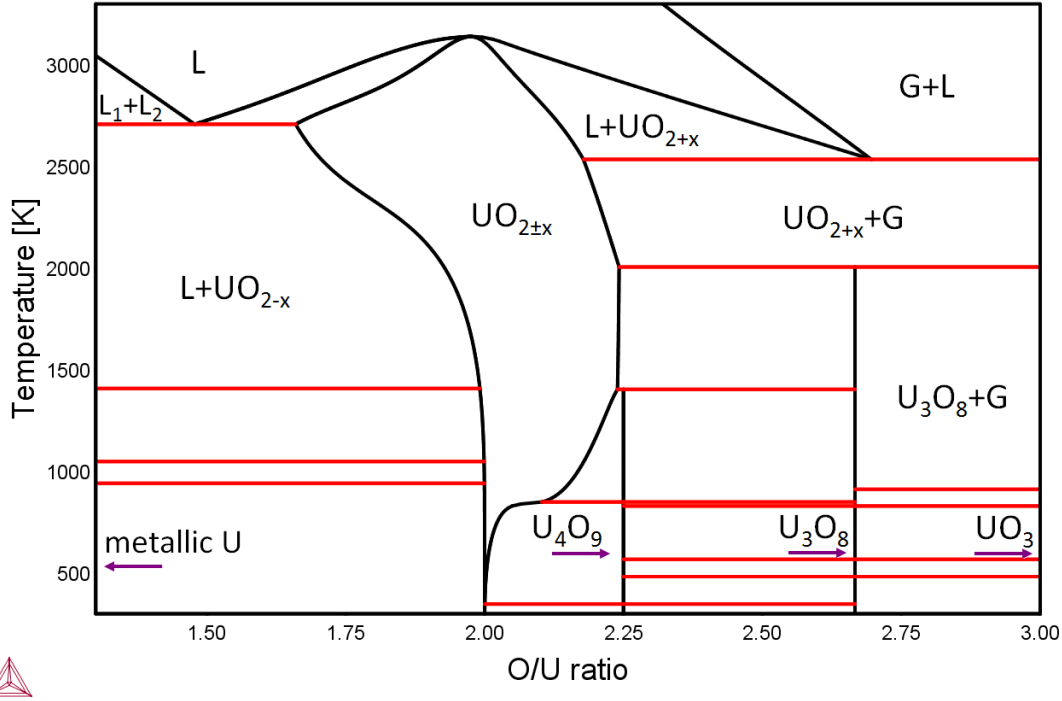
Fig. 2.1: The UO_2 phase diagram according to Guéneau *et al.* [27]. The solid compounds are indicated with their chemical formula, whereas L and G stands for liquid and gas respectively.

comprised between ~1.7 and 3. The four known stable compounds are: UO_2, U_4O_9, U_3O_8 and UO_3. With the exceptions of UO_2, each compound presents several polymorphs. The most important features of the U-O phase equilibria (composition and transition temperatures) are here presented, whereas the crystal structures of the oxide compounds will be described in detail in section 2.2.

U-UO_2 domain

A zoom on the U-UO_{2+x} phase diagram region is shown in Fig. 2.2.

Uranium metal has three crystalline phases, below its melting point at 1407±20 K [28]. At room temperature, the orthorhombic α-phase is stable; the tetragonal β-phase of uranium exists between 961 K and 1048 K; above 1048 K, the body-centered cubic γ-phase appears.

The uranium dioxide is stoichiometric at room temperature and shows both positive and negative deviations from stoichiometry at higher temperatures: the hyper-stoichiometric range appears above 500 K, whereas the hypo-stoichiometry is not observed until 1500 K. This difference is due to the fact that the formation energy of oxygen vacancies in UO_2 is much higher than that of interstitials, which form clusters, as we will discuss in 2.2.

In the uranium rich side of the diagram (O/U<2), metallic and oxide liquids are immiscible in a large range of temperature and composition; a tie-line in this liquid miscibility gap has been experimentally determined at 3090±100 K [29], which is coherent with the present assessment.

According to Guéneau's thermodynamic assessment, the monotectic reaction:

$$L_2(1.46) = UO_{2-x}(1.69) + L_1(0.1688) \tag{2.1}$$
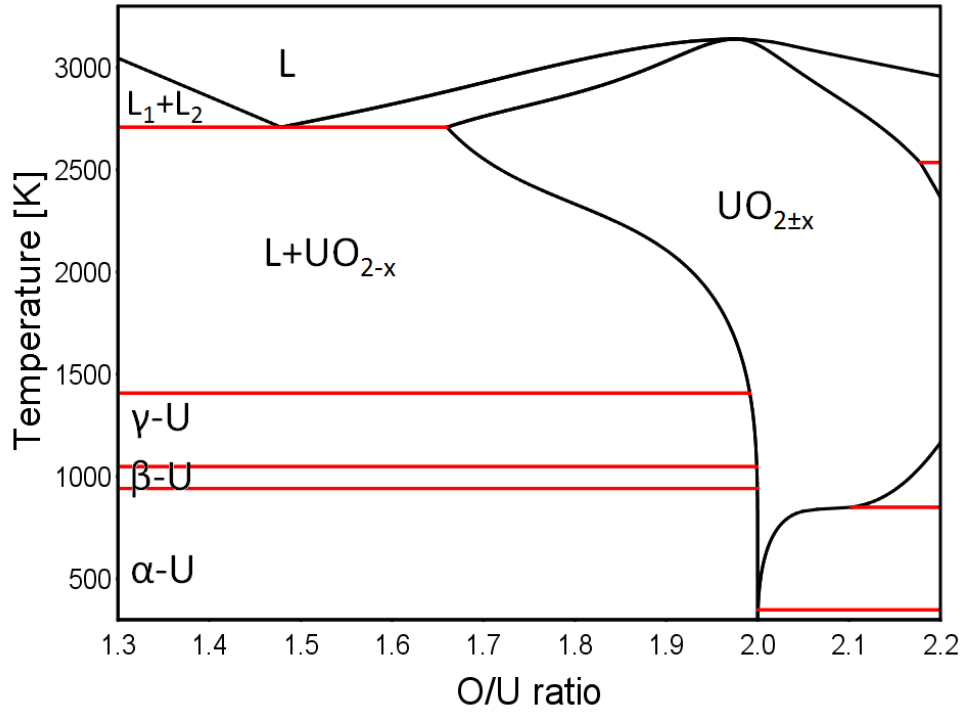
Fig. 2.2: The U-UO$_{2+x}$ domain of the U-O phase diagram according to Guéneau *et al.* [27]

occurs at T=2709 K (in parenthesis, the O/U ratios for the different phases). The calculated temperature and oxygen compositions are in agreement with the experimental data of Latta and Fryxell [30] for O/U< 2. Other slightly different data are available for the monotectic reaction [26,31], but only the Latta and Fryxell experimental points were chosen for the assessment of the liquids-solid UO$_{2-x}$ region. Above the monotectic temperature, the O/U ratio of the lower phase boundary increases until the maximum congruent melting temperature is reached. According to Latta and Fryxell [30], this point corresponds to T = 3138±15 K and to stoichiometric UO$_2$. The assessed congruent melting occurs at 3140 K and for O/U equal to 1.98; the latter is a little low compared with the Latta point but still within the experimental uncertainty (±0.02). A main difference between the first [26] and the second [27] thermodynamic assessment of Guéneau is the better description of the solidus/liquidus temperatures in UO$_{2+x}$, thanks to the new experimental data provided by the laser-melting experiments of Manara *et al.*, [32]. The calculated boiling point of UO$_2$ is at 3820 K and it is not congruent; the congruent boiling occurs for a lower O/U equal to 1.381 [26].

UO$_2$-UO$_3$ domain

The UO$_2$-UO$_3$ phase diagram domain is shown in Fig. 2.3.

The UO$_2$ is stoichiometric at low temperature and exhibits a hyperstoichiometric homogeneous region above 500 K. The UO$_{2+x}$ phase boundary is well known for temperatures ranging from 500 K to 1950 K [33–39]. The oxygen solubility in UO$_2$ increases with temperature up to 1400 K, at which the U$_4$O$_9$ phase decomposes to UO$_{2+x}$ and U$_3$O$_8$ peritectoidally. Above 1400 K, the upper phase boundary increases only slightly with increasing temperature up to 1950 K. To our knowledge, no experimental data are available between 1950 K and 2800 K for the UO$_{2+x}$
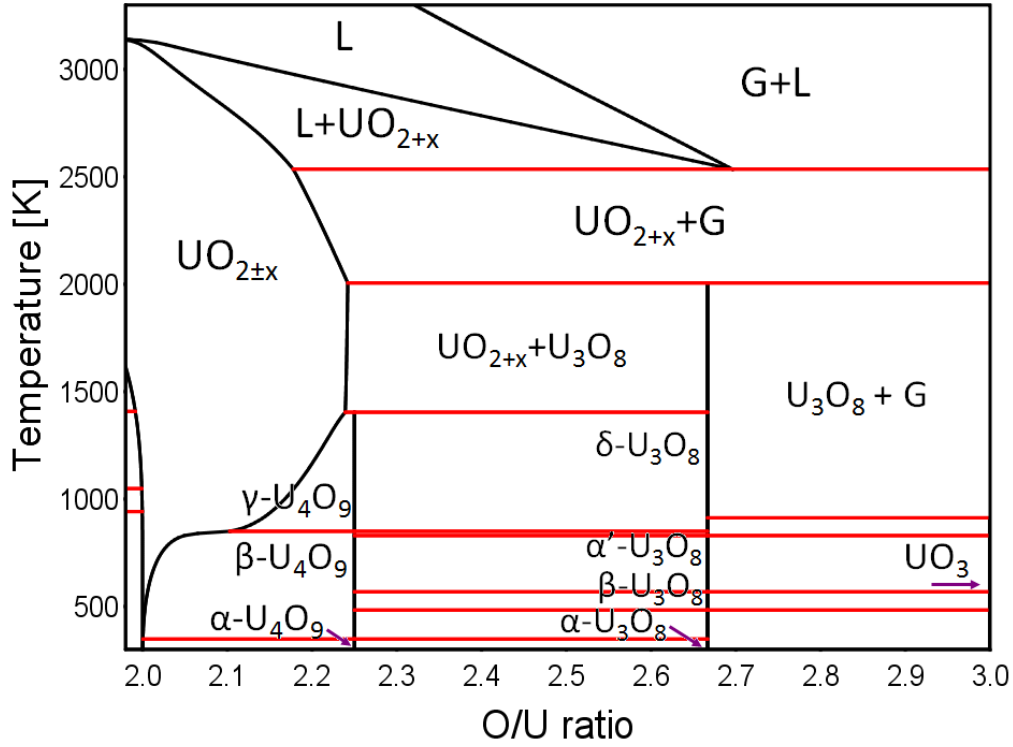
Fig. 2.3: The UO_2-UO_3 domain of the U-O phase diagram according to Guéneau et al. [27]

composition and for the invariant reaction

$$L_2 = UO_2 + G \qquad (2.2)$$

The Guéneau thermodynamic assessment [27] expects a decrease of the O/U ratio above 1950 K and the invariant reaction at 2540 K for $UO_{2.18}$.

For 2<O/U<2.25 (where the lower boundary increases with temperature as previously discussed) and T<1400 K, a biphasic region with UO_{2+x} and U_4O_9 exists. The U_4O_9 exists in three polymorphic phases (α, β and γ). The temperatures for the second order transitions α-U_4O_9= β-U_4O_9 and β-U_4O_9= γ-U_4O_9 are respectively 345±10 K [40, 41] and 850±10 K [42, 43]. Some authors [42, 44] suggested that these transition temperatures vary slightly with the O/U ratio. Indeed, even if it is not shown in 2.3, according to some authors [33–35], the U_4O_9 phase has a narrow homogeneity range between O/U= 2.23 and 2.25, which is almost unchanged from room temperature to the peritectic temperature.

The composition range of U_3O_{8-x} was investigated by different authors [34, 38, 45–49] and the data were not always in agreement. Four polymorphic forms (orthorhombic and hexagonal, as it will be discussed in 2.2) have been identified (α, β, α', γ). An homogeneity range (still not included in the thermodynamic assessment [27, 50]) of this phase exists, whose lower limit was clearly identified [28]. At room temperature, this is equal to O/U=2.6, while at higher temperatures (above 1000 K) is comprised between 2.595 and 2.62 [28].

According to some authors, other intermediate phases between U_4O_9 and U_3O_8 exist: U_5O_{13} [34], U_2O_5 [51] and the metastable phase U_3O_7 [52].

Finally, the UO_3 phase, which does not present any deviation from stoichiometry, presents five

polymorphic forms [53].

2.1.2 The Am-O system

First attempts to define the phase diagram of the Am-O system date back to the sixties. Nevertheless, because of the uncertainties due to the lack- and in some cases discrepancies- of experimental data, none of the phase diagrams presented in the literature is satisfying. Therefore, for the Am-O system, it is not possible to provide a *simple* description of the phase diagram, as in the case of the U-O system. A different strategy is adopted in this case. At first, the experimental data available for the Am-O system will be presented, following a chronological order. Then, the various phase diagram versions presented in the literature will be discussed.

Experimental data

In the $1.5 \leq$ O/Am ratio ≤ 2.0 domain, one dioxide (AmO_{2-x}), one intermediate cubic phase (C-type) and three sesquioxides (A-Am_2O_3, B-Am_2O_3 and a C-type) have been identified. For the C-type phases, since their composition domain are not defined, different nomenclatures were used in the literature. In this work, the intermediate phase is indicated as $AmO_{1.61\pm x}$ and the sesquioxide as $AmO_{1.5+x}$.

The FCC fluorite-type $Fm\overline{3}m$ structure (s.g. (space group) 225) of americium dioxide was identified for the first time by Zachariasen in 1949 [54].

Few years later, Templeton and Dauben indexed two sesquioxide forms [55]. The first one, C-$AmO_{1.5+x}$, was obtained by heating AmO_2 at 873 K under 1/3 atmosphere of hydrogen and it was found to be iso-structural with the BCC $Ia\overline{3}$ C-type rare earth sesquioxide (s.g. 206, prototype Mn_2O_3). The second one, A-Am_2O_3, obtained by reduction under 1/6 atmosphere of hydrogen at 1073 K, is hexagonal $P\overline{3}m1$ (s.g. 164, prototype La_2O_3).

A monoclinic $C2/m$ sesquioxide, called B-type structure, was observed by Chikalla and Eyring in AmO_{2-x} samples reduced at 1200 K, under a hydrogen-containing atmosphere [56] and then quenched. However, the monoclinic phase was never observed alone and it is considered as metastable, probably stabilized by the impurities contained in the studied materials. The structural data available for these phases will be presented in section 2.2, whereas in this part the data providing insight on the phase diagram are presented.

The first attempts to define the Am-O phase equilibria were performed by Chikalla and Eyring, who combined XRD observations and oxygen potential ($\Delta\overline{G}O_2$) measurements by thermogravimetry [56, 57]. XRD samples were obtained by reducing AmO_2 powder under pure helium or helium-hydrogen mixture in a thermobalance, in parallel to the oxygen potential measurements. The composition of the samples was then determined from the weight change. The temperature and the oxygen partial pressure ranged respectively between $1139 < T < 1470$ K and from one to below 10^{-6} atm. The O/Am ratios encountered under these conditions varied from 1.80 to 2.00. The measured $\Delta\overline{G}O_2$, which will be shown in section 2.4.3.2, were never constant, which means that the sample was monophasic, proving that AmO_{2-x} phase has a large hypo-stoichiometric existence domain which reaches at least an O/Am= 1.8. Nevertheless, the

sub-stoichiometric phase was not observed by XRD. Due to too slow quenching rates, it was not possible to retain this single phase: the cooled samples were constituted by a mixture of fluorite and another cubic phase. From these results, Chikalla and Eyring proposed the existence of the intermediate cubic phase $AmO_{1.61\pm x}$ for T < 1300 K between the dioxide and the sesquioxides, probably isostructural with the BCC C-Am_2O_3 (s.g. 206, prototype Mn_2O_3), even if the diffraction patterns were not clearly resolved. Concerning the more reducing conditions, samples quenched from 1070 < T < 1130 K with 1.51 < O/Am < 1.7 showed both cubic and hexagonal phases, while a sample quenched from 730 K exhibited only a BCC phase. Finally, a sample quenched from 1270 K in pure hydrogen was monophasic hexagonal Am_2O_3.

Sari and Zamorani went ahead with the investigation of the Am-O phase equilibria performing ceramographic examinations on quenched and annealed samples and differential thermal analysis (DTA) [58]. Samples with composition between AmO_2 and $AmO_{1.45}$ were prepared by reduction of dioxide pellets at temperatures ranging from 570 K to 1770 K, under various atmospheres (pure H_2, H_2-H_2O and pure He). The O/Am ratio was determined by the mass change.
Similarly to the previous experiments carried out by Chikalla and Eyring [56], it was not possible to quench the AmO_{2-x} phase from high temperature. The materials analysed at room temperature always exhibited two phases. From DTA results, the disproportion into these two phases was estimated in the 1120≤T≤1300 K range. From the shape of the DTA peaks as a function of the composition and for comparison with other lanthanide and actinide oxide systems (Ce-O, Pr-O and Pu-O), Sari and Zamorani attributed the observed reaction to a miscibility gap in the fluorite phase [58]. However, the identified boundaries, on the oxygen rich side, are in conflict with the oxygen potential data of Chikalla and Eyring [57].
At lower temperatures, the DTA measurements of Sari and Zamorani [58] showed another phase transition at around 620 K, in the slightly hypo-stoichiometric region (O/Am >1.7). Because of the sluggishness of DTA measurements for O/Am <1.6, only ceramographic analysis were performed by Sari on the more reduced samples, allowing to estimate the homogeneity of the microstructure. The oxides annealed below 573 K were single phase for O/Am ratios between 1.5 and 1.56, whereas two phases were found for O/Am equal to 1.63. Finally, the samples quenched from temperatures above 573 K exhibited two phases, for O/Am<1.62, and only one phase, for O/Am=1.638. Nevertheless, at these low temperature, whether the equilibrium was reached or not is questionable.

Few decades later (1996), Casalta measured the oxygen potentials of americium oxides (1.5≤O/Am≤2.0) in the 1130≤T≤1425 K range [59]. For all the temperatures, the data-which will be shown and discussed in more detail in 2.4.3.2- showed constant oxygen potentials for an O/Am ratio between 1.66 and 1.9, evidencing the existence of a two-phase region. The latter was identified by Casalta as the miscibility gap. Moreover, the oxygen potentials indicated the existence of a composition domain for the intermediate C-$AmO_{1.61+x}$ phase, for $1.62 \leq$ O/Am ≤ 1.65 and $1140 \leq T \leq 1170$ K.

Otobe *et al.* measured the oxygen potentials of AmO_{2-x} in the 1.5≤ O/Am ≤1.99 at 1333

K [60]. The data showed two abnormal changes for O/Am values equal to 1.78 and 1.71. The latter were interpreted by Otobe *et al.* as the occurrence of intermediate phases, named Am_7O_{12} and Am_9O_{16}, but no direct evidence of their existence was shown. Finally, Otobe *et al.* indicated that the existence domain of the intermediate C-$AmO_{1.61+x}$ phase was comprised between 1.69 < O/Am < 1.67.

Even if the three sets of oxygen potentials (Chikalla and Eyring [57], Casalata [59], Otobe [60]) will be critically revised in section 2.4.3.2, it is important to stress here that these data are not consistent and they indicate different characteristics of the phase diagram. For instance, only the data of Casalta are compatible with the existence of the AmO_{2-x} miscibility gap, suggested by Sari and Zamorani [58].

Finally, recent data on the Am-O phase diagram were provided by an *in situ* high temperature XRD investigation performed by Lebreton *et al.* [61]. Americium dioxide powder was heated between room temperature and 1840 K under an atmosphere containing 5% of H_2 in a neutral gas. A phase transition from the fluorite structure toward a BCC C-type phase (s.g. $Ia-3$) was rapidly observed at 650 K. The composition of this phase was unknown but, considered the highly reducing conditions and the observed lattice parameter increase, it was probably the C-type Am_2O_3 phase or the $AmO_{1.61}$ phase. At 1200 K, another transition toward the hexagonal phase (s.g. $P\bar{3}m1$) occurred. This structure was maintained up to 1840 K and also during the cooling to room temperature, showing a high stability.

Phase diagram representations

The first Am-O phase diagram was proposed by Sari and Zamorani [58], on the basis of their DTA and ceramography investigations and the previous results reported by Chikalla and Eyring [56, 57]. The original phase diagram by Sari and Zamorani is shown in Fig. 2.4; for clarity, a temperature axis in Kelvin and a legend, translating the symbols of Sari and Zamorani with the notation here adopted, were added.

In this representation, for an O/Am ranging from 1.5 to 2, four phases are reported: a dioxide, two sesquioxides (hexagonal A-type and BCC C-type) and an intermediate BBC phase (C′). The americium dioxide is stoichiometric at room temperature and it has a large hypo-stoichiometric domain for T > 1300 K. The lower O/Am limit of this region is not well defined and it has traced at around 1.62. This phase is characterized by a miscibility gap extended from O/Am = 1.7 to O/Am = 1.94, with a critical temperature around 1300 K. For T > 570 K, the intermediate C′ phase has a narrow existence domain in the 1.62 < O/Am < 1.67 range; the upper temperature limit of this phase is not defined. The C-Am_2O_3 is considered the stable sesquioxide form at room temperature. An existence domain with maximum O/Am=1.59 is attributed to this phase. Finally, the stoichiometric phase A-Am_2O_3 appears for T > 500 K.

The Am-O phase diagram proposed by Sari and Zamorani [58] was later updated by Thiriet and Konings [62], as shown in Fig. 2.5. Two main modifications were introduced. First, the two-phase region between the intermediate C-$AmO_{1.61+x}$ phase and the two sesquioxides was
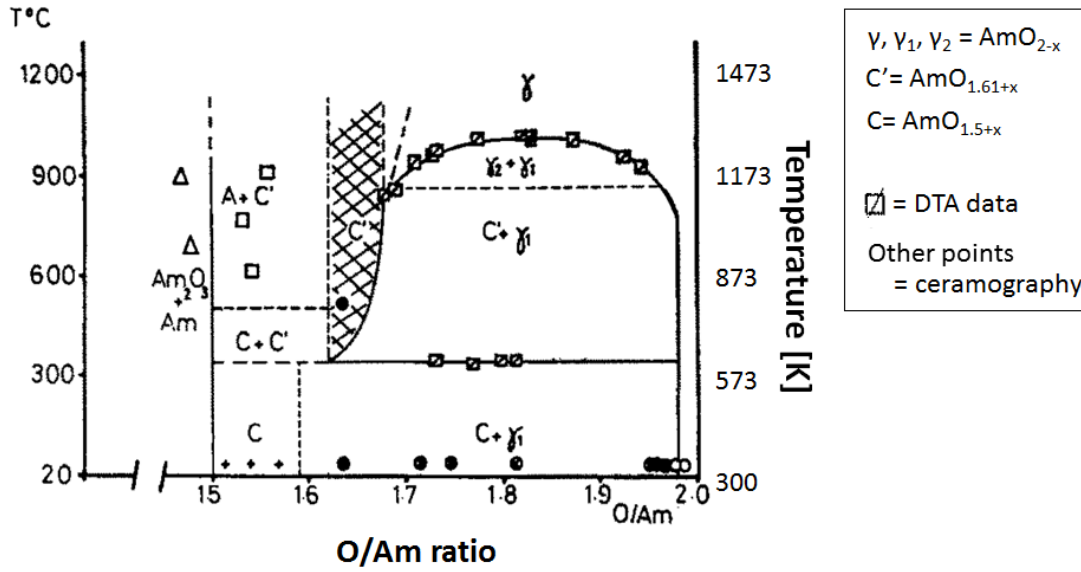
Fig. 2.4: The Am-O phase diagram according to Sari and Zamorani (figure extracted from [58]).

redefined, in the respect of the phase rule. Second, the representation was extended to higher temperatures, up to the liquid region, taking into account the melting temperature measurements performed on A-Am_2O_3 and AmO_{2-x} [63]. The values are 2481±15 K for A-Am_2O_3 and 2386 K for AmO_{2-x} (the O/Am ratio reached during the melting process is unknown).
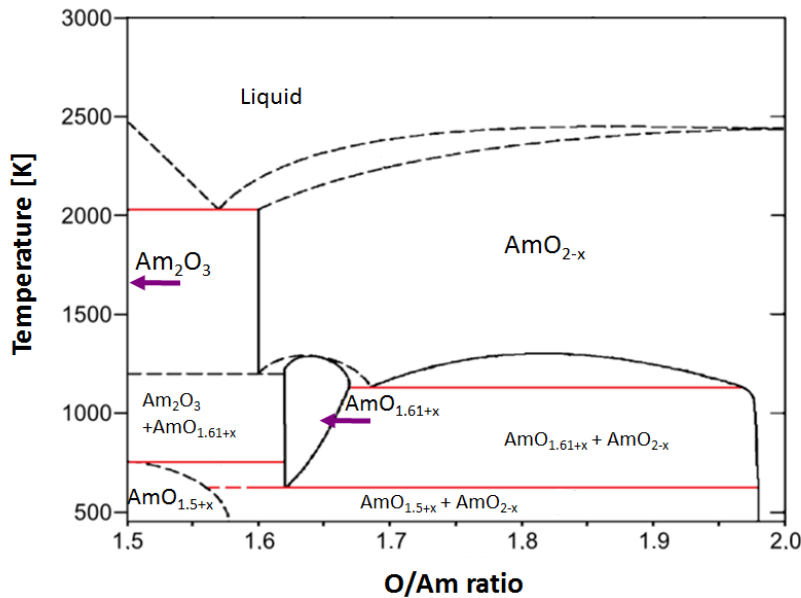
Fig. 2.5: The Am-O phase diagram according to Thiriet and Konings [62].

Gotcu-Freis *et al.* presented for the first time a complete description of the Am-O system based on a CALPHAD assessment [64]. The thermodynamic model will be described in section 2.5.2, whereas here the attention is focused on the resulting phase diagram, which is shown on the left side of Fig. 2.6. The three metallic forms of americium [65] are reported: the double hexagonal closed-(dhcp) α-Am, the FCC β-Am and the BCC γ-Am. The gas phase was in-

cluded for the first time in the phase diagram. However, the lack of thermodynamic data made impossible a complete assessment of all the oxides reported in the previous phase diagrams and some simplifications were necessary. Therefore, in the $1.5 \leq O/Am \leq 2$ range, which is shown on the right side of Fig. 2.6, only three phases are included: the americium dioxide AmO_{2-x}, the intermediate BCC phase (named by Gotcu $AmO_{1.62}$) and the hexagonal sesquioxide (A-Am_2O_3). The intermediate $AmO_{1.62}$ was considered as a stoichiometric compound, stable between 630 K and 1200 K.

The characteristics of the AmO_{2-x} phase are similar to the previous representations: a large hypostoichiometric domain at high temperature and the miscibility gap identified by Sari and Zamorani [58] are reported. However, an important difference in the AmO_{2-x} description of Gotcu derives from including the gas phase in the assessment. Indeed, as shown in Fig. 2.6, the stoichiometric AmO_2 is not thermodynamically stable for $T \gtrsim 1200$ K, not even under one atmosphere of O_2. As a consequence, the assessment indicates an incongruent melting.
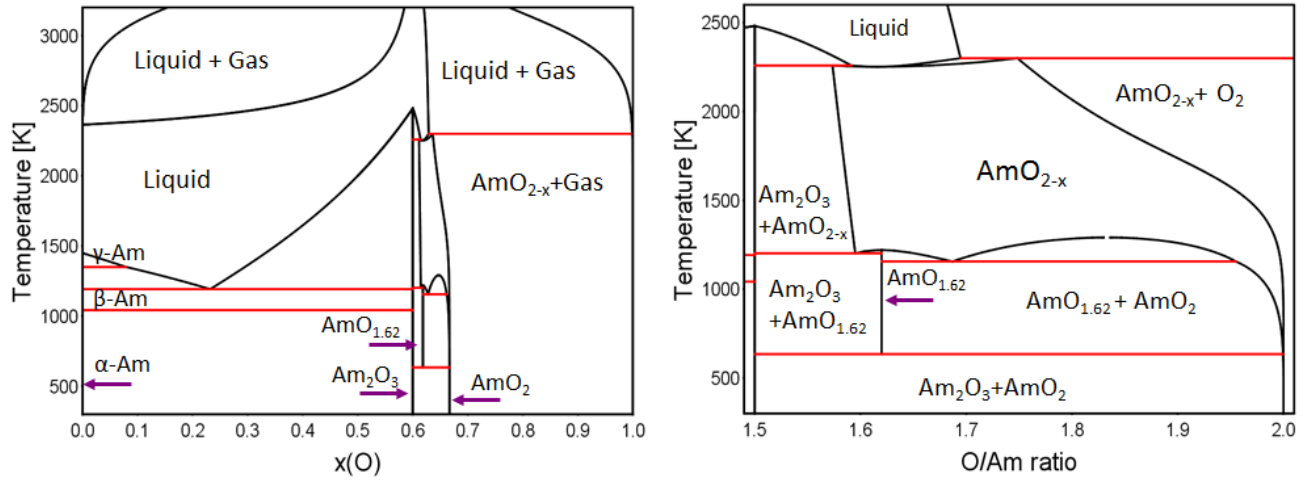
Fig. 2.6: The Am-O phase diagram according to Gotcu *et al.* [64].

2.1.3 The U-Am system

The knowledge of the metallic alloy U-Am is very poor. The results of some solubility tests are the only experimental data available [66]. According to these observations, the solubility between U and Am is extremely low. For instance, the solubility of Am in U was of the order of ∼1 at.% even in samples quenched from the liquid phase, which were prepared by arc-melting method. A first tentative version of the phase diagram was proposed on the basis of these data [66]. An other phase diagram representation was obtained by computational methods by Ogawa [67]. The model was based on the Brewer valence bond model, which allows the estimation of the interaction between metal atoms. The most recent U-Am phase diagram has been proposed by Kurata [66] and is shown Fig. 2.7.
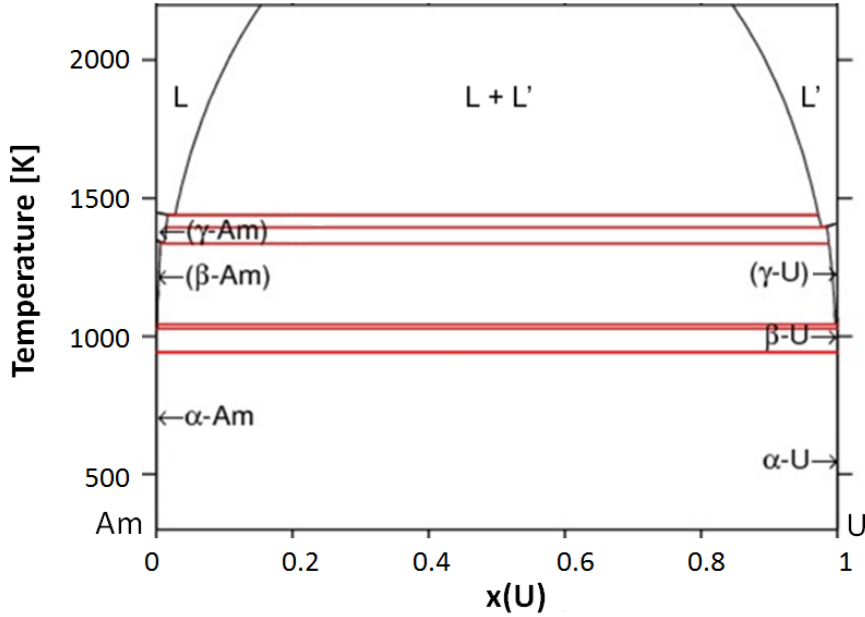
Fig. 2.7: The U-Am phase diagram, according to Kurata [66].

2.1.4   The U-Am-O system

A first tentative-representation of the U-Am-O representation has been recently proposed by Guéneau and Lebreton [68]. This representation is based on a thermodynamic assessment realized using the CALPHAD method, which will be discussed in details in 2.5. No many experimental data are available on the ternary U-Am-O system. The data taken into account for the phase diagram assessment of Lebreton are limited to:

- Various experimental proof of the existence of a $U_yAm_{1-y}O_{2\pm x}$ solid solution with fluorite structure [69–73], at least for americium content up to 50 mol.% .

- The uranium and americium oxidation state data obtained by XAS measurements, which will be discussed in section 2.3.3;

- One set of experimental oxygen potential data for $U_{0.5}Am_{0.5}O_{2\pm x}$ [74], which will be discussed in details in section 2.4.3.3.

Various isothermal sections of the U-Am-O ternary phase diagram, according to Guéneau and Lebreton [68], are shown in Fig. 2.8. According to this representation, a miscibility gap in the dioxide phase exists in the oxygen hypostoichiometric region, with a critical temperature around 1200 K.

Recently, an investigation of the melting behaviour of Am-doped uranium oxide was reported by Prieur *et al* [75]. Three compositions with Am/(Am+U) = 0.10, 0.15 and 0.20 were investigated by a laser-flash technique under an inert argon atmosphere. The study showed a decrease of the melting temperature by increasing the americium content. The results of the measurements are: 3070±24 K, 3071±29 K, 3051±28 K, for Am/(Am+U) = 0.10, 0.15 and
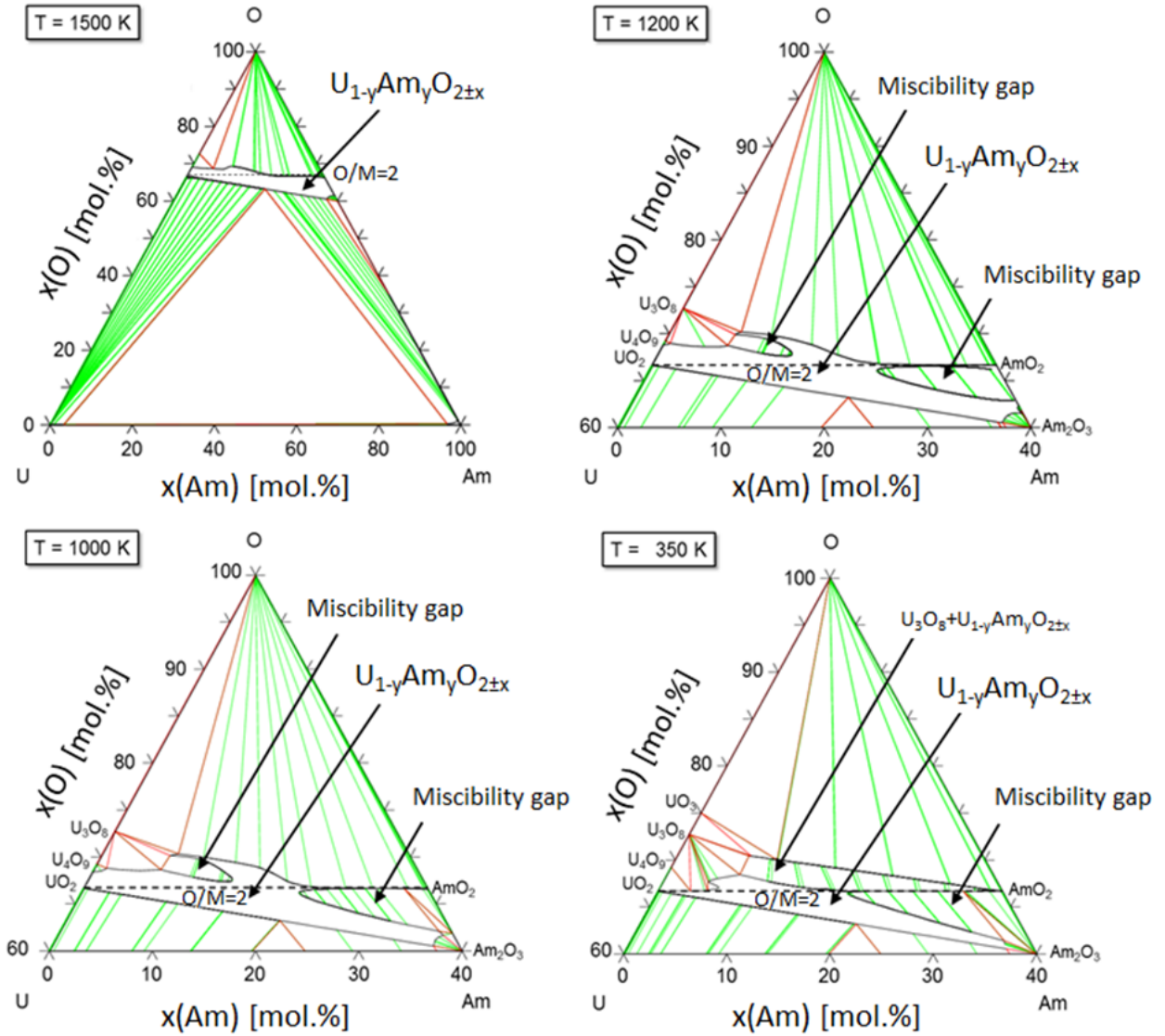
Fig. 2.8: The U-Am-O phase diagram at four different temperatures: 1500 K, 1200 K, 1000 K and 350 K, according to Guéneau and Lebreton [68].

0.20, respectively. The O/M ratios were determined by the XANES technique on the samples recovered after the melting. The oxides with Am/(Am+U)=0.10 and 0.15 were stoichiometric, whereas the Am/(Am+U) = 0.20 had a O/M ratio equal to 2.15.

2.2 Crystallography

In this section, the crystallographic data of the uranium, americium binary and ternary oxides are presented. A description of the crystallographic structures is provided, starting with the fluorite-type structure, which is common to uranium, americium and mixed dioxides, and then approaching the other forms. Then, quantitative structural data, namely the lattice parameters, are reported. Finally, the phenomena which can induce a variation of the crystallographic structure, such as the temperature, the oxygen stoichiometry and the self-irradiation, are discussed.

2.2.1   Crystal structures

2.2.1.1   The fluorite structure

All lanthanide and actinide dioxides reported in the literature, including UO_2, AmO_2 and their solid solution, have a fluorite-type structure (CaF_2) whose space group is $Fm\bar{3}m$ (N°225). Stoichiometric UO_2 and AmO_2 consists of tetravalent cations (U^{4+} and Am^{4+}) and O^{2-} ions. The fluorite structure is described as a FCC lattice where the cations occupy the positions (as fractions of the unit-cell sides) 0,0,0; 1/2, 1/2, 0; 1/2, 0, 1/2 and 0, 1/2, 1/2 and the oxygen atoms occupy the tetrahedral sites (the position 1/4, 1/4, 1/4 and its equivalent ones) [76]. The lattice arrangement is shown in Fig. 2.9. The coordination numbers of uranium/americium and oxygen are respectively 8 and 4.
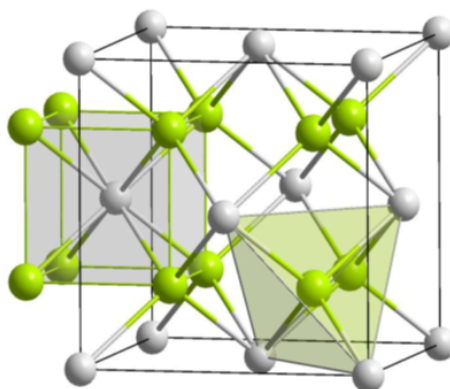
Fig. 2.9: The fluorite structure. In green the O atoms, in grey the U (Am) atoms.

As previously said, the phases which crystallize in a fluorite structure can adapt to hypostoichiometry and hyperstoichiometry. In the fluorite cationic sublattice, the atoms are stable and not very mobile; therefore, the departure from stoichiometry is due to vacancies and interstitials in the anionic sublattice.

In the case of hypo-stoichiometric dioxides, the oxygen vacancies are compensated by a partial reduction of the cations to the trivalent state. This is valid both for UO_{2-x} and AmO_{2-x}, whereas the hyperstoichiometric structure, discussed in the following, is specific to UO_{2+x} since, as said in section 2.1.2, the americium dioxide does not allow hyper-stoichiometry.

Theoretical calculations indicate that in slightly hyper-stoichiometric UO_{2+x} (x<0.01) the additional oxygen atoms occupy the cubic-coordinate sites representing the largest interstices in the lattice (the positions: 1/2, 1/2, 1/2; 1/2, 0, 0; 0,1/2, 0; 0, 0, 1/2) [77]. For stronger departure from the stoichiometry, a more complex structure was pointed out by neutron diffraction experiments on $UO_{2.11}$, $UO_{2.12}$ [78] and $UO_{2.13}$ [79] samples, at 1073 K. The neutron diffraction data led to the formulation of the 2:2:2 Willis cluster [78, 80]. According to the latter, the additional oxygen atoms do not occupy the largest interstitial sites of the fluorite lattice, but two other different positions: one- labeled O′- is displaced by a normal oxygen site by about 1 Å along the <110> direction, whereas the other- labeled O″- is displaced by the same amount in the <111>

direction. The formation of interstitials is accompanied by the formation of oxygen vacancies. According to the neutron diffraction results, the defects are not randomly distributed in the lattice and the addition of oxygen leads to the formation of defect clusters. Each cluster contains two O′ interstitials, two O″ interstitials and two normal oxygen vacancies: this is known as the 2:2:2 cluster and it is shown in Fig. 2.10. As previously mentioned, the cationic sublattice is not affected by the oxygen addition and the uranium atoms remain in their original positions; the only change for them is an increase of their oxidation state to maintain charge balance. In his model, Willis supposed that the uranium oxidation state changes from 4+ to 5+. This hypothesis was later confirmed by a high-resolution XAS investigation [81] (see section 2.3), even if a study by Conradson *et al.* suggested the presence of U^{+6} in hyper-stoichiometric compounds [82]. According to theoretical calculations, the 2:2:2 cluster proposed by Willis is a metastable structure [83]. For higher oxygen contents (O/U > 2.13), different cluster types have been introduced to describe the structure observed during the progressive formation of long-range ordered phases. For example, cuboctahedral clusters have been proposed by several authors [84–87]. These are formed by a complex rearrangement of the oxygen sub-lattice in eight vacancies and twelve interstitials composed of the eight oxygen atoms that were initially in their normal sites and four added interstitials. These rearrengements lead to the formation of the hyperstoichiometric fluorite-related structures of U_4O_9 and U_3O_7.
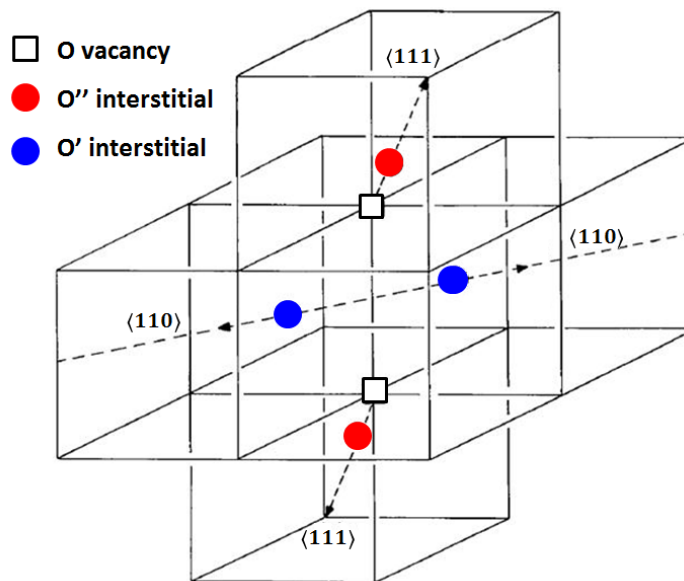
Fig. 2.10: The 2:2:2 cluster representation according to Willis [80]. The corners of the cubes are the sites of normal oxygen atoms. The cluster contains two O′, two O″ atoms and two oxygen vacancies

2.2.1.2   Uranium oxides with O/U>2

As discussed in section 2.1, several uranium oxides, hyperstoichiometric in comparison to UO_2, exist. The polymorphisms of U_4O_9 and the metastable U_3O_7 are closely related to the fluorite structure, whereas the U_3O_8 and UO_3 structures exhibit distinct characteristics.

U$_4$O$_9$

Three polymorphic forms of U$_4$O$_9$ exist.

The α-U$_4$O$_9$ phase is stable only at low temperature and transforms to β-U$_4$O$_9$ at about 350 K [88]. The α-U$_4$O$_9$ stucture is not completely defined yet. A first tentative description based on X-ray diffraction data [89] attributed to this phase a trigonal structure of space group *R3c* (N° 161). According to Belbeoch *et al.*, [89] it would be a slight rhombohedral deformation of a FCC lattice with $\alpha = 90,078°$. Successive studies [84] did not lead to a conclusive description of the atomic arrangement in α-U$_4$O$_9$. According to a recent neutron diffraction investigation [90], the *R3c* space group would be only an approximation of the real structure.

The β-U$_4$O$_9$ phase is cubic, with space group $I\overline{4}3d$ [88]. The β-U$_4$O$_9$ is an ordered super-structure of UO$_{2+x}$, with a unit cell composed of 4x4x4 fluorite-type subcells [84]. The neutron diffraction data of Bevan *et al.*, [84] suggested the cuboctahedral cluster model. A clear representation of the cuboctahedral cluster was provided by Nowicki *et al.*, [52] and it is reported in Fig. 2.11. Looking to the fluorite structure shown in Fig. 2.9, one can observe the cationic FCC cell, inside which a simple cubic anion cell is present. In the β-U$_4$O$_9$, part of the simple oxygen cubes is replaced by cuboctahedral clusters, which are composed of 12 O atoms situated in a cuboctahedron vertices and a 13th oxygen located in its center. Therefore, since it replaces a cube of 8 atoms, the cuboctahedron contains 13-8 = 5 excess oxygen atoms. The cube surrounding the cluster is very close to the FCC cell of the uranium sublattice: the uranium atoms are only slightly shifted from their original positions. According to the cuboctahedral cluster model, β-U$_4$O$_9$ is slightly hypostoichiometric, with an O/M equal to 2.2345 instead of 2.25 [88].
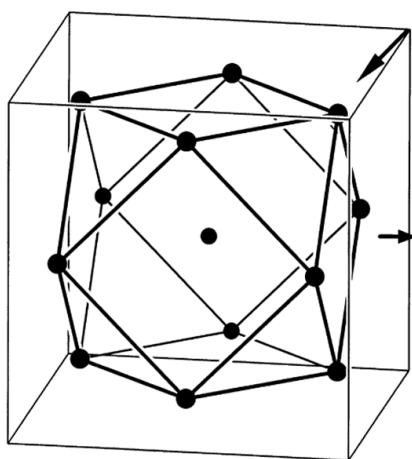
Fig. 2.11: The cuboctahedral oxygen cluster according to Nowicki [52]. The cluster is formed by 12 anions located in the vertices of a cuboctahedron and by a 13th oxygen atom in its centre. The cube which surrounds the cluster represents the FCC cell of the U sublattice. The arrows show (out of scale) displacements of the cations surrounding the cuboctahedron from their ideal positions.

The phase transition from β-U_4O_9 to γ-U_4O_9 occurs at around 850 K [88] and it is based on an order-disorder mechanism. Therefore, the γ-U_4O_9 structure is still cubic but less ordered than the β-U_4O_9 one [89].

U_3O_7

The identification of the U_3O_7 structure was complicated because this phase is not thermo-dynamically stable. Only recently its crystal symmetry and atomic positions were determined thanks to *in situ* neutron diffraction [87]. The U_3O_7 phases are similar to the U_4O_9 ones, with a more important presence of oxygen cuboctahedra. At least three different U_3O_7 polymorphs, named α, β and γ, exist. All of them belong to the tetragonal system and they differ one from the other for the c/a ratio.

α-U_3O_7 was identified as belonging to the space group $I4/m$ (N° 87) and it is the only phase with a c/a ratio lower than 1 [52]. β-U_3O_7 was recently investigated by in situ neutron diffraction at 483 K [87]. The recorded diffraction patterns were refined using the $I\bar{4}2d$ space group (N° 122) and the a and c values were respectively 21.59 Å and 22.23 Å. Finally, few information are available for the γ-U_3O_7, whose structure has not been well identified yet [91].

U_3O_8

The polymorphic forms of U_3O_8 are not related to the fluorite structure. On the contrary, they seem to be hypo-stoichiometric modifications of the UO_3 phases.

The low-temperature α-U_3O_8 and β-U_3O_8 are both orthorhombic, with similar crystal struc-tures, respectively belonging to the space groups $C2mm$ (N° 38) [92] and $Cmcm$ (N° 63) [93]. In the first, uranium occupies the (0.9608, 0, 0; 0, 0.3238, 0) positions, whereas oxygen atoms are on the (0.582, 0, 0; 0.95 ,0, 1/2; 0.194, 0.1239, 0; 0.317, 0.3294, 0; 0.996, 0.3218, 1/2) crystal sites [94]. In the second, uranium is positioned on three c Wyckoff position (0, 0.989, 1/4; 0, 0.350, 1/4; 0, 0.668, 1/4) and oxygen occupies the (0, 0, 0; 0, 0.352, 0.023; 0, 0.165, 1/4; 0.318, 0.024, 1/4; 0.319, 0.312, 1/4) positions [93]. These structures are characterized by short U-O bounds, which are indicative of the U^{6+} presence [93].

Above 480 K, the α'-U_3O_8 appears [94]. This phase has a hexagonal structure with space group $P\bar{6}2m$ (N° 189) [94, 95], with uranium on the (0.3526, 0, 0) position and oxygen on the (0.7453, 0, 0; 0.3609, 0, 0; 1/3, 2/3, 0) positions [94].

Some authors supported the occurrence of another orthorhombic γ-U_3O_8 phase at high tem-perature [49, 96], but others have rejected its existence [97].

UO_3

Several polymorphisms of UO_3 exist and they are mainly based on the layer structures, which are characterized by the existence of $UO_2{}^{2+}$ uranyl groups arranged normal to the plane of the layers [88]. The identified polymorphisms have different symmetries: orthorhombic for α-UO_3

and γ-UO_3, monoclinic for β-UO_3, cubic for δ-UO_3 and triclinic for ϵ-UO_3 [88]. The identification of the space group has been controversial and it is not yet complete.

2.2.1.3   Americium oxides with O/Am<2

As said in section 2.1.2, two sesquioxide compounds and an intermediate phase exist according to Sari and Zamorani [58] and Thiriet and Konings [62], whereas only one sesquioxide and the intermediate phase exist according to Gotcu-Freiss et *al.*, [64]. In spite of the uncertainty about the existence domains of these phases, their structures were easily determined thanks to their isomorphism with the lanthanide sesquioxides.

A-type Am_2O_3

The A-type Am_2O_3 (present in all the phase diagram versions) has a trigonal structure, belonging to the space group $P\bar{3}m1$ [55, 56, 59, 61]. This phase is isomorph with Nd_2O_3 [98]. Thanks to this similarity, the atom positions in A-Am_2O_3 were deduced. The americium atoms occupy the Wyckoff positions *2d* (1/3, 2/3, 0.246) and the oxygen atoms occupy the Wyckoff sites *2d* (1/3, 2/3, 0.647) and *1a* (0, 0, 0).

This structure is known to accept almost only cations with oxidation state 3+ and therefore it does not allow significant departures from stoichiometry.

B-type Am_2O_3

The metastable B-type Am_2O_3 observed in some XRD experiments [56, 61], is isomorph with Sm_2O_3, whose structure has been described by Cromer [99]. It belongs to the $C2/m$ (N° 12) space group of the monoclinic crystal system. The structure is a layer type with all the atoms at y=0 or y=1/2.

C-type phases

The intermediate phase $AmO_{1.61+x}$ and the sesquioxide $AmO_{1.5+x}$ have the same BCC C-type structure of space group $Ia\bar{3}$ (N° 206) [100]. These phases are closely related to the hypostoichiometric fluorite structure, where an increase of oxygen vacancies leads to their ordering into the C-type structure. One oxygen is replaced by one vacancy, at each of the four positions along the <111> direction; the cations located at the center of the faces in the fluorite cell (positions 1/2, 1/2, 0 and equivalent) are displaced to the *24d* Wyckoff sites (on the planes x, y or z=1/4 and 3/4) [101]. The reorganization leads to a new unit cell which is formed by 2x2x2 modified fluorite-type sub-cells.

2.2.2   Crystallographic data at room temperature

In this section, a summary of the room temperature crystallographic data for uranium, americium and mixed oxides is provided. As mentioned, not all the solid phases described above are stable at room temperature. In this case, the data refer to quenched materials, hence out of

	s.g.	Lattice parameters						$\rho[\text{g}\cdot\text{cm}^{-3}]$	ref.
		a[Å]	b[Å]	c[Å]	α	β	γ		
UO_2	$Fm\overline{3}m$	5.471			90	90	90	10.96	[102]
α-U_4O_9	$R3c$	5.444			90.1	90.1	90.1	11.31	[89]
β-U_4O_9	$I\overline{4}3d$	21.77			90	90	90	11.29	[103]
γ-U_4O_9	Cub.				90	90	90		[43]
α'-U_3O_8	$C2mm$	6.716	11.96	4.147	90	90	90	8.40	[94]
α-U_3O_8	$P\overline{6}2m$	6.812	6.812	4.142	90	90	90	8.40	[94]
β-U_3O_8	$Cmcm$	7.069	11.445	8.303	90	90	90	8.33	[93]
α-UO_3	$C222$	6.84	43.45	4.157	90	90	90	7.44	[28]
β-UO_3	$P2_1$	10.34	14.33	3.91	90	99	90	8.3	[28]
γ-UO_3	Fdd	9.813	19.93	9.711	90	90	90	8.0	[28]
δ-UO_3	$Pm3m$	4.16			90	90	90	6.6	[28]
ϵ-UO_3		4.002	3.841	4.165	98.1	90.2	120	8.67	[28]

Table 2.1: Crytstallographic data at room temperature for uranium oxides.

equilibrium.

Room temperature crystallographic data for uranium and americium oxides are reported respectively in Tab. 2.1 and Tab. 2.2. For americium oxides, different values of the lattice parameters can be found in the literature. This uncertainty is due to different factors: first of all, the lattice parameter is affected by the compound purity in a way that is not easily evaluated; second, other factors such as the departure from oxygen stoichiometry and the self-irradiation damage can cause lattice parameter variations. These effects will be discussed in the following sections.

The room temperature $(U,Am)O_{2\pm x}$ lattice parameters found in the literature [69, 71, 105–108] are reported in Tab. 2.3 and represented in Fig. 2.12. As previously said, U-Am mixed dioxides crystallize in a cubic fluorite-type structure, which is isomorph with the UO_2 and AmO_2 compounds. All the lattice parameters in Tab. 2.3 are related to this structure ($Fm\overline{3}m$).

The data are not easy to compare because the lattice parameter depends not only of the americium content, but also of the O/M ratio and the age of the samples, which are not always known precisely. One can qualitatively observe that the lattice parameter decreases as a function of the americium content. However, various authors [105–107] observed that this decreasing is smaller than that one expected by the linear Vegard's law between $UO_2^{4+} - AmO_2^{4+}$ (even taking into account the self-irradiation effecs), as shown in Fig. 2.12. The explanation for this peculiarity was later provided by X-ray absorption spectroscopy investigations, as will be explained in section 2.3.

	O/Am	s.g.	Lattice parameters						Ref.
			a[Å]	b[Å]	c[Å]	α	β	γ	
AmO_2	2.0	$Fm\bar{3}m$	5.377			90	90	90	[56]
	2*		5.372						[104]
	1.96		5.389						[59]
	2*		5.373						[60]
	2*		5.375						[105]
	-		5.391						[61]
$AmO_{1.61+x}$	1.646	$Ia\bar{3}$	10.966			90	90	90	[56]
	1.633		10.92						[56]
	1.616		10.97						[56]
$AmO_{1.5+x}$	1.513	$Ia\bar{3}$	11.013			90	90	90	[56]
	-		11.023						[104]
	-		11.02						[59]
$B\text{-}Am_2O_3$	-	$C2/m$	14.35	3.55	8.92	90	100.4	90	[56]
$A\text{-}Am_2O_3$	1.5	$P\bar{3}m1$	3.805	3.805	5.96	90	90	120	[56]
	1.5*		3.815	3.815	5.975				[104]
	1.5*		3.810	3.810	5.957				[59]
	1.5*		3.821	3.821	5.984				[61]

*: no direct measurement

Table 2.2: Crystallographic data at room temperature for americium oxides (ages of the samples were not provided by the authors).
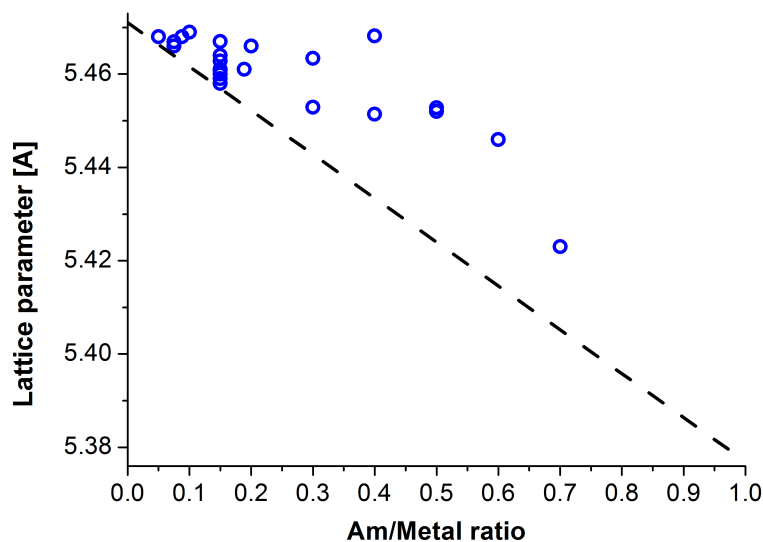
Fig. 2.12: Lattice parameter as a function of the Am content at room temperature for $(U,Am)O_{2\pm x}$ dioxides (uncertainty= symbol size).

2.2.3 Lattice parameter as a function of temperature and oxygen stoichiometry

A rise of the temperature generally causes a dilatation of a crystal lattice. However, in the case of oxide solid solutions, temperature increases can also produce indirect effects on the lattice

Am/M [mol. %]	O/M	a [Å]	Ref.
5.0	2.0	5.468	[108]
7.5	reduced	5.467	[106]
	2.01	5.466	[106]
8,8	5.468	1.96	[105]
10.0	5.469	2.0	[71]
15.0	5.463	reduced	[106]
15.0	5.461	oxidized	[106]
15.0	5.467	2.0	[71]
15.0	5.464	2.0	[71]
15.0	5.461	2.04	[71]
15.0	5.460	2.015	[71]
15.0	5.459	2.017	[71]
15.0	5.458	2.029	[71]
18.9	5.461	1.93	[71]
20.0	5.466	1.99	[71]
30.0	5.4634	reduced	[106]
30.0	5.4529	oxidized	[106]
40.0	5.468	reduced	[106]
40.0	5.451	oxidized, 1.97	[106]
50.0	5.452	2	[107]
50.0	5.483	reduced	[106]
50.0	5.453	oxidized, 1.93	[106]
60.0	5.506	reduced	[106]
60.0	5.446	oxidized	[106]
70.0	5.504	reduced	[106]
70.0	5.423	oxidized	[106]

Table 2.3: Crytstallographic data at room temperature for $(U,Am)O_{2\pm x}$ dioxides with fluorite structure. *Reduced* and *oxidized* refer to two different states of the same sample (not relative to O/M = 2.0).

parameter by changing the oxygen stoichiometry. Indeed, the reduction/oxidation causes an expansion/contraction of the lattice. This is due to the difference between the cationic radii and to the decrease/increase of the cation repulsion shielding provided by oxygen atoms. The ionic radii of uranium and americium are reported in Tab. 2.4 for the oxidation states of interest.

	U^{4+}	U^{5+}	Am^{3+}	Am^{4+}
Ionic radius [Å]	1	0.9	1.09	0.95

Table 2.4: Radii of U and Am ions (coordination 8) [109].

For slightly hyperstoichiometric uranium dioxide UO_{2+x}, an empirical relation between the lattice parameter a and the departure from stoichiometry x (independent from the temperature) was provided [102]:

$$a[\text{Å}] = 5.4705 - 0.132 \cdot x, (0 \leqslant x \leqslant 0.15). \tag{2.3}$$

According to the latter, the lattice parameter varies in first approximation as a linear function of the oxygen content. Similar empirical linear relations were assessed for other actinide oxides, as $(U,Pu)O_{2+x}$ [110], but not for AmO_{2-x} and $(U,Am)O_{2+x}$.

Focusing on the direct effect of temperature, a comparative study of the thermal expansion behavior of different actinide dioxides from thorium to berkelium was firstly proposed by Fahey *et al.*, [111]. According to the latter, the thermal expansion of the lattice parameter as a function of the temperature can be fitted to a second or third order polynomial, which implies that also the thermal expansion coefficients are temperature dependent.

Several data are available for uranium dioxide and the review of Martin [112] recommends:

$$a = a_{273K}(9.9734 \cdot 10^{-1} + 9.802 \cdot 10^{-6} \cdot T - 2.705 \cdot 10^{-10} \cdot T^2 + 4.391 \cdot 10^{-13} \cdot T^3) \tag{2.4}$$

$$a = a_{273K}(9.9672 \cdot 10^{-1} + 1.179 \cdot 10^{-5} \cdot T - 2.429 \cdot 10^{-9} \cdot T^2 + 1.219 \cdot 10^{-12} \cdot T^3) \tag{2.5}$$

where Eq. (2.4) is valid for $273 \leq T \leq 923$ K and Eq. (2.5) is valid for $923 \leq T \leq 3120$ K. These relations are recommended for stoichiometric UO_2 and for UO_{2+x} with x ranging from 0 to 0.13 and from 0.23 to 0.25. The lattice parameter variation of UO_2 as a function of temperature is shown in Fig. 2.13.

The thermal expansion of AmO_2 was measured by Fahey *et al.*, [111], under oxygen, up to 1230 K and by Minato *et al.*, [113] in flowing air, up to 1500 K. The measured lattice parameters are shown and compared to those of UO_2 in Fig. 2.13.

The *a* and *c* lattice parameters of the A-type Am_2O_3 were measured as a function of temperature by Minato *et al.*, [114] and Lebreton *et al* [61]. Their results are shown in Fig. 2.14 (a). Since this phase is almost perfectly stoichiometric, no considerable variation of the O/M ratio occurs and the lattice expansion is only due to the thermal effects. Lebreton *et al* fitted the acquired data using second order polynomials, hence the thermal expansion coefficients were approximated to linear functions of temperature (Fig. 2.14 (b)).

For the $(U, Am)O_{2\pm x}$ mixed oxides, very few high temperature data exist. Some measurements were performed in an $Ar/H_{5\%}$ atmosphere on samples with Am/(U+Am) ratios equal to 0.5, 0.6 and 0.7 by Lebreton [106]. The lattice parameters measured as a function of temperature under reducing atmosphere are shown in Fig. 2.15. However, it is important to remark that the stoichiometry of these samples is unknown and likely not constant during the measurement.

2.2.4 Self-irradiation effects

Heavy atoms, such as the various isotopes of uranium and americium, decay by α-emission:
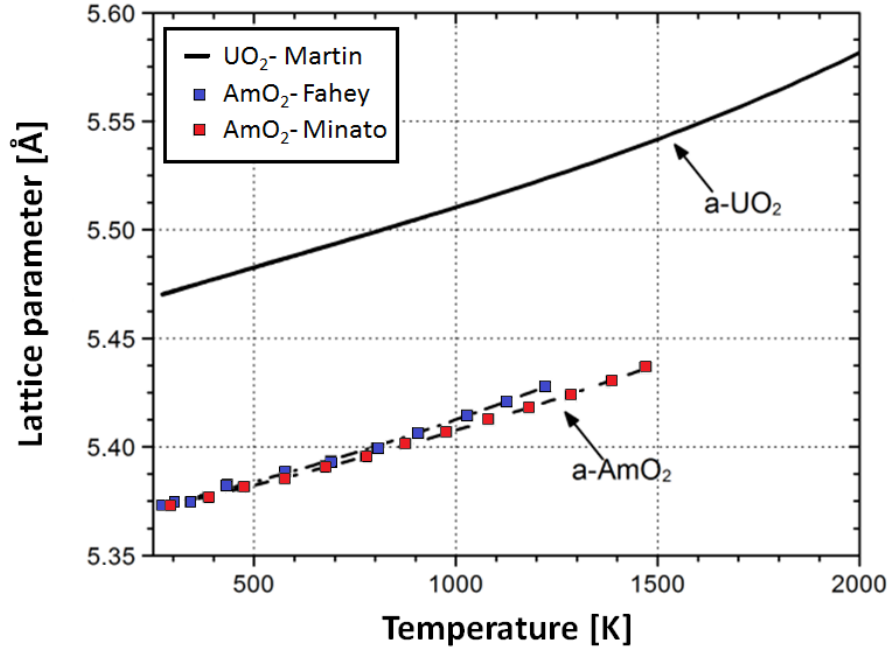
Fig. 2.13: UO$_2$ [112] and AmO$_2$ [111, 113] lattice parameter as a function of temperature.
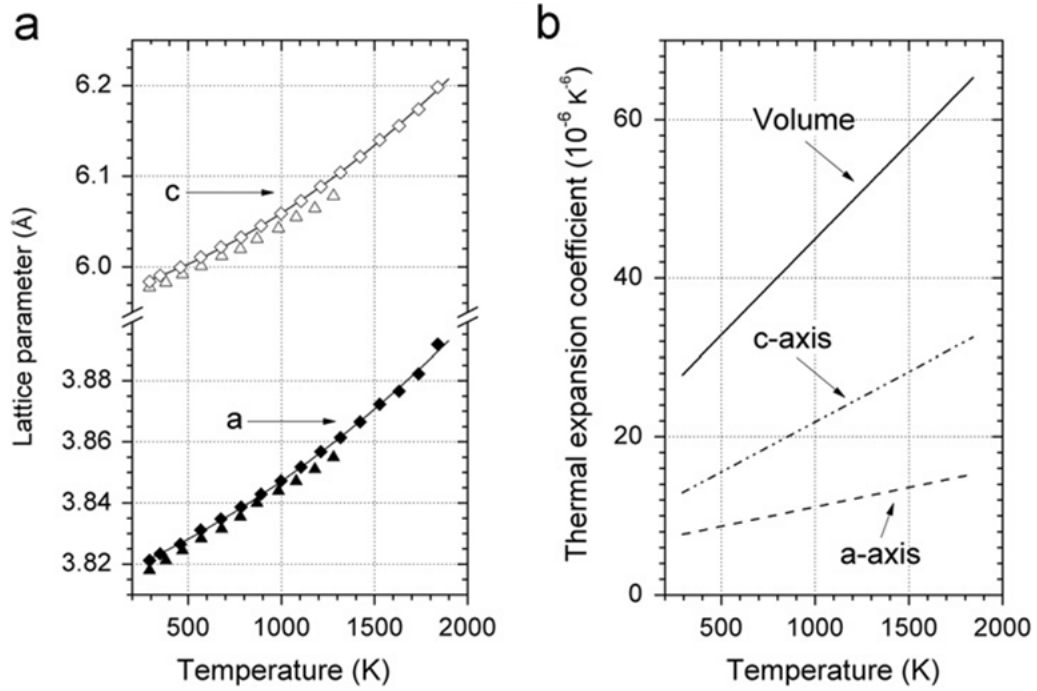
Fig. 2.14: (a) Am$_2$O$_3$ lattice parameters as a function of temperature ($\triangle$: Minato [114] ; $\diamond$: Lebreton [61]) (b) Thermal expansion coefficients from Lebreton. (Figure extracted from [61]).

$$^{A}_{Z}M \rightarrow ^{A-4}_{Z-2} N + ^{4}_{2}\alpha. \qquad (2.6)$$

The α particle is emitted with a kinetical energy of about 5 MeV, whereas the heavy nucleus has a recoil energy of about 100 keV. Considering that the displacement threshold of O and U in the UO$_2$ are respectively 20 and 40 eV, it is evident that an α decay can produce the displacement of many atoms. The ensemble of the point defects (vacancies and interstitials) generated by a
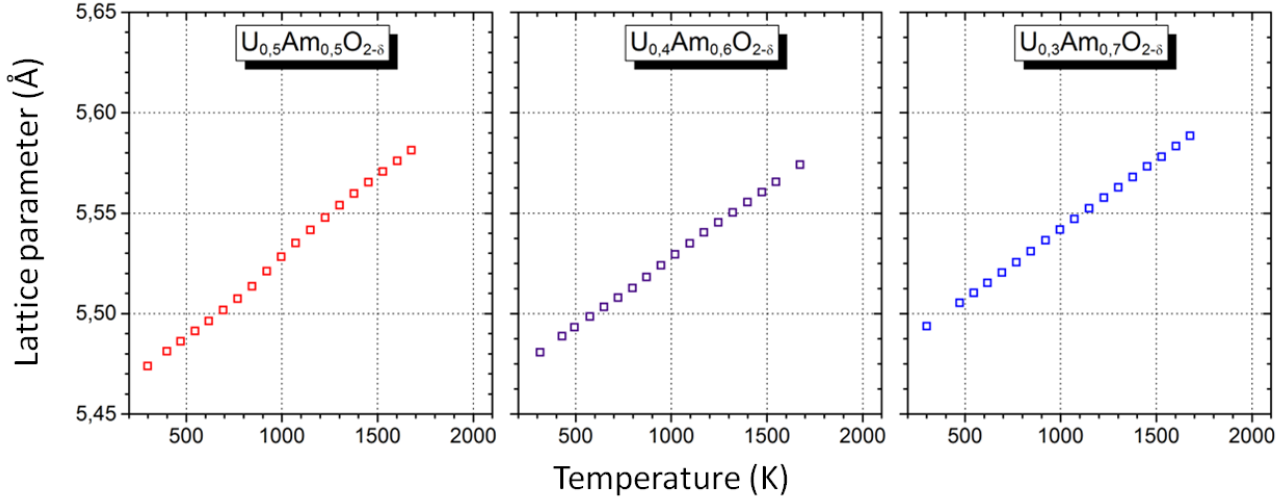
Fig. 2.15: Lattice parameters of U-Am mixed oxides with $Am/(Am+U) = 0.5$, 0.6 and 0.7 as a function of temperature (figure extracted from [106]).

decay is called *displacement cascade*. However, because of the proximity of the point defects, a near-instantaneous annihilation of many of the vacancies and interstitials occurs. The surviving point defects can interact to form defect clusters, dislocations and cavities. The microscopic damages can produce various effects as structural swelling [104], polygonization [115], formation of gas bubbles [116] and phase transitions [104]. Between these self-irradiation effects in actinide oxides, the structural swelling is particularly significant, especially for the elements with high activity such as the Am isotopes (^{241}Am and ^{243}Am). The radiation induced lattice expansion can be expressed, as a function of the time, with an exponential relation of the type [104]:

$$\frac{a_t - a_0}{a_0} = A(1 - e^{-Bt}), \tag{2.7}$$

where a_t is the lattice value at a generic time t, a_0 is the undamaged lattice parameter and A and B are two constants, depending on the particular system. According to this relation, after sufficiently long time, the relative expansion reaches a saturation value, equal to the A constant. The lattice increasing can be equivalently expressed as a function of the accumulated α dose, instead of the time, since the proportionality between these two quantities:

$$\frac{a_t - a_0}{a_0} = A(1 - e^{-B'D}). \tag{2.8}$$

The self-irradiation data presented in the following sections concern studies on samples containing ^{241}Am, which is the most abundant isotope of americium and has a α activity of 128 GBq/g [65].

2.2.4.1   AmO$_2$

Several X-ray diffraction studies were performed in order to investigate the lattice parameter expansion induced by self-irradiation in americium dioxide [56,61,104,117]. All the investigations agreed with an exponential evolution of the type described by Eq. (2.7). The experimental data

and the corresponding fitting curves are shown in Fig. 2.16. The a_0, A, B and B' parameters obtained from Eq. (2.7) and Eq. (2.8) are reported in Tab. 2.5.
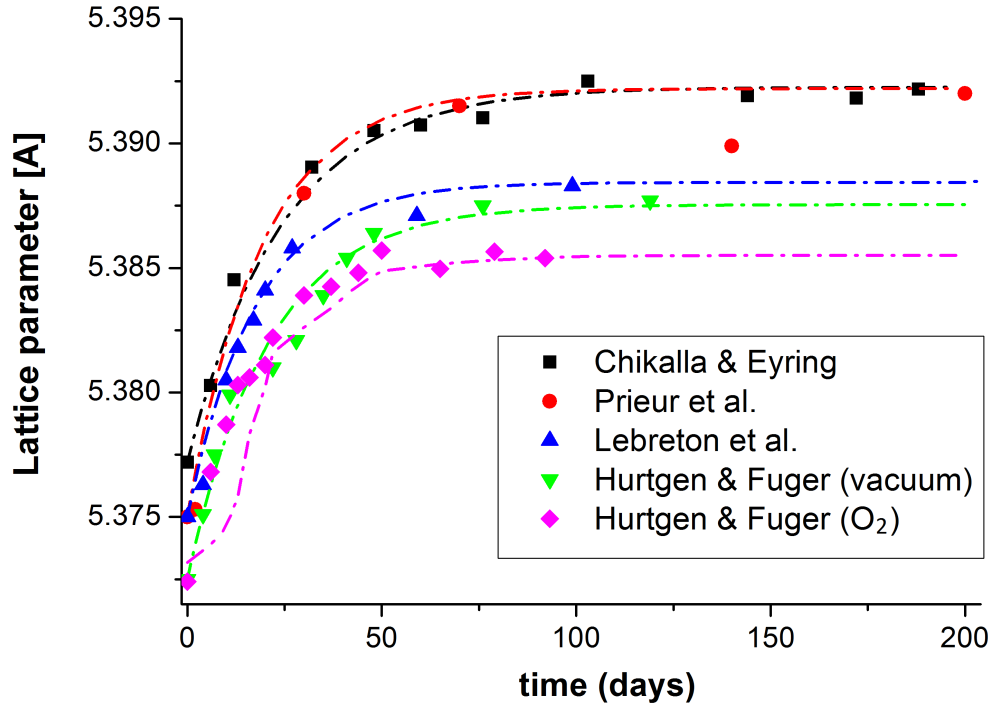
Fig. 2.16: Lattice parameter expansion of AmO_2 as a function of time according to Hurtgen and Fuger [104], Chikalla and Eyring [56], Prieur *et al.* [117] and Lebreton *et al* [61].

The magnitude order of the lattice expansion kinetics is consistent between the different studies, with a saturation achieved in about three months. The maximum relative lattice parameter increasing is included between 0.22 and 0.325 %, according to the different studies. The dispersion between the various lattice parameter data is probably due to impurities, which are usually present in large amount in americium compounds. Moreover, as pointed out from the study of Hurtgen and Fuger, also the atmosphere can have a great importance [104]. Indeed, they followed the self-irradiation effects both in vacuum and in a pure oxygen atmosphere and they found out that the relative expansion at saturation was larger in the first case. They explained the difference with the tendency to lose small quantities of oxygen under effect of the self-irradiation and they estimated an O/M $\sim$1.991 (at saturation) for the sample under vacuum. Nevertheless, contrary to this hypothesis, a recent XAS investigation on a 40 years old AmO_2 sample and a fresh AmO_2 sample (annealed before the measurement) showed no difference in the valence of Am (4+) and therefore on the O/Am ratio [116]. This study also proved that, even after 40 years, corresponding to 36 displacement per atoms (dpa), the fluorite structure was still maintained and the lattice expansion was still limited at the asymptotic value of 0.3%.

2.2.4.2   Other americium oxides

Very few data are available concerning the self-irradiation of other americium oxides. Indeed, only two XRD studies have been presented on the hexagonal Am_2O_3 and the BCC $AmO_{1.5+x}$:

	Chikalla [56]	Hurtgen [104]		Prieur [117]	Lebreton [61]
Atmosphere	-	O_2	vacuum	-	-
A (%)	0.28	0.24	0.28	0.32	0.25
B ($10^{-8}s^{-1}$)	48	70	56	61	66
B' (dpa^{-1})	18	26	21	23	24
a$_0$ (Å)	5.3771	5.3726	5.3725	5.374	5.375

Table 2.5: A, B, B' and a$_0$ parameters according to Eq. (2.7) and Eq. (2.8) which describe the AmO$_2$ lattice parameter expansion due to self-irradiation as a function of time or accumulated dose.

the first one is the old study of Hurtgen and Fuger [104] and the second one is a recent work performed by Horlait *et al.* [118]. Moreover, the two studies show a strong disagreement.

Concerning the hexagonal Am$_2$O$_3$ phase, Hurtgen and Fuger followed the lattice parameter evolution under vacuum and found an exponential increase for both the *a* and the *c* parameters [104], as shown in Fig. 2.17 (black points). The data fitting with the Eq. (2.7) provided the parameters reported in Tab. 2.6. The Hurtgen study shows that the saturation of the lattice expansion is obtained in around 35 days, thus distinctly faster than in the case of the dioxide (3 months).

	a	*c*
A (%)	0.19	0.27
B ($10^{-8}s^{-1}$)	96	110
a$_0$ (Å)	3.8155	5.975

Table 2.6: A, B, and a$_0$ parameters according to 2.7 for the Am$_2$O$_3$ lattice parameter expansion according to Hurtgen and Fuger [104].

Horlait *et al.*, followed the lattice evolution of Am$_2$O$_3$ under air [118]. In this case, considered the instability of this compound, a phase transition toward AmO$_2$ competed with the self-irradiation. Nevertheless, even if the sample underwent an oxidation during the measurements, the oxygen stoichiometry of hexagonal Am$_2$O$_3$ is generally considered constant and thus the evolution of the unit cell parameters of this structure was attributed only to the self-irradiation. As shown in Fig. 2.17, the evolution of the *a* and *c* lattice parameters was very different from that previously reported by Hurtgen: the *a* appeared initially steady and then weakly decreased over twenty days, while the *c* parameter increased almost linearly ($\Delta c/c_0 = 8.2 \cdot 10^{-4} \cdot t$, with *t* in hours). Despite the differences in the lattice parameter evolution, a very similar exponential trend was found for the overall cell volume evolution, as shown in Fig. 2.18. Horlait *et al.* supposed that the discrepancy between the two studies was related to the difference in atmosphere [118]. According to their explanation, the oxidation process under air could affect the way that crystalline structure accommodate self-irradiation defects, thought it remains unclear which mechanism would induce such influence and how it would lead to the same volumetric expansion.
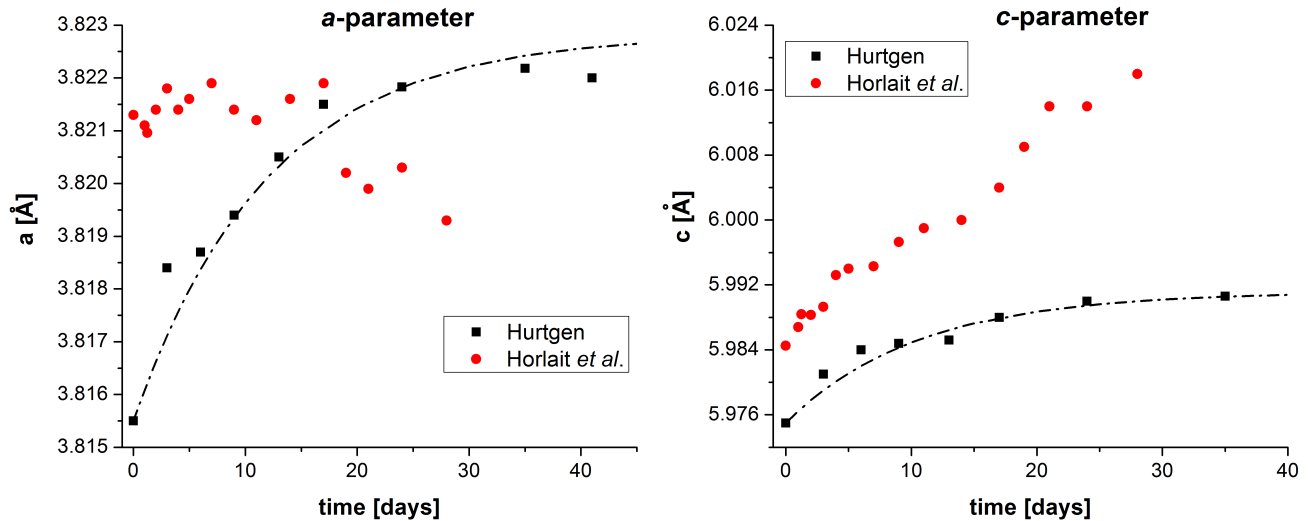
Fig. 2.17: Expansion of the a and c lattice parameters of Am_2O_3 according to Hurtgen and Fuger [104] and Horlait *et al.* [118].

Hurtgen and Fuger [104] and Horlait *et al.*, [118] also studied the evolution of a C-type BCC phase by XRD; even if the exact O/Am was not measured, in both case the compound was identified as the sesquioxide $AmO_{1.5+x}$.

In the Hurtgen investigation [104], the cubic sample was obtained by reduction of americium dioxide under hydrogen at 675 °C and the initial lattice parameter ($a_0 = 11.023$ Å) was consistent with an O/Am around 1.5 [55]. The XRD investigation was performed under vacuum over a period of 3.5 years. Surprisingly, the lattice parameter of the BCC structure did not evolve but a spontaneous transformation toward the hexagonal form was observed after two years.

In the study of Horlait *et al.* [118], the BCC phase was present in small quantities (15 %) in the observed sample and for this reason the lattice parameter determination was quite imprecise. Moreover, as for the hexagonal form, the BCC phase disappeared during the oxidation. Nevertheless, a progressively linear increase was observed over a period of twenty days. The proposed fitting equation is $\Delta a/a_0 = 4 \cdot 10^{-4} t$, with t in hours. Trying to explain the discrepancies with the Hurtgen study, Horlait *et al.* suggested that the no-evolution of the cell parameter observed by Hurtgen could be due to the compensation of self-irradiation effects by the $AmO_{1.5+x}$ oxidation, resulting in a cell parameter decrease. Anyway, this hypothesis is not convincing because the Hurtgen experiment was conducted under vacuum and the BCC structure evolved toward the reduced hexagonal form. In conclusion, the self-irradiation behavior of both the cubic and the hexagonal americium sesquioxides is far from be clear.

2.2.4.3 (U,Am)O$_{2\pm x}$

Horlait *et al.* and Lebreton investigated extensively the self-irradiation effects on uranium and americium mixed dioxides with various americium contents [106], [119]. In particular, Horlait followed the lattice expansion by XRD for samples with Am/(U+Am) equal to 7.5, 15, 30, 40 and 50 mol.%, whereas Lebreton *et al.* completed the investigation on higher americium contents (60 and 70 mol.%). The absolute and relative evolutions of the lattice parameters as
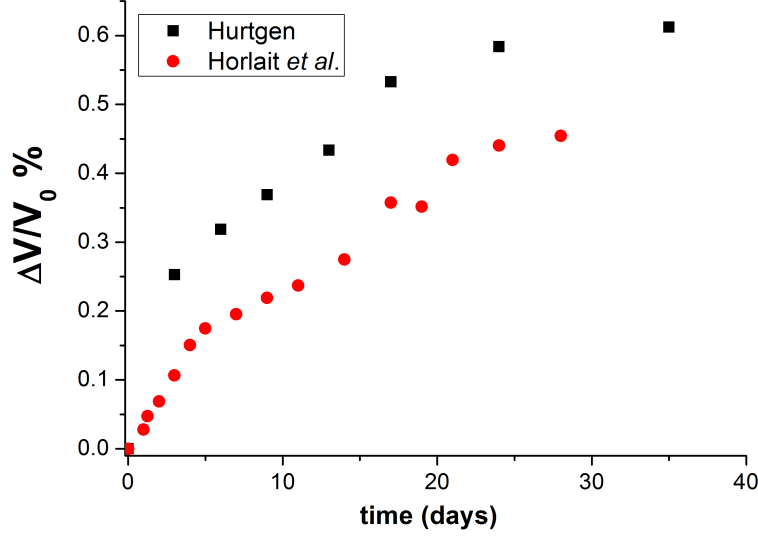
Fig. 2.18: Relative evolution of Am_2O_3 unit cell volume according to Hurtgen and Fuger [104] and Horlait *et al.*, [118].

a function of time for the various compositions are reported in Fig. 2.19. In all the cases, an exponential behavior of the type described by Eq. (2.7) Eq. (2.8) is observed and the A, B, B' and a_0 parameters obtained by the data fitting are reported in Tab. 2.7. The relative parameter expansion at saturation is similar for all the compositions, even if a slightly decrease is observed in the sample with highest americium contents (60% and 70%). As expected, the B parameters increase as a function of the Am content, whereas, expressing the lattice evolution as a function of the accumulated dose, instead of the time, the obtained B' parameters are independent of the Am/(U+Am) ratio.
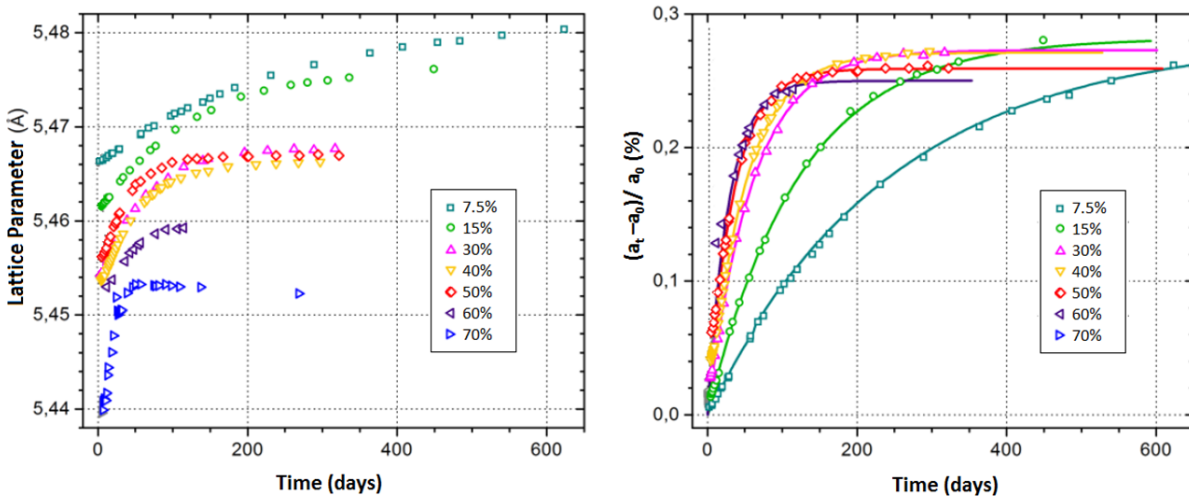
Fig. 2.19: Self-irradiation induced absolute and relative evolution of the lattice parameter for $(U,Am)O_{2 \pm x}$ with Am/(U+Am) = 7.5, 15, 30, 40, 50, 60 and 70 mol.% [106, 119].

Am/(U+Am) [mol. %]	a_0[Å]	A[%]	$B[10^{-8}s^{-1}]$	$B'[10^{-18}g]$
7.5	5.466	0.282	4.8	5.7
15	5.461	0.283	9.5	5.7
30	5.453	0.273	19.4	5.3
40	5.451	0.271	23.1	5.3
50	5.453	0.259	33.6	6.0
60	5.446	0.25	41	6.1
70	5.423	0.57	103	9

Table 2.7: A, B, B′ and a_0 parameters of Eq. (2.7) and Eq. (2.8) for (U,Am)O$_{2\pm x}$ oxides wih various Am contents, according to [106] and [119].

2.3 Oxidation states and local structure

X-ray absorption spectroscopy (XAS) has recently proved to be a very useful technique to investigate the local and electronic structure surrounding cations in actinide oxides [69, 120–123]. X-ray Absorption Near-Edge Structure (XANES) provides information on the average oxidation state and local symmetry of the probed element and Extended X-ray Absorption Fine Structure (EXAFS) allows determining the distances from its neighbour atoms. A description of these techniques will be given in Appx. A, whereas the data acquired on uranium, americium and U-Am mixed oxides are presented here.

2.3.1 Uranium oxides

As mentioned in section 2.2, uranium is purely tetravalent in stoichiometric UO$_2$. The oxidation states in hyperstoichiometric UO$_{2+x}$, mixed-valence U$_4$O$_9$ and U$_3$O$_8$ had been debated for a long time. Various XANES investigations at the U L$_{III}$ edge ($\sim$ 17.1 keV) were performed [82,124,125], but the chemical shift of the main edge transition for U oxidation states between 4+ and 6+ is about 1.0 eV and this value is small compared to the 7.4 eV line broadening, due to the core hole life time of the U 2$p_{3/2}$ level. Moreover, the XANES spectrum shape depends on the symmetry around the probed atom, hence it is considerably different when passing from the cubic environment, of UO$_2$ and U$_4$O$_9$, to the less symmetric structures of U$_3$O$_8$. Under these conditions, a certain conclusion on the presence of U^{5+} rather than U^{6+} was not possible. A straightforward identification of the oxidation state changes during the conversion of UO$_2$ to the mixed-valence U$_4$O$_9$ and U$_3$O$_8$ was finally achieved by Kvashnina *et al.* [81]. In this work, the U M$_{IV, V}$ absorption edges were probed by high energy resolution fluorescence detection (HERFD) X-ray absroption spectroscopy, at the beam line ID26 of the European Synchrotron Radiation Facility (ESRF), in Grenoble (France) [81]. Thanks to the smaller lifetime broadening of the core hole at the 3$d_{3/2,5/2}$ levels and to the HERFD set-up, an energy resolution of 0.7 eV was achieved. Calculated and experimental HERFD spectra acquired by Kvashnina *et al.*, [81] at the U M$_{IV}$ edge of UO$_2$, U$_4$O$_9$, U$_3$O$_8$ and an uranyl acetylacetonate UO$_2$(acac)$_2$, are shown in Fig. 2.20. The latter presents two peaks: the first one at $\sim$3727.0 eV is characteristic of U^{+6}. The dashed lines indicate the energy position of the main peaks corresponding to uranium in oxidation state +4 and +6. Two intense peaks were observed for U$_4$O$_9$: the first, at $\sim$ 3725.0 eV,

corresponds to U^{+4}, whereas the second peak was associated to U^{+5}, since it is at lower energy than the U^{+6} peak. For the U_3O_8, the intense structure at ~ 3727.5 eV was attributed to U^{+5}, whereas the asymmetry at the higher energy was identified as the U^{+6} contribution. Therefore, no contribution of U^{+4} was identified for this compound.
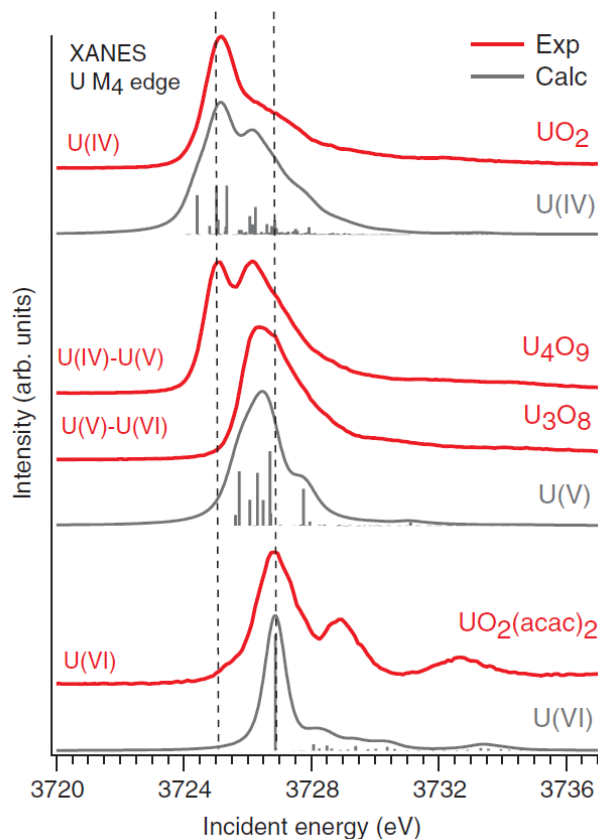
Fig. 2.20: HERFD-XANES experimental and calculated spectra at the U M_{IV} edge of U_4O_9 and U_3O_8, compared to U_4O_9, UO_2 and $UO_2(acac)_2$ (figure extracted from [81]).

Concerning the local environment in the UO_2 $Fm\bar{3}m$ fluorite structure, the cations are surrounded in the first four shells by 8 anions, 12 cations, 24 anions and 6 cations. The Fourier Transforms (FT) of a k^3-weighted EXAFS spectrum collected at the U L_{III} edge is shown in Fig. 2.21. Two main peaks can be observed: the first, at ~ 1.8 Å, corresponds to the first cation-oxygen shell, whereas the second one, at ~ 3.8 Å, is mainly due to the closest U atoms. Typical neighbour distances are reported in Tab. 2.8. In the oxidation process of UO_{2+x} toward U_4O_9, oxygen atoms are accommodated in the fluorite structure, as already explained in section 2.2.1.1. The resulting disorder causes a decrease of the amplitude of the EXAFS signal, as shown in Fig. 2.21. Moreover, the first peak, which is clearly the most affected by the oxygen cluster formation, is broadened and shifted towards lower R. This shift is due to the partial oxidation of uranium from the tetravalent to the pentavalent state and to the accumulation of interstitials, which cause a decrease in the U-O distances. A different structural model was presented by Conradson *et al.* [82] who, analysing EXAFS spectra, concluded that oxygen atoms were incorporated in U_4O_9 as oxo-groups with U-O distances lower than 1.77 Å. However, this model was later contradicted by the neutron diffraction study of Garrido *et al.* [86].
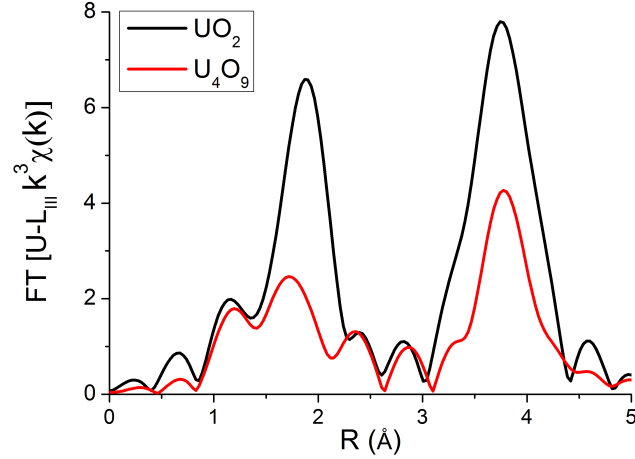
Fig. 2.21: Fourier transform of the $k^3 \cdot \chi(k)$ EXAFS spectra at the L_{III} edge of UO_2 and U_4O_9 [73].

		UO_2, U L_{III}	
Shell	Distance [Å]	Coordination number	σ^2 [Å^2]
O1	2.355(5)	7.9(5)	0.0031(5)
U1	3.866(5)	11.9(5)	0.0015(5)
O2	4.52(1)	26(5)	0.005(2)
U2	5.46(2)	6(1)	0.003(1)

Table 2.8: Atomic distances, coordination numbers and Debye-Waller factors of UO_2 [73].

2.3.2 Americium Oxides

Nishi *et al.*, investigated $^{243}AmO_2$ [126] and $^{243}Am_2O_3$ [123] by XAS, probing the Am-L_{III} absorption edge at the hard X-ray station BL-27 in the Photon Factory of High Energy accelerator Research Organization (KEK).

The AmO_2 white line position (maximum of the peak) was found at 18.522 keV (calibration with the Zr K-edge = 17.998 keV) [126], whereas the Am_2O_3 white line was 4 eV lower. The difference is consistent with the chemical shift between Am^{3+} and Am^{4+}. The absorption peak energy later found by Prieur *et al.* on $^{241}AmO_2$ is in good agreement: 18521.3 eV for the white line and 18513.6 eV for the edge energy (inflection point) [116].

The atomic positions and coordination number obtained from the EXAFS data for the fluorite-type AmO_2 and the hexagonal Am_2O_3 structures determined by Nishi *et al.* [123] [126], fitting the EXAFS data, are reported in Tab. 2.9. The AmO_2 values of Nihi *et al.* are in very good agreement with those later determined by Prieur *et al* [116].

2.3.3 U-Am mixed oxides

The first study of the oxidation states of uranium and americium in mixed dioxides was performed by Mayer *et al.* [107], who investigated an equimolar sample by photoelectron spectroscopy. The

Shell	Distance [Å]	Coordination number
AmO_2		
O1	2.318	8.1
Am1	3.803	11.7
O2	4.461	24.5
Am2	5.401	5.8
Am_2O_3		
O1	2.299	3
O2	2.386	1
O3	2.650	3
O4	3.594	1
Am1	3.676	3
Am2	3.753	3
Am3	3.818	6
O5	4.457	3
O6	4.502	6
O7	4.648	3

Table 2.9: Atomic distances and coordination numbers of AmO_2 and Am_2O_3 [126] [123].

results revealed that americium was purely trivalent, whereas uranium had a mixed 4+/5+ oxidation state.

Prieur *et al.* investigated several $(U,Am)O_2$ samples, manufactured in different conditions and with Am/(Am+U) ratios ranging between 0.1 and 0.2, by probing the U L_{III}, L_{II} and Am L_{III} edges [69,71].
XANES spectra always showed identical Am L_{III} edges, which were at lower energy than AmO_2 and perfectly aligned with a $(U^{4+}_{0.9},Am^{3+}_{0.1})_2$ (C_2O_4), $6H_2O$ oxalate reference. This allowed to conclude that americium was purely trivalent in the mixed dioxides, confirming the results of Mayer *et al.* [107]. Concerning uranium, the XANES spectra showed a slight shift of the white line positions compared to $UO_{2.00}$, but they remain in any case below the position observed for U_4O_9. The U^{+4}/U^{+5} cation fractions were assessed by Prieur *et al.* performing a linear combination fit of the XANES spectra with the $UO_{2.00}$ and U_4O_9 references [69,71]. Moreover, from the average oxidation states of cations, the O/M ratios of the investigated samples could be determined. It was found out that, for almost stoichiometric compounds (O/M $\sim$ 2.00(1)), the U^{+5} fraction was very close to the (trivalent) Am content, suggesting a charge compensation mechanism. A slightly oxidized $U_{0.85}Am_{0.15}O_{2.04}$ sample exhibited an U^{+5} fraction around 0.23, indicating an additional contribution due to the oxygen accommodation in interstitial positions. The EXAFS spectra collected at the U L_{II} and Am L_{III} edges showed that the peculiar charge distribution between Am and U occurs without dramatic modifications of the structure [69,71]. Indeed, these data were correctly fitted using a fluorite $Fm\bar{3}m$ model. However, the charge distribution induced some effects on the local structure. The reported first Am-O distance was about 2.42 Å, which is significantly longer than that of AmO_2 (2.32 Å). This is consistent with the trivalent oxidation state of Am, since the cation radius of Am^{3+} is larger than that of Am^{4+}

(see Tab. 2.4). The first U-O distance was about 2.34 Å, hence shorter than that in UO_2 (2.36 Å), in agreement with the partial oxidation of uranium to 5+. Finally, a decrease of the spectral amplitude with the Am content was observed by Prieur *et al.*, indicating an increasing disorder of the solid solution.

Lebreton *et al.* continued the study of the local structure of $(U,Am)O_{2\pm x}$ dioxides, investigating an equimolar sample [73]. The XANES data collected at the Am L_{III} edge, showed on the left side of Fig. 2.22, confirmed the presence of Am only in the trivalent state. For uranium, the shift of the edge toward higher energy than that of UO_2 was more important than the previous cases: the white line position was between those of U_4O_9 and U_3O_8, as shown in Fig. 2.22, and the average oxidation state equal to 4.65(3). The EXAFS spectra of the Am L_{III} edge confirmed a local fluorite structure around americium. On the contrary, the EXAFS data collected at the U L_{II} edge showed some differences from the fluorite structure. The Fourier transform of the spectrum remained composed by two main peaks, but their intensity was considerably lower than that of UO_2, especially for the first peak (first oxygen shell), which was also significantly broader. Lebreton *et al.* fitted these data using a modified fluorite structural model, in which one of the oxygen of the first shell was replaced by two interstilial atoms in cuboctahedral position [73].
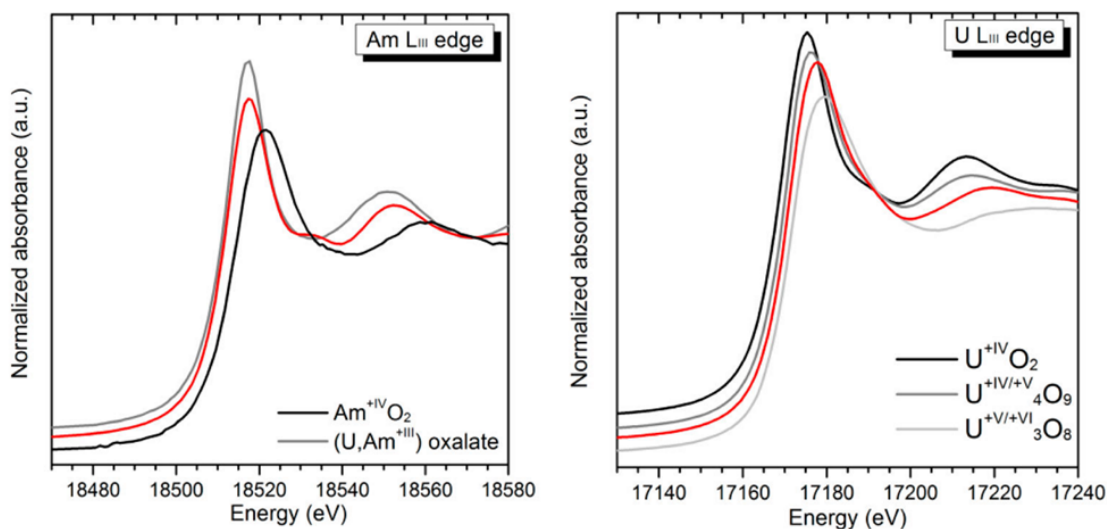
Fig. 2.22: XANES spectra at the Am L_{III} edge (left) and at the U L_{III} edge (right) of a $U_{0.5}Am_{0.5}O_{1.94}$ sample (in red), compared to reference compounds (figure extracted from [73]).

2.4 Thermodynamic properties

Thermodynamic data for uranium, americium and mixed oxides will be presented here. In section 2.4.1, the room temperature enthalpies of formation and standard entropies will be reported. Then, the variation of enthalpy with the temperature and the derived heat capacity functions will be shown in section 2.4.2. Finally, oxygen potentials, which are fundamental thermodynamic properties for oxide solid solution, and partial vapour pressures for the different systems will be discussed, respectively in section 2.4.3 and 2.4.4.

2.4.1   Standard enthalpy of formation, entropy and Gibbs energies

2.4.1.1   Uranium oxides

Standard entropy and enthalpy of formation at 298.15 K of the different uranium oxides were critically reviewed by Konings *et al.* [127] and the recommended values are reported in Tab. 2.10.

Oxide	$\Delta_f H°$	$S°$	$\Delta_f G°$
UO_2	-1085.0 $\pm$ 1.0	77.03 $\pm$ 0.2	1032 $\pm$ 1
U_4O_9	-4512 $\pm$ 7	334.1 $\pm$ 0.7	-4535 $\pm$ 7
U_3O_8	-3574.8 $\pm$ 2.5	285.55 $\pm$ 0.50	-3369.5 $\pm$ 2.5
γ-UO_3	-1223.8 $\pm$ 2.0	96.11 $\pm$ 0.40	-1112.7 $\pm$ 2.0

Table 2.10: Standard enthalpy of formation, standard entropy and standard Gibbs energy of formation at 298.15 K for various uranium oxides [127].

2.4.1.2   Americium oxides

The enthalpy of formation of AmO_2 was measured by Morss and Fuger, who determined the enthalpy of solution in H_2SO_4 + KI [128]. The Born-Haber cycle used in that work was based on the dissolution of $AmCl_3$ in the same solution. The resulting value is reported in Tab. 2.11.

The enthalpy of formation of the hexagonal americium sesquioxide Am_2O_3 was measured by Morss *et al.* from the enthalpy of solution in hydrochloric acid [129]. The Born-Haber cycle used in that work was based on the dissolution of metal americium in the same medium. The resulting value is reported in Tab. 2.11.

No experimental values are available for the standard entropies of AmO_2 and Am_2O_3. The estimations of Konings [127], based on the systematics in the entropies of actinide(3+) and actinide(4+) compounds, are reported in Tab. 2.11.

Oxide	$\Delta_f H°$	$S°$	$\Delta_f G°$
AmO_2	-932.2 $\pm$ 3.0	75.5 $\pm$ 3.0	-877 $\pm$ 5
Am_2O_3	-1690 $\pm$ 7	134.2 $\pm$ 5.0	-1605 $\pm$ 10

Table 2.11: Standard enthalpy of formation, standard entropy and standard Gibbs energy of formation at 298.15 K of americium dioxide and hexagonal sesquioxide.

2.4.2   High-T enthalpy increment and heat capacity

2.4.2.1   Uranium oxides

Several measurements of both low and high temperature heat capacity and of enthalpy increments for T > 300 K were performed on the various uranium oxides. The various data were

re-fitted by Konings *et al.*, and the relative recommendations for U_4O_9, U_3O_8 and UO_3 can be found in this review [127]. Only the UO_2 case will be detailed here.

There are numerous studies of the thermal properties of UO_2 above room temperature, extending into the liquid range up to 8000 K. The high temperature data have been obtained as enthalpy increments [130–138] and heat capacity values [41, 139–142]. These are reported respectively in Fig. 2.23 and Fig. 2.24.
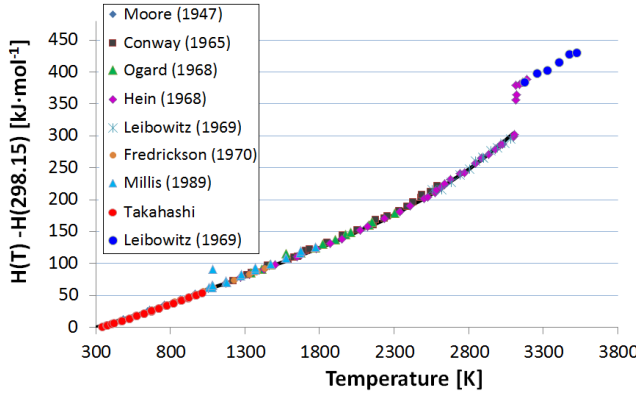
Fig. 2.23: High temperature enthalpy increments of UO_2 [130–138].
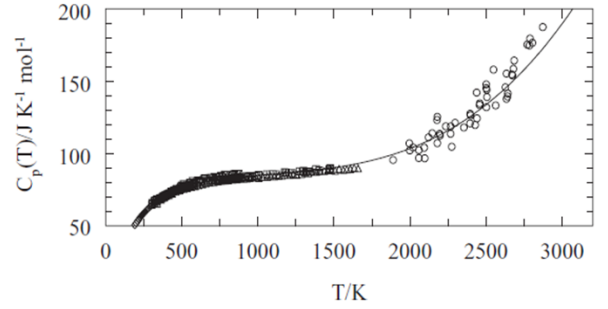
Fig. 2.24: Heat capacity of UO_2 [41, 139–142].

Ronchi and Hyland [143] provided a theoretical description of the contribution from the different physical process to the heat capacity. They explained that from room temperature to 1000 K, the heat capacity trend is governed by harmonic lattice vibrations, which can be approximated by a Debye model. From 1000 K up to 1700 K, the increase in heat capacity is due to anharmonicity of the lattice vibrations. It is now well established that the UO_2 heat capacity shown an anomalous increase above 1700 K. The latter is due to the formation of lattice and electronic defects with the main contribution from Frenkel pairs. The heat capacity measurements in the pre-melting region by Hiernaut *et al.* [139] showed a λ-transition at around 2670 K ($\sim 0.8\cdot$ melting temperature), which was then confirmed by neutron scattering [144]. Finally, Ronchi *et al.* [140] measured the thermal diffusivity and the heat capacity from 2000 to 2900 K using 1 and 10 ms laser pulses, but these measurements lacked the sensitivity for detecting the λ peak. A combined fit of all the enthalpy and heat capacity data was performed by Konings *et al.* [127]. The recommended equation for the heat capacity is:

$$C_p(J \cdot K^{-1} \cdot mol^{-1}) = 66.7437 + 43.1393 \cdot 10^{-3}T - 35.640 \cdot 10^{-6}T^2 +$$
$$+ 11.655 \cdot 10^{-9}T^3 - 1.16863 \cdot 10^6 T^{-2}. \quad (2.9)$$

For the enthalpy increment above room temperature, the recommendation of Fink is [25]

$$H(T) - H(298.15K) = -21.1762 + 52.1743 \cdot t - 43.9735 \cdot t^2 +$$
$$- 28.0804 \cdot t^3 + 7.88552 \cdot t^4 - 0.52668 \cdot t^5 + 0.71391 \cdot t^{-1}, \quad (2.10)$$

where $t = T/1000$, T is the temperature in Kelvin and the enthalpy is in $kJ \cdot mol^{-1}$.

2.4.2.2   Americium oxides

The enthalpy increment with temperature of AmO_2 and Am_2O_3 were measured respectively between 335 and 1080 K and from 335 to 1086 K by Nishi *et al.*, using drop calorimetry [145]. The $^{243}AmO_2$ and $^{243}Am_2O_3$ samples were encapsulated in platinum containers in order to avoid their degeneration, but this also increased the uncertainty of the measurements. The enthalpy values $H(T) - H(298.15K)$, measured by Nishi *et al.* [145], are shown in Fig. 2.25, normalized to 1 mole of metal, and compared to the enthalpy function of UO_2. The two dioxides share a very similar trend in the investigated temperature range, whereas the enthalpy values of the sesquioxide are lower.

Nishi *et al.* [145] fitted the enthalpy data using the least square minimization and the found correlations, respectively for AmO_2 and Am_2O_3, are:

$$H(T) - H(298.15K) = -37.847 + 0.088240 \cdot T - 6.5749 \cdot 10^{-7} \cdot T^2 +$$
$$+ 3422.7 \cdot T^{-1} \quad (2.11)$$

$$H(T) - H(298.15K) = -29.149 + 0.070067 \cdot T - 1.8034 \cdot 10^{-6} \cdot T^2 +$$
$$+ 2414.4 \cdot T^{-1} \quad (2.12)$$

where the enthalpy is in kJ·mol^{-1}. By derivation of these two equations, the heat capacity functions, shown in Fig. 2.25 (right side), were assessed by Nishi *et al.* [145]. However, according to Konings *et al.* [127], these fits yielded to too low values near room temperature, because of the high uncertainty of the experimental points [127, 145]. Therefore, they re-fitted the data constraining the $C_p(298.15K)$ to 116.5 J·K^{-1}·mol^{-1} for Am_2O_3 and to 64.3 J·K^{-1}·mol^{-1} for AmO_2, from the systematics in lanthanide and actinide oxides. The heat capacity function obtained in this way are also shown in Fig. 2.25.

2.4.2.3   U-Am mixed oxides

For mixed uranium and americium dioxide, only one set of high temperature enthalpy increments has been reported in the literature, by Vălu *et al.* [146]. The authors investigated by drop calorimetry $(U_{1-y}, Am_y)O_{2\pm x}$ dioxides with y = 0.09 and 0.19 in the 425-1790 K temperature range. The samples were manufactured by a sol-gel process [105], with a sintering under humidified Ar/H_2 atmosphere at 1920 K (hydrogen fraction not specified). No direct measurement of the O/M ratios was possible, but XRD was performed before and after the enthalpy measurements and, even if the *ages* of the samples were not specified, a decrease of the lattice parameters was highlighted by the authors: from 5.477(2) Å to 5.463(2) Å for y = 0.09, and from 5.469(3) Å to 5.454(3) Å for y = 0.19. Therefore, an oxidation likely occurred in the drop calorimeter, despite the inert atmosphere of He used for the measurements. From comparison of the lattice parameter with literature data, Vălu *et al.* estimated the final O/M ratios of the
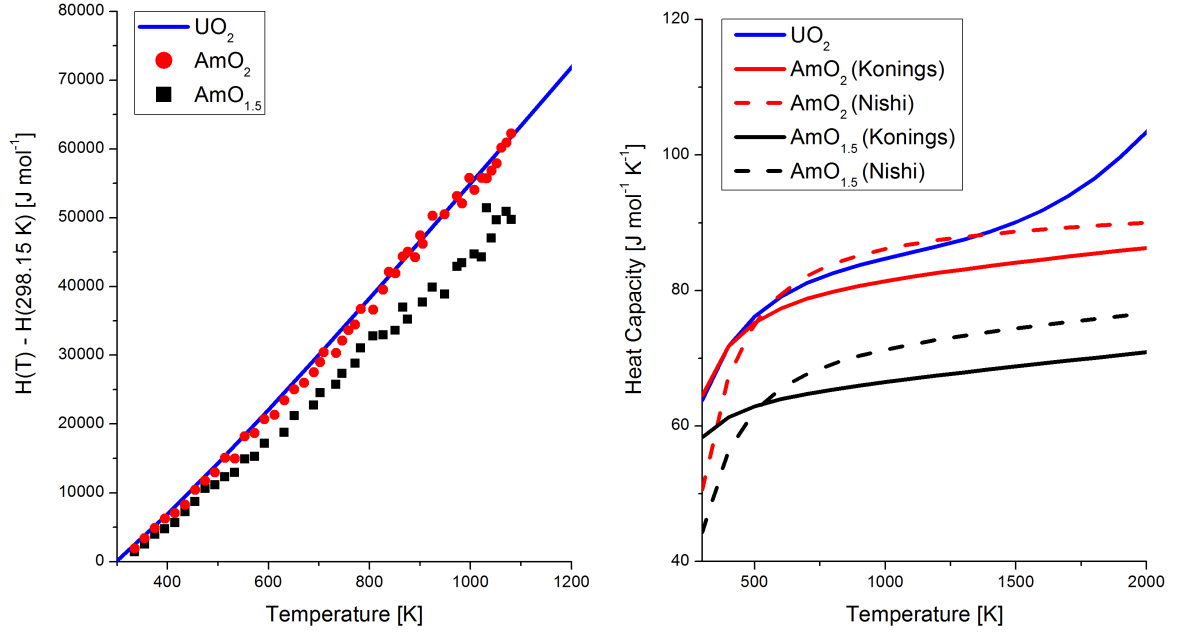
Fig. 2.25: Left: enthalpy increment with temperature of AmO_2, Am_2O_3 [145] and UO_2 [120] (normalized to 1 mole of metal). Right: heat capacity of UO_2, and two possible fits of the Nishi data for Am_2O_3 and AmO_2 [127, 145].

samples in the range 1.97-1.99 [146].

The obtained enthalpy values, shown on the left of Fig. 2.26, followed the same trend as the UO_2 and AmO_2 end members and the authors concluded on the validity of the Kopp-Neumann additivity rule for the studied compositions. The latter was applied to constrain the heat capacity value at room temperature for the fit of the data. The obtained heat capacity functions, respectively for y = 0.09 and 0.19, are:

$$C_p(J \cdot K^{-1} \cdot mol^{-1}) = 74.172 + 14.601 \cdot 10^{-3}T - 1.321384 \cdot 10^6 T^{-2}; \tag{2.13}$$

$$C_p(J \cdot K^{-1} \cdot mol^{-1}) = 62.367 + 23.054 \cdot 10^{-3}T - 0.489837 \cdot 10^6 T^{-2}. \tag{2.14}$$

The latter are represented on the right side of Fig. 2.26.

2.4.3 Oxygen potentials

The partial molar free energy of oxygen, commonly named oxygen potential and denoted by $\Delta\overline{G}(O_2)$, is a fundamental property of an oxide solid solution. It can be expressed as

$$\Delta\overline{G}(O_2) = RTln(pO_2), \tag{2.15}$$

where T is the temperature (in K), R is the gas constant equal to 8.314 J mol^{-1} K^{-1} and pO_2 is the partial pressure of gaseous oxygen which is in thermodynamic equilibrium with the solid. This implies that, if the solid oxide (s) is in contact with a gas (g) with a different oxygen potential, hence a pO_2 that does not correspond to the equilibrium, there will be a net exchange of oxygen
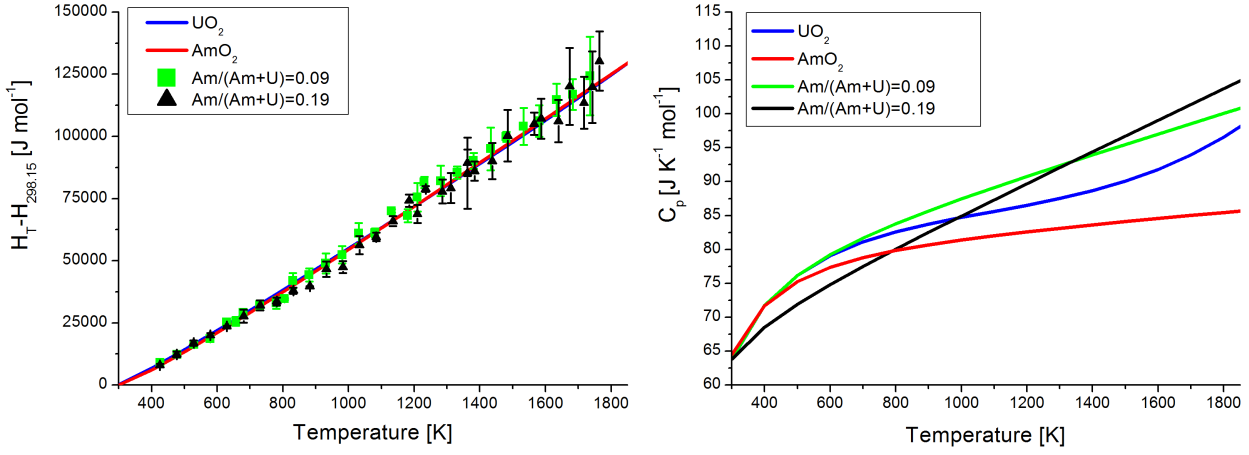
Fig. 2.26: Left: H increment with temperature of $(U_{1-y}, Am_y)O_{2\pm x}$ with y=0.09 and 0.19 [146], compared to binary systems. Right: C_p functions derived by fitting the enthalpy data.

between the solid and the gas. If $\Delta\overline{G}(O_2)_s > \Delta\overline{G}(O_2)_g$, the oxide will release oxygen toward the atmosphere and it will be reduced; vice versa, if $\Delta\overline{G}(O_2)_s < \Delta\overline{G}(O_2)_g$, the oxygen will move from the gas toward the solid.

2.4.3.1   Uranium oxides

Several oxygen potential measurements were reported in the literature for $UO_{2\pm x}$ and these were critically reviewed by Labroche [147] and Baichi [148]. $\Delta\overline{G}(O_2)$ data as a function of the O/U ratio, for various temperatures, are shown in Fig. 2.27, extracted from [27]. The oxygen potential curves for $UO_{2\pm x}$ have a peculiar *S shape*, with a steep variation near O/U=2. This shape is due to the possibility to both reduce and oxidize $UO_{2\pm x}$.
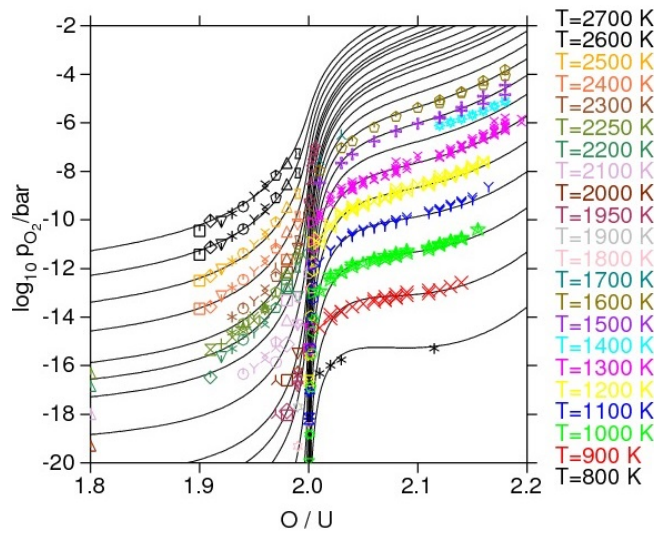
Fig. 2.27: Oxygen potentials of $UO_{2\pm x}$: experimental data and computed curves by Guéneau *et al.* [27].

2.4.3.2 Americium oxides

As mentioned in section 2.1.2, three sets of oxygen potentials were reported in the literature for americium oxides. These are compared in Fig. 2.28.
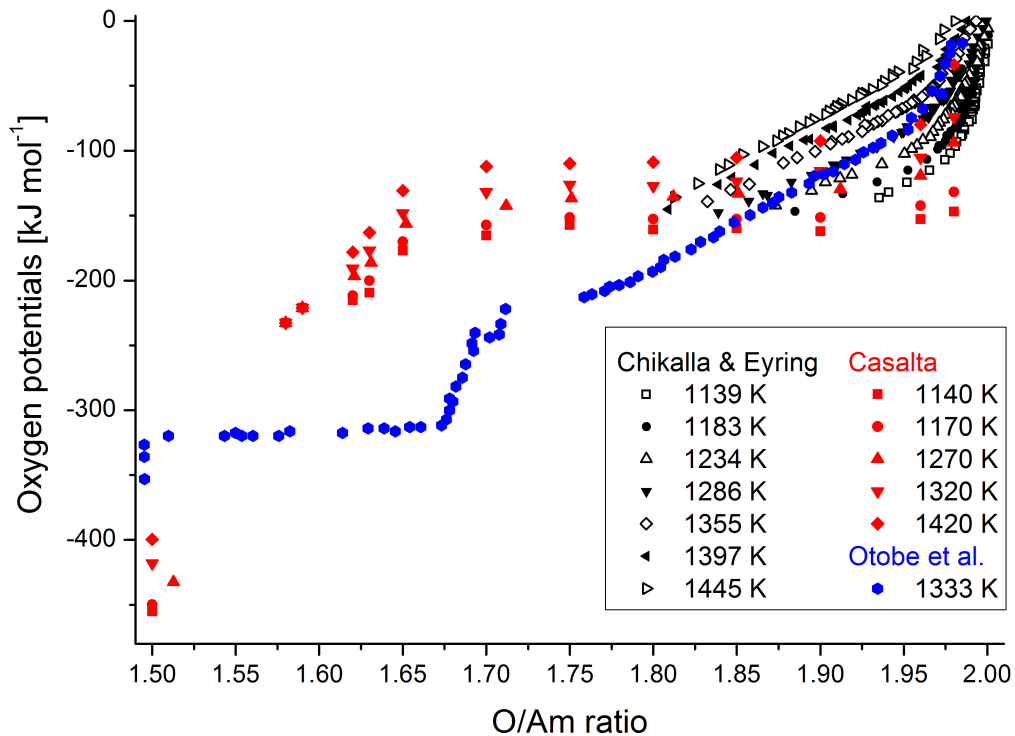
Fig. 2.28: Oxygen potentials reported for $AmO_{2\pm x}$ by Chikalla and Eyring (black) [57], Casalta (red) [59] and Otobe *et al.* (blue) [60].

Chikalla and Eyring [57] measured the oxygen partial pressure over hypo-stoichiometric AmO_{2-x} using the thermogravimetric analysis (TGA). The experimental set-up consisted of a thermobalance which allowed monitoring the weight change of the sample, while a sweep gas with known oxygen pressure was imposed in the system, in isothermal conditions. Temperature and partial oxygen pressure ranges were respectively $1139 < T < 1470$ K and $10^{-6} < pO_2 < 1$ atm. The latter were obtained using a He gas flowing in a furnace containing a copper oxide, whose dissociation (CuO/CuO_2 equilibrium) was controlled by changing the temperature. For the high oxygen pressures, near 1 atm, oxygen was physically added to the system. The encountered O/Am ratios range from 1.80 to 2.00, with an uncertainty equal to ± 0.004. Oxygen potentials between 0 and -150 kJ·mol^{-1} were measured, with an uncertainty of 2 kJ·mol^{-1}. In this range, the values were never constant, which means that the sample was monophasic and excludes the presence of a miscibility gap or a two-phase region, in contrast with the DTA data of Sari and Zamorani [58]. Nevertheless, the low reaction rates could have lead to errors in the measurements at low temperature and pO$_2$. Indeed, the authors indicated that, in some cases, more than 8 days were necessary to obtain a single data point.

Casalta [59] measured the oxygen potentials of several americium oxide samples, with $1.5 \leq$

O/Am ≤ 2, using the electromotive force method (EMF). The various O/Am ratios were obtained through thermal treatments under air, inert and reducing atmospheres and then measured by TGA. The oxygen potential measurements were performed using a galvanic cell with a Y_2O_3-ThO_2 electrolyte and a FeO/Fe reference. The entire system worked under vacuum. The oxygen potentials were measured between 1130 and 1425 K. No details on the experimental uncertaintes were provided. As one can observe in Fig. 2.28, the data of Casalta [59] are generally lower than those of Chikalla and Eyring [57]. Moreover, they show constant oxygen potentials for O/Am between 1.7 and 1.90, which indicates the existence of a two phase region, possibly a miscibility gap. However, the two upper isotherms (1420 K and 1320 K) are outside the miscibility gap boundaries identified by Sari and Zamorani [58]. For O/Am ≤ 1.65, the data of Casalta show a further decrease of the oxygen potential, which was identified by the author as the existence domain of the intermediate phase $AmO_{1.61+x}$. Therefore, this should be between $1.62 \leq$ O/Am ≤ 1.65.

Otobe *et al.* [60] measured the oxygen potentials at 1333 K of americium oxides, in the $1.5 \leq$ O/Am ≤ 1.99 range, by EMF using a zirconia solid-electrolyte. The samples were reduced by coulometric titration inside the galvanic cell. The O/Am ratios were then determined by TGA, with a maximum error of 0.05, whereas the estimated uncertainty for the oxygen potentials was 2 kJ·mol^{-1}. The data show a steep decrease for AmO_{2-x} and then two abnormal changes for O/Am equal to 1.71 and 1.78. The latter were identified by Otobe *et al.* as intermediate phases and named Am_7O_{12} and Am_9O_{16}. They also identified the existence domain of the intermediate phase $AmO_{1.61+x}$ as comprised between $1.69 \leq$ O/Am ≤ 1.67.

The experimental data of Chikalla and Eyring [57], Casalta [59] and Otobe *et al.* [60] are not trivial to compare since they do not cover exactly the same temperatures and O/Am ratios. Nevertheless, a critical analysis was performed by Gotcu-Freis *et al.* [64], who fitted and extrapolated the data of Casalta and Chikalla [57]. The results of this analysis are shown in Fig. 2.29. On the left (a), one can remark that, for any temperature and any O/Am ratios, the oxygen potentials measured by Chikalla and Eyring [57] are always higher than those of Casalta [59]. On the right (b), the three series of data are compared at 1333 K. An acceptable agreement is observed for the narrow $1.9 <$ O/Am ≤ 2 range, especially between the data of Chikalla and Eyring [57] and Otobe *et al.* [60], but the difference becomes dramatic for lower oxygen contents, up to about 200 kJ·mol^{-1} for O/Am=1.67. In conclusion, the three series of data are not consistent one with the other. The measurements of Chikalla and Eyrings [57] are generally considered the most reliable, thanks to the accuracy and completeness of their work. However, besides the differences between the three sets of data, it is important to remark that the oxygen potentials of AmO_{2-x} are considerably higher than those of $UO_{2\pm x}$.

2.4.3.3 U-Am mixed oxides

The oxygen potential data for uranium-americium mixed oxides are limited to one single set, reported by Bartscher and Sari for $U_{0.5}Am_{0.5}O_{2\pm x}$ [74], shown in Fig. 2.30. The measurements
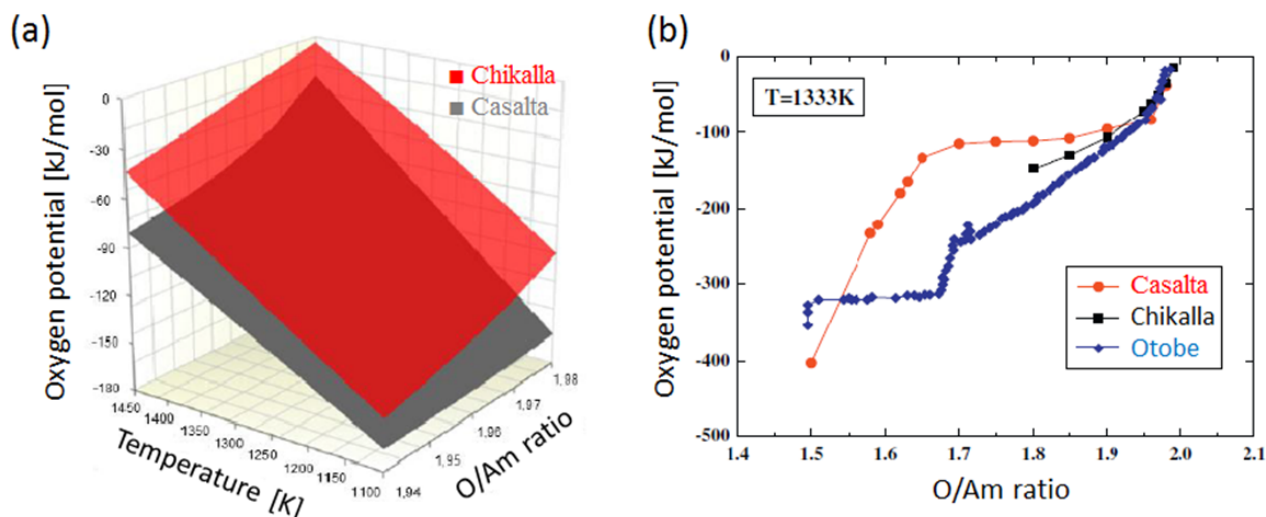
Fig. 2.29: Comparison of the oxygen potentials reported for $AmO_{2\pm x}$: (a) Chikalla and Eyring [57] vs Casalta [59] as a function of temperature and O/Am; (b) comparison of the three set of data at 1333 K (figure extracted from [64].

were performed by TGA, on samples manufactured by a sol-gel process, with a sintering at 1900 K under a CO_2/CO (90/10) atmosphere, corresponding to $\Delta\overline{G}(O_2) \simeq -165$ kJ·mol^{-1}. CO_2/CO, H_2O/H_2 mixtures and pure oxygen were used and the oxygen partial pressure was controlled by changing the CO_2/CO, H_2O/H_2 ratios and the pressure of the pure oxygen. No details on the pO_2 uncertainties were provided, whereas the maximum errors on temperature and O/M were indicated, respectively, as ± 1 K and ± 0.004. The initial O/Am ratio of the as-sintered samples was determined by potential coulometry, with dissolution in phosphoric acid, supposing that U^{4+} was oxidized by Am^{4+} to the hexavalent state. However, as seen in section 2.3.3, the charge distribution in $(U,Am)O_{2\pm x}$ dioxides is different than that supposed by Bartscher and Sari [74], hence their methodology could be affected by some errors.

The oxygen potentials of $U_{0.5}Am_{0.5}O_{2\pm x}$ measured by Bartscher and Sari have a *S shape*, as those of UO_2, indicating the existence of both an hypostoichiometric and a hyperstoichiometric domain for the solid solution.

2.4.4   Vapour pressures

Equilibrium vapour pressures are very important thermodynamic properties for predicting the behaviour of a material at high temperature, as in the case of a nuclear fuel, under both normal and accidental situations. The actinide dioxides present a complex vaporisation behaviour. This is reasonably well characterized for the U-O system [26] and it will not be treated here, since this is out of the scope of this review. On the contrary, the vaporization behaviour of americium oxides and uranium-americium mixed oxides is not well known. Recent measurements, performed by Knudsen effusion mass spectrometry (KEMS), provided data whose thermodynamic interpretation is not trivial. These data will be presented here, whereas the difficulties to reproduce them through thermodynamic modeling will be discussed in 2.5.
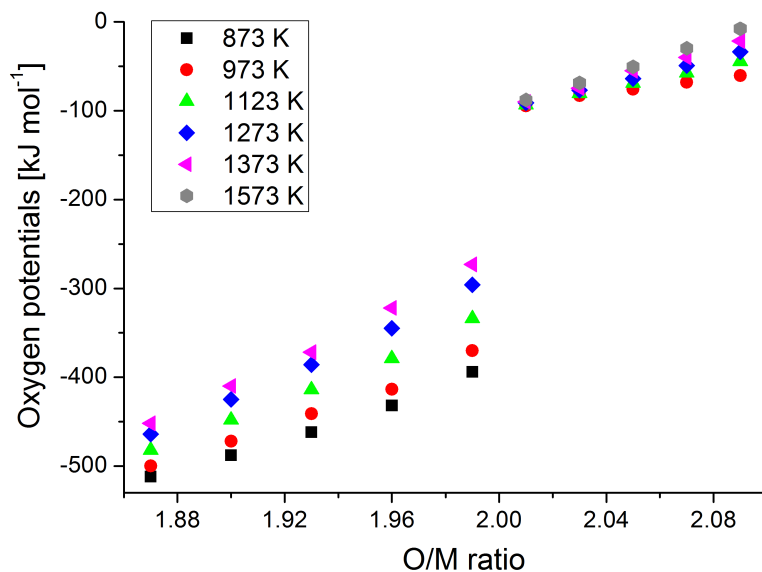
Fig. 2.30: Oxygen potentials of $U_{0.5}Am_{0.5}O_{2\pm x}$, according to Bartscher and Sari [74].

2.4.4.1 Americium oxides

The vapour pressure above an americium dioxide sample was measured, using KEMS, by Gotcu-Freis *et al.* [149]. The measurements were performed under vacuum, in several isotherms, between 2000 and 2200 K. The authors indicated that, at these temperatures, constant signals were reached in relatively short time [149]. The results are shown in Fig. 2.31. Americium dioxide is the major vapour species, closely followed by the AmO species, whereas the metal is about one decade lower. The Am(g) presence is peculiar: in other actinide oxides, as PuO_2 and NpO_2, the metallic species was not observed in the vapour [149]. However, it is important to remark that the O/Am of the AmO_2 sample during the KEMS measurement was unknown and, according to the oxygen potential data seen in section 2.4.3.2, likely very low.
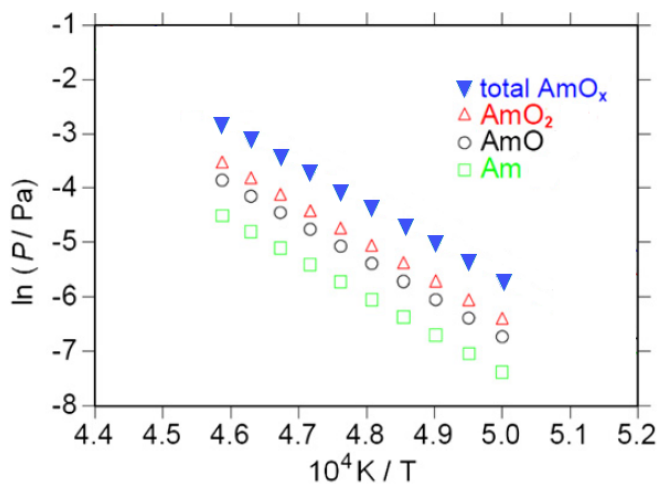
Fig. 2.31: Partial vapour pressure above americium dioxide, under vaccum, at 2000<T<2200 K, according to [149].

2.4.4.2   U-Am mixed oxides

Vapour pressures above $U_{1-y}Am_yO_{2-x}$ samples, with y = 0.3, 0.4 and 0.5, were reported by Lebreton [106]. The measurements were performed by KEMS, under vacuum, in isothermal conditions, at about 2300 K, trying to reach the congruent vaporization. Even if this was likely not reached, both the O/(Am+U) and the Am/(Am+U) ratios varied during the measurements. Unfortunately, the final chemical composition could not be determined. Therefore, the results, which are shown in Fig. 2.32, are identified with the initial Am content y of the samples.

The measured total vapour pressure was very similar for the samples with y=0.4 and 0.5, whereas it was higher for y=0.3. For the Am/(Am+U) ratios equal to 0.3 and 0.4, the contribution given by all the uranium species (total U) was higher than that of the americium species (total Am), whereas, for the equimolar sample, the Am contribution increased and it was slightly higher than that of U. For the uranium, the most abundant species was UO_2, followed by UO_3 and UO. The U(g) signal was the lowest between all the species. For americium, the vapour pressure was mostly given by, in order, the AmO(g) and the Am(g) species. This is very different than the behaviour of the pure americium dioxide, seen in section 2.4.4.1. Indeed, the $AmO_2(g)$ was the major species in the binary oxide, whereas it was very low for the mixed dioxides, even if an increase was observed for the sample with Am/(Am+U)=0.5.

2.5   Thermodynamic models

Semi-empirical thermodynamic modeling for the U-O, Am-O binary systems and the ternary U-Am-O system will be described in this section. Two different kinds of model will be presented: the first concerns the description of a single solid solution; the second type is based on the CALPHAD (CALculation of PHAse Diagram) method [150] and it consists in a simultaneous assessment of all the phases of a system, by minimization of the total Gibbs energy.

2.5.1   The U-O system

The first thermodynamic representation of the $UO_{2\pm x}$ was provided by Lindemer and Besmann [151]. Their model consists in describing a non-stoichiometric phase as a solid solution of a solute in a solvent, both stoichiometric, in order to reproduce the oxygen potential-temperature-O/M experimental data. The solvent was chosen as the stoichiometric form of the modeled phase, hence UO_2. Several solutes U_aO_b were tested: known uranium oxides as U_4O_9, U_3O_7 and UO_3, but also fictitious compounds as U_2O_5, which represents the U^{5+} oxide. The $T - x - ln(pO_2)$ relations of each hypothetical solid solution were then compared to the experimental data. The best agreement was found with:

- an UO_2-$U_{1/3}$ solution for the hypo-stoichiometric region;

- an UO_2-U_3O_7 solution for the highly hyper-stoichiometric region;

- an UO_2-$U_2O_{4.5}$ solution for slightly hyper-stoichiometric region
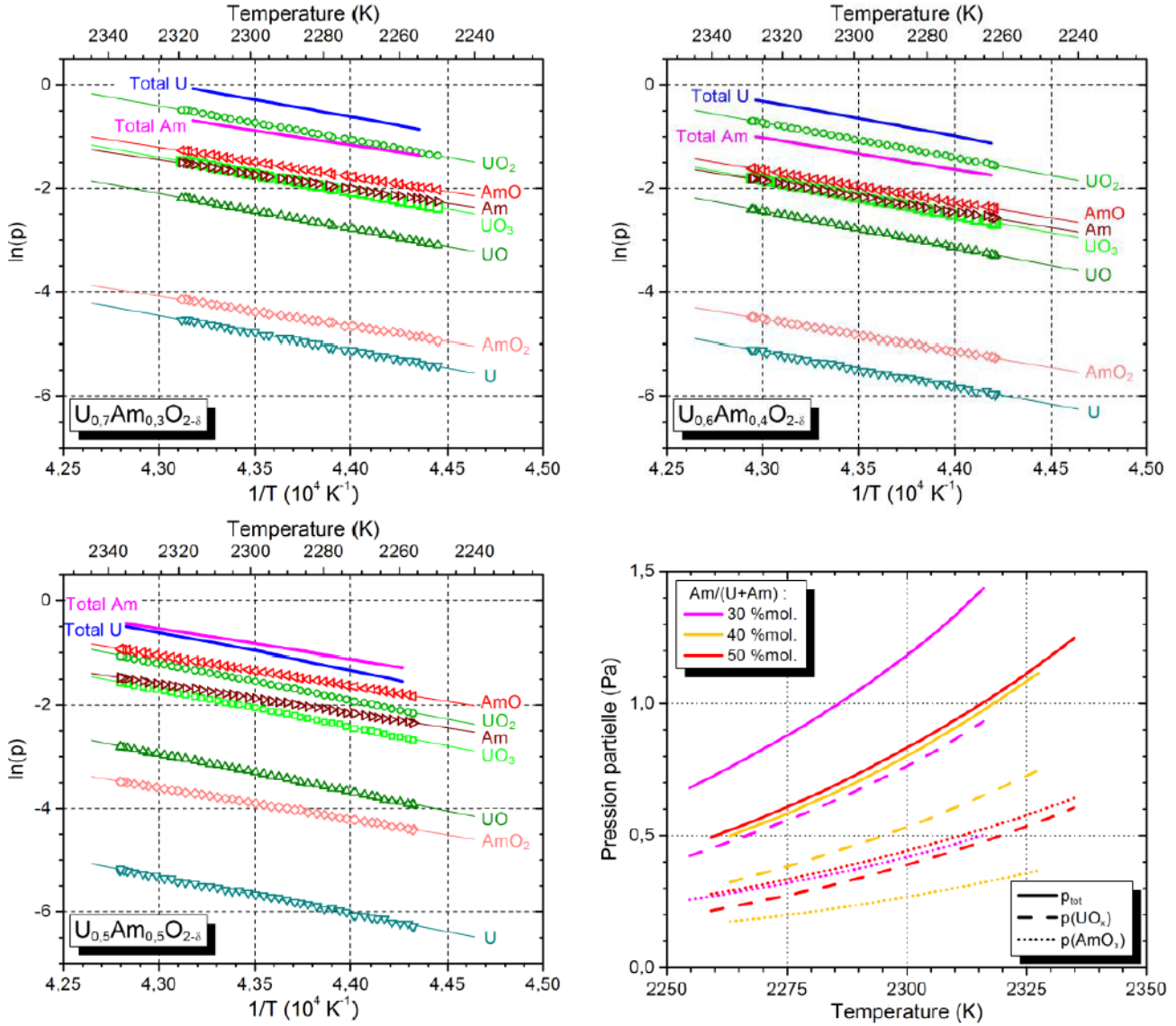
Fig. 2.32: Partial and total vapour pressures above U-Am dioxide with Am/(U+Am)=0.3, 0.4 and 0.5, at ∼2300 K (figure extracted from [106]).

This modeling led to a useful mathematical representation for the $T - x - ln(pO_2)$ behavior, but the description does not provide insight into the real structure and chemistry of the solid solution.

A complete CALPHAD thermodynamic model was later provided by Guéneau *et al.* [27,50], as already mentioned in section 2.1, which led to the computed phase diagram shown in Fig. 2.1. In this assessment, all the phases were included. Metals and the U_4O_9, U_3O_8 and UO_3 oxides were described as stoichiometric compounds, whose Gibbs energy is dependent only on the temperature.

The ionic two-sublattice model was adopted for the description of the liquid phase:

$$(U^{4+})_P(O^{2-}, Va^{-Q}, O)_Q, \tag{2.16}$$

where *Va* are the vacancies and P and Q are equal to the average charge of the opposite sublattice. The gas phase was described as an ideal mixture containing the gaseous species U, O, O_2, O_3, O_1U_1, O_2, O_2U_1 and O_3U_1.

Finally, the $UO_{2\pm x}$ was described with a three sublattice model:

$$(U^{3+}, U^{4+}, U^{5+})_1 (O^{2-}, Va)_2 (O^{2-}, Va)_1. \tag{2.17}$$

The first sublattice corresponds to the cationic crystallographic site. In the first version of the assessment, U^{6+} was present [50], but this was then replaced by U^{5+} in order to get a more physical description of the electronic defect $(2U^{4+} = U^{3+} + U^{5+})$ [27]. In the second sublattice, corresponding to the normal oxygen site, the vacancies were introduced to describe the hypo-stoichiometry. Finally, the third sub-lattice was needed in order to take into account the hyper-stoichiometry. To avoid an increasing complexity of the model and then of the number of adjustable parameters, no clustering of defects was considered.

Several phase diagram data (phase boundaries, transition temperatures) and thermodynamic data (oxygen potentials, enthalpies, heat capacity) were available for the optimization of the model parameters and, thanks to this, a reliable CALPHAD assessment of the U-O system was achieved.

2.5.2 The Am-O system

The first thermodynamic representation of the AmO_{2-x}, based on the modeling proposed by Lindermann and Besmann [151], was reported by Thiriet and Konings [62]. The AmO_{2-x} fluorite structure was described as a solid solution of a solvent, chosen as stoichiometric AmO_2, and a solute of the form Am_aO_b. The assessment was based on the fitting of the oxygen potential data of Chikalla and Eyring [57], presented in section 2.4.3.2. A good agreement was achieved with both the solute species tested: $AmO_{3/2}$ and $Am_{5/4}O_2$. The second one, which corresponds to an O/Am = 1.6 and hence represent the intermediate $AmO_{1.61+x}$ phase, was preferred on the basis of the phase diagram, as it is the end composition of the AmO_{2-x} phase.

An improved model of the AmO_{2-x} solid solution was later proposed by Besmann [152]. This assessment was based on the Compound Energy Formalism (CEF) [150], which addresses the mixing of constituents on multiple sublattice and then it gives a physical description of the entropy behavior in the system. The following two-sublattice model was adopted:

$$(Am^{3+}, Am^{4+})_1 (O^{2-}, Va)_2, \tag{2.18}$$

where the first corresponds to the cationic crystallographic site and the second sublattice represents the oxygen site, with the possibility to include vacancies, in order to reproduce the hypostoichiometry. In this representation, the AmO_{2-x} phase is considered as a solid solution of four species, named *end members*: $(Am^{3+})_1(O^{2-})_2$, $(Am^{4+})_1(O^{2-})_2$, $(Am^{3+})_1(Va)_2$, $(Am^{3+})_1(Va)_2$. The Gibbs energy of the solid solution is then expressed as the sum of the Gibbs energies of each end member, plus an entropic term, plus an excess free energy contribution due to the interac-

tions between the constituents. As for the model of Thiriet and Konings [62], the parameters were optimized using the experimental oxygen potentials of Chikalla and Eyring [57].

Finally, Gotcu *et al.* [64] presented a more complex thermodynamic model of the entire Am-O system, based on the CALPHAD approach, which led to the computed phase diagram shown in Fig. 2.6. All the phases, including metals, oxides, liquid and gas, were included in this representation. However, since almost no data were available for the high temperature domains of the liquid and gas phases, the assessment mostly focused on the solid domain of the phase diagram, comprised in the $1.5 \leq$ O/Am ≤ 2.0 range. The lack of thermodynamic data for the C-type phases made impossible a complete assessment of all the phases reported in the previous phase diagrams, already discussed in section 2.1.2, and some simplifications were necessary. Therefore, three oxides were included: the fluorite-type americium dioxide AmO_{2-x}, the intermediate BCC phase $AmO_{1.61+x}$ and the hexagonal sesquioxide Am_2O_3. Moreover, even if some data suggested the existence of a composition domain, the intermediate $AmO_{1.61+x}$ was modeled as a stoichiometric compound with O/Am $= 1.62$ (the phase was hence named $AmO_{1.62}$ by Gotcu *et al.* [64]). The AmO_{2-x} phase was instead described with the two sublattice of Eq. (2.18).

The parameters of the model were assessed using not only the oxygen potentials data of Chikalla and Eyring, as in the two previous cases, but all the experimental data available. These include the phase diagram data obtained by XRD [56] , DTA [58] and ceramography [58], which were described in section 2.1.2, as well as the other thermodynamic data available for Am_2O_3 and AmO_2 (enthalpy of formation [128, 129], standard entropies [127], enthalpy increments [145]), already presented in section 2.4. The miscibility gap in the AmO_{2-x} region suggested by Sari and Zamorani [58] was included in the assessment. For this reason, only the oxygen potential data of Chikalla and Eyring [57] with compositions and temperature outside the miscibility gap were selected.

The resulting model achieved a general good agreement with the available experimental data, with the exception of the partial vapour pressures, presented in section 2.4.4.1. Indeed, the experimental high partial pressure of Am(g) could not be reproduced by the calculations for the AmO_{2-x} phase. On the contrary, a close reproduction of the vapour pressure data was obtained for the congruency calculation above the sesquioxide Am_2O_3, hence Gotcu *et al.* supposed that the dioxide was rapidly reduced during the KEMS measurements under vacuum [64].

2.5.3   The U-Am-O system

A tentative CALPHAD assessment of the U-Am-O ternary system was proposed by Lebreton in his PhD thesis [106]. The starting point was the extrapolation of the CALPHAD models of the binary systems U-O [27] and Am-O [64], presented respectively in 2.5.1 and 2.5.2. Only few experimental data were available to optimize the interaction parameters, namely the oxidation states of U and Am in the solid solution (see section 2.3.3) and the oxygen potentials by Bartcher and Sari [74] (see 2.4.3.3). Therefore, even if a good fit of these data was achieved, the model is still not accurate. For instance, a satisfying interpretation of the vapour pressure data (reported

in section 2.4.4.2) could not be provided by this model.

2.6 Conclusions

A thorough knowledge of the U-Am-O ternary system requires the comprehension of the thermodynamic properties of the binary U-O and Am-O systems. However, this is not sufficient since these properties are altered by the interactions between U and Am. Therefore, direct investigations of the ternary system are also necessary.

This review pointed out that an extensive knowledge of the binary U-O system, especially of the UO_2 solid solution, is available. Indeed, numerous structural, thermodynamic and phase diagram experimental data were reported in the literature for this system and, thanks to them, a reliable thermodynamic model, based on the semiempirical CALPHAD method, was developed [27]. On the contrary, the comprehension of the Am-O system is far from complete, because the high radioactivity of Am isotopes slowed down the experimental investigation of these compounds. Even if the structures of the various americium oxides were quite easily identified, thanks to the similarity with other actinide and lanthanide oxides, their phase equilibria are not determined yet. This is due to the scarcity and, in some cases, the incompatibility of the experimental data, as for example the oxygen potentials, for which three sets of measurements were reported [57, 59, 60], none of them consistent with the others. Despite these difficulties, after an attentive selection between the experimental data, a CALPHAD thermodynamic assessment of the Am-O system was performed [64], moving the comprehension a step forward. Nevertheless, several uncertainties still exist on the Am-O phase equilibria, as the existence of a FCC miscibility gap for the dioxide, the stable sesquioxide form at room temperature and the existence domain of the intermediate $AmO_{1.61}$ phase.

The experimental data reported in the literature for $(U,Am)O_{2\pm x}$ dioxides concern mostly their structural properties, whereas phase diagram and thermodynamic data are very rare. The latter are limited to the high temperature enthalpy increments [146], for dioxides with $Am/(Am+U) = 0.09$ and 0.19, and to one set of oxygen potential measurements [74], reported for the equimolar composition $Am/(Am+U) = 0.5$. Further investigations of the thermodynamic properties are necessary, especially because the structural investigations showed peculiar characteristics for uranium and americium dioxide. Indeed, XAS data highlighted a not usual charge distribution [71], in which americium is purely trivalent, whereas uranium has a mixed $4+/5+$ oxidation state. Therefore, considering the specialty of the $(U,Am)O_{2\pm x}$ solid solution formation, a not ideal behavior can be expected.

Chapter 3

Experimental study and thermodynamic modeling of the Am-O system

In chapter 1, the CALPHAD method has been introduced and it has been mentioned that the thermodynamic assessment of a ternary system, such as U-Am-O, is not possible without a thorough knowledge of each binary sub-system. Among the respective binaries, very few experimental data are available in the literature for the Am-O system, as seen in chapter 2. For this reason, this chapter is dedicated to the study of this system. Initially, the uncertainties concerning the Am-O phase equilibria are summarized in section 3.1. In order to answer some of the open questions, an experimental investigation by High-Temperature X-Ray Diffraction (HT-XRD) was conducted and the results are shown in section 3.2. Finally, the CALPHAD modeling of the Am-O system, reported in the literature and discussed in section 2.5.2, was updated according to the new experimental data and the new assessment is presented in section 3.3.

3.1 Open questions on the Am-O system

The critical review of chapter 2 has highlighted that the phase equilibria of the Am-O system are challenging to assess. The major uncertainties are listed below.

1. The low temperature (300<T<600 K) sesquioxide region (O/Am~ 1.5) is not well determined. The phase boundaries between A-Am_2O_3 and C-$AmO_{1.5+x}$ are not defined and it is not clear which is the most stable sesquioxide form at room temperature. According to the phase diagram of Sari and Zamorani [58] (see Fig. 2.4), it is the cubic phase, whereas this was excluded in the assessment of Gotcu-Freis *et al.* [64] (see Fig. 2.6). The recent XRD investigation of Lebreton *et al.* proved the stability of the hexagonal A-Am_2O_3 at low temperature [61], giving reason to Gotcu-Freis *et al.* [64]. However, it remains unclear if a cubic sesquioxide domain should be included in the phase diagram.

2. The limits of the existence domain (T and O/Am ratio ranges) of the intermediate C-$AmO_{1.61+x}$ phase are not identified.

3. Several uncertainties exist also for the AmO_{2-x} existence domain:

   - It is known that a hypo-stoichiometric region exists at high temperature, but the minimum O/Am ratio and the relative phase boundary with the $A-Am_2O_3$ phase are not clearly identified.

   - The three sets of oxygen potential data reported in the literature [57, 59, 60] do not agree one with the other; the data of Chikalla and Eyring [57] are generally considered the most reliable.

   - A miscibility gap for O/Am>1.7 and 1100<T<1300 K was introduced by Sari and Zamorani [58] on the basis of DTA measurements. However, these data do not agree wih the oxygen potentials of Chikalla and Eyring [57], but they could be consistent with those of Casalta [59], who found a two-phase region. A definitive confirmation of the miscibility gap was never reported, since two fluorite structures were never directly observed, and its existence remains controversial.

   - Only one set of measurements was reported for the melting temperatures of the A-Am_2O_3 and AmO_2 oxides [63]. Besides, for the dioxide, the O/Am ratio was not determined after the melting and hence the value is not associated to a defined composition.

   - The vaporization behaviour of americium oxides is not well known. As shown in section 2.4.4.1, one investigation by KEMS was reported in the literature on an AmO_2 sample. Unfortunately, the evolution of the O/Am ratio could no be controlled during the measurement. The reproduction of the measured vapour pressures by thermodynamic modeling is not very good [64]. A recent review by Konings *et al.* proposed new revised thermodynamic functions for the gaseous species [127].

The experimental investigation, described in the following, aimed to answer some of these open questions. More specifically, the focus was on the uncertainties of the points (2) and (3), hence the AmO_{2-x}-$AmO_{1.6+x}$-Am_2O_3 domain for T >700 K.

3.2 Experimental HT-XRD investigation

In situ high-temperature XRD was chosen to study the AmO_{2-x}-$AmO_{1.6+x}$-Am_2O_3 phase equilibria because this technique has proven to be very useful for this purpose in several studies [61, 153, 153–159]. In particular, HT-XRD allows the characterization of miscibility gaps, namely the determination of the critical temperature [155, 158].

3.2.1 Experimental conditions

Two batches of AmO_2 were used for the measurements, named AmO_2-A and AmO_2-B, respectively. The latter was only used for the isothermal XRD measurements shown in section 3.2.2.3. The isotopic and chemical characteristics of the two powders are reported in Appx. B. For

both the batches, the major americium isotope was ^{241}Am and some percent of impurities were present, namely Np (from α-decay) and mostly Ce for AmO$_2$-A and Pu for AmO$_2$-B.

The HT-XRD measurements were performed on about 20-40 mg of powder samples using a X-ray diffractometer in Bragg-Brentano geometry, with copper radiation from a conventional tube source (Kα_1 + Kα_2 radiation). From previous experiments, a constant temperature uncertainty of ± 15 K is estimated, for the $300 \leq T < 1900$ K range explored in this work. The atmosphere in the experimental chamber was controlled through a constantly flowing gas and the oxygen partial pressure was regulated using an oxygen pump and gauge, at the inlet of the gas circuit. The used device can measure pO$_2$ from 10^{-35} to 0.25 atm and the provider indicates a relative uncertainty of 3% for this entire range; however, according to the repeatability of the performed measurements, higher uncertainties up to 20% were considered for pO$_2 < 10^{-6}$ atm. Details on the experimental set-up, XRD pattern acquisition and refinement are provided in A, whereas the temperatures, heating rates and atmospheres of the measurements will be described here.

3.2.1.1   Preliminary thermodynamic computations

In order to choose the most appropriate temperature-atmosphere conditions for the investigation of the AmO$_{2\text{-x}}$-AmO$_{1.61+\text{x}}$-Am$_2$O$_3$ domain, preliminary thermodynamic computations were performed with the Am-O CALPHAD model of Gotcu-Freis *et al.* [64], using the Thermo-Calc software. Calculations were set according to two different strategies:

1. Selecting a point in the phase diagram, that is fixing the temperature T and composition O/Am, and computing the corresponding oxygen potential of the solid phase $\Delta\overline{G}(O_2)_s$. At equilibrium, this latter must coincide with the oxygen potential of the surrounding atmosphere $\Delta\overline{G}(O_2)_g$ and therefore one can derive the oxygen partial pressure pO_2 using the relation:

$$\Delta\overline{G}(O_2) = RTln(pO_2). \tag{3.1}$$

   An example of this calculation is shown by the purple points in Fig. 3.1: to observe the $AmO_{2-x} \rightarrow AmO_{2-x} + A\text{-}Am_2O_3$ phase transition at 1500 K (overall O/Am ratio equal to 1.589), an oxygen potential of ~ -140 kJ·mol^{-1} is necessary. Using Eq. (3.1), it is found that, at 1500 K, this corresponds to an oxygen partial pressure $pO_2 \simeq 1.2 \cdot 10^{-5}$ atm. The computed oxygen potential is constant in the two phase region, as imposed by the phase rule.

2. Imposing a constant oxygen partial pressure and computing the evolution of the O/Am ratio as a function of temperature. This strategy is useful for predicting measurements under an atmosphere with fixed composition. In Fig. 3.1, the calculated equilibrium points in air (blue line) and under lower pO$_2$ (green line), ranging from 10^{-4} to 10^{-8} atm, are shown Fig. 3.1.

Several considerations can be made on the basis of the latter computations:

- AmO$_2$ is reduced to AmO$_{2\text{-x}}$ under air, for T > 1100 K.
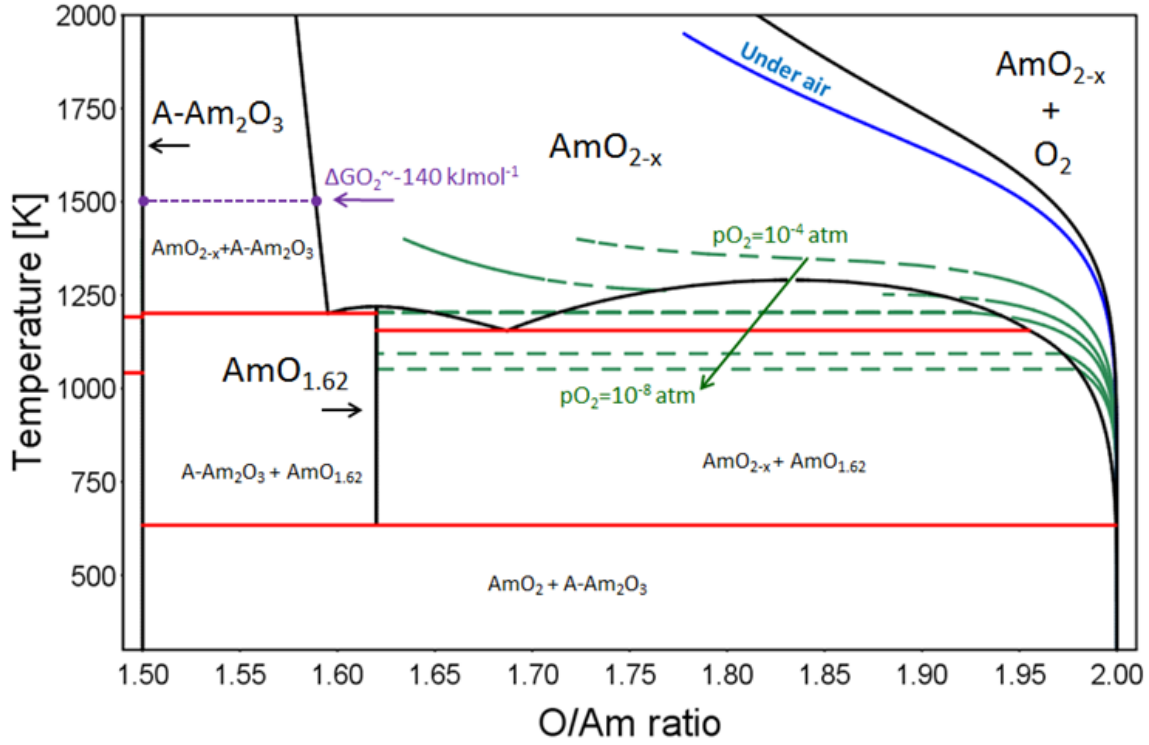
Fig. 3.1: Am-O phase diagram (1.5<O/Am<2 range) according to the CALPHAD model of Gotcu-Freis *et al.* [64] and results of thermodynamic computations: —— equilibria in air as a function of temperature; - - equilibria as a function of temperature under fixed pO_2 (10^{-4}, 10^{-5}, 10^{-6}, 10^{-7}, 10^{-8} atm) ; - - A-Am$_2$O$_3$/AmO$_{2-x}$ two phase region at 1500 K.

- For $10^{-6} \leq pO_2 \leq 10^{-5}$ atm, according to the model, the miscibility gap should be crossed. It is important to remember that these partial oxygen pressures are higher than those expected according to the experimental oxygen potentials of Casalta [59]. For instance, according to Casalta [59], the miscibility gap should be observed at 1220 K for $pO_2 \sim 10^{-8}$ atm.

- For $pO_2 \leq 10^{-7}$ atm, the AmO$_{2-x}$/AmO$_{1.61+x}$ biphasic region should be observed for T < 1150 K.

- The green curves of Fig. 3.1 show that, by fixing the oxygen partial pressure at high temperature and then cooling, the material is always oxidized; vice versa, if the temperature is increased under atmosphere with constant pO_2, the material is reduced. This is immediately clear observing for example the curve computed for $pO_2 = 10^{-4}$ atm, which falls in a monophasic domain. This means that, even if both $\Delta \overline{G}(O_2)_s$ and $\Delta \overline{G}(O_2)_g$ are monotonically decreasing functions of temperature, the $\Delta \overline{G}(O_2)_g$ is a steeper function of the temperature than $\Delta \overline{G}(O_2)_s$. As a consequence, during cooling, the atmosphere becomes more oxidizing for the sample and the driving force leads towards higher O/Am ratios to maintain the equilibrium.

3.2.1.2 Out of equilibrium conditions

Reaching the equilibrium during heating/cooling and following the green curves of Fig. 3.1 is not straightforward: if the heating/cooling rate is not slow enough, the thermodynamic equilibrium between sample and atmosphere cannot be reached and, in this case, the computation results are clearly no longer valid. Nevertheless, fast cooling can be very useful because it allows *exploring* various regions of the phase diagram. One can object that if the equilibrium is not reached by the system (solid phase + surrounding gas), the XRD observations cannot be related to phase equilibria. Nevertheless, Belin *et al.* have proven that in some cases, even if the sample is out of equilibrium with the atmosphere, the internal bulk equilibrium can be preserved and the observed features can be representative of the phase diagram [155,160]. In fact, if the material enters a new domain of the phase diagram, the transition can occur in the volume probed by XRD, despite the atmosphere, since the difference in oxygen potential of each solid phase is the main driving force. For instance, this phenomenon allows observing the miscibility gap in hypostoichiometric $U_{1-y}Pu_yO_{2-x}$ mixed oxides with y>0.2, even for atmospheres not reducing enough to enter this domain in total (gas + solid) thermodynamic equilibrium [155,160]. An example, showing a HT-XRD study on a $U_{0.54}Pu_{0.64}O_{2-x}$ sample, is reported in Fig. 3.2 (extracted from [155]). In this case, the oxide was reduced at high temperature, about 1600 K, under an atmosphere composed of $He/5\%H_2$ + 10 ppm H_2O and subsequently cooled down to room temperature. On the left side of Fig. 3.2, the isointensity map of the (311) peak of the fluorite structure (obtained from the XRD patterns) clearly exhibits the formation of a second FCC phase during the cooling, for T < 800 K. However, the thermodynamic calculations (Fig. 3.2, right side) indicate that, under the used atmosphere, the equilibrium state of the oxide does not cross the miscibility gap. The CALPHAD model of the system is reliable, since it is based on several oxygen potentials data, hence an error of the calculations can be excluded. Therefore, it was concluded that, during the cooling, the oxidation of the sample was not fast enough and the O/M of the solid corresponded to that of the miscibility gap, inducing a phase separation.

If the mechanism described above were valid also for the Am-O system, it could lead to the observation of the miscibility gap for oxygen partial pressures higher than those of equilibrium. For example, as shown in 3.3, the equilibrium curve for $pO_2=10^{-4}$ atm (green) is completely inside the monophasic domain of AmO_{2-x}. A sample that is equilibrated at 1500 K under this atmosphere and, subsequently cooled down, it could *follow* the equilibria points or, for fast cooling, the alternative paths inside the miscibility gap and the $AmO_{2-x}/AmO_{1.61+x}$ domain (blue dashed lines).

3.2.1.3 Choice of the experimental conditions

Considering the thermodynamic computations and the previous experiments on similar systems, various experimental strategies were adopted to investigate the Am-O system:

1. Measurements from high temperature to 300 K in air to acquire new crystallographic data on AmO_{2-x}, with an oxygen content close to the stoichiometry.

2. Measurements in very reducing conditions (at elevated temperatures and low pO_2) in order
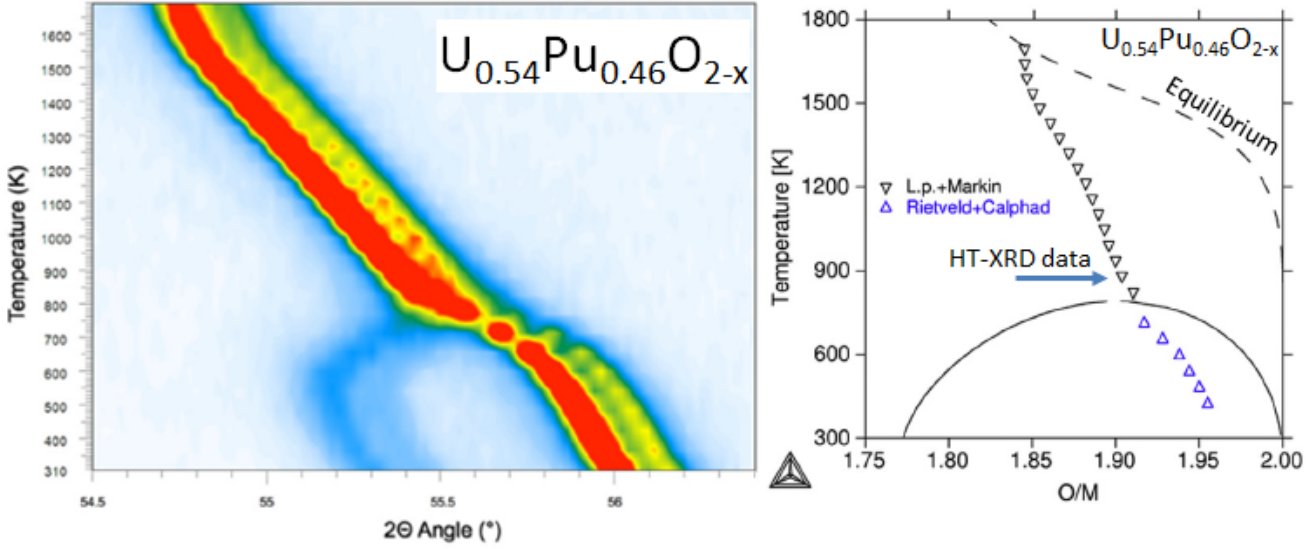
Fig. 3.2: HT-XRD study on $U_{0.54}Pu_{0.64}O_{2-x}$ by Belin *et al.* [155]: left, iso-intensity map of the (311) XRD peak of the fluorite structure as a function of temperature; right, isopleth section of the U-Pu-O phase diagram for Pu/M=0.64, with the FCC miscibility gap. HT-XRD experimental points ($\triangle$) and expected themodynamic equilibria (- -) for an atmosphere of He/5%H$_2$ + 10 ppm H$_2$O.

to investigate the AmO$_{2-x}$/A-Am$_2$O$_3$ phase boundary and collect crystallographic data on hypo-stoichiometric AmO$_{2-x}$.

3. Measurements in isothermal reductions in the expected temperature of the miscibility gap, in order to cross it from oxidized to reduced compositions.

4. Measurements from 1400 to 700 K, with a fast cooling rate, under fixed pO$_2$, in order to investigate the miscibility gap. In this case, a fast detector with an angular window of $2\theta = 3°$ was used, recording only one of the main diffraction peak of the fluorite structure.

5. Measurements from 1400 to 700 K, with a slow cooling rate, under fixed pO$_2$, in order to investigate the intermediate phase C-AmO$_{1.61+x}$ and the miscibility gap.

The conditions used in the experiments are summarized in Tab. 3.1, whereas the results are presented in the following sections.

	Measurement	T [K]	pO$_2$	Conditions
1	In air	300-1900	0.21	$20° \leq 2\theta \leq 140°$, cooling
2	*Reducing* conditions	1200-1500	$\leq 10^{-5}$	$20° \leq 2\theta \leq 120°$, cooling
3	Isothermal reduction	1220-1280	$0.21 - 10^{-11}$	$20° \leq 2\theta \leq 140°$, isotherm
4	*Fast* cooling	1400-700	$10^{-8} - 10^{-4}$	$2\theta = 3°$, cooling
5	*Slow* cooling	1400-700	$10^{-8} - 10^{-4}$	$20° \leq 2\theta \leq 140°$, cooling

Table 3.1: Selected experimental conditions
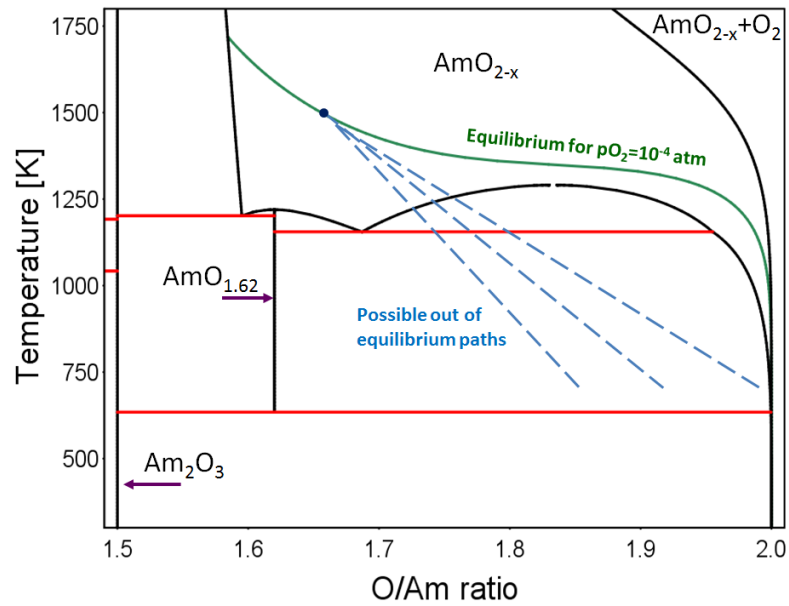
Fig. 3.3: Expected evolution of an AmO_{2-x} sample which is cooled from 1500 K (equilibrium under pO_2=10^{-4} atm) to 700 K: equilibria points (green) and possible alternative paths for fast cooling rates (dashed blue lines).

3.2.2   Results

3.2.2.1   Measurements in air

A diffraction pattern (shown in Fig. 3.4) was recorded at room temperature on the AmO_2 sample *aged* two years, confirming the presence of a single $Fm\overline{3}m$ structure (the $*$ indicate the peaks due to the Pt sample holder). As seen in section 2.2.4, the saturation value (reached in about 3 months) of the AmO_2 lattice parameter ranges between 5.385 and 5.392 Å, according to the different authors. The lattice parameter obtained here was 5.391(1) Å, consistent with the values reported by Chikalla, Eyring [56] and Prieur *et al* [116].

The sample was then heated at 300 K min^{-1} up to 1900 K and then maintained at this temperature for 5 hours in order to both anneal the defects induced by α self-irradiation and to reach equilibrium. During cooling toward room temperature, diffraction patterns were collected every 100 K. The recording of one diffraction pattern required around 30 minutes.

In Fig. 3.5, the lattice parameters (■), obtained by refinement of the XRD patterns, are compared to the data collected by Fahey (■) under pure oxygen [111]. As expected, the lattice parameter decreased during the cooling, from 5.527(2) Å at 1900 K to 5.375(1) Å at room temperature. As expected, the latter value is smaller than that obtained on the aged sample, since the thermal treatment recovered the defects due to the self-irradiation. At T≃1200 K, a change in the slope of thermal expansion is observed. This behavior can be attributed to the reaching of the stoichiometry O/Am, whereas the sample was reduced at high temperature. This would be consistent with the predictions of the Gotcu-Freis *et al.* model [64], as shown in Fig. 3.5 by the O/Am ratios in air computed as a function of temperature (●). A small difference between our lattice parameters and those of Fahey [111] under O_2 (Fig. 3.5) is observed. This can be due to the different contents of impurities, the temperature uncertainty, or a slight
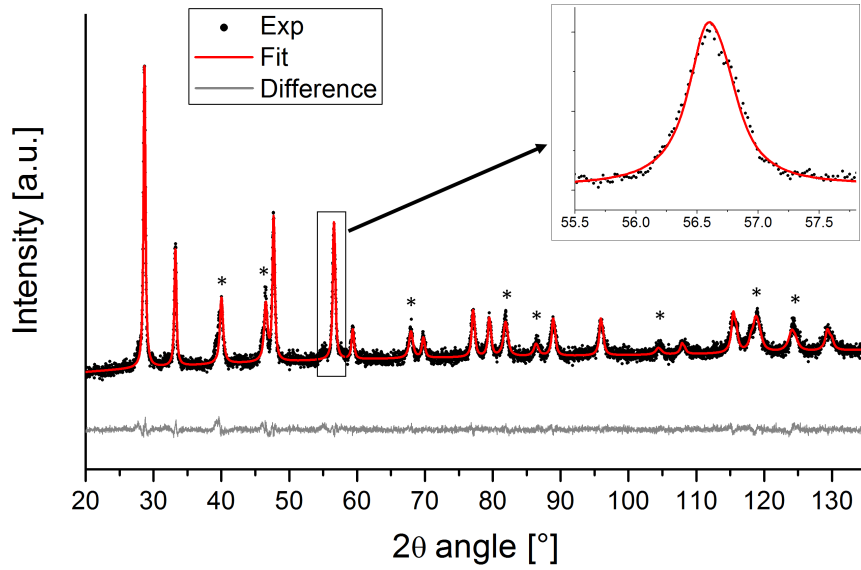
Fig. 3.4: XRD pattern acquired on the aged AmO_2 sample at room temperature and Pawley refinement ($*$ indicate the diffraction peaks due to the Pt sample holder).

residual hypo-stoichiometry during cooling in the 473<T<1173 K range, due to a possibly slow re-oxidation rate. The latter hypothesis seems likely since the gap between our data and those of Fahey becomes smaller and smaller as the temperature decreases, to become negligible at room temperature.

3.2.2.2 Measurements in reducing conditions

Several measurements were performed under 10^{-5}<pO$_2$<10^{-8} atm in the temperature range 1200-1500 K in order to investigate the phase boundary between AmO_{2-x} and the A-Am_2O_3 + AmO_{2-x} two-phase region.

The main goal was to observe the hexagonal sesquioxide A-Am_2O_3 at T=1500 K. According to the thermodynamic computations, the phase transition should occur at this temperature under $pO_2 \simeq 2 \cdot 10^{-5}$ atm. The experiment was performed in two steps: the desired oxygen partial pressure was initially stabilized at 298 K and then the sample was heated at 300 K min^{-1} up to 1500 K. Selected portions of the collected XRD patterns corresponding to the most intense peaks of both the fluorite ($Fm\overline{3}m$) and the hexagonal ($P\overline{3}m1$) structures are shown in Fig. 3.6. The peak shift between the first diffraction pattern collected at 1500 K (t=0 s, red pattern) and the one at room temperature (green pattern) indicates a rapid cell parameter increase. This is due to both thermal expansion and reduction of $AmO_2 \rightarrow AmO_{2-x}$. In fact, the peaks corresponding to the hexagonal structure are already slightly visible at $\sim 30.5°$. After one hour, the sesquioxide phase can be more clearly observed. Finally, the diffraction patterns collected at t=2 h do not show variations in both the positions and the intensities of peaks, suggesting that equilibrium was reached. The Rietveld refinement of the diffraction patterns acquired at 1500 K (2 h) was performed using the Am_2O_3 and AmO_2 structures (space groups and atomic positions) presented in section 2.2 and the obtained fit is shown in Fig. 3.7. The sample was composed for the 15 wt.% by Am_2O_3 and for the 85 wt.% by AmO_{2-x}. The found lattice parameters are
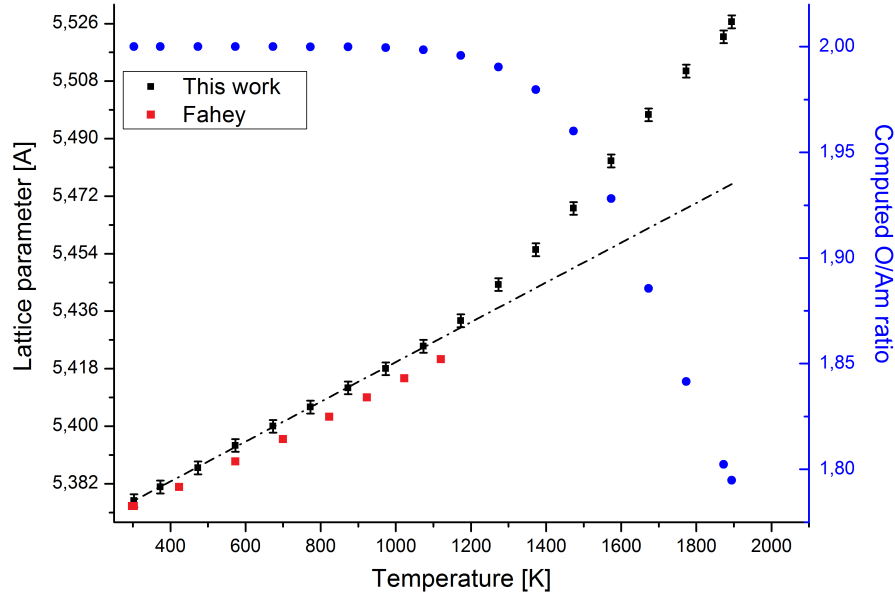
Fig. 3.5: Lattice parameters of AmO_{2-x} (primary axis) and computed O/Am ratios (secondary axis) as a function of temperature with CALPHAD. ■: this work (in air). ■ : Fahey data [111] (in pure O_2). ● : computed O/Am ratios.

a=5.510(2) Å for AmO_{2-x} and a=3.850(2) Å, c=6.070(2) Å for Am_2O_3.

In further experiments, attempts to explore this two-phase region were made at lower temperatures ($1200 < T < 1400$ K). According to the thermodynamic computations, the phase transition should occur at T=1400 K for $pO_2 \simeq 5 \cdot 10^{-6}$ atm and at T=1200 K for $pO_2 \simeq 1 \cdot 10^{-7}$ atm, but in these conditions the hexagonal phase was never observed by XRD.

3.2.2.3   Measurements during isothermal reduction

Isothermal measurements of 20 hours were performed at 1220 K and 1280 K during the reduction of the sample. According to the previous model of Gotcu-Freis *et al.* [64], at these two temperatures AmO_{2-x} should enter the miscibility gap for $pO_2 = 8 \cdot 10^{-6}$ and $3 \cdot 10^{-5}$ atm respectively. Therefore, by reducing the sample, two FCC phases should be observed as the overall O/Am ratio of the sample decreases.

The sample was first heated in air at 300 K·min⁻¹, up to the desired temperature. Then, the atmosphere was switched from air to He/O_2 and the pO_2 was slowly and continuously changed from 10^{-3} to 10^{-11} atm. It is important to underline that, in this case, also pO_2 lower than those computed with the CALPHAD model were tested. Indeed, as mentioned before, the oxygen potential data by Casalta [59], not considered in the assessment of Gotcu-Freis *et al.* [64], indicate a two phase region (possibly a miscibility gap) around 1200 K for more reducing conditions. For instance, according to Casalta, the phase separation should be observed at 1220 K for $pO_2 \simeq 10^{-8}$ atm.

The obtained results were similar at both 1220 and 1280 K. Thus, for simplicity, only those obtained at 1220 K are detailed. Selected sections of the collected XRD patterns are shown in Fig. 3.8. The first one, corresponding to the XRD pattern at 1220 K in air (t=0), shows
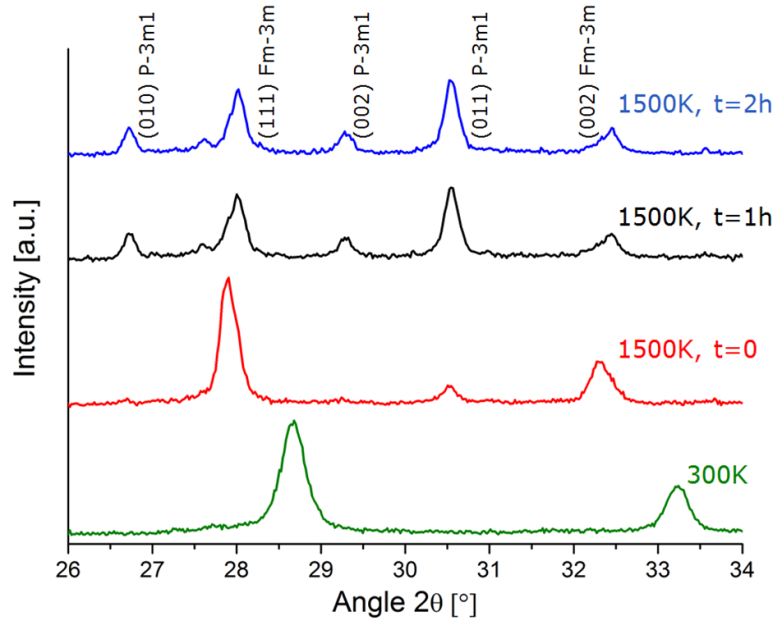
Fig. 3.6: Diffraction patterns collected at 300 K and 1500 K for 2 hours under controlled atmosphere ($pO_2 \simeq 2 \cdot 10^{-5}$ atm). The characteristic diffraction peaks of the $Fm\bar{3}m$ (AmO_2) and $P\bar{3}m1$ (Am_2O_3 structures are identified.

the characteristic peaks of the fluorite $Fm\bar{3}m$ structure (the presence of a double peak for each reflection is due to the two X-ray wavelengths). After 30 min, the atmosphere was switched from air to He/O_2 inducing the reduction of the americium dioxide. As a result, the XRD peaks shifted to lower angles (t=10 h) because of the lattice parameter expansion (black points in Fig. 3.9). Despite the relatively elevated temperature, the reduction process took more than 12 hours as reflected by the continuous increase in the lattice parameter of the FCC structure. The stabilized value was 5.514(2) Å. Then (t=14 h), a phase transition from the FCC to the BCC $C-AmO_{1.61+x}$ form ($Ia\bar{3}$ structure) began, as shown by the distortion of the diffraction peaks, the loss in intensity and the appearance of faint superlattice reflections (black stars). This indicates a structural change, even if the most intense reflections of both the $Fm\bar{3}m$ and the $Ia\bar{3}$ structures appeared at the same angles because the BCC phase is a super-structure of the fluorite form, resulting from an expansion of the cell due to the oxygen loss. For this reason, the $AmO_{1.61+x}$ phase is characterized by lattice parameters approximately twice those of AmO_{2-x} and, for clarity, they were halved in Fig. 3.9. The two phases coexisted for a couple of hours and finally the $Fm\bar{3}m$ AmO_{2-x} phase disappeared. One can note that during the phase separation, the lattice parameters of the two phases, especially those of AmO_{2-x}, were mostly constant, indicating constant O/Am ratios for the two phases. Once the transformation from AmO_{2-x} to $AmO_{1.61+x}$ was complete (after 15 h), the lattice parameter of the BCC phase increased (Fig. 3.9 (blue points)). This finally confirms the existence of a composition domain for this phase.
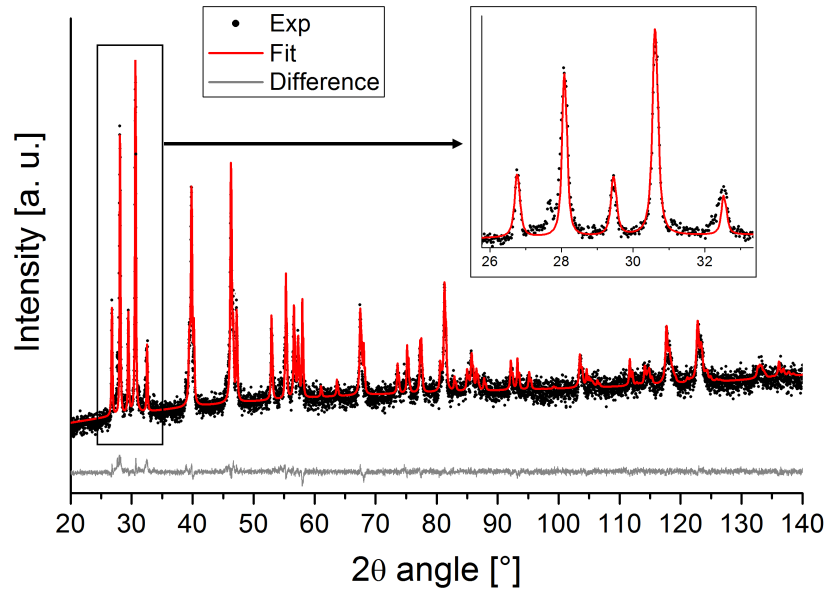
Fig. 3.7: Diffraction pattern at 1500 K and relative fit with the Am_2O_3 and AmO_2 structures.

3.2.2.4 Measurements during cooling

In order to extend the investigation of the intermediate composition domain $1.6 < O/Am < 2$, the strategy detailed in section 3.2.1.2 was adopted. Therefore, thermal cycles were performed between 700 and 1400 K, under a given atmosphere, with pO_2 ranging from 10^{-4} to 10^{-8} atm. A schematic representation is reported in Fig. 3.10. The measurements were performed with the following steps:

1. the AmO_2 sample was heated, under air, from room temperature to 1400 K at $300\ K \cdot min^{-1}$;

2. at 1400 K under air, the AmO_{2-x} sample should be slightly reduced, as shown by the point (2) on the phase diagram, in Fig. 3.10. The flowing gas was then switched from air to He and the pO_2 was regulated to the desired value. This latter was kept constant for the rest of the measurement.

3. The sample was reduced at 1400 K under the given atmosphere for 5 hours; the *expected* final point (3) is shown on the phase diagram.

4. The sample was cooled down to 700 K. The cooling step, as previously explained, is supposed to induce a re-oxidation of the sample. According to the discussion in section 3.2.1.2, two strategies were adopted: *slow* cooling, lasting between 4 and 10 hours, and *fast* cooling at $1\ K \cdot s^{-1}$. Equilibrium (green curve) and out-of-equilibrium (blue dashed lines) paths are expected for the slow and fast cooling, respectively.

During the *fast* cooling, XRD patterns were collected in fixed-angle mode between 26° and 29° 2θ. This angular range includes the (111) peak of the fluorite structure (regardless of the
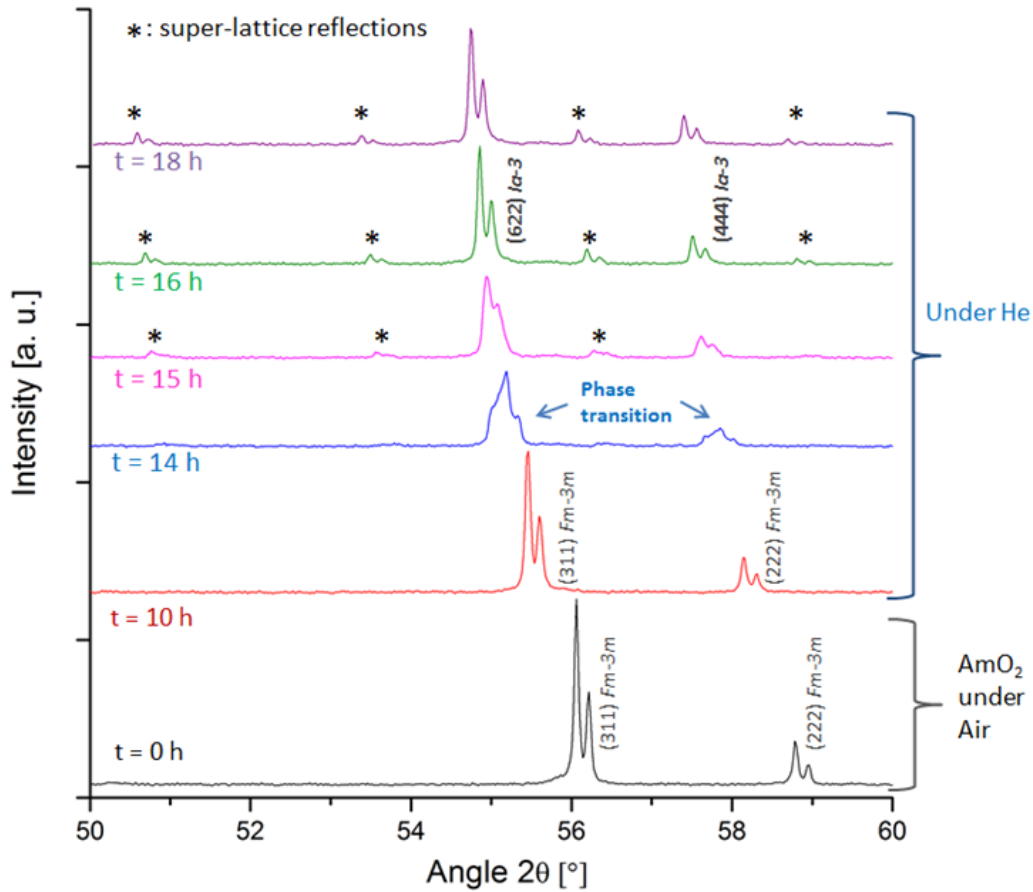
Fig. 3.8: XRD patterns sections between 50° and 60° 2θ during iso-T measurements at 1220 K during reduction. After 14 h, the BCC structure (super-lattice reflections) appears.

temperature). The obtained results, for all the used pO_2 conditions, are shown in Fig. 3.11, where the diffraction patterns were combined to create iso-intensity maps. No splitting or broadening of the (111) peak was ever observed, showing that no phase separation took place during the cooling process.

For the *slow* cooling experiments, complete diffraction patterns ($25° < 2\theta < 140°$) were collected at each temperature step (50 K or 100 K, according to the specific heat treatment) for $pO_2=10^{-4}$, 10^{-6}, 10^{-7} and 10^{-8} atm. For $pO_2= 10^{-6}$ and 10^{-7} atm, multiple measurements were consecutively performed: after the cooling step, the sample was immediately reheated and the cycle was identically repeated. In all the cases, only one phase was observed and the best refinement was always achieved with the fluorite structure ($Fm\overline{3}m$). The computed lattice parameters are reported in Fig. 3.12, where colors are used to distinguish the atmospheres, whereas different symbols are used to identify the consecutive cycles performed in the same pO_2 conditions ($\blacksquare$ = 10^{-4} atm, $\blacksquare\blacklozenge\blacktriangledown\bullet$ = respectively 1st, 2nd, 3rd and 4th cycles at 10^{-6} atm, $\blacksquare$ ◄ ▼ = respectively 1st, 2nd, 3rd cycles at 10^{-7} atm, $\blacksquare$ 10^{-8} atm). On the same figure, the linear variation of the lattice parameter in air (for T<1200 K) is reported as a reference.

The lattice parameter reported for T= 1400 K is the one obtained at the end of the reduction plateau (5 hours), during which an increase in the lattice parameter was systematically observed. At 1400 K, the sample was always reduced regardless of the pO_2, since the lattice parameter is
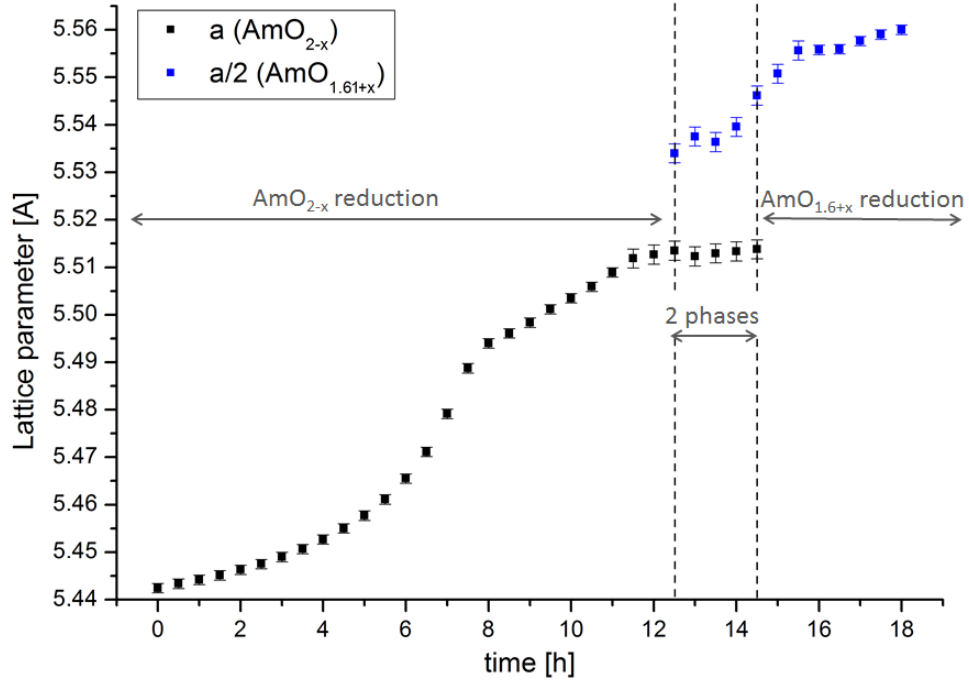
Fig. 3.9: Lattice parameter variation as a function of time during an isothermal measurement at 1220 K in He: ■ AmO_{2-x} phase (s.g. $Fm\bar{3}m$); ■ $AmO_{1.61+x}$ phase (s.g. $Ia\bar{3}$).

higher than the linear variation observed at T < 1200 K for stoichiometric AmO_2.

For the highest pO_2 (10^{-4} atm), the steep slope of the lattice parameter variation indicates that the reoxidation process occurred relatively quickly during cooling. Moreover, at 700 K, since the lattice parameter coincides with the value found in air, the O/Am ratio is estimated to be close to 2.00.

For $pO_2=10^{-6}$ atm, the first observation is that the consecutive heat treatments (■♦▼● in Fig. 3.12) give different results, meaning that equilibrium was not achieved. For the first measurement (■), conclusions similar to the previous case at $pO_2=10^{-4}$ atm can be drawn. On the contrary, the following heat treatments (2nd, 3rd and 4th cycles) in this atmosphere showed a completely different behavior, with lattice parameters (♦▼● in Fig. 3.12) systematically higher compared to those of the estimated O/Am = 2.00 line. As observed in Fig. 3.12, for these three measurements, the trend slope is lower than that in air, and therefore the decrease in the lattice parameter with temperature is slower. This indicates that the sample was not oxidized or even reduced during these cooling steps.

Finally, for lower pO_2, the sample seems to be stabilized in a reduced state, as evidenced by the reproducibility of large lattice parameters obtained in successive measurements with both $pO_2=10^{-7}$ and 10^{-8} atm. Moreover, the variation as a function of temperature appears to be linear in first approximation, with a slope similar to that of the reference line plotted for O/Am = 2.00 (variation in air). This probably indicates that the O/Am ratio was constant and the observed lattice contraction may be only affected by the decrease in temperature. Fig. 3.12 shows that there is an empty region in the graph, corresponding to intermediate lattice parameters (and therefore intermediate O/Am ratios), despite the small pO_2 variations between the measurements. It seems that, in the consecutive cooling steps, the sample abruptly moves
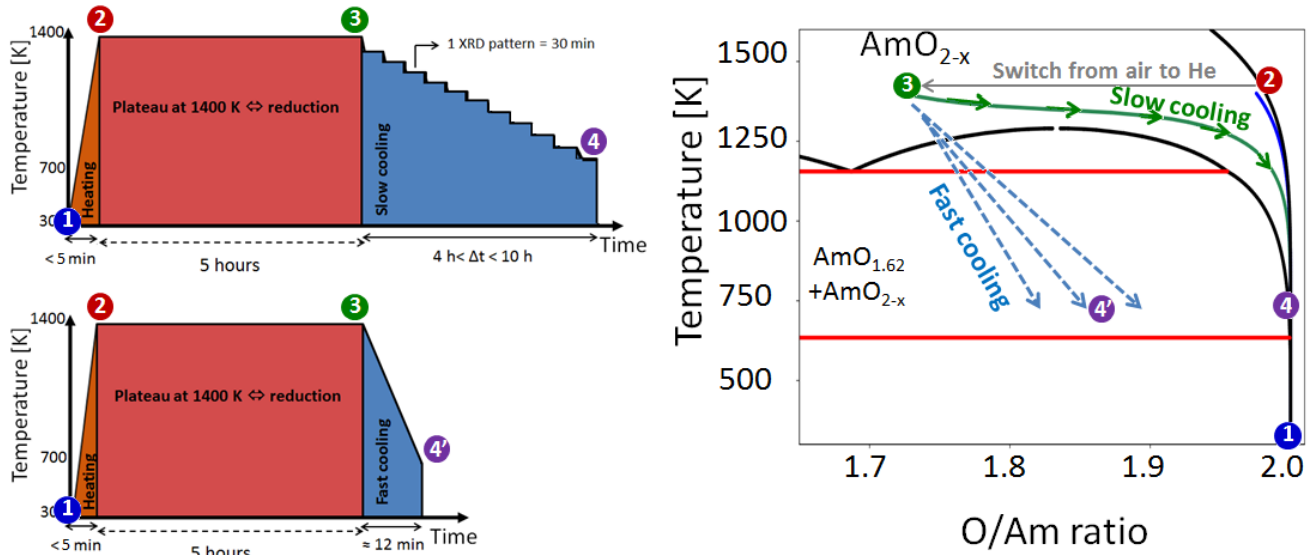
Fig. 3.10: Schematic representation (not in scale) of the temperature profiles under a given atmosphere and expected corresponding points on the phase diagram.
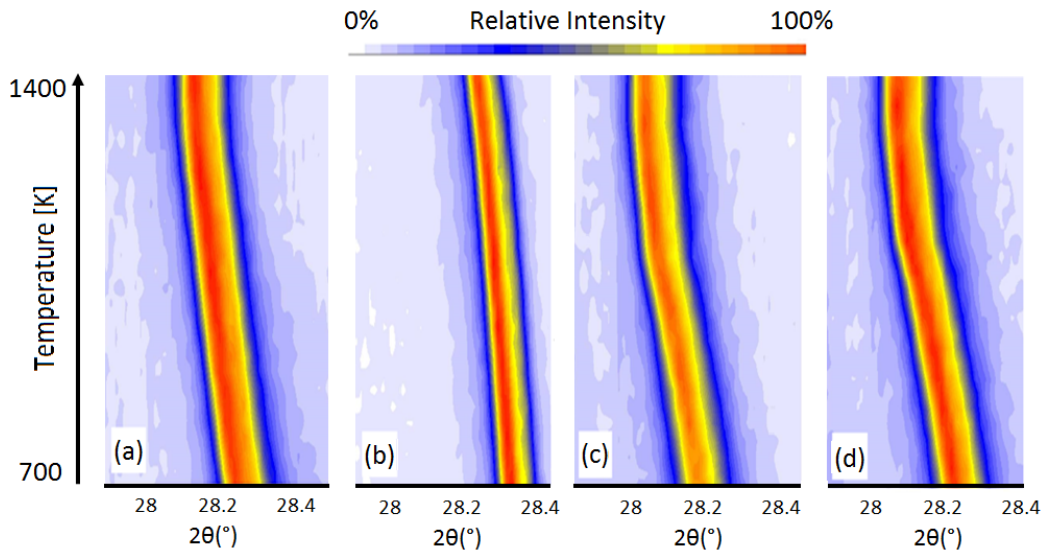
Fig. 3.11: Iso-intensity maps of the main fluorite-structure peak (111) collected during *fast* cooling under different atmospheres: $pO_2 = 10^{-5}$ atm (a), 10^{-6} atm (b), 10^{-7} atm (c), 10^{-8} atm (d).

from being rapidly oxidized at O/Am~2 to keeping a reduced state. An interpretation for this peculiar behavior is presented in the following discussion.

3.2.3   Discussion

3.2.3.1   Comparison between experimental results and model predictions

The measurements performed in air are consistent with the CALPHAD model. In fact, the lattice parameter variation (Fig. 3.5) exhibits a slope change at around 1200 K that can be interpreted as the onset of the AmO_2 reduction. This temperature is in excellent agreement with
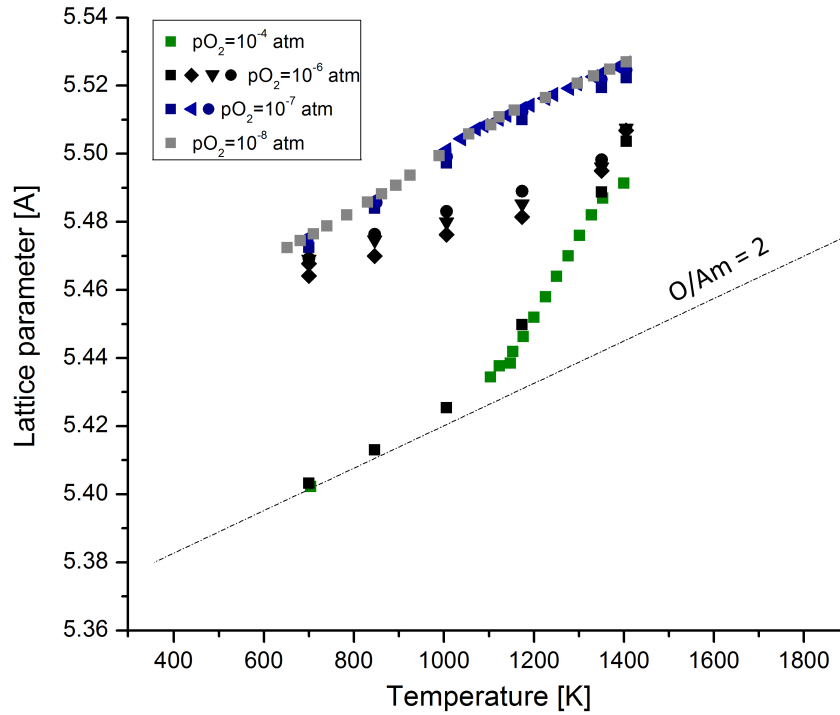
Fig. 3.12: Experimental lattice parameters as a function of T for pO_2 ranging from 10^{-4} atm to 10^{-8} atm (different symbols with same colors refer to consecutive cycles under the same pO_2).

the model predictions, as shown by the O/Am ratios calculated from the equilibrium between AmO_{2-x} and air, also represented in Fig. 3.5. This is not surprising because, as detailed before, the near-stoichiometric domain of AmO_{2-x} is quite well known since experimental data were available for the assessment. A good agreement is also obtained for the experiment performed at 1500 K in reducing conditions: the biphasic region $AmO_{2-x}/A-Am_2O_3$ was observed under the oxygen potential computed using the model ($T = 1500K$, $\Delta\overline{G}(O_2) = -140 \ kJ \cdot mol^{-1} \rightarrow pO_2 \simeq 2 \cdot 10^{-5}atm$).

Whilst a good agreement between the model and the experimental points was observed in both oxidizing and reducing conditions at 1500 K, it was not the case in the intermediate phase diagram region within the $1.6 < O/Am < 1.9$ and $700 < T < 1400$ K ranges. For instance, the hexagonal $A-Am_2O_3$ phase was never observed when the samples were reduced at 1400 K (at the beginning of the thermal cycles under a given atmosphere), not even for the lowest pO_2 (10^{-8} atm), in contrast with the CALPHAD computations ($T = 1400K$, $\Delta\overline{G}(O_2) = -140$ $kJ \cdot mol^{-1} \rightarrow pO_2 \simeq 5 \cdot 10^{-6}atm$). In this case, the discrepancy could be due to both inaccurate predictions of the model or kinetic problems, preventing the achievement of equilibrium.

Certain conclusions can be drawn from the isothermal measurements. First, the BCC $AmO_{1.61+x}$ phase exists up to at least 1280 K, whereas it was limited at ∼1200 K in the model of Gotcu-Freis *et al* [64]. Moreover, evidence of the existence of a composition domain for this phase were presented, whereas it was previously modeled as a stoichiometric compound. Finally, as already mentioned, a separation in two FCC phases was not experimentally observed, contrary to the CALPHAD model. According to the latter, on the basis of Sari and Zamorani data [58], at 1220 K the two FCC phases constituting the miscibility gap should have O/Am ratios equal to 1.71

and 1.93, respectively. This large difference in oxygen stoichiometry would induce a significant difference in the corresponding lattice parameters and consequently should be discernible by XRD. Considering the duration of the isothermal measurement at 1220 K ($\sim$20 h) and the constant variation in the lattice parameter shown in Fig. 3.9, it can be deduced that the entire O/Am range between the AmO_2 and the $AmO_{1.61}$ was crossed. Therefore, the miscibility gap described by Sari and Zamorani [58] is not compatible with the new HT-XRD results. The same conclusion can be drawn by looking at the results of the reducing-cooling measurements under a given atmosphere composition: no phase separation was ever observed, for fast or for slow cooling rates, despite the large oxygen potential range explored. However, for the slow cooling measurements, a peculiar lattice parameter behavior was observed, as shown in Fig. 3.9 and pointed out before. In fact, by decreasing pO_2, the lattice parameters at low temperature increase drastically, in a discontinuous way. This reflects variations in the oxygen stoichiometry of the sample that seems to switch from O/Am=2.00 at 700 K to a more reduced state, avoiding intermediate O/Am ratios. In order to understand the phenomena occurring in the samples, it would be necessary to know the exact stoichiometry of the material during the measurement. A method developed for this purpose is discussed in the following section.

3.2.3.2   Lattice parameter dependence on temperature and O/Am ratio

The major problem in the interpretation of HT-XRD experiments is the impossibility to determine the sample stoichiometry during the experiment. Furthermore, the sample mass retrieved at the end of the experiment is too low for oxygen/metal (O/M) determination using gravimetric methods. This problem can be overcome when one works with well-known compounds such as $UO_{2\pm x}$, PuO_{2-x} and $(U,Pu)O_{2\pm x}$, for which correlations between O/M ratio, temperature and lattice parameter are available in the literature (see section 2.2.3). However, regarding americium oxides, the dependence of the lattice parameter upon the O/Am ratio is unknown. A methodology based on coupling experimental data and CALPHAD thermodynamic computations is here used to assess a relation for the lattice parameter of the FCC structure of AmO_{2-x} as a function of both temperature and oxygen stoichiometry.

The measurements in agreement with the model predictions were selected: the data collected in air, in the $A\text{-}Am_2O_3/AmO_{2-x}$ biphasic region and under pure oxygen by Fahey [111]. For all these measurements, the O/Am ratios were computed with the CALPHAD model of Gotcu-Freis *et al* [64]. The results are summarized in Tab. 3.2.

The uncertainty on the computed O/Am ratios was not easy to estimate, since it depends on both the experimental and the model uncertainties. The maximum fluctuation in the computed O/Am caused by the temperature ($\pm$ 15 K) and pO_2 (3%-10%) uncertainties was equal to ±0.0094. In a conservative approach, this value was considered for all the calculations. The imprecision of the model was more complicated to evaluate. For the region near the AmO_{2-x}/O_2 equilibrium boundary, the computation results depend on the model parameters of the AmO_{2-x} phase which were optimized using the oxygen potentials measured by Chikalla and Eyring [57], in the $1140 \leq T \leq 1445$ K temperature range. The fit of these data by the model of Gotcu *et*

T [K]	a [Å]	Computed O/Am	T [K]	a [Å]	Computed O/Am
	Measured under air (this work)			Am$_2$O$_3$/AmO$_{2-x}$ domain (this work)	
1894	5.527(2)	1.79(3)	1500	5.527(2)	1.59(5)
1873	5.522(2)	1.80(3)		Measured under oxygen (Fahey [111])	
1773	5.511(2)	1.84(3)	303	5.375	2.00(1)
1673	5.497(2)	1.89(3)	423	5.381	2.00(1)
1573	5.483(2)	1.93(3)	573	5.389	2.00(1)
1473	5.468(2)	1.96(1)	700	5.396	2.00(1)
1373	5.455(2)	1.97(1)	823	5.403	2.00(1)
1273	5.444(2)	1.98(1)	923	5.409	2.00(1)
1173	5.436(2)	1.98(1)	1023	5.415	2.00(1)
1073	5.428(2)	1.98(1)	1120	5.421	2.00(1)
973	5.418(1)	1.98(1)			
873	5.414(1)	1.98(1)			
773	5.408(1)	1.98(1)			
673	5.402(1)	1.99(1)			
573	5.396(1)	1.99(1)			
473	5.389(1)	1.99(1)			
373	5.383(1)	2.00(1)			
303	5.377(1)	2.00(1)			

Table 3.2: Measured temperatures/lattice parameters and computed O/Am ratios for selected measurements.

al. [64] was very good and within the experimental uncertainty, equal to $\pm$ 0.002 for the O/Am ratio [57]. Several cases were then considered for the calculations of this work. For the computations performed in the 1140$\leq$ T $\leq$ 1445 K range, the accuracy of the model can be estimated equal to $\pm$0.002. Considering the propagation of the uncertainties (model and experiment), an overall value of $\pm$0.01 was obtained. This value can be adopted also for T < 1140 K, since AmO$_2$ is known to be almost stoichiometric at low temperature and therefore the uncertainty on the O/Am is low. On the contrary, for T > 1445 K, no experimental data are available for AmO$_{2-x}$ and the computations are then based on an extrapolation of the CALPHAD model. Following a conservative approach, the overall uncertainties on the O/Am ratios was then multiplied by 3. Finally, the O/Am ratio of AmO$_{2-x}$ on the phase boundary with A-Am$_2$O$_3$ is likely imprecise, since no experimental data were available for that domain of the phase diagram, and an uncertainty equal to $\pm$0.05 was then considered.

Similarly to UO$_{2\pm x}$ and PuO$_{2-x}$, at least in first approximation, the lattice parameter is supposed to vary as a linear function of both temperature and O/Am in our temperature and composition range. The following equation was used to fit the selected data:

$$a(T, O/Am) = 5.376 + C_1 \cdot (T - 298.15K) + C_2 \cdot x, \tag{3.2}$$

where T is the temperature in K and x is the departure from stoichiometry ($O/Am = 2 - x$). The C_1 and C_2 constants were found by least squares minimization method. The obtained values are

$C_1 = 6 \cdot 10^{-5}$ [Å K^{-1}] and $C_2 = 0.248$[Å] and the resulting fit is shown in Fig. 3.13. Considering all the approximations introduced, in a conservative approach, an uncertainty equal to ± 0.05 must be considered for the O/Am ratios computed using Eq. (3.2). This value is quite high compared to the experimental ones: for instance, by TGA, uncertainties around 0.001 can be achieved.
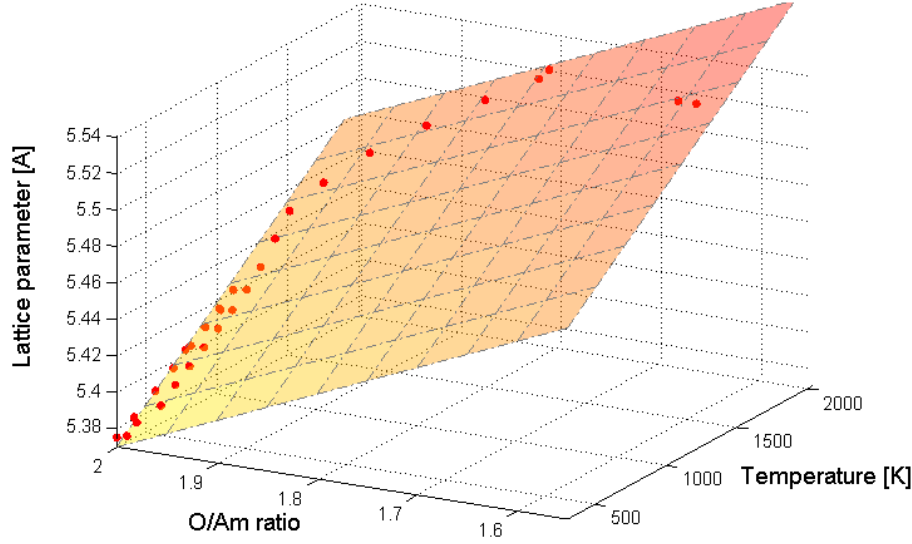
Fig. 3.13: Fit of the T-a-O/Am data points obtained by least square minimization method.

3.2.3.3 Re-interpretation of the XRD data

The lattice parameters of Fig. 3.12, collected during the cooling step in given atmospheres, are represented again in Fig. 3.14, together with iso-O/Am lines (O/Am ratios = 2, 1.9, 1.8, 1.7 and 1.6) calculated using Eq. (3.2). The same symbols as in Fig. 3.12 are adopted in Fig. 3.14: colors are used to distinguish the different pO$_2$, whereas different symbols of the same color indicate successive cycles under the same atmosphere conditions. On the same graph, the data collected in air and the AmO$_{2-x}$ lattice parameters obtained in the two biphasic regions AmO$_{2-x}$/A-Am$_2$O$_3$ (■) and AmO$_{2-x}$/AmO$_{1.61+x}$ (■) are also plotted. The experimental composition-temperature points are reported on the phase diagram of Gotcu-Freis *et al.* [64] in Fig. 3.15. The same symbols and colors were used in the two figures for the corresponding lattice parameters and points in the phase diagram. All the data points refer to the observation of a single fluorite structure, except for the two points in the biphasic regions (■, ■). The estimated O/Am ratios for these latter appear reasonable. In fact, for the point in the A-Am$_2$O$_3$/AmO$_{2-x}$ region, an O/Am$\simeq$1.6 was assessed, which is the limit of the AmO$_{2-x}$ hypostoichiometry usually accepted in the literature at T = 1500 K [56, 62, 64]. For the phase boundary where the C-AmO$_{1.61+x}$ phase precipitates at 1220 K, the evaluated O/Am ratio is 1.67. This value is consistent with the few data available in the literature for this intermediate phase, whose maximum O/Am ratio is reported as ranging between 1.65 [59] and 1.67 [60]. This proves the qualitatively goodness of Eq. (3.2).

Several conclusions can be drawn looking at Fig. 3.14 and 3.15. First, concerning the measurements in air and with pO$_2$=10^{-4} atm, as previously discussed, it is confirmed that for a given
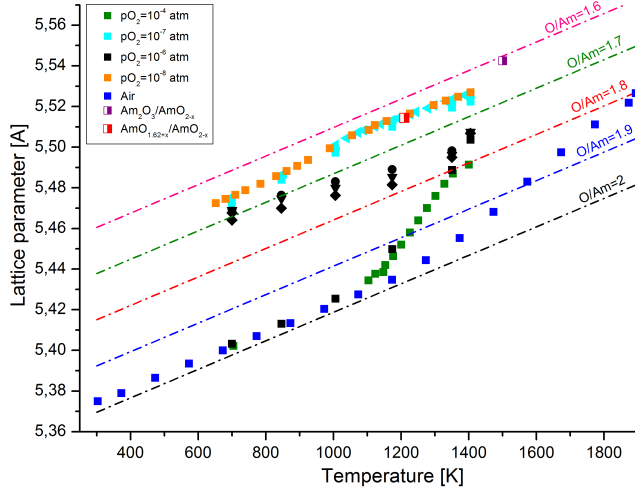
Fig. 3.14: Experimental lattice parameters as a function of temperature obtained in this work. Dashed lines are computed using Eq. (3.2) and they represent thermal expansion for compounds with fixed O/Am ratios.
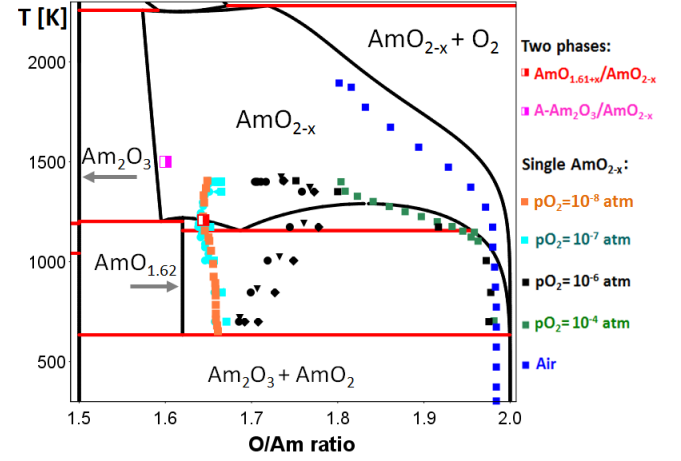
Fig. 3.15: The O/Am-T points observed in this work according to our composition assessment are reported on the phase diagram of Gotcu-Freis *et al.*

gas composition, AmO_2 is reduced at elevated temperature and then re-oxidized during cooling. A different behavior was observed for lower pO_2. In fact, with $pO_2=10^{-6}$ atm, different results were obtained in successive experiments: in the first case, the sample was oxidized during cooling, whereas in the following three measurements it was more and more reduced as evidenced by the increase in the lattice parameters. The lack of reproducibility of these measurements makes difficult to give them a thermodynamic meaning, since no steady state was reached in these experiments. Anyway, the results show that an intermediate region of O/Am ratio and temperature (Fig. 3.15) was not crossed during the experiments with a tendency to go towards more reduced compositions during cooling. Finally, all the measurements with $pO_2=10^{-7}$ and $pO_2=10^{-8}$ atm gave consistent and reproducible results, within the limit of the experimental uncertainties, and lead to a stabilized reduced state with $1.64<O/Am\leq1.67$ from 1400 to 700 K. The lattice parameters obtained during cooling at about 1200 K are similar to those found for the $AmO_{2-x}/AmO_{2-x}+AmO_{1.61+x}$ phase boundary (▮). It is then realistic to consider the points collected in the $1200<T<1400$ K range in these iso-pO_2 measurements close to the phase boundary where the $AmO_{1.61+x}$ phase precipitates. This would explain the reproducibility of these points, even for two different oxygen partial pressures (10^{-7} and 10^{-8} atm). In these measurements during cooling, the non-observation of the second BCC phase could be explained by several reasons. It could be due to a kinetics reason; in fact, for the isothermal measurements, it took more than 12 hours to reach the phase boundary whereas the heat treatments in a given atmosphere were significantly shorter (the reduction heat treatment duration was 5 hours). It is also possible that a second phase was present but not detectable by XRD since only about 20 mg of material were used. Finally, since the AmO_{2-x} samples of the isothermal reduction and cooling measurements were different, it is possible that small differences in impurities could stabilize a phase rather than the other. The hypothesis that the points measured during cooling under

reducing conditions ($pO_2 = 10^{-7}$ and 10^{-8} atm) are close to the $AmO_{2-x}/AmO_{2-x}+AmO_{1.61+x}$ phase boundary cannot be extended to the entire temperature range (until 700 K). In fact, all the literature data indicate that the large AmO_{2-x} hypostoichiometric domain exists for T>1100 K, whereas at lower temperatures only O/Am$\simeq$2 are thermodynamically stable. Therefore, the oxygen stoichiometry of AmO_{2-x} in equilibrium with the $AmO_{1.61+x}$ phase boundary, estimated to be O/Am$\simeq$1.67 for T$\simeq$1220 K, must increase as the temperature decreases. This means that the extent of the two phase region ($AmO_{1.61+x} + AmO_{2-x}$) also has to increase when temperature is decreased. Therefore, the experimental points in the 700<T<1100 K range with O/Am$\simeq$1.66 should fall in this biphasic domain. The non-observation of the $AmO_{1.61+x}$ phase could be explained by the fact that during cooling the sample reached a metastable state. At high temperature (1400 K) and in reducing conditions ($pO_2 < 10^{-6}$ atm), the dioxide was almost reduced to the BCC phase transition. When decreasing the temperature, the kinetics was slowed down and the driving force toward the $AmO_{1.61+x}$ became lower (cooling under given atmosphere implies more oxidizing conditions). At the same time, the atmosphere conditions were too reducing for a prompt re-oxidation of the sample. Therefore, the fluorite structure remained even with the low oxygen stoichiometry. It would probably have evolved toward the BCC phase or the re-oxidation in a longer time frame. In summary, according to this explanation, the points observed during cooling with $pO_2=10^{-7}$ and 10^{-8} atm would correspond to the $AmO_{2-x}/\ AmO_{2-x}+AmO_{1.61+x}$ phase boundary for a $\overline{T} < T < 1400$ K and to a metastable state for $T < \overline{T}$, where $\overline{T}$ should be about 1100-1280 K.

3.3   Calphad modeling

As shown above, the Am-O CALPHAD model of Gotcu-Freis *et al.* [64] is not consistent with part of the new experimental data acquired in this work. Therefore, in the following, a modification of the thermodynamic CALPHAD model of Gotcu-Freis *et al.* is presented. As it will be shown, **the introduced modifications concern the AmO$_2$, AmO$_{1.61}$ and the americium oxide gas species**. The other phases, namely the **metal phases, the liquid and the Am$_2$O$_3$ were not modified**.

As explained in Ch. 1, the CALPHAD method consists of three principle steps: the research and selection of the experimental data, the modeling of each phase and the optimization of the Gibbs energy parameters. Some changes were necessary in all these three steps. The experimental data selected for the thermodynamic assessment are revised in section 3.3.1. Then, a new model for the $AmO_{1.61+x}$ is proposed in section 3.3.2. Finally, the result of the assessment will be compared with the experimental data.

3.3.1   Selection of the experimental data

All the phase diagram data reported in the literature, which were summarized in section 2.1.2, were considered by Gotcu-Freis *et al.* [64], with the exception of the XRD data indicating the existence of a low temperature (T<600 K) BCC sesquioxide [56]. Indeed, it is questionable whether the equilibrium was reached or not in the reported temperature range and no other

evidence of this phase exists in the literature. This choice was maintained here. Besides, the recent review by Konings *et al.* was taken into account [127]. In particular, new thermodynamic functions for the gaseous species were proposed in this work. Finally, the new experimental evidences of this work were considered:

- the point on the phase boundary between AmO_{2-x} and the biphasic region AmO_{2-x}/A-Am_2O_3: T=1500 K and O/Am=1.59 (computed with Eq. (3.2);

- the existence of a composition domain for the BCC $AmO_{1.61+x}$ phase;

- the stability of the $AmO_{1.61+x}$ phase up to at least 1280 K;

- a point on the phase boundary between $AmO_{1.61+x}$ and the biphasic region AmO_{2-x}/ $AmO_{1.61+x}$: T=1220 K and O/Am=1.67;

- the absence of an AmO_{2-x} miscibility gap for T≥1220 K. Both the oxygen potentials computed with the model of Gotcu-Freis *et al.* and those proposed by Casalta [59] were tested in this work: a domain with two FCC phases was never observed for either of them.

- The inconsistency of the DTA data of Sari and Zamorani [58] indicating the miscibility gap between 1180 K and 1300 K. Indeed, our results indicate that, in this temperature range, the hypostoichiometric domain of the fluorite phase is extended down to the limit with the $AmO_{1.61+x}$ phase. No other transitions were observed for 1.7 < O/Am < 1.9, contrary to the DTA data. A possible explanation for this inconsistency could be that the reaction detected by DTA did not originate from AmO_2, but from the sample impurities, for instance Ce and Pu. Indeed, both CeO_2 and PuO_2 present a miscibility gap, which could induce these effects. No details on the composition of the analyzed material were provided by Sari and Zamorani [58] but, keeping into account the difficulty to separate Am from other actinides and lanthanides, high impurity contents were likely present. In conclusion, the DTA data around 1200 K were excluded from the assessment.

The same thermodynamic data selected by Gotcu-Freis *et al.* were used for the new CAL-PHAD assessment. These include the enthalpy of formation [128, 129] and the standard entropies [127] of AmO_2 and A-Am_2O_3, the enthalpy increments with temperature up to 1180 K of AmO_2 and A-Am_2O_3 [145] and the AmO_{2-x} oxygen potential data by Chikalla and Eyring [57] (see section 2.4). For the latter, as explained in 2.5.2, the experimental points with O/Am<1.9 and T<1300 K were excluded by Gotcu-Freis *et al.* because they were not consistent with the AmO_{2-x} miscibility gap. Since this is no more included here, the entire set of oxygen potential data was adopted for this assessment.

3.3.2 Models

The Gibbs energy functions of all the phases refer to the enthalpy H of the pure elements i, in the Stable Element Reference (SER) state, i. e. the stable state for the element at 298 K

and 10^5 Pa [21]. The thermodynamic models (the general mathematical expressions) chosen by Gotcu-Freis *et al.* for the elements, the stoichiometric compound A-Am$_2$O$_3$, the gas, the liquid and the AmO$_{2-x}$ phase were maintained in this work.

For the intermediate BCC AmO$_{1.61+x}$ phase, on the contrary, a change of the model was necessary, since this phase was previously described as a stoichiometric compound. To include a non-stoichiometric region, the compound energy formalism [21] was applied. The three-sublattice model previously used to describe the cubic Ce$_3$O$_{5\pm x}$ [161] and PuO$_{1.61+x}$ [162] phases in the TAF-ID [?] was adopted:

$$(Am^{3+}, Am^{4+})_2(O^{2-})_3(O_{2-}, Va)_1 \tag{3.3}$$

where Va stands for vacancy. A schematic representation of the model is reported in Fig. 3.16.
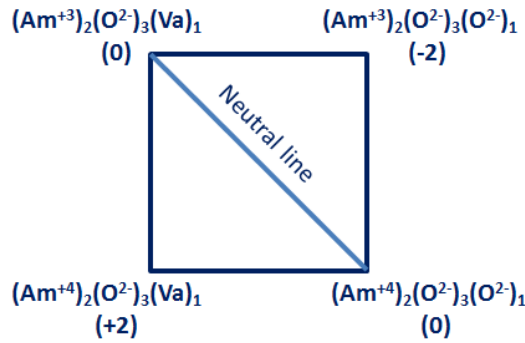
Fig. 3.16: Scheme of the sublattice model $(Am^{3+}, Am^{4+})_2(O^{2-})_3(O_{2-}, Va)_1$ describing the AmO$_{1.61+x}$ phase.

Four end members are obtained by combining one by one the species of each sublattice:

1. $(Am^{4+})_2(O^{2-})_3(O^{2-})_1$ with a composition AmO$_2$ which corresponds to a metastable BCC AmO$_2$ phase with respect to the fluorite form;

2. $(Am^{3+})_2(O^{2-})_3(Va)_1$ with a composition Am$_2$O$_3$ which corresponds to the metastable cubic Am$_2$O$_3$ phase with respect to the hexagonal form;

3. $(Am^{4+})_2(O^{2-})_3(Va)_1$ with a net charge of $+2$;

4. $(Am^{3+})_2(O^{2-})_3(O^{2-})_1$ with a net charge of -2.

The latter two end members are hypothetical and have no physical meaning on their own, but only in electrically neutral combination. The AmO$_{1.61+x}$ phase exists as a combination of the four end members, only along the neutral line of Fig. 3.16. The corresponding Gibbs energy of the AmO$_{1.61+x}$ phase G^ϕ is:

$$G^\phi - \sum_i n_i^\phi H_i^{SER}(298.15K) = y_{Am^{4+}}y_{O^{2-}}{}^\circ G_{(Am^{4+})_2(O^{2-})_3(O^{2-})_1} + y_{Am^{4+}}y_{Va}{}^\circ G_{(Am^{4+})_2(O^{2-})_3(Va)_1} +$$
$$+ y_{Am^{3+}}y_{Va}{}^\circ G_{(Am^{3+})_2(O^{2-})_3(Va)_1} + y_{Am^{3+}}y_{O^{2-}}{}^\circ G_{(Am^{3+})_2(O^{2-})_3(O^{2-})_1} + 2RT(y_{Am^{3+}}lny_{Am^{3+}} +$$
$$+ y_{Am^{4+}}lny_{Am^{4+}}) + RT(y_{O^{2-}}lny_{O^{2-}} + y_{Va}lny_{Va}) + y_{Am^{3+}}y_{Am^{4+}}[L^0_{(Am^{3+},Am^{4+})_2(O^{2-})_3(O^{2-})_1} +$$
$$+ (y_{Am^{3+}} - y_{Am^{4+}})L^1_{(Am^{3+},Am^{4+})_2(O^{2-})_3(O^{2-})_1} + L^0_{(Am^{3+},Am^{4+})_2(O^{2-})_3(Va)_1} +$$
$$+ (y_{Am^{3+}} - y_{Am^{4+}})L^1_{(Am^{3+},Am^{4+})_2(O^{2-})_3(Va)_1}] \quad (3.4)$$

Where n_i^ϕ is the number of atoms of the ith element in the oxide formula; y_i are the fraction of the species i in the sublattice (Am^{4+} or Am^{3+} in the first sublattice and O^{2-} or Va in the third sublattice), $^\circ G$ are the Gibbs energies of the different end members and L^i are interaction parameters which can have a linear dependence on temperature. According to Eq. (3.4), the Gibbs energy of the $AmO_{1.61+x}$ phase is given by the sum of several terms: the Gibbs energy reference term corresponding to a mixture of the four end members, a configurational entropy term for the mixture of the different species in the first and third sublattices and an excess mixing term on the first sublattice.

The new assessed thermodynamic parameters of the $AmO_{1.61}$ phase and the re-assessed paramaters (modified in comparison to Gotcu-Freis) of the AmO_2 and gas phases are reported in Appx. C.

3.3.3 Calculated phase diagram

The resulting phase diagram is shown in Fig. 3.17-(a), with a magnification on the solid phases of the 1.49<O/Am<2.01 range in Fig. 3.17-(b). The latter includes the differences in comparison to the phase diagram of Gotcu-Freis et $al.$ (3.1), namely the absence of the miscibility gap in AmO_{2-x} and the hyperstoichiometric domain of $AmO_{1.61+x}$.
The new description agrees generally well with the selected experimental data from the literature [56, 58] and the new ones collected in this work. The invariant $AmO_{1.61+x} = Am_2O_3 + AmO_{2-x}$ reaction identified by DTA at around 630 K is perfectly replicated. The biphasic $AmO_{1.61+x}/Am_2O_3$ and $AmO_{1.61+x}/AmO_{2-x}$ regions observed by Chikalla and Sari are correctly reproduced in the calculated diagram. Moreover, the XRD data of the single $AmO_{1.61+x}$ phase by Chikalla ($\bullet$ in Fig. 3.17-(b)) are now in agreement with the computed non-stoichiometric domain, except for those at T<800 K (not included in the assessment). The temperature stability for this phase was extended here up to 1315 K.
The hypo-stoichiometric domain of the AmO_{2-x} phase was extended to lower temperature than in the model of Gotcu-Freis et $al.$, according to the new data ($\blacksquare$). The possibility to substantially reduce AmO_2 at T$\simeq$1200 K without the occurrence of a miscibility gap is here included. Finally, the phase boundaries AmO_{2-x}/Am_2O_3 at 1500 K and $AmO_{2-x}/AmO_{1.61+x}$ at 1220 K are in good agreement with the observed experimental points (respectively $\blacksquare$ and $\blacksquare$), in the limits of the experimental uncertainties, which are indicated by the error bars in Fig. 3.17-(b).
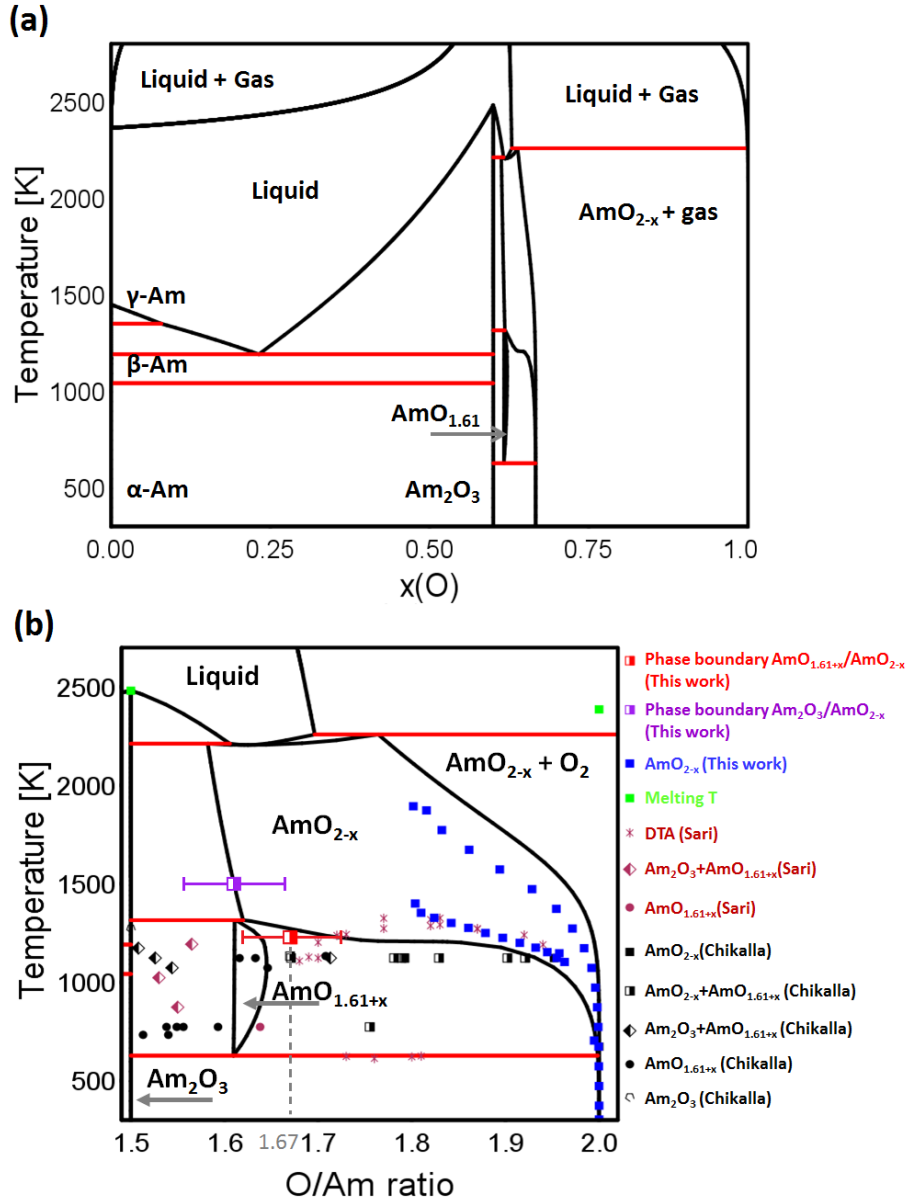
Fig. 3.17: (a) Am-O phase diagram calculated with the CALPHAD model of this work; (b) magnification in the stoichiometry range 1.49<O/Am<2.01. The experimental data are from [56, 58, 63] and this work.

3.3.4 Calculated oxygen potentials

The oxygen potentials versus O/Am ratios calculated at 1140, 1180, 1235, 1285, 1355, 1400 and 1445 K (solid lines) are compared to the experimental data [57] used for the assessment and to the previous results of Gotcu-Freis *et al.* [64] (dashed lines) in Fig. 3.18. For both the models, the computed $\Delta \overline{G}(O_2)$ curves are in reasonable agreement with the experimental points. For O/Am<1.94, the variation of the experimental points with hypostoichiometry is better reproduced by our computations, whereas the curves of Gotcu-Freis *et al.* are too flat because of the influence of the miscibility gap. This is particularly true for the two data sets at 1139 K and 1183 K, where a notable improvement of the fit is achieved in the 1.92 < O/Am < 1.97 range. On the contrary, the near stoichiometry points (1.99 < O/Am < 2) are better fitted by the model of Gotcu-Freis *et al.* However, since the oxygen potentials vary rapidly in a narrow

composition range, these data are affected by significant uncertainty and they are therefore the least reliable.

In Fig. 3.19, the two models are compared to the other oxygen potential data available in the literature [59, 60], but not used for the assessment. The data of Otobe *et al.* [60] are consistent
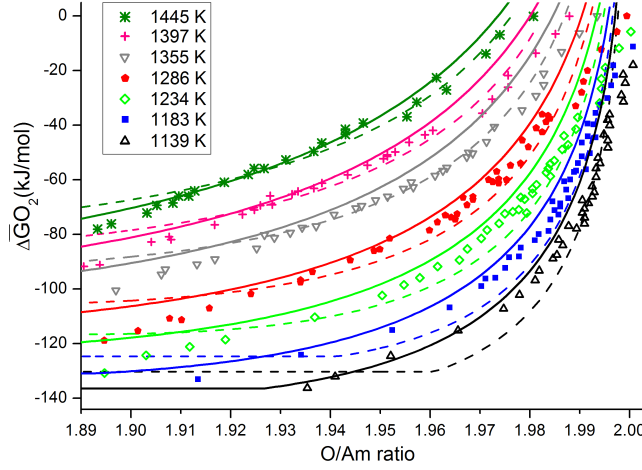
Fig. 3.18: Oxygen potentials by Chikalla and Eyring [57]. Computations using the CAL-PHAD model of this work (solid lines) and of Gotcu-Freis *et al.* (dashed lines) are reported, using the corresponding color for each temperature.
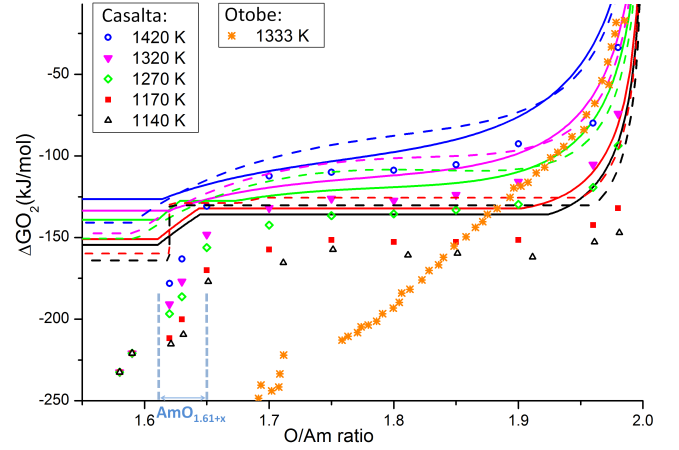
Fig. 3.19: Oxygen potentials by Casalta [59] and Otobe [60]. Computations using the CAL-PHAD model of this work (solid lines) and of Gotcu-Freis *et al.* (dashed lines) are reported with the corresponding color for each temperature.

with the models only in a narrow range near the stoichiometry, but a strong disagreement is observed for O/Am<1.9. As already mentioned, the oxygen potential measured by Casalta [59] are too low even near the stoichiometry in comparison to those of Chikalla and Eyring [57], hence they could not be used for the CALPHAD assessment. As a result, the $\Delta \overline{G}(O_2)$ curves computed with the two models are generally higher than Casalta's data, even if the deviation is slightly smaller for the new model than for the previous one. Furthermore, it is interesting to observe that the experimental trend is qualitatively reproduced by the CALPHAD model proposed here. In the $1.7 < O/Am < 1.9$ range, the computed curves are almost flat because of the vicinity of the $AmO_{1.61+x}/AmO_{2-x}$ biphasic region. Indeed, constant oxygen potentials are not necessarily proof of a miscibility gap, but of a biphasic domain: this could be the BCC+FCC region. For $1.61 < O/Am < 1.65$, a continuous decrease is consistent with the existence domain of the $AmO_{1.61+x}$ phase. This qualitative agreement could suggest some imprecisions in the calibration of the experimental set-up used by Casalta for the oxygen potential measurements.

The re-assessment of some of the thermodynamic parameters of the AmO_{2-x} phase could question the analysis of the experimental data previously performed, and especially the derivation of Eq. (3.2). However, it must be underlined that small changes were introduced and the two CALPHAD assessments provide very similar results for the near stoichiometric AmO_{2-x} domain, as shown in Fig. 3.20, where the equilibrium curves under air and oxygen, computed with both

the models, are shown on the phase diagram. The difference between the two assessments is
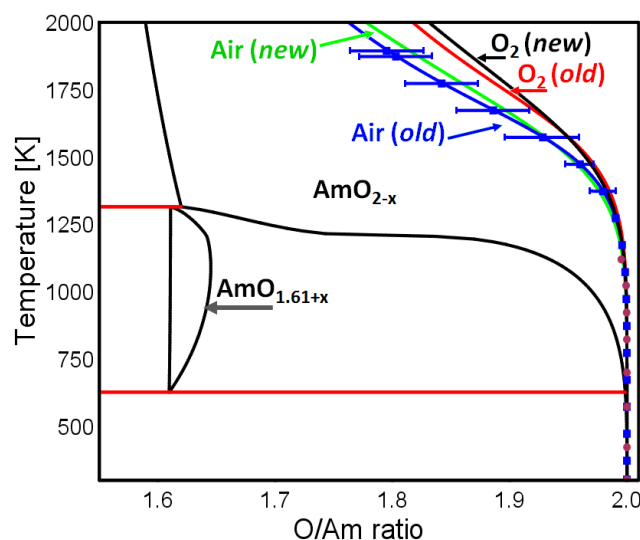
Fig. 3.20: Comparison of the models of this work (new) and of Gotcu-Freis (old) *et al.* ■ (air), ● (O_2): points computed with the model of Gotcu-Freis and used to derive the $O/Am - T - a$ relation of Eq. (3.2).

almost non-existent for T< 1500 K, whereas it increases above this temperature. However, the deviation is always smaller than the confidence band assigned to the computations (represented by the blue error bars in the figure), according to the discussion of section 3.2.3.2. The agreement between the new proposed model and that of Gotcu-Freis *et al.* in this domain of the phase diagram proves the self-consistency of the method adopted in this work, where the goodness of the previous model in this O/Am-T range was supposed for the analysis of the XRD experimental data.

3.3.5   Calculated high temperature enthalpy

The enthalpy increments for stoichiometric AmO_2 as a function of temperature are calculated and compared to the fit of Gotcu-Freis *et al.* [64] and to the measurements of Nishi *et al.* [145], in Fig. 3.21. The results obtained with the model of Gotcu-Freis *et al.* and the new ones are almost identical. This is consistent since, as already said, the parameters of the AmO_{2-x} phase re-assessed in this work concern only the Gibbs energy terms relative to the hypostoichiometric domain at high temperature. The description of stoichiometric AmO_2 from room temperature to 1200 K is unchanged.

3.3.6   Calculated vapour pressures

Vapour pressure measurements above AmO_{2-x} were performed by Gotu-Freis *et al.* [149], between 2000 and 2200 K, under vacuum, as discussed in section 2.4.4.1. During the experiment, the stabilization of the mass signals was observed and the authors supposed that the sample had reached the congruent vaporization, where the compositions of the gas and solid phases are equal. The variation of the O/Am ratio could not be determined. However, considering the
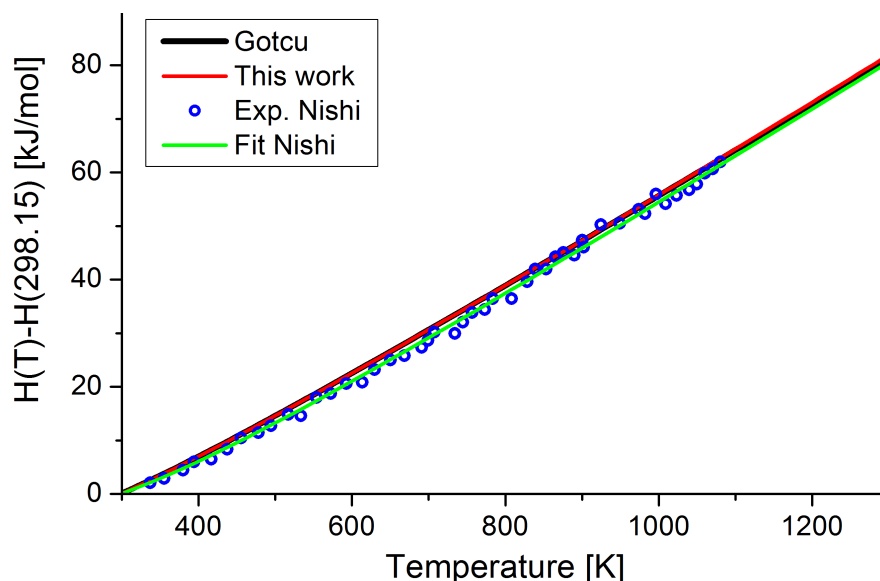
Fig. 3.21: Enthalpy increment as a function of temperature for AmO_2: this work model $(-)$, the Gotcu-Freis *et al.*'s model $(-)$, experimental data $(\circ)$ and relative Nishi's fit $(-)$.

experimental results presented above, in particular the reduction of AmO_{2-x} in air for T >1200 K, it is reasonable to assume a rapid decrease of the O/Am ratio, above 2000 K, under vacuum. Therefore, the congruent vaporization is expected for an O/Am ratio lower than 2. According to the thermodynamic assessment here presented, as well as to the previous one by Gotcu-Freis, the congruent vaporization does not occur for AmO_{2-x}, but for the A-Am_2O_3 sesquioxide. A fair reproduction of the experimental vapour pressures was provided by Gotcu-Freis, calculating the congruent vaporization above Am_2O_3, as shown in Fig. 3.22-(a). The magnitude order between the three species of the gas, $AmO_2(g)$, $AmO(g)$ and $Am(g)$, is respected. However, the calculated vapour pressure are systematically lower than the experimental ones, of a factor 10 or almost 100. As previously mentioned, a review of the thermodynamic properties of actinide oxides was recently reported in the literature by Konings *et al* [127]. In this work, a new expression of the Gibbs free energy was proposed for $AmO_2(g)$, on the basis of theoretical calculations. This function was tested in the Calphad assessment, but the resulting vapour pressures for the congruent vaporization of Am_2O_3 were higher than in the previous model, as shown in Fig. 3.22-(b).

It must be underlined that, since the same Gibbs free energy function of the Am_2O_3 phase was not changed in this work, the differences are strictly due to the Gibbs free energies of the gas. The high values calculated for the partial pressures suggest that the vapour species are too stable, compared to what the experimental data indicate. For this reason, taking the Gibbs free energy of the review as input values, the enthalpic terms of the $AmO(g)$ and $AmO_2(g)$ species were increased during the assessment, whereas the heat capacities proposed by Konings *et al.* were maintained [127]. The optimized enthalpies of formation are compared to the previous values of Gotcu-Freis *et al.* [64] and Konings *et al.* [127], in Tab. 3.3. The complete Gibbs energy functions are reported in Appx. C. A very good agreement with the experimental data was finally achieved, as shown in Fig. 3.23.
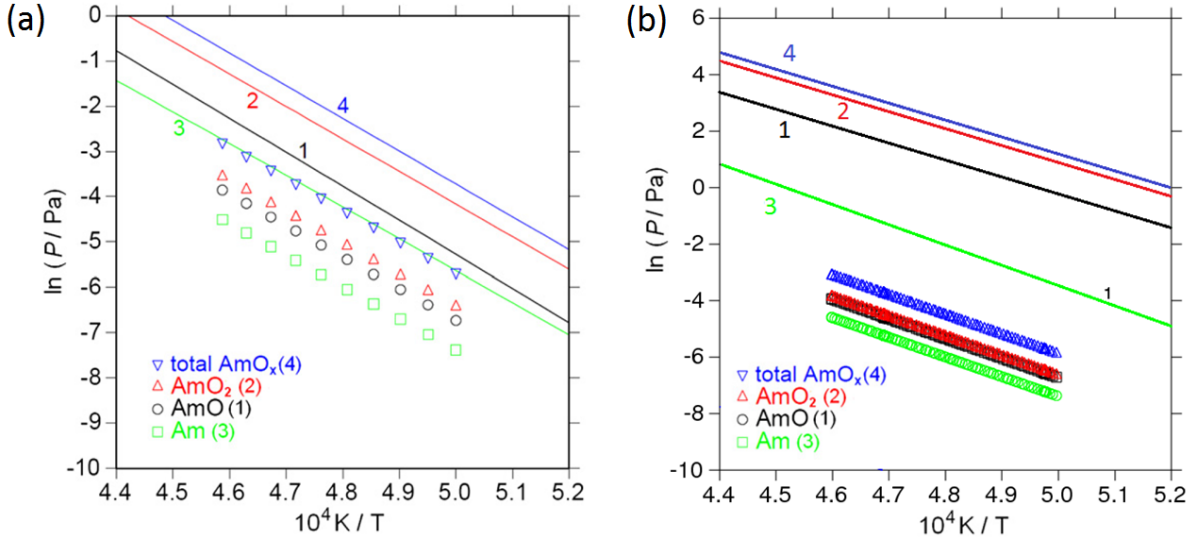
Fig. 3.22: (a) Exp. data and calculated vapour pressures for Am_2O_3 using the Calphad model of Gotcu-Freis [64]. (b) Exp. data and calculated vapour pressures for Am_2O_3 by replacing (only) the Gibbs energy function of $AmO_2(g)$ with the one proposed in [127].

	Δ_f H° (298.15 K) [kJ·mol^{-1}]		
	Gotcu-Freis *et al.* [64]	Konings *et al.* [127]	This work
AmO(g)	-15	-15±50	-3.8
$AmO_2(g)$	-389	-514±30	-350

Table 3.3: Enthalpies of formation of AmO(g) and $AmO_2(g)$.

Furthermore, in an independent work, C. Chatillon (private communications) reviewed the experimental data of the ionization process of the gaseous americium oxides [163–165]. From this analysis, Chatillon suggested that the enthalpy of formation of $AmO_2(g)$ should be between -278 and -243 kJ/mol. However, the values are too high to reproduce the experimental vapour pressures measured by Gotcu-Freis [166]. In the end, enthalpy of formation values close to those here assessed were hence suggested by Chatillon.

3.4   Conclusions

The Am-O system was investigated by combining experimental HT-XRD and thermodynamic modeling assessment. The starting point of this study was the CALPHAD assessment proposed by Gotcu-Freis *et al* [64]. This model was affected by several uncertainties due to the lack of experimental data available for americium oxides or, in some extent, to the inconsistency between different measurements, as the oxygen potentials. For this reason, the model of Gotcu-Freis *et al.* was used to select the experimental conditions, namely the temperature and the oxygen potentials, in order to study the undefined domains of the Am-O phase diagram. However, also other atmosphere conditions, reproducing the data of the literature inconsistent with the model
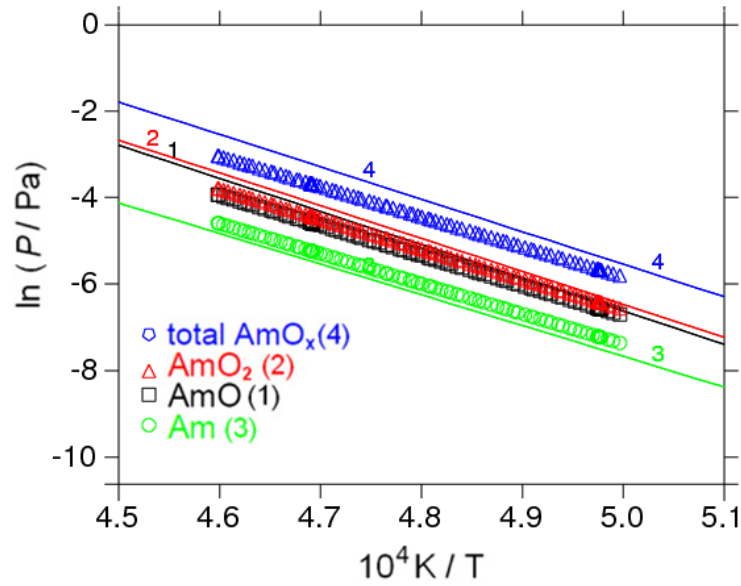
Fig. 3.23: Exp. data and calculated vapour pressures for Am_2O_3 using the new Calphad model.

of Gotcu-Freis *et al.*, were investigated, namely the oxygen potential of Casalta [59]. HT-XRD measurements were then performed up to 1900 K, under both air and helium atmosphere, with a precise control of the oxygen partial pressure. In two of the explored regions, the experimental results were consistent with the CALPHAD computations. First, AmO_2 was reduced in air for T > 1200 K, as foreseen by the model. Second, the $AmO_{2-x} \rightarrow AmO_{2-x} + A\text{-}Am_2O_3$ phase transition was observed at 1500 K by imposing the calculated oxygen potential $\Delta\overline{G}(O_2) \simeq -140$ kJ·mol^{-1}. Thanks to this agreement, by combining O/Am computations and XRD data, it was possible for the first time to assess the relation between temperature, lattice parameter and hypostoichiometry for $AmO_{2\text{-}x}$ with 0<x<0.4. On the contrary, the remaining measurements concerning the 700 < T < 1300 K and 1.6 < O/Am < 2.0 ranges evidenced some inconsistencies with the existing CALPHAD model. XRD measurements in the 1200 < T < 1300 K range showed that AmO_2 can be continuously reduced ($AmO_2 \rightarrow AmO_{2-x}$) until the transition towards the BCC $AmO_{1.61+x}$ phase ($AmO_{2-x} \rightarrow AmO_{2-x} + AmO_{1.61+x} \rightarrow AmO_{1.61+x}$). This denies the existence of the miscibility gap in $AmO_{2\text{-}x}$, as reported in the phase diagram of Gotcu-Freis *et al.* Furthermore, a variation in the lattice parameter of $AmO_{1.61+x}$ was observed at constant temperature. This evidences the existence of a composition domain for this phase.

The analysis of the experimental data was helped by the thermodynamic computations based on the model of Gotcu-Freis *et al* [64]. Subsequently, thanks to the obtained information, adopting an iterative approach, the CALPHAD assessment of the Am-O system was improved. The compound energy formalism was used to describe the thermodynamic properties of the non-stoichiometric $AmO_{1.61+x}$ phase. The new Gibbs energy parameters were assessed together with the interaction parameters of $AmO_{2\text{-}x}$. The features of the phase equilibria between $AmO_{2\text{-}x}$, $AmO_{1.61+x}$ and Am_2O_3 highlighted by the HT-XRD results were well reproduced as well as the oxygen potential data of Chikalla and Eyring [57]. In comparison to the model of Gotcu-Freis *et al.*, an improvement in fitting these latter data was achieved for the lowest O/Am ratios

and temperatures, thanks to the exclusion of the miscibility gap from our description. On the contrary, the result was slightly poorer with the data near stoichiometry (O/Am=2). However, the previous and the new assessments are generally similar in the near-stoichiometric domain of AmO_{2-x}, proving the selfconsistency of the adopted iterative approach. Finally, considering the Gibbs energy functions proposed for the gaseous actinide oxide in a recent review [127], the thermodynamic parameters of the $AmO(g)$ and $AmO_2(g)$ species were re-assessed. The new optimization led to a better reproduction of the vapour pressure data reported in the literature [64].

To conclude, in this first part of the PhD work, a step towards the understanding of the Am-O system was achieved. Nevertheless, difficulties remain to explain significant scattering between the measurements on the oxygen potentials of AmO_{2-x}. Thermodynamic data are missing for the intermediate $AmO_{1.61+x}$ phase and very few data exist on the $AmO_{1.61}$-Am_2O_3 domain. More specifically, the existence of another sesquioxide with BCC structure (not included in this work) is still controversial. Therefore, further experimental work would be necessary to establish the thermodynamic description of the Am-O system.

Chapter 4

Manufacture and structural investigation of (U,Am)O$_{2\pm x}$ oxides

In order to investigate the structural and thermodynamic properties of U-Am mixed dioxides, the availability of homogeneous, well-characterized samples is mandatory. Therefore, the starting point of the work on the U-Am-O ternary system was the manufacture of (U,Am)O$_{2\pm x}$ oxides with various Am/(Am+U) ratios, ranging from 7.5 to 70 mol.%. Among the various CEA laboratories, the LFC unit (*Laboratoire de Fabrication du Combustible*)- previously named LEMA (*Laboratoire d'Etudes des Matériaux à base d'Actinides*)- developed innovative powder metallurgy processes to manufacture U-Am mixed oxide pellets. In particular, two processes were put in place for MABB fuels. The first one is the reactive sintering of UO$_{2+x}$ and AmO$_{2-x}$ powders [70, 167], in which both solid solution formation and densification ($< 92\%$ TD) are achieved during a sole thermal treatment. The second process is named UMACS (Uranium Minor Actinides Conventional Sintering) and it dissociates solid solution formation and its densification by performing two distinct thermal treatments [168] [106], with temperature and atmosphere conditions optimized for americium oxides (high oxygen potential). The UMACS process has proven to achieve better densities (up to 95.7% TD) than the reactive sintering and it has already been used to manufacture high Am content oxides, up to 70 mol.%. For this reason, it was chosen for the manufacture of this work and the application. This process and its application will be described in the first part of this chapter, in section 4.1.1. Then, the characterizations performed on the produced samples, in order to evaluate their homogeneity and composition, will be presented in section 4.1.2.

In the second part of the chapter (section 4.2), the investigation of the structure of the as-sintered (U,Am)O$_{2\pm x}$ oxides will be presented. The solid solution formation was studied by powder XRD, XAS and micro-Raman spectroscopy.

4.1 Manufacture of (U,Am)O$_{2\pm x}$ oxides

Several (U,Am)O$_{2\pm x}$ pellets with Am/(Am+U) ratio ranging from 7.5 to 70 mol.% were manufactured in the hot cells of the Atalante facility, at CEA-Marcoule, using remote manipulators.

Indeed, about 5 grams of ^{241}Am powder were handled for the ensemble of the pellets and this relatively high quantity of material required an adapted shielding. All the following characterizations were instead performed in glove boxes, manipulating smaller quantity of materials.

4.1.1   The UMACS process

The UMACS process is presented as a flow chart in Fig. 4.1. As mentioned before, the main feature of this process is the separation of the solid solution formation and the densification, in two thermal treatments.
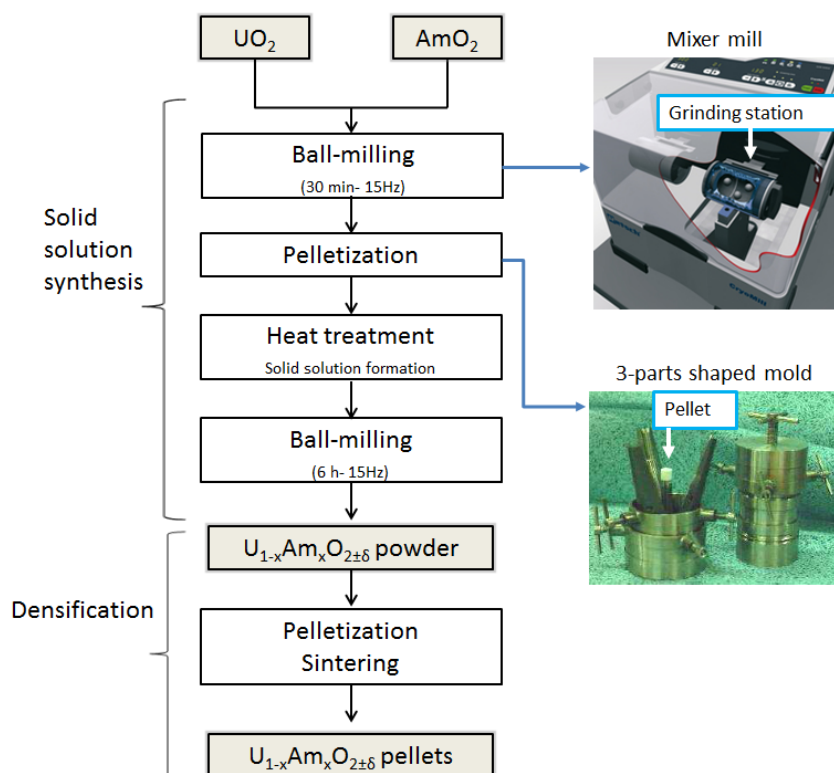
Fig. 4.1: Schematic representation of the UMACS process.

The starting materials of the UMACS process are uranium and americium dioxide powders. Two different batches were used for both the UO_2 and AmO_2 precursors (for material availability reasons). For UO_2, the first batch, named *Natural-UO₂*, was composed of natural uranium; the second one, named *UO₂-Cad*, of depleted uranium. The two AmO_2 batches were respectively named *Am-Tch* and *Am-C9*. The first one was of Czech origin and the second one came from a test of liquid-liquid extraction from spent fuel with the EXAM process [7], performed at CEA-Marcoule. Both the UO_2 batches had impurity concentrations lower than 0.002 wt.%, whereas few percent of impurities were presented in the AmO_2 precursors, mostly Ce for *Am-C9* and Pu for *Am-Tch*. Details on the chemical and isotopic compositions are provided in Appx. B.

The first step of the manufacture process was the preparation of a homogeneous UO_2-AmO_2 powder mixture with the targeted Am/(U+Am) ratio. In Tab. 4.12 (end of this chapter), it is specified which UO_2 and AmO_2 batch was used for each target composition. The powder

mixtures were prepared using a RETSCH mixer mill MM20, as the one represented in Fig. 4.1. The grinding jars of the mixer mill perform radial oscillations at 15 Hz, in a horizontal position. The inertia of two grinding balls causes them to impact with high energy on the material at the rounded ends of the grinding jars and to pulverize it. Also, the movement of the grinding jars combined with the movement of the balls result in the intensive mixing of the sample. Subsequently, to further increase the precursor contacts and thus the reactivity, the powder mixtures were pelletized. The pelletization was achieved applying a uniaxial pressure of 400 MPa for around 20 seconds into a three parts shaped mold, as those shown in Fig. 4.1.

The thermal treatments were performed in a VAS vertical furnace, whose inner part are made of tungsten. The temperature was controlled by two C-type thermocouples, placed at the extremities of the furnace. The goal of the first thermal treatment was the solid solution formation. The plateau temperature ranged from 1873 K (for Am/(Am+U)>50 mol.%) to 2023 K and the atmosphere was composed of an Ar/H$_2$(4%)-Ar/O$_2$(1000 ppm) flowing mixture. The oxygen potential $\Delta \overline{G}(O_2)_g$ was calculated using the Wheeler and Jones formula [169], which is derived from the molar free enthalpy of the reaction $2H_2O_{(g)} \longleftrightarrow O_{2(g)} + 2H_{2(g)}$:

$$\Delta \overline{G}(O_2)_g = -479070 + 4.18 \cdot T \cdot [8.96 \cdot \log_{10} T - 4.42 - 9.152 \cdot \log_{10} \frac{p_{H_2}}{p_{H_2O}}], \qquad (4.1)$$

with the temperature in K and the oxygen potential in $J \cdot mol^{-1}$. The targeted oxygen potentials were -450 kJ/mol at 2023 K and -440 kJ/mol at 1873 K. The conditions of the first thermal treatment are summarized in Tab. 4.1. The high-temperature XRD studies of Lebreton *et al.* showed that, in the selected conditions, the Am^{4+} is firstly reduced to Am^{3+} and then the (U^{4+}, U^{5+})$_{1-y}$Am$_y^{3+}$O$_{2\pm x}$ solid solution is formed.

	Heat treatment for solid solution formation	
	Am/(Am+U)≤0.5	Am/(Am+U)>0.5
Heating rate [K/min]	3	3
Plateau temperature [K]	2023	1873
Atm and gas flow	Ar/H$_2$(4%)* at 45 l/h	+Ar/O$_2$(1000 ppm) 7 l/h
Oxygen potential [kJ/mol]	-450	-440
Plateau duration [h]	8	8
Cooling rate [K/min]	5	5

Table 4.1: Specifics of the first thermal treatment. $*$ H$_2$O$_{(g)}$ impurities $\sim$ 10 ppm.

After the first thermal treatment, the pellets were ground using the mixer mill for six hours to obtain a powder, which is then re-pelletized. These new pellets were sintered using a thermal cycle with the same plateau temperatures of the first heat treatment. The atmosphere was constituted of Ar/H$_2$(4%), for compounds with Am/(Am+U)<0.5, and of an Ar/H$_2$(4%)-Ar/O$_2$(1000 ppm) mixture, for higher americium-content compounds. The specifics of the sintering are summarized in Tab. 4.2.

	Sintering	
	Am/(Am+U)<0.5	Am/(Am+U)⩾0.5
Heating rate [K/min]	5	5
Plateau temperature [K]	2023	1873
Atm and gas flow	Ar/H$_2$(4%)*,45 l/h	Ar/H$_2$(4%),45 l/h+Ar/O$_2$(1000 ppm), 7 l/h
Oxygen potential [kJ/mol]	-570	-440
Plateau duration [h]	4	4
Cooling rate [K/min]	5	5

Table 4.2: Specifics of the sintering. $*$ H$_2$O$_{(g)}$ impurities $\sim$ 10 ppm.

Lebreton *et al.* performed XRD characterizations on powdered (U,Am)O$_2$ oxides (from UMACS process) within few hours after the sintering [106]. The presence of two or three fluorite structures was highlighted for the samples with 0.3$\leq$ Am/(Am+U)$\leq$0.7. However, a rapid evolution of these phases toward a single more oxidized fluorite phase was observed. This oxidation process was completed within 50 hours for Am/(Am+U)$\leq$0.5 and in few weeks for Am/(Am+U)=0.6 and 0.7. At the end, a homogeneous stable solid solution was obtained. Despite the observed oxidation process, the final O/M ratios measured for the samples with Am/(Am+U)=0.4 and 0.5 were lower than 2, respectively equal to 1.97(2) and 1.93(2). This indicates that, despite the optimization, the atmosphere conditions of the UMACS process are still very reducing for the oxides with high americium contents.

4.1.2   Characterizations

All the sintered pellets presented rectilinear shapes and no visible defects nor cracks. Their mass, height and diameter were measured, respectively, with an analytical balance (precision 0.1 mg), a comparator (10 μm resolution) and a laser profile sensor (2 μm precision). The latter measured the diameter every 16 μm in height, which allowed to precisely check any pellet deformation. For all the samples, the diameter was about 5 mm, whereas the height ranged from 2.5 to 5 mm. Masses were between 0.4 to 0.8 g. Based on mass and dimensions, a volumetric mass density ρ was calculated, with an uncertainty of 0.5 g/cm^3. The theoretical density (TD) was calculated, from the XRD data, as the ratio between the molar mass of a U$_{1-y}$Am$_y$O$_2$ repeating unit and the elementary cell volume. This latter was computed using the lattice parameters reported in section 4.1.2.2. Finally, the relative densities (%TD) were calculated as the ratio between the volumetric density and the theoretical density. The values are reported in Tab. 4.3 for all the manufactured compositions.

Am/(Am+U) [mol.%]	7.5	10	15	20	30	40	50	60	70
Density [% TD]	97(1)	95(1)	94(1)	91(1)	92(1)	79(1)	87(1)	86(1)	83(1)

Table 4.3: Relative densities.

The obtained densities are relatively high, but they diminish as a function of the americium

content. This effect was previously observed [72] and it is probably due to two main effects. First, the americium precursor powders contained a significant amount of impurities, which can delay and impede the sintering. Second, even in the UMACS process, the sintering conditions are closer to the stability domain and sintering of UO$_2$ rather than AmO$_2$ (see section 2.4.3). Indeed, AmO$_2$ is not stable in a fluorite-type structure at high temperature, under reducing conditions. The stabilization of the fluorite structure was possible thanks to the combination with the uranium in the solid solution. It is then reasonable that the density decreased with the americium content, since the sintering conditions were less and less appropriate for the densification.

The density values here obtained are comparable to those of the previous work of Lebreton *et al.* [72, 170], except in the case of Am/(Am+U)= 40 and 70 mol.%. For the 70%, the achieved relative density was about 83%, whereas values around 89% were obtained in the previous works. The difference remain limited. For the 40 %, the relative density (79%) was very low compared to the densities previously obtained (91 %). This could indicate a departure from the nominal conditions during the sintering. However, the low density is not problematic for the objectives of this work, as long as the samples are homogeneous. This point is discussed in the following sections.

4.1.2.1 Chemical composition

The Am/(Am+U) ratio was measured for each targeted composition using Thermal Ionization Mass Spectrometry (TIMS). The measurements were performed by the L27 laboratory of the Atalante facility on about 20 mg samples. The results are reported in Tab. 4.4.

Am/(Am+U) [mol.%]									
Target	7.5	10	15	20	30	40	50	60	70
Measured	7.0(2)	10.5(8)	15(2)	19(2)	28(2)	39(3)	48(1)	57(3)	67(3)

Table 4.4: Nominal (target) and measured Am/(Am+U) ratios.

The measured Am/(Am+U) ratios are systematically slightly lower than the nominal ones for the high Am content samples (Am/(Am+U)≥0.3). This is consistent with the high volatility of americium oxide species in reducing conditions, which lead to a partial sublimation. For simplicity, the samples will be usually identified with their nominal Am/(Am+U) compositions herein, but the measured ratios were adopted for the quantitative analysis.

4.1.2.2 Crystal structure

A XRD characterization was performed on a powderized sample extracted from one pellet of each composition. For Am/(Am+U) ratios equal to 7.5, 10, 15, 30, 50 mol.%, the XRD was performed between 4-6 days after the manufacture, using the XRD diffractometer of the Atalante facility, described in Appx. A.1. During this period, the pellets were stocked under air. For the samples with Am/(Am+U) ratios equal to 40, 60 and 70 mol.%, the XRD was performed using the HT-XRD experimental set-up of the LEFCA facility (Appx. A), about three months after

the manufacture. The obtained XRD patterns are reported in Fig. 4.2. They indicate, for all the compositions, the presence of one single phase with fluorite structure (space group $Fm\overline{3}m$, N° 225). The lattice parameters, obtained by refinement of the XRD patterns with the Le Bail method [171], are reported in Tab. 4.5. The corresponding ages of the samples are also reported because, as discussed in section 2.2.4, the self-irradiation due to ^{241}Am decay causes a swelling of the lattice cell. As reported in section 2.2.4.3, Lebreton *et al.* [106] proposed equations for $U_{1-y}Am_yO_{2\pm x}$ oxides (manufactured with the UMACS process) to compute the lattice parameter as a function of the age, keeping into account the self-irradiation. The equations were used to compute the lattice parameters for ages equal to those of the analysed samples and the values are compared in Tab. 4.5 (last column). For all the cases, the values found by XRD are very similar to those expected from the self-irradiation equations of Lebreton.
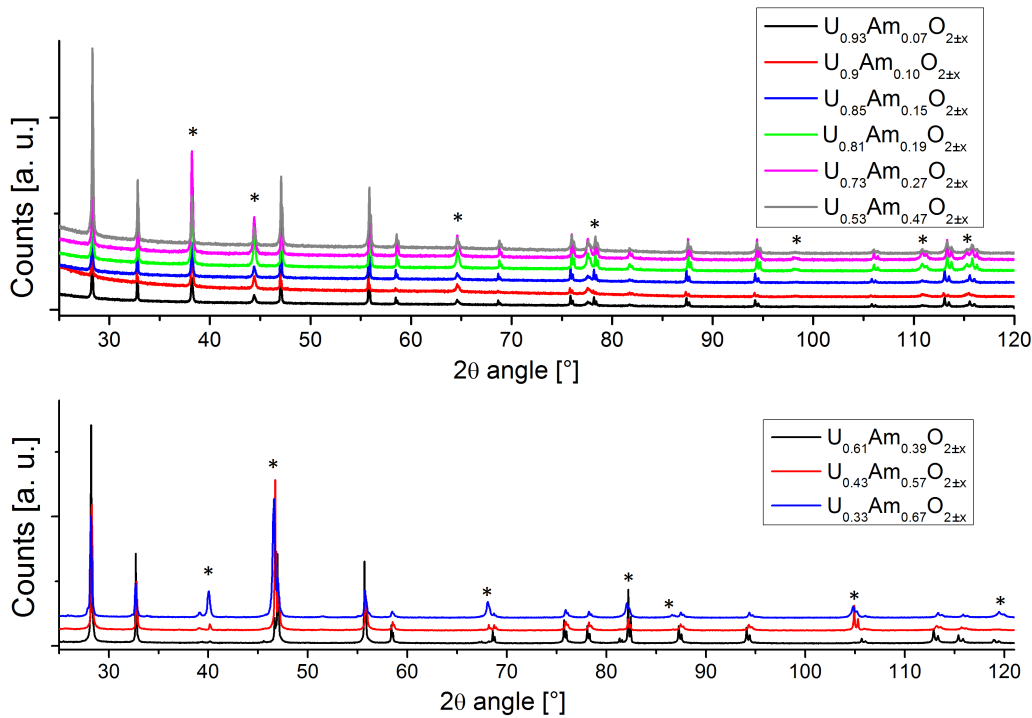
Fig. 4.2: XRD patterns on powders of $U_{1-y}Am_yO_{2\pm x}$ oxides with $0.07 \leq y \leq 0.70$. The * indicate the XRD peaks due to the gold reference (top) and the Pt-Rh sample holder (bottom).

4.1.2.3 Microstructure

Scanning electron microscopy (SEM) imaging analysis were performed on fractured surfaces taken from some of the manufactured pellets. The acquired images are shown in Fig. 4.3. For the samples with Am/(Am+U)=10 (b) and 40 mol.% (c), the SEM analysis was carried out at CEA Marcoule; for Am/(Am+U)=7.5 (a) and 50 mol.% (d), at the JRC-Karlsruhe centre. For all the compositions, the characterization was performed few months after the manufacture of the pellets. However, these were broken and the fragments were collected only few hours before the SEM analysis.

The SEM observations reveal a typical ceramic microstructure, with well-faceted grains of about 5-20 μm. Pores of size ranging from 0.1 μm to few μm are observed in the samples, both in

Nominal Am/(Am+U) [mol.%]	Age [days]	a [Å] (this work)	a [Å] (Lebreton)
7.5	6	5.467(1)	5.466
10	5	5.466(1)	-
15	5	5.462(1)	5.461
20	4	5.460(1)	-
30	5	5.455(1)	5.454
40	90	5.466(1)	5.464
50	4	5.456(1)	5.454
60	95	5.459(1)	5.459
70	100	5.450(1)	5.454

Table 4.5: Lattice parameters of U$_{1-y}$Am$_y$O$_{2\pm x}$ oxides, obtained in this work and compared to those of Lebreton, corrected for the ages.

intra-granular and inter-granular regions. The 40% sample (c) shows a higher porosity than the others and some of the grain boundaries do not seem very cohesive. This is consistent with the low density measured for these samples, previously discussed.
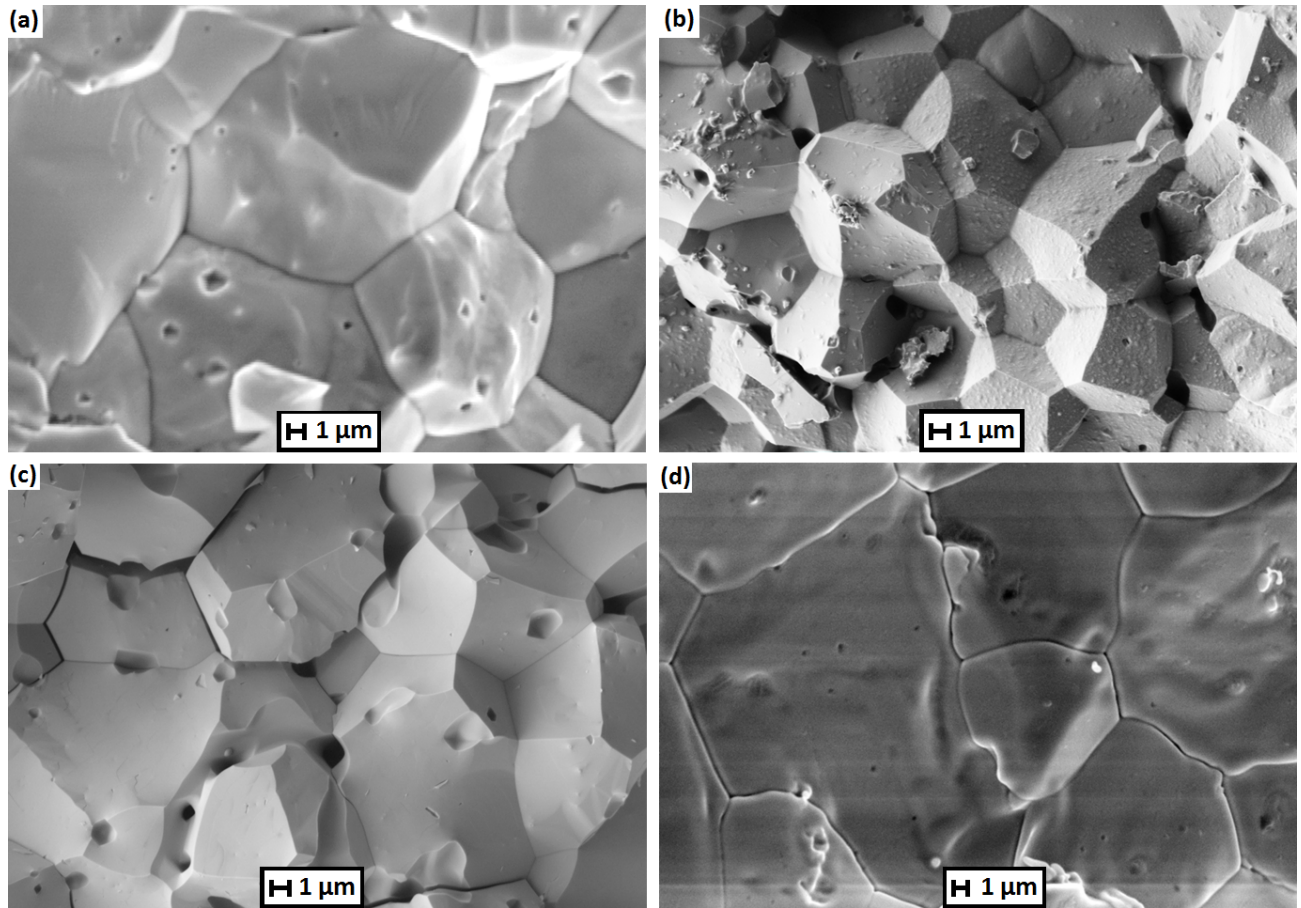
Fig. 4.3: SEM images of fractured surfaces of U$_{1-y}$Am$_y$O$_{2\pm x}$ pellets with y=0.075 (a), 0.10 (b), 0.40 (c) and 0.50 (d).

4.1.3   Conclusions

The first part of this work consisted in the manufacture of (U,Am)O$_2$ pellets, with Am/(Am+U) ratio ranging from 7.5 to 70 mol.%. The UMACS process, recently developed at CEA-Marcoule, was selected for this purpose. Thanks to the separation of the solid solution formation and the densification in two thermal treatments, this process allows obtaining homogenous (U,Am)O$_2$ materials, also for high americium contents, as demonstrated by the previous PhD work of F. Lebreton [106].

Subsequently, one pellet from each batch was characterized by several techniques, in order to ensure the success of the manufactures. The TIMS analysis confirmed that the obtained Am/(Am+U) ratios were close to the targeted compositions. The XRD confirmed the formation of a single phase solid solution with fluorite structure. Besides, the found lattice parameters were consistent with the literature data. SEM imaging revealed a microstructure typical of ceramic materials, with well-faceted grains of 5-20 μm. In summary, the characterizations confirmed the success of the manufactures. The obtained samples were then suitable for the further investigations of this work.

4.2   Insight on the structure of (U,Am)O$_{2\pm x}$ oxides

As discussed in section 2.3.3, the (U,Am)O$_{2\pm x}$ solid solution has peculiar structural properties. XAS spectroscopy measurements on (U,Am)O$_2$ samples with Am/(Am+U) ratios up to 20 mol.% highlighted an unusual behavior for actinide dioxides: the Am is purely trivalent, while the U is partially oxidized to the pentavalent state, with very close Am^{3+} and U^{5+} contents, suggesting a charge compensation mechanism [71]. This mechanism seems not sufficient to maintain the oxygen stoichiometry (O/M=2) for higher americium contents. A XAS experiment performed on an (U$_{0.5}$Am$_{0.5}$)O$_{2-x}$ sample pointed out that the dioxide was hypo-stoichiometric, with an O/M ratio equal to 1.93(2) [73]. The americium was once again purely trivalent, whereas the uranium had an average oxidation state equal to 4.65(3). EXAFS and Raman spectroscopy confirmed the preservation of an average fluorite structure also for this high-Am content oxide, but they indicated a high concentration of defects in the oxygen sublattice.

Several questions rise from the previous results. For instance, it is logic to wonder whether Am^{4+} can exist in U-Am mixed oxides and which is the maximum possible oxidation state of uranium in this solid solution. More specifically, it is questionable if U^{6+} can be accommodated in the fluorite structure. Furthermore, from the results of Lebreton *et al.* on the U$_{0.5}$Am$_{0.5}$O$_{2-x}$ oxide, questions about the oxygen existence domain and the thermodynamic stability of the stoichiometric state O/M=2 rise for high Am contents. Finally, the changes in the oxygen sublattice induced by the americium dilution need to be studied more in details. In this part, the investigation of the structural properties of (U,Am)O$_{2\pm x}$ is hence continued. The XAS study of these oxides is extended to Am/(Am+U) ratios equal to 30, 60 and 70 mol.%. Besides, samples with Am content equal to 15, 50 mol.% were also analysed in order to verify the previous results of the literature. Finally, a Raman spectroscopy investigation on all the manufactured compositions is presented.

4.2.1 Cationic charge distribution by XANES

XANES measurements were performed on the samples with nominal Am/(Am+U)= 15, 30, 50, 60 and 70 mol.%. The experiment was performed between 3-4 months after the manufacture of the pellets, at the ROBL beamline of the ESRF (Grenoble). Few mg of powdered samples were used for the measurements. Spectra were acquired both at room temperature and 15 K and no difference was highlighted for the XANES, as expected. Details on the acquisition conditions and procedures are provided in Appx. A.

4.2.1.1 Results

The XANES spectra collected at the L$_3$ edge of Am and U and their corresponding second-derivatives are shown respectively in Fig. 4.4 and Fig. 4.5. The XANES spectra of the (U,Am)O$_2$ samples are compared between them (top-left of the figures) and each composition is compared to reference compounds. For uranium, U^{4+}O$_2$, (U$^{4+}_{1/2}$, U$^{5+}_{1/2}$)$_4$O$_9$, (U$^{5+}_{2/3}$, U$^{6+}_{1/3}$)$_3$O$_8$ were used as a references. For americium, Am^{4+}O$_2$ and an oxalate (U$^{4+}_{0.9}$, Am$^{3+}_{0.1}$)$_2$(C$_2$O$_4$)$_5$· 6H$_2$O were adopted for the tetravalent and the trivalent state, respectively. The energy positions of inflection points and white lines (maxima of the spectra) for the mixed oxides and the reference compounds are summarized in Tab. 4.6.

Sample	Am L$_3$ edge [eV]		U L$_3$ edge [eV]	
	Inflection point	White line	Inflection point	White line
U$_{0.85}$Am$_{0.15}$O$_{2\pm x}$	18512.8	18517.3	17169.0	17175.4
U$_{0.7}$Am$_{0.3}$O$_{2\pm x}$	18512.7	18517.4	17171.6	17176.4
U$_{0.5}$Am$_{0.5}$O$_{2\pm x}$	18512.5	18517.4	17171.6	17177.7
U$_{0.4}$Am$_{0.6}$O$_{2\pm x}$	18512.9	18517.8	17171.5	17177.5
U$_{0.3}$Am$_{0.7}$O$_{2\pm x}$	18513.0	18518.0	17171.2	17177.9
Oxalate [Am^{3+}]	18513.0	18517.3	-	-
AmO$_2$	18514.5	18521.5	-	-
UO$_2$	-	-	17170.2	17175.4
U$_4$O$_9$	-	-	17170.9	17176.3
U$_3$O$_8$	-	-	17171.9	17179.6

Table 4.6: Energy positions of the inflection points and white lines of the XANES spectra presented in Fig. 4.4 and Fig. 4.5. Values are given with a 0.2 eV uncertainty.

For the Am L$_3$ edge, the inflection points and the white lines positions of all the (U,Am)O$_2$ samples are very close to the Am^{3+}-oxalate reference. The AmO$_2$ spectrum is shifted to higher energies, of about 1.5 and 4 eV, respectively for the inflection point and the white line. Considering the white lines, identical values (within the experimental uncertainty) are observed for the Am^{3+} reference and the (U,Am)O$_2$ oxides with Am/(Am+U)≤0.5. However, the structural differences between the oxalate and the mixed dioxides cause different post-edge shapes. For the samples with Am/(Am+U) equal to 0.6 and 0.7, a slight shift of the white line toward
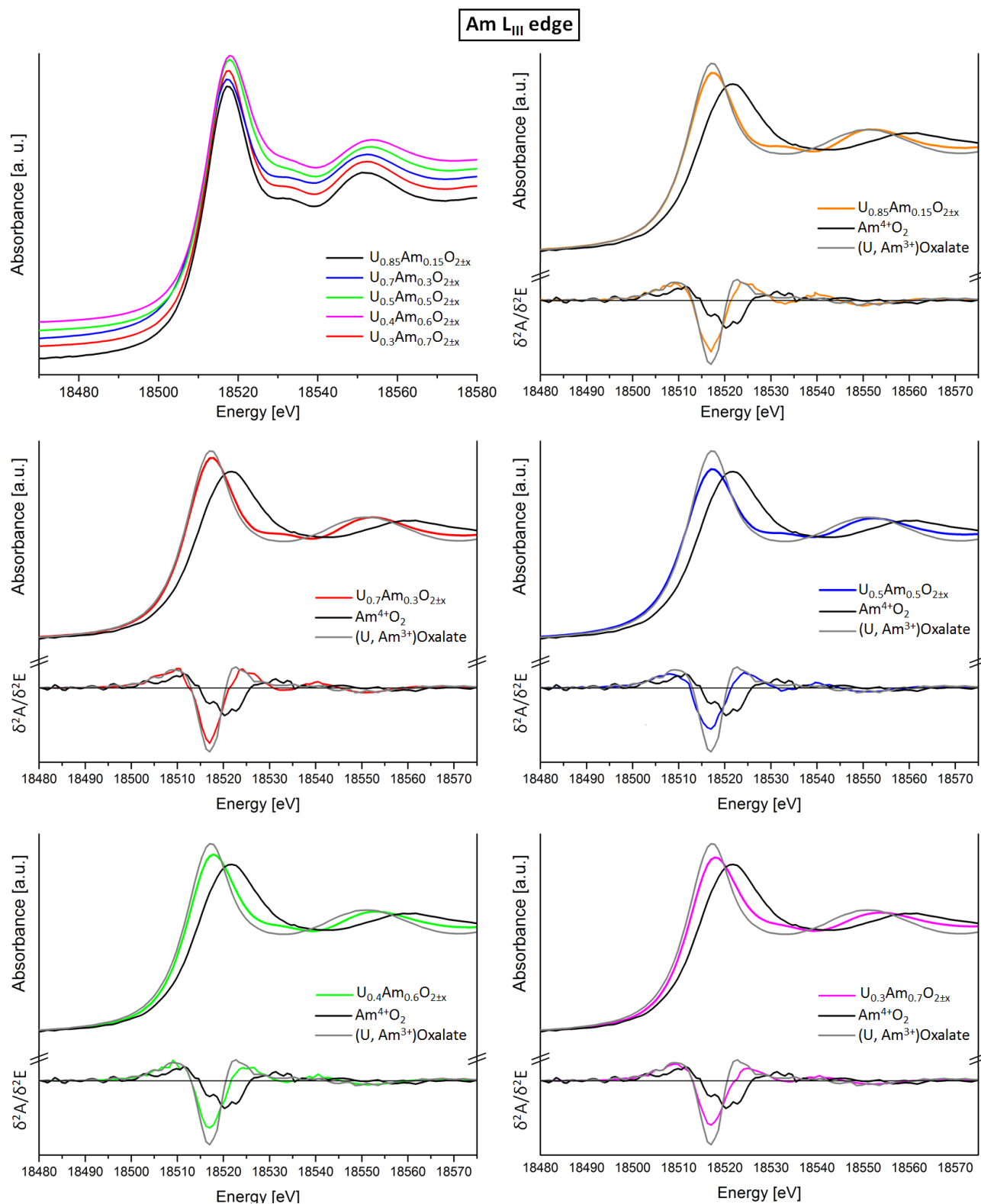
Fig. 4.4: XANES spectra collected at the L$_3$ edge of Am and their second-derivatives for the (U,Am)O$_2$ samples with Am/(Am+U) ratio equal to 15, 30, 50, 60 and 70 mol.%. The spectra of reference compounds are also shown.

high energy is observed. Besides, their white lines are more broadened than the other mixed oxides. This probably indicate an higher oxidation state of americium in these two compositions.
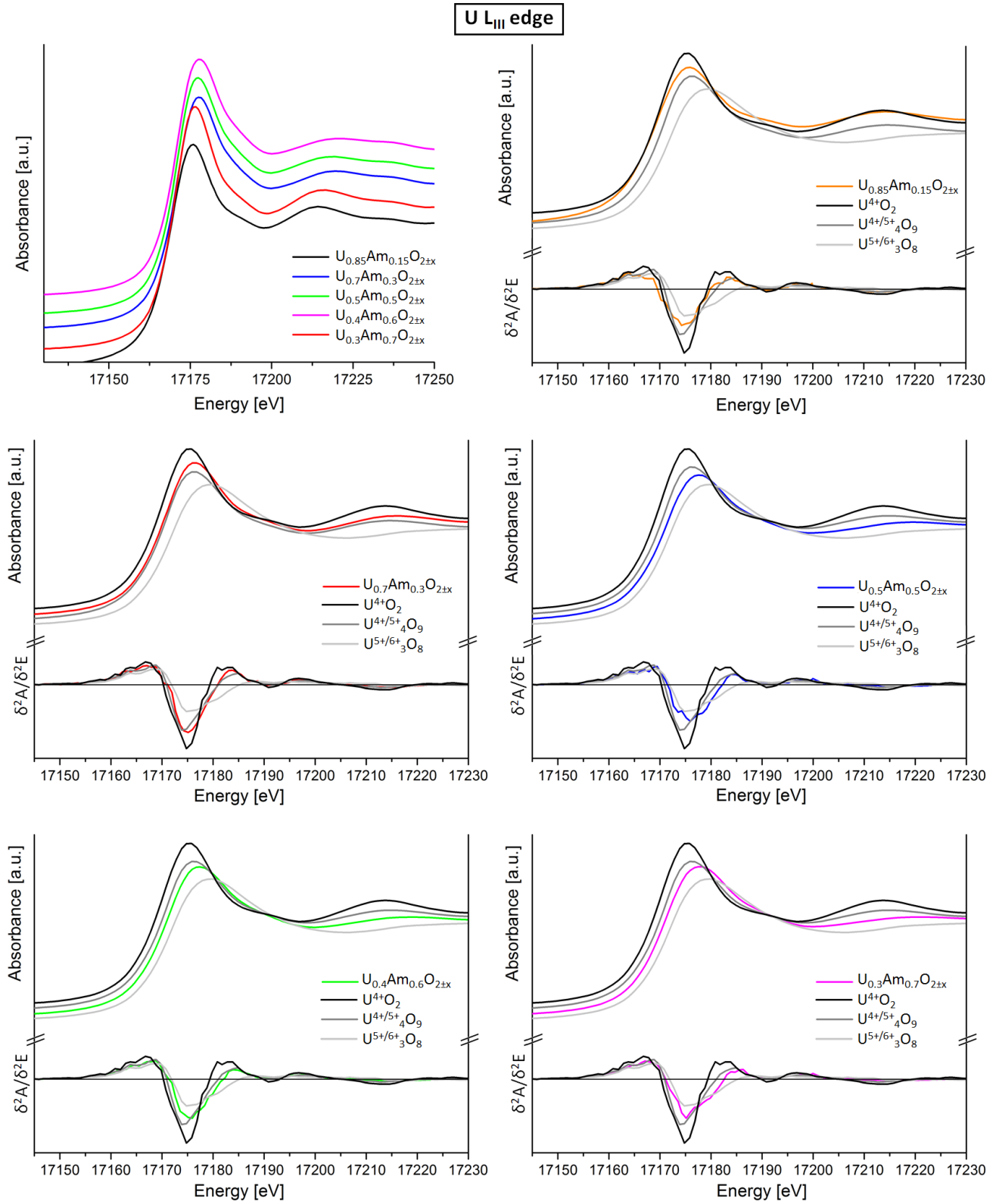
Fig. 4.5: XANES spectra collected at the L$_3$ edge of U and their second-derivatives for the (U,Am)O$_2$ samples with Am/(Am+U) ratio equal to 15, 30, 50, 60 and 70 mol.%. The spectra of reference compounds are also shown.

For the U L$_3$ edge, the inflection point and white line positions of all the (U,Am)O$_2$ samples are shifted toward higher energies than that of UO$_2$. The energy of the white line increases

with the Am/(Am+U) ratio, with the only exception of the 50 and 60 mol.% compositions. For Am/(Am+U) equal to 15 and 30 mol.%, the white line positions are comprised between those of UO_2 and U_4O_9. For higher Am contents, the white line positions are comprised between those of U_4O_9 and U_3O_8. Finally, the white lines are more and more broadened by increasing the Am/(Am+U) ratio. These characteristics indicated an increasing oxidation of the uranium. A quantitative determination is performed in the following section.

4.2.1.2 Determination of the oxidation states

The XANES spectra collected at the L_3 edges of uranium and americium of the $(U,Am)O_2$ oxides were fitted by linear combination, using the spectra of the reference compounds. The obtained fits are compared to the experimental data in Fig. 4.6 (for $U_{0.85}Am_{0.15}O_{2\pm x}$ and $U_{0.3}Am_{0.7}O_{2\pm x}$) and Fig. 4.7 (for $U_{0.5}Am_{0.5}O_{2\pm x}$, $U_{0.4}Am_{0.6}O_{2\pm x}$, $U_{0.3}Am_{0.7}O_{2\pm x}$). The quantitative results of the fits are provided in Tab. 4.7: the fraction of reference compounds in the linear combination, the R-factor of the fit, the average oxidation state of the probed atom, the O/M ratios computed from the oxidation states of Am and U. From the R-factors and the graphs of Fig. 4.6 and Fig. 4.7, it can be seen that a very good agreement between the experimental data and the fit was generally achieved. The only exception is the U L_3 edge of the $U_{0.85}Am_{0.15}O_{2\pm x}$ sample, for which the fit is quite poor. This is due to a anomalous low intensity of this XANES spectrum. A high decrease of the absorbance intensity would usually indicate an increase in the oxidation. However, a high oxidation state can be excluded since the white line position is very close to that of UO_2. It is more likely that the low intensity is due to technical problems or samples preparation, as a not suitable regulation of the ionization chambers used for the acquisition.

Am/M	Am L_3 edge				U L_3 edge					
[mol.%]	Am^{3+}	AmO_2	R-factor	AOS	UO_2	U_4O_9	U_3O_8	R-factor	AOS	O/M
15	1	0	0.002	3	0.57	0.43	0	0.014	4.22	2.02(2)
28	1	0	0.003	3	0.1	0.9	0	0.001	4.45	2.01(1)
48	1	0	0.001	3	0	0.62	0.38	0.001	4.82	1.97(2)
57	0.87	0.13	0.003	3.13	0	0.63	0.37	0.001	4.81	1.93(2)
67	0.74	0.26	0.002	3.26	0	0.54	0.46	0.001	4.89	1.90(2)

Table 4.7: Results of the linear combination fit of the U-L_3 and Am-L_3 XANES spectra using the spectra of the reference compounds: fraction of the combinations, R-factor of the fit, average oxidation state (AOS) and O/M ratio computed from the oxidation states.

For the Am L_3 edge, the linear combination fit confirmed the presence of americium exclusively in the trivalent state for the samples with (nominal) Am/(Am+U) ratio up to 50 mol.%. On the contrary, for the 60 and 70 mol.% compositions, a partial oxidation to the tetravalent state was highlighted, in agreement with the slight shifts of the white lines previously discussed. According to the fit, for the $U_{0.4}Am_{0.6}O_2$ sample (measured Am/M =0.57 as discussed in section 4.1.2.1), the molar fractions of Am^{3+} and Am^{4+} are respectively 50% and 7%. For the $U_{0.3}Am_{0.7}O_2$ sample (measured Am/M=0.67), they are 49% and 18%. From these results, it
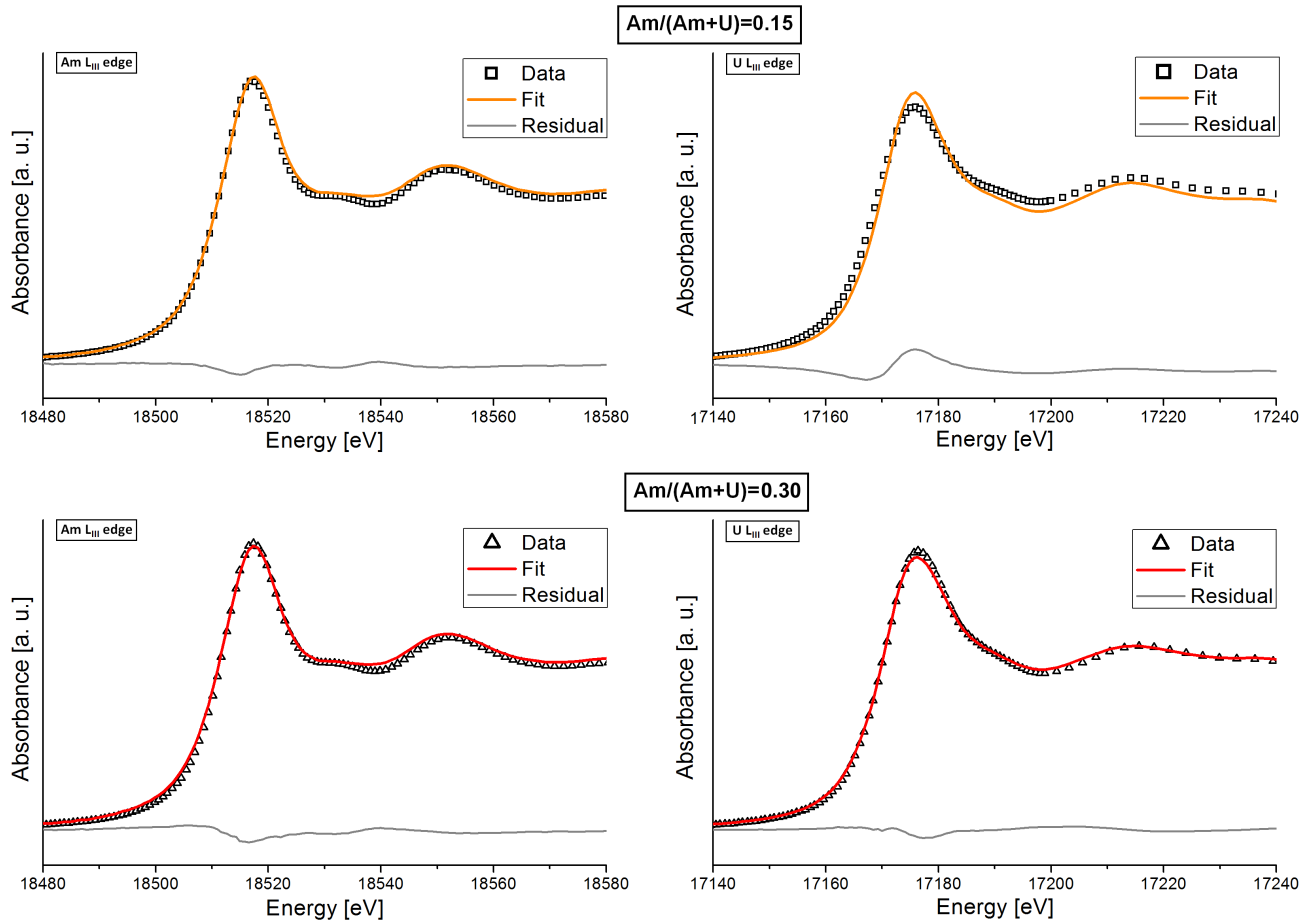
Fig. 4.6: Experimental XANES spectra and linear combination fits at the L$_3$ edge of Am (left) and U (right) for the (U,Am)O$_2$ samples with Am/(Am+U) ratio equal to 15 and 30 mol.%.

seems that the maximum possible fraction of trivalent americium in (U,Am)O$_{2\pm x}$ oxides must be around 50 mol.%.

For the U L$_3$ edge, the linear combination fit confirmed the continuous increase of the average oxidation state of U with the americium content in the solid solution.

For Am/(Am+U)=15 and 30 mol.%, the best fit was obtained using the UO$_2$ and U$_4$O$_9$ references. Since it has been proved that the latter is a mixture of 50% U^{4+} and 50% U^{5+} (see section 2.3), it can be concluded that there is a U^{4+}/U^{5+} mixed valence. For Am/(Am+U)=15 and 30 mol.%, the obtained molar fraction of U^{5+} are 18 and 32 mol.%, respectively. The values are very close to the Am molar fractions in the samples.

For Am/(Am+U)>0.3, it was previously observed that the U L$_3$ white lines were lying between those of U$_4$O$_9$ and U$_3$O$_8$. Indeed, the best fits were obtained using these two references, obtaining oxidation states ranging from 4.81 to 4.89. It must be noticed that, for these samples, the molar fractions of the U cations cannot be directly deduced from the linear combinations because references with mixed U^{4+}/U^{5+} and U^{5+}/U^{6+} oxidation states were adopted. The U$_3$O$_8$ reference was necessary for the fit because it was the only available oxide with an U oxidation state higher than 4.5. However, since the obtained oxidation states for the mixed oxides are strictly lower than 5, one cannot trivially conclude on the presence of U^{6+}, which will be dis-
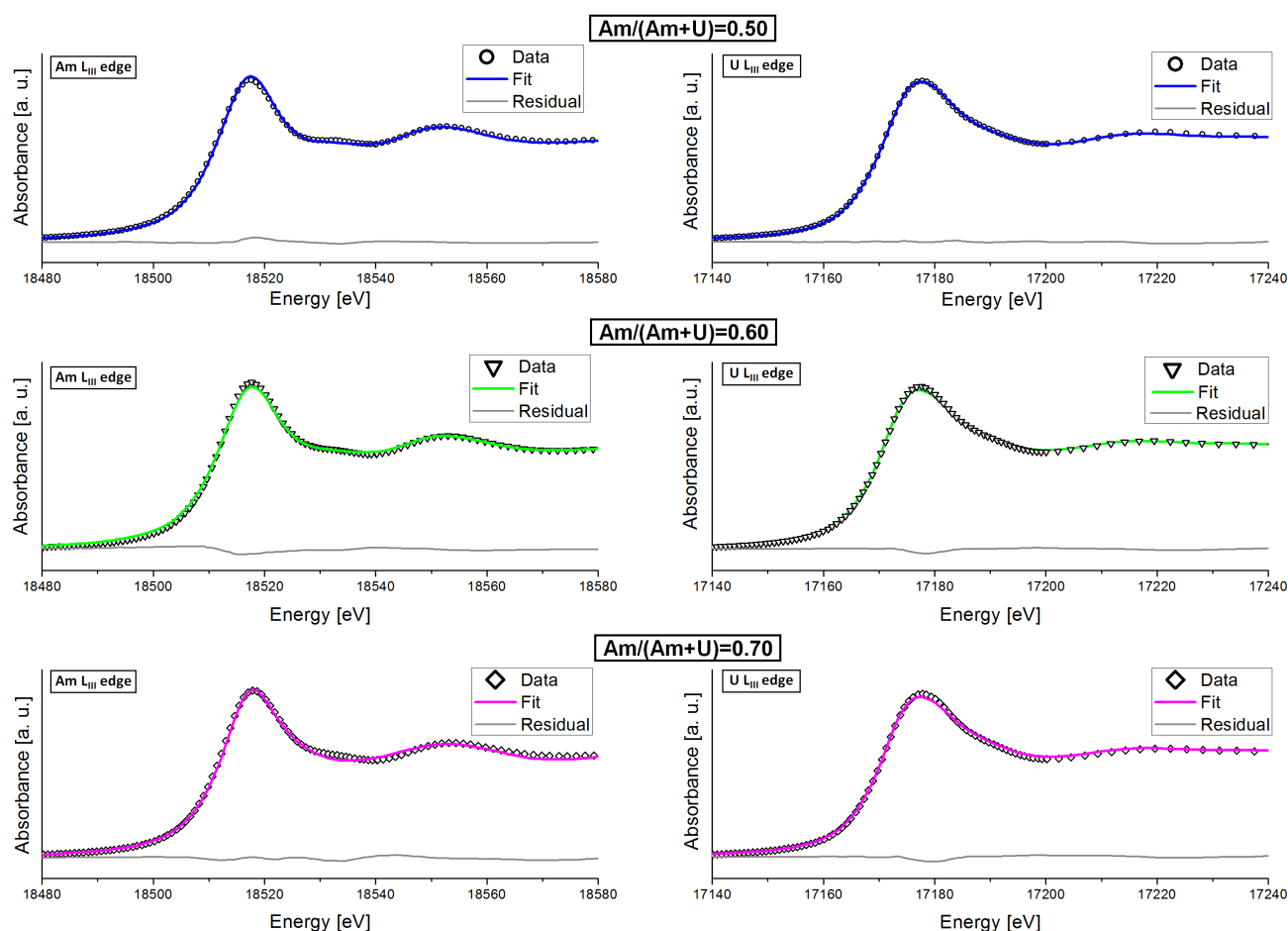
Fig. 4.7: Experimental XANES spectra and linear combination fits at the L_3 edge of Am (left) and U (right) for the $(U,Am)O_2$ samples with Am/(Am+U) ratio equal to 50, 60 and 70 mol.%.

cussed later, in comparison with the EXAFS and Raman results. Finally, it can also be observed that the adoption of U_3O_8 as reference is not ideal, since the symmetry around uranium in this compound (see section 2.2.1.2) is not cubic, contrary to the fluorite structure identified for the mixed $(U,Am)O_2$ samples. For this reason, even if the R-factor were low, a higher uncertainty was estimated for the computed O/M ratios.

4.2.1.3   Discussion

The O/M ratios, shown in Tab. 4.7, were computed (from the electroneutrality) using the average oxidation states of U and Am (the Am/(U+Am) ratios measured by TIMS (see section 4.1.2.1) were adopted for the calculations). The results of this work are compared to the data of the literature in Fig. 4.8.

The resulting O/M ratios decrease by increasing the Am content in the solid solution. The oxides with Am/(Am+U)=15 and 30 mol.% were close to the stoichiometry (O/M=2.02 and 2.01, respectively), with the molar fraction of U^{5+} very close to the molar content of americium (purely trivalent). This confirms the charge compensation mechanism previously observed for $(U,Am)O_2$ oxides with Am/(Am+U)=0.10, 0.15 and 0.20 [69, 71]. This mechanism can be then
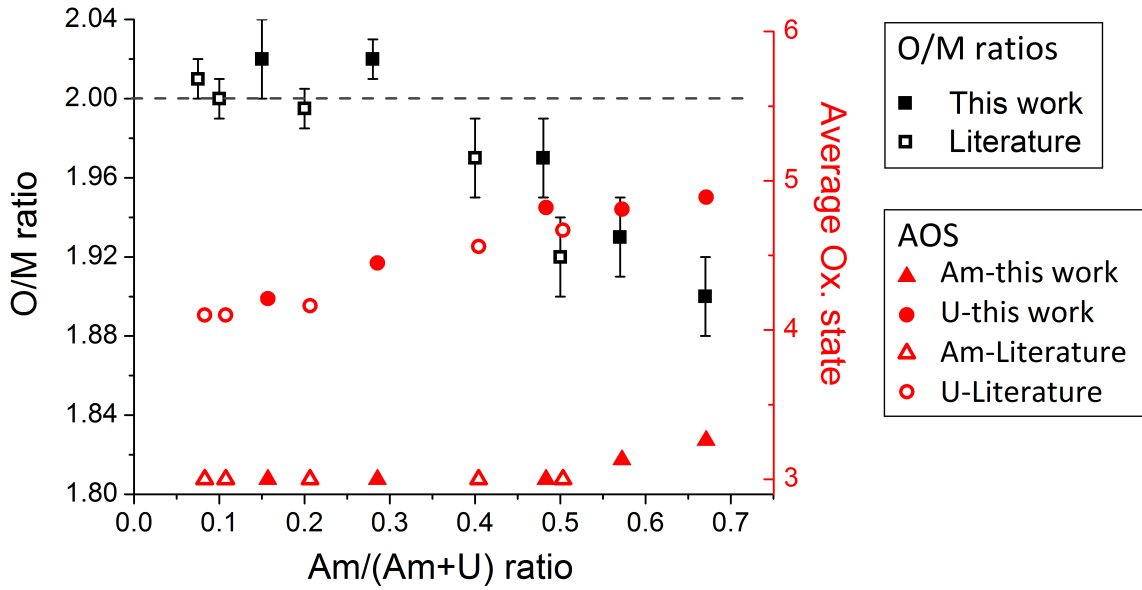
Fig. 4.8: O/M ratios (left axis) and average oxidation states (right axis) of U and Am in (U,Am)O$_2$ oxides, from this work and the literature [106, 117].

extended up to Am content equal to 30 mol.%.

The oxidation of uranium is not sufficient to completely compensate the Am^{3+} content in Am-U equimolar oxides: the U$_{0.53}$Am$_{0.47}$O$_{2-x}$ sample was hypostoichiometric. However, the O/M ratio of 1.97(2) is higher than the O/M=1.93(2) value previously observed by Lebreton *et al.* in a sample with Am/(Am+U)=0.49 (manufactured using the UMACS process) [73, 106]. This difference could be due to slight different atmosphere conditions during the manufactures. Indeed, in both this work and that of Lebreton, the oxygen potential was regulated by mixing gases at the entrance of the furnace, but the oxygen content inside it could not be precisely monitored. Another possible explanation for the different O/M ratios could be an oxidation subsequent to the manufacture. It was previously pointed out in section 4.1.1 that a rapid oxidation occurs within the 50 hours following the sintering for oxides with Am/(Am+U)=0.5. It is possible that the oxidation is not really completed within 50 hours, but only slowed down. Nevertheless, the stability of low O/M ratios was confirmed also by the observations on the U$_{0.4}$Am$_{0.6}$O$_{2-x}$ and U$_{0.3}$Am$_{0.7}$O$_{2-x}$ oxides. Indeed, the observed O/M ratio keeps decreasing with the Am content, passing from 1.97(2) for Am/(Am+U)=0.47 to 1.93(2) and 1.90(2), for Am/(Am+U)=0.57 and 0.67, respectively. The decrease occurs despite the further oxidation of uranium and the appearance, for the first time, of Am^{4+} in the solid solution. Moreover, the Am^{3+} was very close for the three oxides with Am/(Am+U)≥0.5. This suggests that the maximum content of trivalent americium that can be accommodated in the (U,Am)O$_2$ solid solution is around 50 mol.%. Above this value, the americium is partially oxidized to the 4+ state.

4.2.2   Local structure by EXAFS

The results of the previous section showed the coexistence of various cations in (U,Am)O$_{2\pm x}$ dioxides. The americium is very stable in the trivalent state and Am^{4+} appears only for

Am/(Am+U)>0.5. Uranium has a mixed 4+/5+ oxidation state, which increases with the Am content in the solid solution. This charge distribution is unusual in mixed actinide dioxides. For example, in $(U,Pu)O_{2\pm x}$ dioxides, tetravalent cations coexist with Pu^{3+} for O/M<2 and with U^{5+} for O/M>2, but the simultaneous presence of trivalent, tetravalent and pentavalent cations has never been reported [27]. Despite these dissimilarities, the XRD analysis presented in 4.1.2.2 did not highlight deviations from the fluorite structure for $(U,Am)O_{2\pm x}$ dioxides. However, because of the high difference in the electronic density between the actinides and the oxygen, the XRD is almost only sensitive to the cationic sublattice. The EXAFS provides precious complementary information. Indeed, by separately probing the local environment around uranium and americium, EXAFS allows obtaining data on the anionic sublattice and how this is affected by the different oxidation states.

4.2.2.1   Results

Am L_{III} and U L_{II} EXAFS spectra were acquired at 15 K, according to the conditions and procedures described in Appx. A. For uranium, the L_{II} (20948 eV) edge was selected, instead of the L_{III} (17166 eV), because of the presence of neptunium (L_{III} edge at 17610 eV) from ^{241}Am decay. The obtained EXAFS spectra and their Fourier transforms are reported in Fig. 4.9 and Fig. 4.10, for Am and U, respectively.
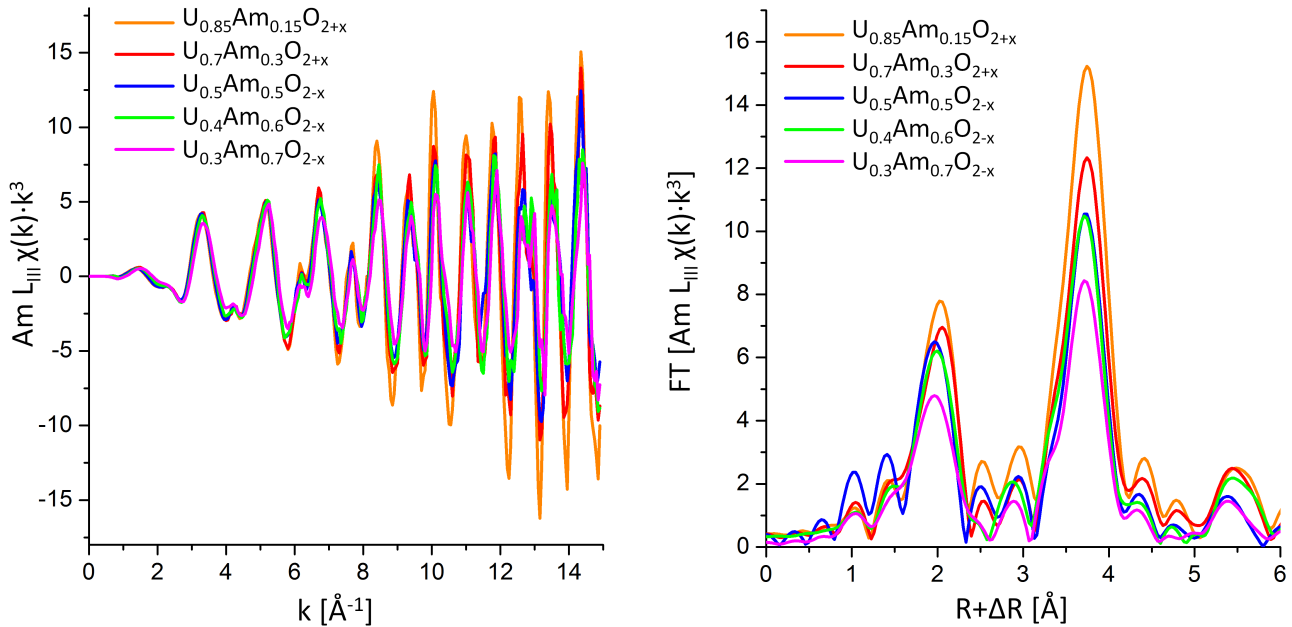
Fig. 4.9: Experimental EXAFS spectra at the L_{III} edge of Am (left) and their Fourier transforms (right) for the $(U,Am)O_2$ samples with Am/(Am+U) ratio equal to 15, 30, 50, 60 and 70 mol.%. FT boundaries: 3.5-13.5 Å^{-1}, $dk = 2$Å^{-1}.

The Am L_{III} EXAFS spectra shown in Fig. 4.9 are similar for all the compositions. The only remarkable difference is a loss of intensity with the increasing of the americium content, indicating an increasing disorder. The Fourier transforms of the spectra present two main peaks, the
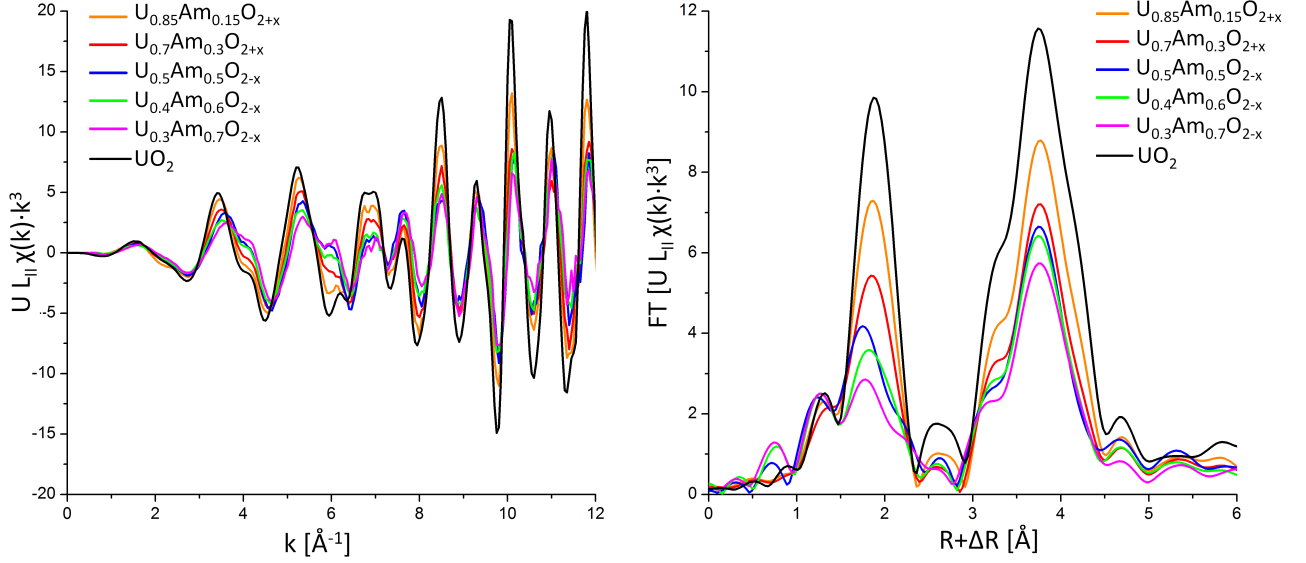
Fig. 4.10: Experimental EXAFS spectra at the L$_{II}$ edge of U (left) and their Fourier transforms (right) for the (U,Am)O$_2$ samples with Am/(Am+U) ratio equal to 15, 30, 50, 60 and 70 mol.% and an UO$_2$ reference. FT boundaries: 3.0-11.2 Å^{-1}, $dk = 2$Å^{-1}.

first at about 1.9 Å and the second at about 3.8 Å. These features are characteristic of the fluorite structure: the first peak corresponds to the first oxygen shell and the second one is mainly due to the first cationic shell. Besides the loss of intensity with the Am/(Am+U) ratio increase, the main differences in the Fourier transforms are observable for the peak at about 1.9 Å. For the samples with high americium content, and especially for Am/(Am+U)=0.7, the peaks are slightly broadened and shifted toward lower R. This is consistent with the appearance of the Am^{4+} cation, with a smaller ionic radius than Am^{3+} (r(Am^{3+})= 1.09 Å, r(Am^{4+})= 0.95 Å [109]).

The U L$_{II}$ EXAFS spectra and their Fourier transforms shown in Fig. 4.10 present remarkable differences between the various compositions. The U L$_{II}$ EXAFS spectrum of UO$_2$ is reported as a reference. The Fourier transforms of the spectra collected on the oxides with Am/(Am+U)=0.15 and 0.30 are very similar to that of UO$_2$. The only evident difference is the loss of intensity with the increasing Am content. This indicates that the addition of americium leads to structural disorder. For the oxides with Am/(Am+U)=0.5, 0.6 and 0.7, in addition to the loss of intensity, the EXAFS spectra present different features from the UO$_2$ spectrum in the k region between 3-8 Å^{-1}. A zoom on this part of the spectra and the respective Fourier transforms is reported in Fig. 4.11 for these oxides, with a comparison to the UO$_2$, U$_4$O$_9$ and U$_3$O$_8$ references. To highlight the influence of the first oxygen shell, a k^1 weight was applied. The Fourier transforms of Fig. 4.11 show that, for the mixed oxides, the peak at about 1.9 Å (first oxygen shell) has a very low intensity and it is very broadened compared to UO$_2$. Indeed, these spectra are very similar to the U$_4$O$_9$ reference. These features are due to a sum of different U-O bonds and hence they probably indicate the presence of oxygen defects (interstitials and/or vacancies). Therefore, the anionic sublattice seems remarkably affected by the addition of americium, even if the cations maintain the fluorite structure. The refinement of the EXAFS data, presented in the

next section, will allow obtaining quantitative data and hence drawing more precise conclusions on the local structure.
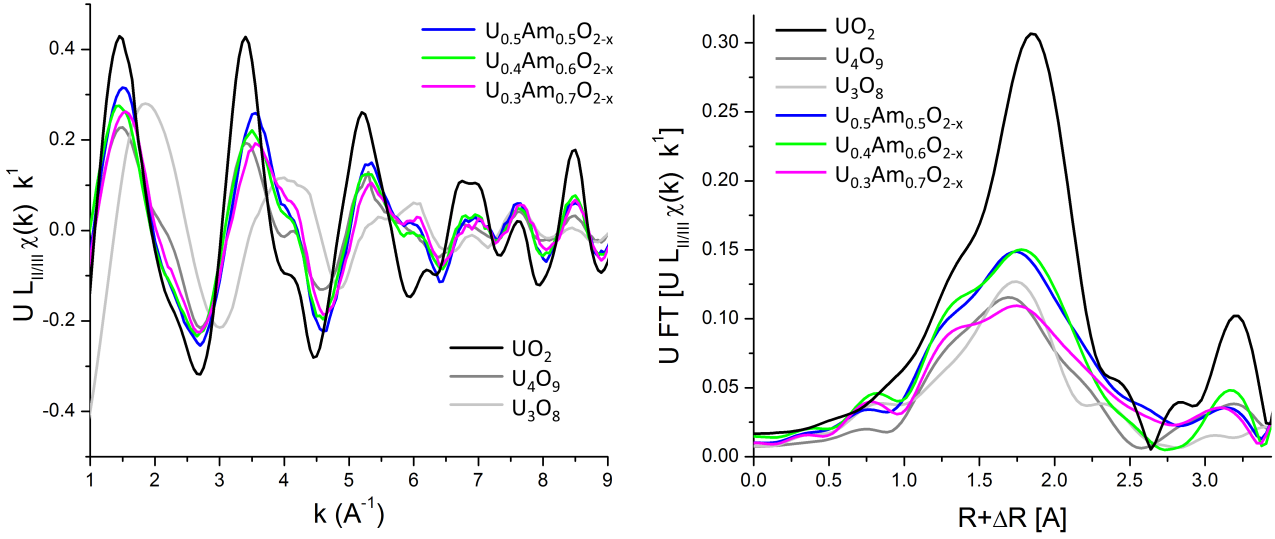
Fig. 4.11: k^1-weighted EXAFS spectra at the U L$_{II}$ edge and their Fourier transforms for the (U,Am)O$_2$ samples with Am/(Am+U)=0.5, 0.6 and 0.7. The U L$_{II}$ spectrum of UO$_2$ and the U L$_{III}$ spectra of U$_4$O$_9$ and U$_3$O$_8$ are also reported. FT boundaries: 3.5-11.5 Å^{-1}, $dk = 2$Å^{-1}.

4.2.2.2   Refinement of the EXAFS data and discussion

The EXAFS data were refined to a theoretical structural model, according to the procedure described in Appx. A. In a perfect fluorite structure, the U/Am is surrounded by 8 oxygen atoms. The second neighbour shell is constituted of 12 cations; 24 oxygen and 6 cations follow. For the starting model, the lattice parameters of the samples, corrected for the self-irradiation at the time of the XAS measurements, were used as input. These are reported in Tab. 4.8, together with the corresponding first metal-oxygen and metal-metal distances. The fits were then per-

Am/(Am+U)	a$_t$ (Å)	M-O distance (Å)	M-M distance (Å)
15	5.474	2.370	3.871
30	5.468	2.368	3.866
50	5.466	2.367	3.865
60	5.459	2.364	3.860
70	5.450	2.360	3.854

Table 4.8: XRD lattice parameters and corresponding interatomic distances.

formed by optimizing the interatomic distances R, the number of atoms N in the neighbour shells and the Debye-Waller factors σ^2. The resulting parameters and the R-factors of the fits are reported in Tab. 4.10. The obtained interatomic distances and the Debye-Waller factors, corresponding to the fluorite neighbours shells, are compared in Fig. 4.13 and Fig. 4.14, respectively.

For the Am L_{III}, all the spectra could be refined using the model based on a fluorite structure, obtaining a good agreement, as shown by the generally very low R-factors. The comparison between data and fits is given in Fig. 4.12. The only exception is constituted by the oxide with Am/(Am+U)=0.6, with an error factor of 0.021. However, the two main peaks of the Fourier transform are well reproduced by the fit. The high value of the R-factor is likely due the signal/noise ratio, which was higher for this sample than for the others.
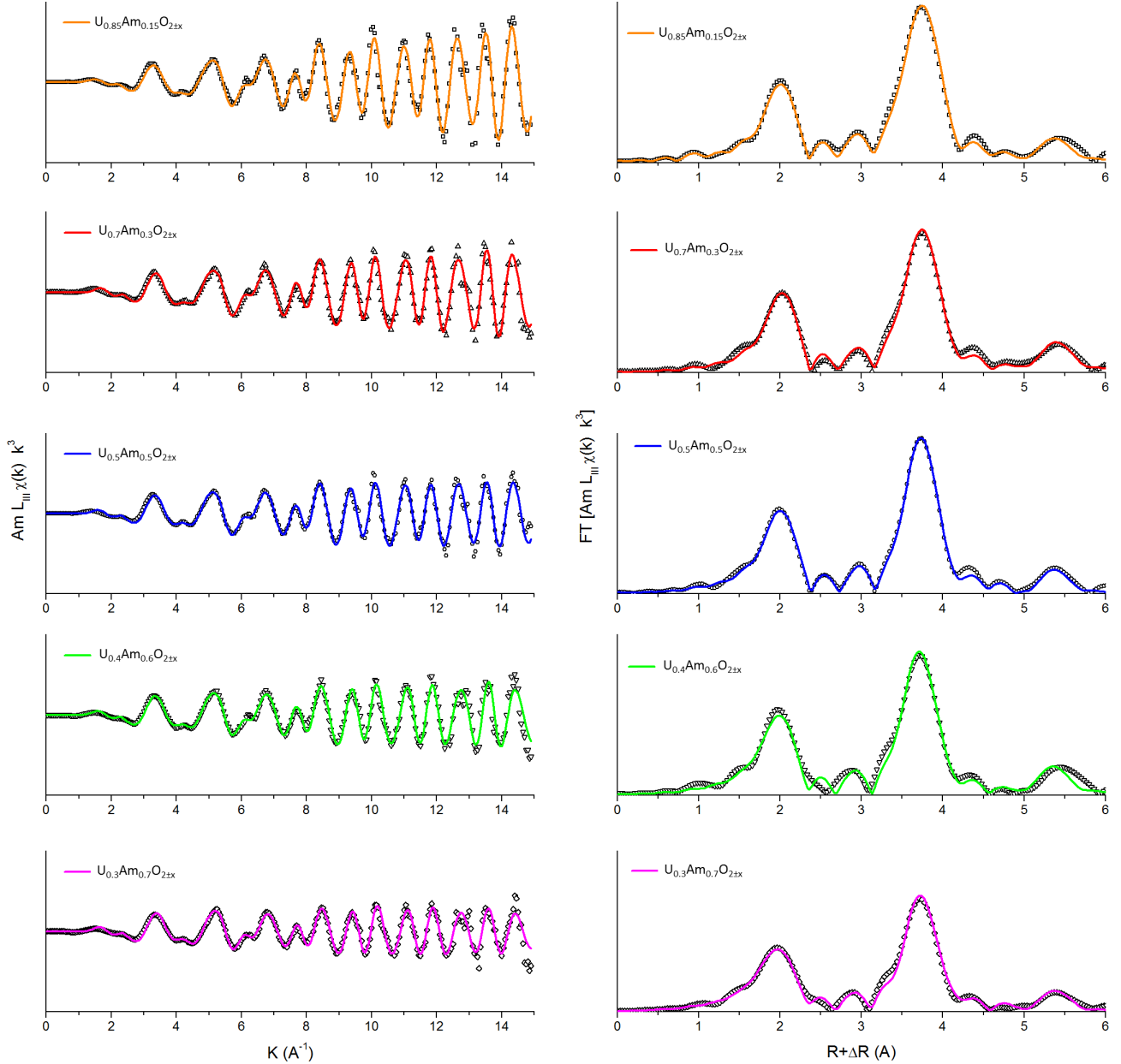
Fig. 4.12: Refinement of the Am L_{III} EXAFS spectra and their Fourier transforms (FT boundaries 3.5-13.5 Å^{-1}, $dk = 2$Å^{-1}).

For the first Am-O shell, the distances obtained by EXAFS are considerably larger than those expected from XRD and they generally agree with the other EXAFS data reported in the literature [69,71,73]. This elongation is consistent with the preferred trivalent state of americium, since the ionic radius of Am^{3+} is larger than the other identified cations: r(Am^{3+})= 1.09 Å, r(Am^{4+})= 0.95 Å, r(U^{4+})= 1.00 Å, r(U^{5+})= 0.89 Å [109]. Moreover, the Am-O distance is

constant to about 2.430(5) Å for the samples with Am/(Am+U)=0.15, 0.30 and 0.5, whereas a decrease is observed for Am/(Am+U)=0.6 and 0.7 (2.417(5) and 2.404(5) Å, respectively). This is consistent with the XANES results, that showed only Am^{3+} for Am/(Am+U)≤0.5, whereas Am^{4+} appeared in the two other compositions.

For the first Am-U/Am shell, the distances obtained by EXAFS are slightly lower than those expected by XRD, but within the uncertainty limits. However, the decrease of this distance with the Am content is consistent with the XRD evolution.

The Debye-Waller factors obtained by the EXAFS data are generally low because the data were recorded at low temperature. The thermal contribution can be neglected and the Debye-Waller factors can be attributed only to the structural disorder. The obtained values are always larger for the oxygen shells than for the cations, as expected from the higher mobility of oxygen compared to that of uranium/americium. A general increase of the structural disorder is observed by increasing the americium content.

Finally, the refinement of the coordination numbers around the americium did not highlight significant deviations from the defect-free fluorite structure for the samples with Am/(Am+U)=0.15, 0.30 and 0.5. For Am/(Am+U)=0.6, considering the high signal/noise ratio of the data already mentioned, the coordination numbers were not refined. For Am/(Am+U)=0.7, the refined coordination numbers for the two oxygen shells are lower than the theoretical ones, probably indicating the presence of oxygen vacancies around americium.
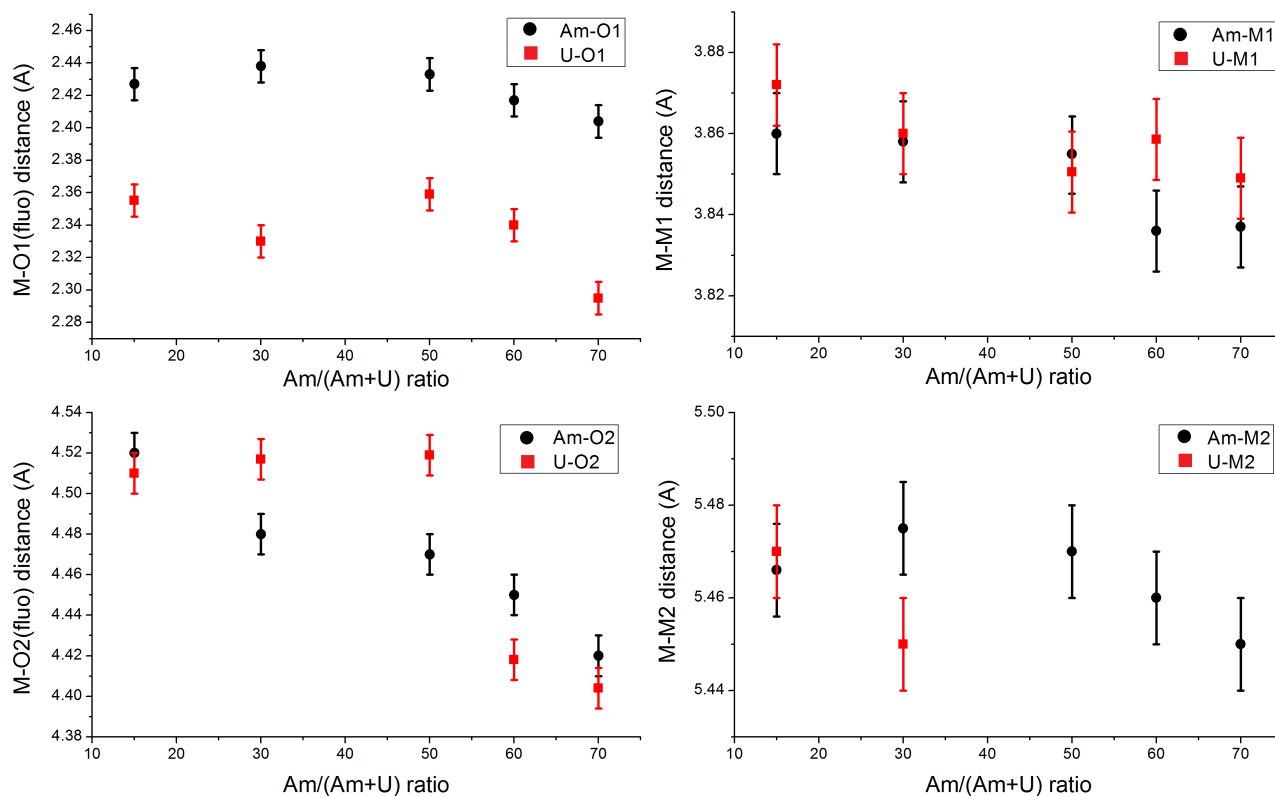
Fig. 4.13: Refined distances from EXAFS of the neighbour atoms in fluorite-type positions around Am and U.
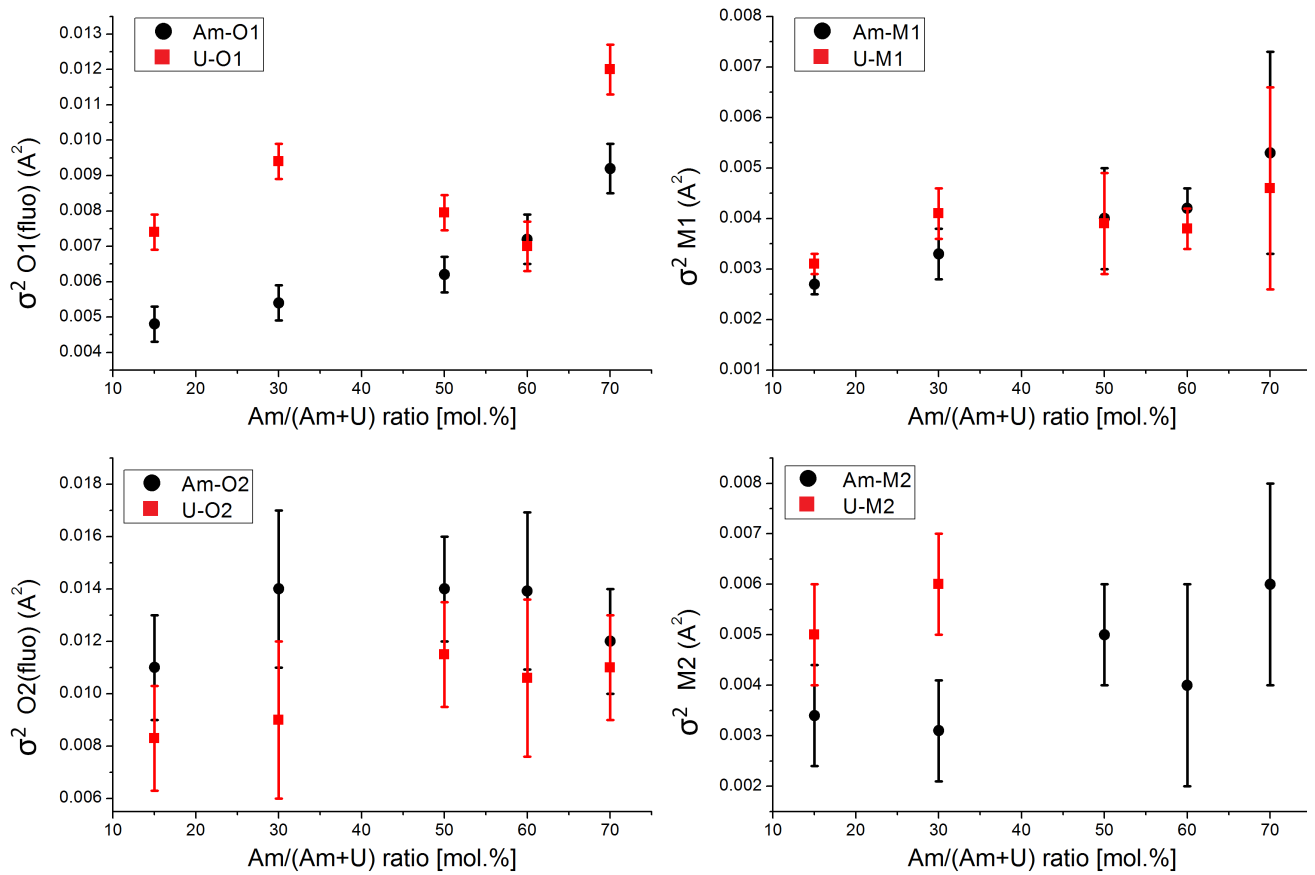
Fig. 4.14: Debye-Waller factors obtained for the fluorite-type shells around Am and U.

For the U L$_{\mathrm{II}}$ edge, prior to the mixed oxides, the EXAFS spectrum of the UO$_2$ reference was refined, in order to determine the S_0^2 factor of the EXAFS equation (see Appx. A), which was not found in the literature for this edge. First, the data were refined keeping S_0^2=1. The resulting fit, shown in Fig. 4.15, had a very low R-factor and the provided interatomic distances, coordination numbers and Debye-Waller factors were very close to those available in the literature and presented in Tab. 2.8 (chapter 2). Subsequently, all the parameters were fixed and the S_0^2 factor was refined separately in k^1, k^2 and k^3. Values between 0.995 and 1 were obtained. Hence, the S_0^2 factor was fixed to 1 for the refinement of the U L$_{\mathrm{II}}$ EXAFS spectra.

The U$_{\mathrm{II}}$ EXAFS data of the oxides with Am/(Am+U)=0.15 and 0.3 could be refined using a defect-free fluorite model. The agreement between the experimental points and the fits were very good in both cases, as shown in Fig. 4.15 and confirmed by the low R-factor (Tab. 4.10). The resulting U-O distances are shorter than those expected by the XRD and those obtained for the UO$_2$. Moreover, a decrease of the first U-O distance of 0.025 Å is observed from U$_{0.85}$Am$_{0.15}$O$_2$ (2.355(5) Å) to U$_{0.7}$Am$_{0.3}$O$_{2+x}$ (2.330(5) Å). This is consistent with the increase of the U^{5+} molar fraction highlighted by XANES, since this has a ionic radius smaller than U^{4+}. In the same way, also a slight decrease of the cation-cation distances is observed between these two samples.
As previously observed for the Am L$_{\mathrm{III}}$, the Debye-Waller factors are generally low because of the low temperature of the measurements, with higher values for the U-O shells than for the U-U/Am, as expected. For all the shells, a regular increase of the Debye-Waller factors with the
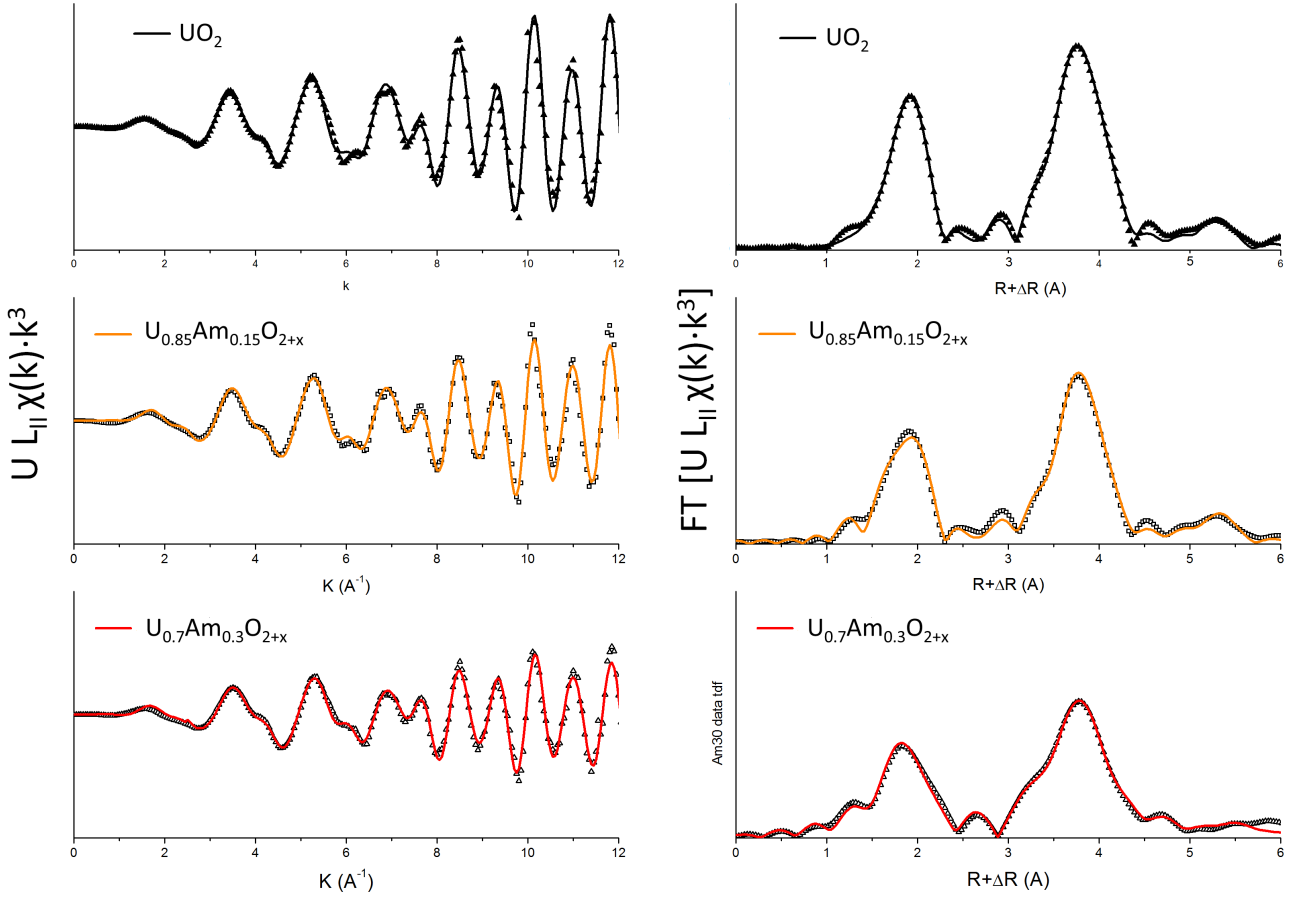
Fig. 4.15: Refinement of the U L$_{\text{II}}$ EXAFS spectra and their Fourier transforms for UO$_2$, U$_{0.85}$Am$_{0.15}$O$_{2+x}$, U$_{0.7}$Am$_{0.3}$O$_{2+x}$ (FT boundaries 3.5-11.5 Å^{-1}, $dk = 2$Å^{-1}).

americium content is observed moving from UO$_2$ to U$_{0.7}$Am$_{0.3}$O$_2$. This proves again that the dilution of americium, hence the mixing of cations with at least three different oxidation states (Am^{3+}, U^{4+}, U^{5+}), causes a general increase of the disorder in the strucutre.

Finally, the refinement did not highlight a departure of the coordination numbers from the crystallographic values.

As mentioned in the previous section, the U L$_{\text{II}}$ EXAFS data of the oxides with Am/(Am+U) = 0.5, 0.6 and 0.7 present very different features from those of UO$_2$ for $1 \leq k \leq 7$ Å^{-1} (corresponding to $1.3 \lesssim R + \Delta R \lesssim 2.8$ Å in the Fourier transform space). Indeed, the tentative to fit these data using a simple fluorite model gave very poor results for this region. Since the EXAFS data were similar to those of the U$_4$O$_9$, firstly, a refinement of this reference was performed in the $1.3 \lesssim R + \Delta R \lesssim 2.8$ Å range. The model based on the "average" β-U$_4$O$_9$ structure (s.g. $F\bar{4}3m$), proposed by Cooper and Willis [172], was adopted. In this structure, the cations and most of the O atoms are located at fluorite-type positions. However, the fluorite-type oxygen sublattice (O$_{\text{fluo}}$ Tab. 4.9 and in Tab. 4.10) presents a significant proportion of vacancies. Two other interstitial positions are available for the oxygen: the 48(h) (x= y= 0.617 and z= 0.5) and the 16(e) (x= y= z= 0.608) Wyckoff positions. Since the 16(e) position has a very low occupancy (0.010), only the 48(h) interstitial oxygen atoms were included in the EXAFS model (O$_{\text{cubo}}$ in

Tab. 4.9 and Tab. 4.10). The main effect of including these cuboctahedral oxygen atoms is the appearance of two additional U-O distances. The first one, of about 2.20 Å, is smaller than the U-O$_{fluo}$ distance ($\sim$ 2.33 Å); the second distance, of about 2.87 Å, is larger than the U-O$_{fluo}$ distance. A good agreement between the refined curve and the experimental data was obtained for U$_4$O$_9$, as shown in Fig. 4.16 and confirmed by a low R-factor of 0.009. The fitted parameters for U$_4$O$_9$ are reported in Tab. 4.9. In Fig. 4.16, one can observe that the fit does not reproduce the shoulder of the experimental data for $1.0 \lesssim R \lesssim 1.3$ Å. As previously explained by Hennig [173], this originates from the excitation of secondary electrons, which occurs in the L$_3$-edge spectra of various lanthanides and actinides [173–175]. Being an electronic effect, independent on the crystallographic structure, its modeling is out of the scope of this work.
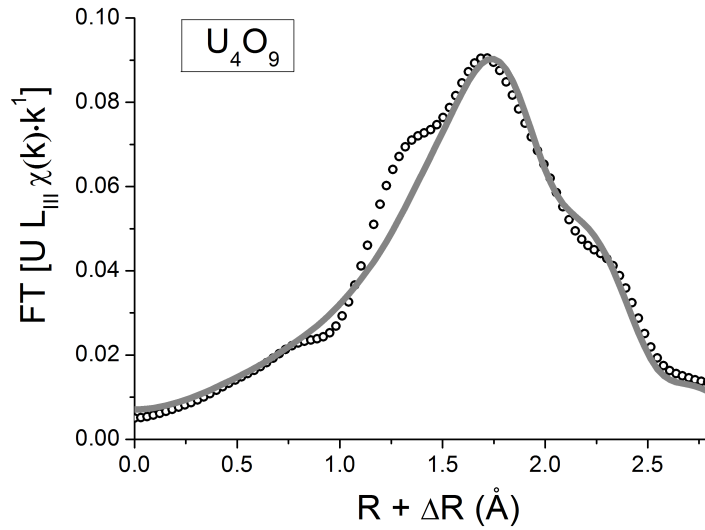
Fig. 4.16: Refinement of the U L$_{III}$ EXAFS Fourier transform of U$_4$O$_9$ (3.5-14 Å^{-1}, $dk = 2$Å^{-1}).

Shell	R (Å)	N	σ^2(Å^2)
O$_{cubo}$	2.248(5)	1.7(5)	0.006(1)
O$_{fluo}$	2.327(5)	6.3(5)	0.025(2)
O$_{cubo}$	2.84(1)	1.7(5)	0.006(2)

Table 4.9: Refined parameters of the U-L$_{III}$ EXAFS Fourier transform of U$_4$O$_9$.

Using the β-U$_4$O$_9$ structural model, a good agreement between the fitted curves and the experimental data was achieved for the three compositions with high americium content, as shown in Fig. 4.17 (except for the shoulder at $R \simeq 1.2$ Å already discussed). However, the increase of the structural complexity, with two additional U-O distances, multiplies the number of parameters to refine with the same number of data points. Therefore, a higher uncertainty affects the results of these EXAFS fits. Moreover, considering the complexity of the spectra, the second cationic shell was not refined for these three samples.

The good results obtained with the β-U$_4$O$_9$ structural model prove the presence of oxygen vacancies in the normal fluorite sites and of oxygen interstitial atoms in cuboctahedral sites

for (U,Am)O$_{2-x}$ oxides with Am/(Am+U)$\geq$ 0.5. However, interesting differences compared to the U$_4$O$_9$ can be noticed. First, for the three (U,Am)O$_2$ samples, the number of oxygen atoms in the fluorite position, equal to 5.4(5), is lower than that of U$_4$O$_9$, equal to 6.3(5), whereas the number of atoms in the interstitial positions are identical (within the uncertainty). This indicates a higher concentration of oxygen vacancies, which is understandable since the mixed oxides are hypostoichiometric (O/M<2), contrary to U$_4$O$_9$. Second, the first U-O$_{cubo}$ distance of the mixed (U,Am)O$_2$- 2.18(1), 2.17(1), 2.17(1) Å respectively for Am/M=0.5, 0.6 and 0.7- is shorter than that observed for U$_4$O$_9$, equal to 2.248(5) Å. This is likely due to the average oxidation state of uranium, which is higher in the (U,Am)O$_2$ oxides than in U$_4$O$_9$, as seen in the previous section. However, it must be noticed that the obtained U-O distances are, in any case, considerably higher than the uranyl U^{+6}-O distance of 1.8 Å observed in U$_3$O$_8$ or UO$_3$. The presence of hexavalent uranium can hence be excluded, solving the doubt met in the previous section.

Considering the U-cation shell, the distance and the Debye-Waller factors are comparable to the values obtained for the other compositions and for the americium shell, as shown in Fig. 4.13 and Fig. 4.14. This confirms that the cationic fluorite sublattice is maintained also by the U ions.
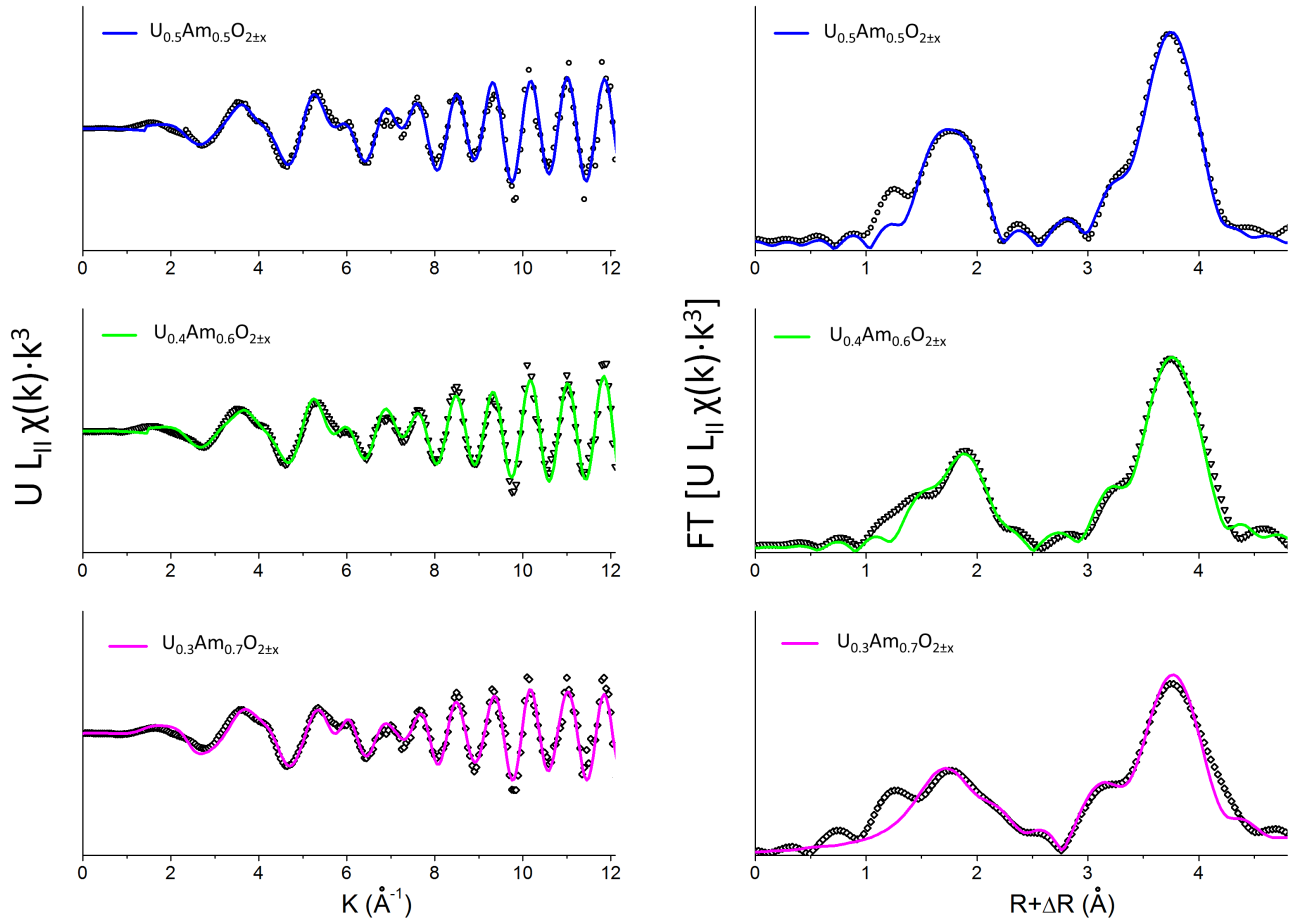
Fig. 4.17: Refinement of the U L$_{II}$ EXAFS spectra and their Fourier transforms for U$_{0.5}$Am$_{0.5}$O$_{2-x}$, U$_{0.4}$Am$_{0.6}$O$_{2-x}$ and U$_{0.3}$Am$_{0.7}$O$_{2-x}$. (FT boundaries: 3.5-14 Å^{-1}, dk = 2Å^{-1}).

Sample	Edge	Shell	R (Å)	N	$\sigma^2(\text{Å}^2)$	R-factor
UO$_2$	U-L$_{II}$	O1	2.357(5)	8.0(5)	0.0041(4)	0.005
		U1	3.867(5)	11.9(5)	0.0021(2)	
		O2	4.52(2)	24(2)	0.006(1)	
		U2	5.45(2)	6(1)	0.005(2)	
U$_{0.85}$Am$_{0.15}$O$_2$	Am-L$_{III}$	O1	2.427(5)	7.8(5)	0.0048(4)	0.008
		Am/U1	3.860(5)	11.9(5)	0.0027(1)	
		O2	4.52(1)	24	0.011(2)	
		Am/U2	5.466(9)	6(1)	0.0034(8)	
	U-L$_{II}$	O1	2.355(5)	7.9(5)	0.0074(5)	0.009
		Am/U1	3.872(5)	11.7(5)	0.0031(2)	
		O2	4.51(1)	24(2)	0.008(1)	
		Am/U2	5.47(1)	6(1)	0.005(2)	
U$_{0.7}$Am$_{0.3}$O$_2$	Am-L$_{III}$	O1	2.438(4)	7.9(5)	0.0054(4)	0.009
		Am/U1	3.858(5)	11.8(5)	0.0033(5)	
		O2	4.48(1)	24	0.014(3)	
		Am/U2	5.475(5)	6	0.0031(4)	
	U-L$_{II}$	O1	2.330(6)	8.1(5)	0.0094(4)	0.007
		Am/U1	3.860(5)	11.9(5)	0.0041(2)	
		O2	4.517(8)	24	0.009(1)	
		Am/U2	5.45(1)	6	0.006(1)	
U$_{0.5}$Am$_{0.5}$O$_2$	Am-L$_{III}$	O1	2.433(5)	7.9(5)	0.0062(4)	0.006
		Am/U1	3.855(5)	11.9(5)	0.004(1)	
		O2	4.47(1)	24	0.014(2)	
		Am/U2	5.47(1)	5(1)	0.005(1)	
	U-L$_{II}$	O$_{cubo}$1	2.183(5)	1.7(5)	0.004(1)	0.017
		O$_{fluo}$1	2.359(5)	5.4(5)	0.008(2)	
		O$_{cubo}$2	2.87(1)	1.7(5)	0.021(2)	
		Am/U1	3.85(1)	12	0.004(1)	
		O$_{fluo}$2	4.52(1)	22(3)	0.012(1)	
U$_{0.4}$Am$_{0.6}$O$_2$	Am-L$_{III}$	O1	2.417(8)	8	0.0072(7)	0.02
		Am/U1	3.836(5)	12	0.0042(2)	
		O2	4.45(4)	24	0.014(3)	
		Am/U2	5.46(1)	6	0.004(2)	
	U-L$_{II}$	O$_{cubo}$1	2.172(5)	1.5(5)	0.004(1)	0.018
		O$_{fluo}$1	2.340(5)	5.4(5)	0.007(2)	
		O$_{cubo}$2	2.84(1)	1.5(5)	0.001(1)	
		Am/U1	3.86(1)	12	0.0038(8)	
		O$_{fluo}$2	4.42(1)	22(3)	0.011(1)	
U$_{0.3}$Am$_{0.7}$O$_2$	Am-L$_{III}$	O1	2.404(6)	7.3(5)	0.0092(6)	0.011
		Am/U1	3.837(5)	12	0.0053(2)	
		O2	4.42(1)	22(2)	0.012(2)	
		Am/U2	5.45(2)	6	0.006(3)	
	U-L$_{II}$	O$_{cubo}$1	2.17(1)	1.7(5)	0.009(1)	0.03
		O$_{fluo}$1	2.29(1)	5.4(5)	0.012(1)	
		O$_{cubo}$2	2.82(1)	1.7(5)	0.008(1)	
		Am/U1	3.85(1)	12	0.0046(8)	
		O$_{fluo}$2	4.404(1)	22(3)	0.011(1)	

Table 4.10: Data resulting from the refinement of the EXAFS spectra. The parameters without uncertainties were fixed during the fit.

4.2.2.3   Conclusion on the XAS investigation

The first XANES/EXAFS studies performed by Prieur *et al.* [69, 71] on (U,Am)O$_2$ oxides with Am/(Am+U) ratio ranging from 0.10 to 0.20 highlighted that the formation of this fluorite-type solid solution occurs in a peculiar way. Indeed, the simultaneous existence of three different oxidation states, with Am^{3+}, U^{4+} and U^{5+}, was observed by XANES, contrary to the other actinide dioxides, where only cation couples (An^{3+}/An^{4+} or An^{4+}/An^{5+}) have been observed. Moreover, the oxygen stoichiometry close to 2.00 and the similar Am^{3+}-U^{5+} molar fractions suggested a charge compensation mechanism. The EXAFS did not highlight remarkable changes on the local structure for these oxides. The only evident effect of the charge distribution was a shortening of the U-O distance and a lengthening of the Am-O distance, attributable to the the different ionic radii. Lebreton *et al.* extended the XANES/EXAFS investigations on (U,Am)O$_2$ oxides with higher americium contents, equal to 40 mol.% and 50 mol.%. Both the samples were found hypostoichiometric in oxygen, with an O/M ratio respectively equal to 1.97 and 1.93. The americium was still found purely trivalent, whereas the uranium average oxidation state was +4.6 and +4.7, respectively for the 40 mol.% and 50 mol.%. Moreover, in this case, stronger changes in the local structure were highlighted by the EXAFS results. Oxygen vacancies were found around americium. For uranium, the first oxygen shell signal was found very different from that expected from a fluorite-type structure, suggesting the presence of cuboctahedral oxygen clusters as in U$_4$O$_9$. Here, the study of the (U,Am)O$_2$ solid solution was continued by exploring different compositions. The obtained XAS results highlighted that the formation of almost stoichiometric (U,Am)O$_2$ oxides, without dramatic changes in the fluorite structure, can be extended to Am/(Am+U) equal to ∼30 mol.%. Indeed, the investigated U$_{0.72}$Am$_{0.28}$O$_{2.01}$ sample presented EXAFS spectra with typical fluorite features at both the Am L$_3$ and U L$_2$ edges, despite the purely trivalent state of Am and the high average oxidation state of U, equal to +4.45. In this case, as in the investigations of Prieur *et al.* [69, 71], the only structural effect highlighted by the EXAFS refinements was the shortening of the U-O distance and the lengthening of the Am-O distance, compared to the theoretical ones. No deviation from the theoretical coordination numbers, which could indicate the existence of vacancies or interstitials, was observed.

The oxide with nearly equal Am and U contents, the U$_{0.53}$Am$_{0.47}$O$_{1.97}$ sample, presented some differences from the equimolar oxide investigated by Lebreton. The sample had a higher O/M ratio (1.97 versus 1.93), which suggests that the oxygen stoichiometric state could be stable at room temperature. The higher oxygen content was compensated by a further oxidation of uranium (+4.82 versus +4.72), whereas americium was still purely trivalent. The local oxygen sublattice around uranium presented distortions similar to those observed by Lebreton. These distortions indicate the co-existence of oxygen vacancies, in the normal fluorite sublattice, and oxygen interstitials in cuboctaedral sites. The reorganization of the oxygen sublattice around the uranium is even more stressed for the oxides with Am/(Am+U)=0.6 and 0.7, especially for the second one, in which the average oxidation state of uranium reaches +4.89. This represents a very strong oxidation state, since the value is even higher than that of U$_4$O$_9$ (4.5). As previously said, the oxide references available for the XANES did not allow to conclude on the presence

of U^{6+}. A cubic oxide with pure pentavalent uranium would have been necessary to draw sure results. However, the presence of U^{6+} was excluded in view of the EXAFS results, since the U-O distances were considerably larger than the typical uranyl distance (1.8 Å). Looking to americium, in the two samples with Am/(Am+U)= 60 and 70 mol. %, not negligible fractions of Am^{4+} were observed for the first time, respectively 13 % and 26 mol.%. The presence of Am^{4+} induced a slight shortening of the Am-O distance, still maintaining the local fluorite structure around americium. Despite the increasing oxidation states of both uranium and americium, the overall O/M ratio kept to decrease with the americium content, passing from the 1.97 value of U$_{0.53}$Am$_{0.47}$O$_{1.97}$ to 1.93, for Am/(Am+U)=60 mol.%, and to 1.90 for Am/(Am+U)=70 mol.%. Finally, only for this latter sample, the coordination numbers obtained by EXAFS proved the precense of oxygen vacancies around americium, consistently with the oxygen hypostoichiometry. However, if this technique is very sensitive to the interatomic distances (below 0.01 Å), higher uncertainties (>0.5) affect the number of atoms, especially for light atoms as oxygen. For this reason, in order to have an insight on the point defects in the oxygen sublattice (both vacancies and interstitials), a Raman spectroscopy was performed on (U,Am)O$_2$ oxides with 0.075<Am/(Am+U)<0.7, whose results are presented in the following section.

4.2.3   Structural defects by Raman spectroscopy

In general, crystals with fluorite structure have simple vibrational properties. The group theory predicts, for the $Fm\bar{3}m$ space group, only one infrared T$_{1u}$ active mode and one triply degenerate T$_{2g}$ Raman-active mode [176]. This latter is originated from the M-O stretch, M being coordinated in a cubic environment of 8 oxygen. The T$_{2g}$ mode was experimentally observed for several fluorite materials, including rare earth and actinide dioxides [177, 178]. However, experimental studies on UO$_2$ and mixed U-actinide or U-rare earth dioxides highlighted a more complicated situations. Additional Raman-active modes have been observed for these materials [179–183]. Indeed, it was found out that several factors, as irradiation, doping and oxidation, cause the formation of structural defects, leading to a break of the local cubic symmetry. The latter seems at the origin of the additional Raman-active modes. Even if a complete understanding of these peculiarities in the Raman spectroscopy results is still not achieved, several steps forwards have been made in the last decades in this field. The connection between the additional Raman modes and the various possible structural defects in the fluorite structure seem now clearer. Therefore, the Raman spectroscopy is suitable for the structural investigation of actinide oxides. Indeed, in addition to several experimental advantages (small masses needed, rapidity, remoteness...), this technique allows identifying the fluorite structure (with the T$_{2g}$ mode) and, at the same time, determining the presence and the kind of defects.

Only two Raman studies were reported on (U,Am)O$_2$ oxides. The first, by Naji *et al.* [184], was performed on samples with Am/(Am+U)=0.1 and 0.2; the second, by Lebreton e*t al.* [73], on samples with Am/(Am+U)=0.15 and 0.5. The Raman bands associated to the structural defects were observed in both the studies. However, it is hard from these results to follow the variation of these defects with the Am content, since only two compositions were investigated by

each author and the two studies are difficult to compare because of different experimental set-ups (laser wavelengths and power) and sample manufactures. Here, a first systematic Raman spectroscopy investigation on (U,Am)O$_2$ oxides with Am/(Am+U) ratio between 7.5 and 70 mol.% is presented.

4.2.3.1   Results

The Raman investigation was performed at the JRC-Karlsruhe, using the experimental set-up and procedure described in Appx. A. The samples concerned by the investigations are the manufactured compositions with Am/(Am+U)=0.075, 0.1, 0.2, 0.3, 0.4, 0.5, 0.6 and 0.7. The age of the samples at the time of the measurements was of 10 months.

The Raman spectra, obtained using an excitation wavelength λ= 647 nm (corresponding to 1.92 eV), are reported in Fig. 4.18. For all the compositions, one can observe a first symmetric band, at wavenumber$\sim$450 cm^{-1}, and a large envelope, likely including 2-3 modes, between 500-650 cm^{-1}. A variation of the relative intensities between the bands is clearly observable varying the Am/(Am+U).

The Raman spectra were deconvoluted using 4 Lorentzian bands, whose positions are reported in Tab. 4.11 for the various compositions. The first symetric band has a position ranging from 445-462 cm^{-1}. These values are close to those of the T$_{2g}$ modes in actinide dioxides (445 cm^{-1} for UO$_2$, 460 cm^{-1} for NpO$_2$, 472 cm^{-1} for PuO$_2$) [178], hence the identification with this mode was immediate. For the large band at $500 < \nu < 650$ cm^{-1}, the deconvolution was performed using 3 bands, indicated as ν_1, ν_2, ν_3, whose identifications will be discussed in the next section. The relative intensities of these three bands as a function of the Am content are shown in Fig. 4.19. An approximately constant intensity is observed for ν_1. The ν_2 band is always the most intense and it shows a maximum for Am/(A+U)$\sim$40-50 mol.%. Finally, the intensity of the ν_3 band is approximately constant for Am/(Am+U)$\leq$40 mol.% and then it decreases for the highest americium contents.

Am/(Am+U) mol.%	T$_{2g}$ cm^{-1}	ν_1 cm^{-1}	ν_2 (LO) cm^{-1}	ν_3 cm^{-1}
7.5	445(3)	536(5)	574(5)	632(5)
10	445(3)	535(5)	570(5)	630(5)
20	449(3)	532(5)	571(5)	630(5)
30	450(3)	535(5)	581(5)	633(5)
40	451(3)	554(5)	601(5)	633(5)
50	450(3)	555(5)	606(5)	633
60	463(3)	525(5)	582(5)	633(5)
70	451(3)	535(5)	594(5)	633(5)

Table 4.11: Wavenumber positions of the bands used for the deconvolution of the Raman spectra.
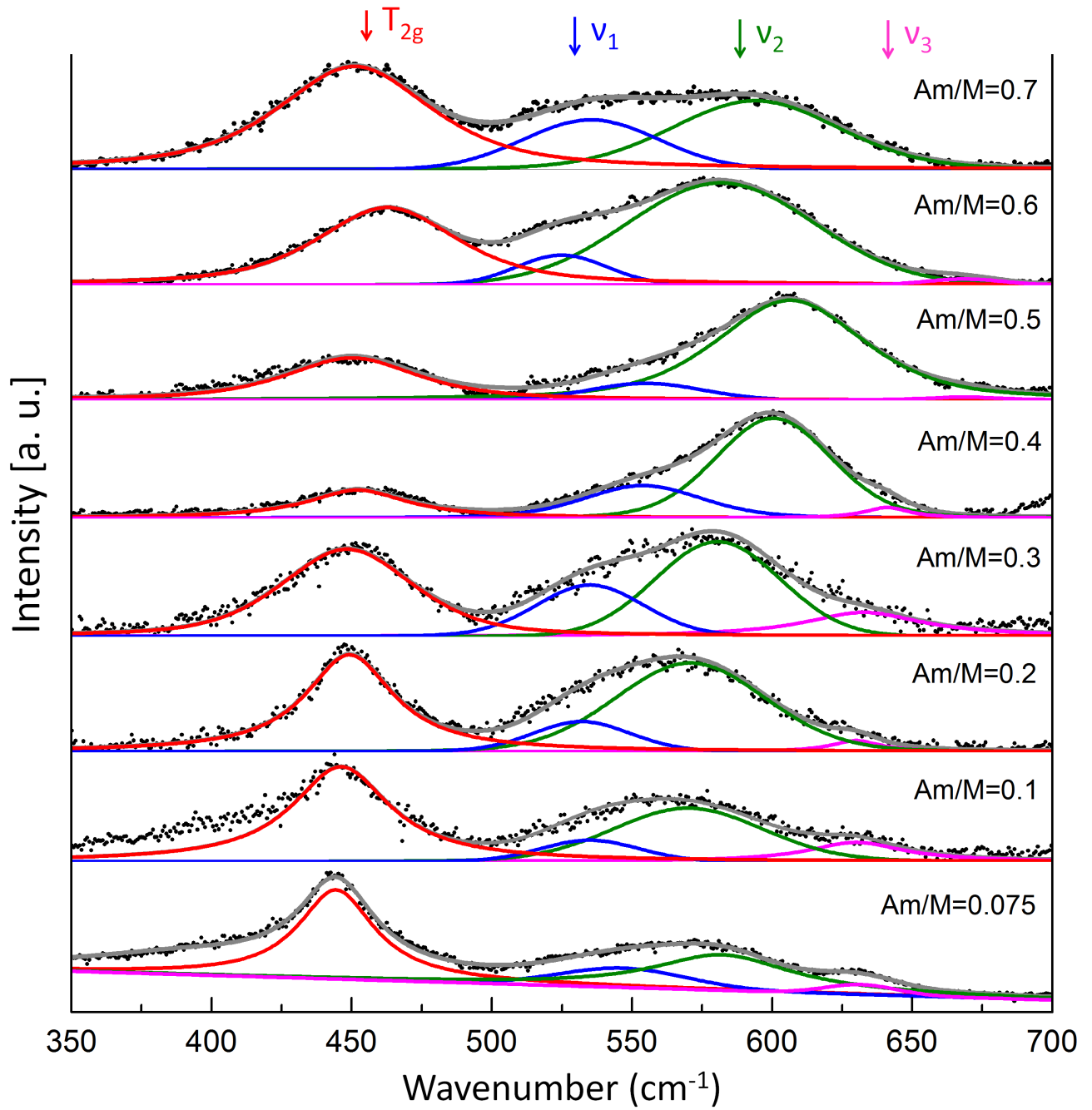
Fig. 4.18: Raman spectra of (U,Am)O$_2$ oxides with Am/(Am+U)=0.075, 0.1, 0.2, 0.3, 0.4, 0.5, 0.6 and 0.7. ● = experimental points; − = deconvolution. The 4 bands used for the deconvolution (T_{2g}, ν_1, ν_2, ν_3) are also indicated.

4.2.3.2   Discussion

T$_{2g}$ band

As previously said, for all the (U,Am)O$_2$ oxides, a single intense band was observed at about 450 cm^{-1}. This was easily associated to the T$_{2g}$ mode, originated by the U-O and Am-O stretch, with U and Am being coordinated in a cubic environment of 8 oxygen. Therefore, the maintaining of an overall fluorite symmetry is confirmed also by the Raman spectroscopy.

The variation of the T$_{2g}$ position found out in this work for the (U,Am)O$_2$ samples is compared to those of the actinide dioxides [178,184] in Fig. 4.20. In the literature, a regular increasing trend of the T$_{2g}$ wavenumber was highlighted for actinide dioxides, with An=U, Np, Pu. This reflects the regular decreasing trend of the lattice parameter in these compounds (the frequency of the mode increases when the An-O stretch decreases). Therefore, a T$_{2g}$ mode around 488 cm^{-1} would be expected for AmO$_2$, but this was never experimentally observed. Indeed, two independent Raman measurements on AmO$_2$, by Horlait *et al.* [118] and Naji *et al.* [184], did not report the presence of this line. On the contrary, an intense Raman band was observed at about 390 cm^{-1} in both cases. Different interpretations were provided by the two authors. According to Horlait *et al.*, the 390 cm^{-1} line represents the T$_{2g}$ mode and hence the AmO$_2$ would constitute an anomaly in the actinide series. Naji *et al.* observed that a mode close to 390 cm^{-1} is expected for the Am$_2$O$_3$ sesquioxide. In consequence, they supposed that a photo-induced reduction was occurred. Even if solving the *mystery* of the AmO$_2$ T$_{2g}$ mode is out the scope of this work, the data here collected provide a new piece of the puzzle. The results of Fig. 4.20 show a slow increase of the T$_{2g}$ wavenumber with the americium content for Am/(Am+U)≤0.60, but an inverse of the tendency is observed for Am/(Am+U)=0.70. This seems to confirm the anomaly of AmO$_2$ suggested by Horlait *et al.*, even if the departure from the oxygen stoichiometry of the samples (see Tab. 4.7) and the corresponding effects on the lattice parameter should be considered more carefully.
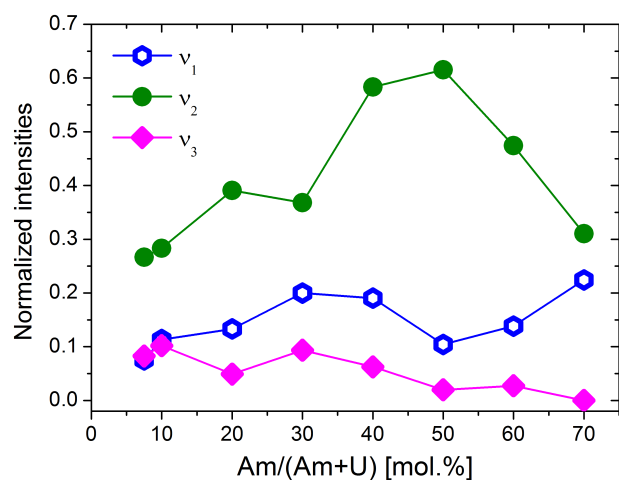
Fig. 4.19: Relative intensities (normalized to the total intensities) of the ν_1, ν_2, ν_3 bands.

Fig. 4.20: Positions of the T$_{2g}$ bands for (U,Am)O$_2$ and An-dioxides.

Defect bands

The ν_1, ν_2, ν_3 bands are found at positions similar to the defect bands observed in UO$_2$, which appear as effect of irradiation [183, 185], oxidation [179, 181, 186] or doping [182, 186]. Their attribution is based on these similarities.

The ν_1 band ranges from 535(5) to 555(5) cm^{-1} for the various (U,Am)O$_2$ investigated. In the literature, a Raman mode in this wavenumber range was reported for several U$_{1-y}$Ln$_y$O$_{2-x}$ oxides, where Ln is a trivalent lanthanide [182, 183, 186]. The authors supposed that this mode is originated from a M-O stretching (M= actinide or lanthanide), being M coordinated in a MO$_8$

cubic environment with at least one oxygen vacancy. According to this hypothesis, the ν_1 mode can be seen as the signature of oxygen vacancies. It must be stressed that this mode is present for all the investigated (U,Am)O$_2$ samples with comparable intensity. Therefore, these results indicate that the addition of americium leads to the formation of oxygen defects, including vacancies, also for the samples with O/M $\gtrsim$ 2.00 (see Tab. 4.7).

The ν_2 band, at about 575 cm^{-1} can be associated to the LO mode. In the literature, this mode was reported several times for actinide dioxides and its origin has been debated for long [178–180, 187]. Livneh and Sterer [180] showed that the activation of the LO modes occurs via a resonance process and hence it depends on the difference between the energy of the laser and the band gap energy. This latter is equal to 2-2.5 eV for UO$_2$ [188–191] whereas a lower value of 1.3 eV was measured for AmO$_2$ [192]. Interestingly, a strong decrease of the LO mode occurs from Am/(Am+U)=0.4 to Am/(Am+U)=0.7. The increase of the Am content could be at the origin of the band gap contraction, considering the difference between UO$_2$ and AmO$_2$. However, for Am/(Am+U)$\geq$0.4, an important departure from the oxygen stoichiometry was highlighted by XANES (see section 4.2.1.1), with O/M ratio passing from 2.0 to 1.9. A more precise analysis, taking into account the oxygen content, would hence be necessary.

The ν_3 band has a position almost constant at about 632 cm^{-1}. Raman bands with this wavenumber were observed several times in UO$_{2+x}$ and U$_4$O$_9$ oxides [181]. This band has been attributed to vibration modes involving oxygen atoms in cuboctahedral clusters. It can be surprising that the ν_3 band was observed for all the compositions, since the EXAFS results highlighted the presence of oxygen interstitials around uranium only for Am/(Am+U)$>$ 30 mol. %. However, one must be careful in the interpretation of this band presence. Indeed, this mode was often observed in initially stoichiometric UO$_2$ because of a surface oxidation induced by the laser. A similar phenomenon is likely at the origin of the ν_3 band of the (U,Am)O$_2$ oxides with Am/(Am+U)$\leq$0.30. On the contrary, a surface oxidation can be excluded for the (U,Am)O$_2$ oxides with higher Am/(Am+U), since the americium stabilizes the solid solution toward the O/M increase, as it will be shown in the next chapter. In this case, ν_3 band can be safely attributed to the structure of the sample. It can be surprising that, for 0.4$\leq$ Am/(Am+U) $\leq$0.7, the intensity of this mode decreases with the Am content (see Fig. 4.19), whereas the U L$_{\text{II}}$ EXAFS spectra had shown a more and more distorted oxygen sublattice. It must be kept in mind that the EXAFS is an element-selective technique, whereas the Raman spectroscopy probes simultaneously the U-O and Am-O vibrations. It is true that the oxygen sublattice around uranium is more and more affected by increasing the americium content, but the total amount of uranium diminishes. Therefore, the main contribution to the Raman spectrum intensity comes from the Am-O stretches. Since the sublattice around americium is not affected by oxygen interstitials, the Raman spectroscopy *sees* a sample as a whole more ordered.

4.3   Conclusions

This chapter represents the starting point of the study on the U-Am-O ternary system. Indeed, with the objective to experimentally investigate this system, $U_{1-y}Am_yO_{2\pm x}$ pellets, with $0.075 \leq y \leq 0.70$, were manufactured. The different steps of the applied process were described in section 4.1.1. The characterizations performed on the obtained samples, presented in section 4.1.2, proved the success of the manufacture. Indeed, homogeneous $(U,Am)O_2$ samples, with fluorite structure, were obtained for all the compositions. A summary of the properties of the as-sintered samples is reported in Tab. 4.12, including the O/M ratios and the molar fraction of each cationic species. These quantitative data, which are precious for the development of a reliable CALPHAD model, as explained in section 1.2, were obtained thanks to an in-depth investigation of the $U_{1-y}Am_yO_{2\pm x}$ structural properties. XRD, XAS and Raman spectroscopy were here combined, completing the previous works of D. Prieur [117] and F. Lebreton [106]. The new data, together with the previous results, allowed to achieve a more thorough understanding of the structure of the $U_{1-y}Am_yO_{2\pm x}$ solid solution.

Contrary to other mixed U-An mixed dioxides, the $U_{1-y}Am_yO_{2\pm x}$ solid solution presents the co-existence of three/four different cationic species, namely Am^{3+}, U^{4+}, U^{5+} and, for Am/(Am+U) > 0.5, also Am^{4+}. For Am/(Am+U) ratios up to 30 mol.%, $U_{1-y}Am_yO_2$ oxides are stable for O/M~2.00. In these cases, the U^{5+} concentration is similar to the molar fraction of americium (purely Am^{3+}), allowing the maintaining of the oxygen stoichiometry. The co-existence of Am^{3+}, U^{4+}, U^{5+} does not alter in a dramatic way the fluorite structure of $U_{1-y}Am_yO_{2\pm x}$ oxides with $y \leq 0.3$. The only structural effect highlighted by EXAFS is a shortening of the U-O distance and a lengthening of the Am-O distance, in comparison to the theoretical ones (from XRD lattice parameters). The difference in the U-O and Am-O bond length is consistent with the different ionic radii of the present cations. Nevertheless, the new Raman data indicated also the presence of vacancies in the oxygen sublattice. Based on the charge data, one can assume that oxygen vacancies are mostly accommodated around Am^{3+}. This would imply that complex defects, including oxygen interstitials, are likely present around U^{4+}-U^{5+}, since the overall O/M is close to 2.00. However, the extent of the distortions in the oxygen sublattice is probably very small for Am/(Am+U)$\leq$0.30. The effects become instead more and more important by increasing the americium content in the solid solution. For Am/(Am+U) equal to 0.4 [106] and 0.5, the EXAFS revealed important changes in the oxygen sublattice around uranium, including both vacancies in the normal fluorite sites and interstitials in cuboctahedral positions. These arrangements are possible thanks to the high average oxidation state of uranium, which increases with the americium content, reaching values even higher than that assumed in U_4O_9. However, this is not sufficient to compensate the purely trivalent state of americium: all the investigated samples with Am/(Am+U)=0.4 and 0.5 were slightly hypostoichiometric (O/M<2.0). The stability of the $(U,Am)O_2$ solid solution in the oxygen poor domain was confirmed also for Am/(Am+U) equal to 0.6 and 0.7. For these two compositions, O/M respectively equal to 1.93(2) and 1.90(2) were observed. This decrease of the O/M ratio with the Am content occurs despite the high oxidation state of uranium (maximum value=+4.89 for Am/(Am+U)=0.7) and the appearance,

for the first time, of Am^{4+}. The XANES results seem to indicate that the maximum possible molar fraction of the Am^{3+} is about 50%; above this value, Am^{4+} appears. Once again, this complicated cationic charge distribution occurs without breaking the overall fluorite symmetry. More specifically, the distortions of the oxygen sublattice around uranium are accentuated, but the local structure around americium is not dramatically affected. For the latter, only a shortening of the average Am-O distance (due to the smaller Am^{4+} ionic radius) and a slight increase of the Debye-Waller factors were highlighted by the EXAFS. Besides, the overall order of the samples was also confirmed by the Raman results, which showed a decrease in the intensity of the defect bands for Am/(Am+U)=0.6 and 0.7. This is coherent since the highest contribution to the Raman signal, for these samples, come from the americium (more abundant than uranium), which preserves its local order.

Target	Precursors		Measured compositions [mol.%]				O/M
Am/M [mol.%]	UO_2	AmO_2	Am^{3+}	Am^{4+}	U^{4+}	U^{5+}	ratio
7.5	Nat	C9					2.01^a
10	Cad	TCH					2.01^a
15	Cad	C9	15	0	67	18	2.02
20	Nat	C9					2.01^a
30	Cad	C9	28	0	40	32	2.02
40	Cad	TCH					1.97^a
50	Cad	C9	48	0	10	42	1.97
60	Nat	C9	50	7	8	35	1.93
70	Nat	C9	49	18	4	29	1.90

Table 4.12: Summary of the properties of the as-sintered $(U,Am)O_2$ samples.
a: values not measured but supposed from the previous results [106, 117].

Chapter 5

The oxygen rich domain of the U-Am-O phase diagram

In the previous chapter, the structural investigation of $(U,Am)O_2$ oxides highlighted their stability in the stoichiometric state, i.e. O/M~2, for Am/(Am+U)≤0.3. For higher americium contents, all the investigated samples were hypostoichiometric, proving the stability of the $(U,Am)O_2$ solid solution for O/M<2. In this chapter, the investigation will be extended to the oxygen rich domain of the U-Am-O phase diagram, for which the data in the literature are rare. Indeed, only two studies are reported for uranium-americium mixed oxides with O/M>2. The first concerns the oxygen potential measurements performed on $U_{0.5}Am_{0.5}O_{2\pm x}$ by Bartscher and Sari [74]; these data indicate that the fluorite-type solid solution can reach O/M values of about 2.09, for $973 \leq T \leq 1573$ K and $-60 \leq \Delta \overline{G} O_2 \leq -7$ kJ/mol. The second is a recent investigation, by Caisso *et al.* [193], that indicates a small solubility (Am/M=10 mol.%) of americium in the hexagonal $\alpha' M_3 O_8$ structure (s.g. $P\overline{6}2m$). However, no data exist on the transition temperatures and the phase limits in the MO_2-M_4O_9-M_3O_8 domain. Here, this domain will be investigated by coupling High-Temperature XRD in air and subsequent XAS spectroscopy at room temperature. First, in section 5.1, the differences between the UO_2 and AmO_2 behaviour under air will be recalled. Then, the results of the HT-XRD measurements performed in air on $(U,Am)O_2$ samples, with $0.1 \leq Am/(Am+U) \leq 0.7$, will be shown in section 5.2. Finally, a room temperature XAS characterization on the oxidized samples will be presented in section 5.3.

5.1 HT behaviour in air: UO_2 vs AmO_2

The U-O system has a complex thermodynamics and the corresponding phase diagram (see Fig. 2.1) includes several oxides with O/M>2, namely U_4O_9, metastable U_3O_7, U_3O_8 and UO_3. Several studies of the oxygen-rich domain of the U-O phase diagram and of the UO_2 oxidation process under air are available [90, 194–198]. Here, only a HT-XRD experiment reported by Chollet *et al.* [199] is detailed, since this study can be directly compared to the results on the mixed oxides, presented in the following section. The HT-XRD results of Chollet *et al.* [199] are reported, as an iso-intensity map, in Fig. 5.1-(a). The measurements were performed from 300 K to 1673 K, recording a diffraction pattern every 100 K. For T > 473 K, evident distortions
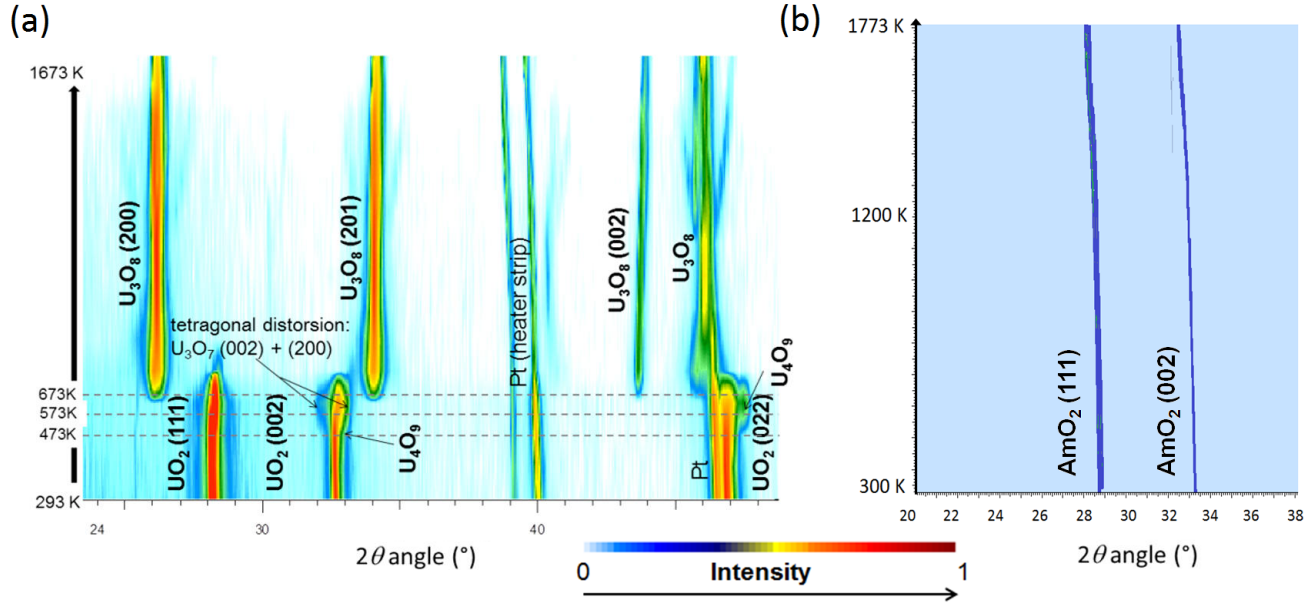
Fig. 5.1: Iso-intensity map of HT-XRD measurements in air on (a) UO$_2$ (figure extracted from [199]) and (b) AmO$_2$.

and shifts toward higher angles of the UO$_2$ diffraction peaks are observable. These indicate the $UO_2 \rightarrow U_4O_9$ transition and likely also the formation of the metastable U$_3$O$_7$ phase. The identification of these phases by XRD is not trivial, since they are superstructures of the fluorite lattice, originated mainly by the re-organization of the oxygen sublattice. Thus, their most intense reflections coincide with those of the fluorite, as it can be seen in Fig. 5.1-(a). Clearly detectable is instead the U$_3$O$_8$ phase since, as explained in section 2.2.1.2, all its polymorphs have symmetries different from the fluorite structure. The U$_3$O$_8$ appears at 673 K and a fast phase transition is observed (less than 2 hours on powder sample). At the end of the thermal treatment under air, the UO$_2$ is hence completely transformed in U$_3$O$_8$.

AmO$_2$ behaves under air in a very different way than UO$_2$, as discussed in chapter 3. In 5.1-(b), the isointensity map of the XRD measurements already presented in section 3.2.2.1 is shown. During the heating under air, AmO$_2$ maintains its fluorite structure and it also starts to be reduced (O/M<2) for T > 1200 K. This is shown by the shift of the diffraction peaks toward lower angles and it has been confirmed by the thermodynamic modeling presented in chapter 3.

In summary, the pronounced differences between the Am-O and the U-O phase diagram lead to a completely different behaviour of the respective dioxides under air. Therefore, it is difficult to infer on the oxygen rich domain of the ternary U-Am-O phase diagram and the behaviour of (U,Am)O$_2$ oxides in oxidizing conditions. For this reason, an experimental investigation will be presented below.

5.2 HT behaviour in air: (U,Am)O$_2$

HT-XRD measurements in air were performed at the LEFCA facility of CEA Marcoule, using the experimental set-up and procedure detailed in Appx. B. The (U,Am)O$_2$ oxides with Am/(Am+U) ratio equal to 10, 15, 30, 50, 70 mol.% were investigated in this work. The samples were stored for about 7 months before the measurements, with the exception of the 10 % sample which was annealed before the HT-XRD experiment. The annealing treatment was initially planned for all the samples but it could no be performed for technical problems.

All the studied compositions underwent, in the HT-XRD, the same thermal treatment under air. They were heated from 300 K up to about 1473 K, with temperature steps of 50 K. At each step, a diffraction pattern in the $18° \leq 2\theta \leq 140°$ range was acquired. One acquisition requires about 30 minutes. The heating rate between the steps was 5 K/s. At the end of the heating stage, a plateau of 4 hours was performed at the maximum temperature. Finally, the sample was cooled down recording a diffraction pattern every 100 K. A cooling rate of 5 K/s was applied between the steps.

Two completely different behaviours were exhibited by the oxides with Am/(Am+U)≤0.30 and those with Am/(Am+U)≥0.50. For this reason, these two composition domains will be separately addressed in the next sections.

5.2.1 Domain with Am/(Am+U) ≤ 0.3

An overview of the behaviour in air of the (U,Am)O$_2$ oxides with Am/(Am+U)≤0.30 is provided in Fig. 5.2, where isointensity maps were created from the diffraction patterns, recorded at different temperatures. Both the heating and the cooling stages are included in the representation. The specific angular range in Fig. 5.2 was selected because it includes intense diffraction peaks of all the observed phases.

At the beginning of the measurements, at T = 300 K, only the reflections corresponding to the fluorite-type MO$_2$ phase were present, as expected. By increasing the temperature, from about 473 K, some distortions and shifts of the diffraction peaks were observed. These correspond to variations of the lattice cell parameter, which can be caused by several factors (thermal dilatation, O/M variation, annealing of defects). The most evident shifts and distortions were observed for Am/(Am+U)=0.10 and 0.15, similarly to those observed for UO$_2$ in Fig. 5.1-(a). This likely indicates the transition toward the fluorite-related M$_4$O$_9$ phase.

Going to higher temperatures, a second phase appeared. The additional diffraction peaks correspond to the hexagonal structure (s.g. $P\bar{6}2m$, N° 189) typical of α'-U$_3$O$_8$ (see section 2.2.1.2). It must be observed that, since the solubility of Am in U$_3$O$_8$ is unknown, one cannot trivially conclude on the distribution of americium between the two phases. Therefore, in the biphasic region, the Am/(Am+U) ratio of each phase is unknown and, for this reason, the phases are here generally indicated as "MO$_2$", "M$_4$O$_9$" and "M$_3$O$_8$", where M = Am, U.

Interestingly, the appearance of the M$_3$O$_8$ phase was shifted to higher temperatures by increasing the total amount of americium. Moreover, strong differences were observed for the MO$_2$/M$_3$O$_8$
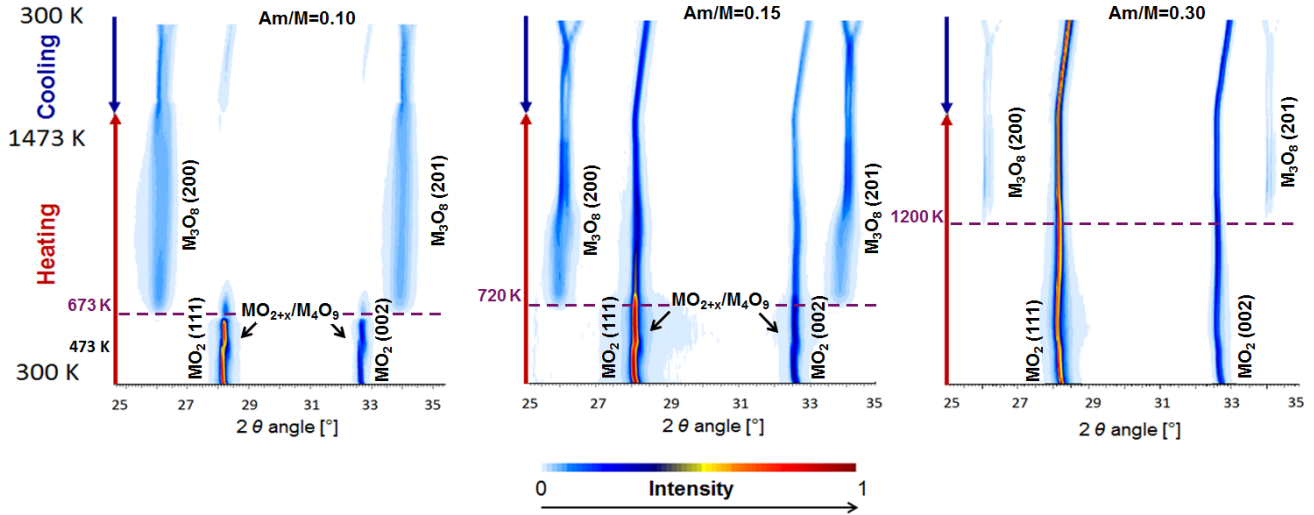
Fig. 5.2: Iso-intensity map of HT-XRD measurements in air on $(U,Am)O_2$ with (from left to right and from top to bottom) $Am/(Am+U)=0.10$, 0.15, 0.30.

relative intensities between the three samples. The behaviours of the three oxides will be singularly detailed in the following. The XRD patterns acquired during the thermal treatments under air were refined according to the Pawely method [200]. For the cubic phase, the $Fm\overline{3}m$ structure was always used. However, the adoption of the fluorite-related M_4O_9 superstructure (4x4x4 fluorite cells) would have given equivalent results for the fit of XRD patterns. The $Fm\overline{3}m$ structure was preferred in order to directly compare all the cubic lattice parameters.

5.2.1.1   Oxide with Am/(Am+U)=0.10

The $Am/(Am+U)=0.10$ sample, previously to the measurements under air, was thermally treated at 1273 K under $Ar/H_2(5\%)$ for 4 hours, in order to anneal the defects induced by the self-irradiation. The oxide was about 3 hours old when the first XRD pattern was recorded at room temperature. The corresponding lattice parameter, $a = 5.464(1)$Å, is consistent with a defect-free $U_{0.9}Am_{0.1}O_2$ oxide, with $O/M\sim 2.0$. Indeed, the value is between the lattice parameters of defect-free $U_{0.925}Am_{0.075}O_2$ and $U_{0.85}Am_{0.15}O_2$, reported by Lebreton [106], respectively equal to $a_0 = 5.466(1)$Å and $a_0 = 5.461(1)$Å (see section 2.2.4.3).

The lattice parameter variations of the cubic phase can be directly linked to its composition changes. Therefore, these are represented as a function of the temperature in Fig. 5.3-(a). A constant uncertainty of ± 15 K can be considered for the temperature (see Appx. B for more details) and it won't be reported in the figures. The data of both the heating (red) and the cooling (blue) are shown. On the right side of the figures, portions of the XRD patterns for selected temperatures are also reported.

The evolution of the lattice parameter highlights several sequences during the thermal treatment in air. A possible composition-temperature path is represented on the U-O phase diagram, in Fig. 5.5 (red path). The represented phase diagram domain is a modified version (unpublished) of the Gueneau [27] model presented in section 2.1.1, where the composition ranges of the U_4O_9
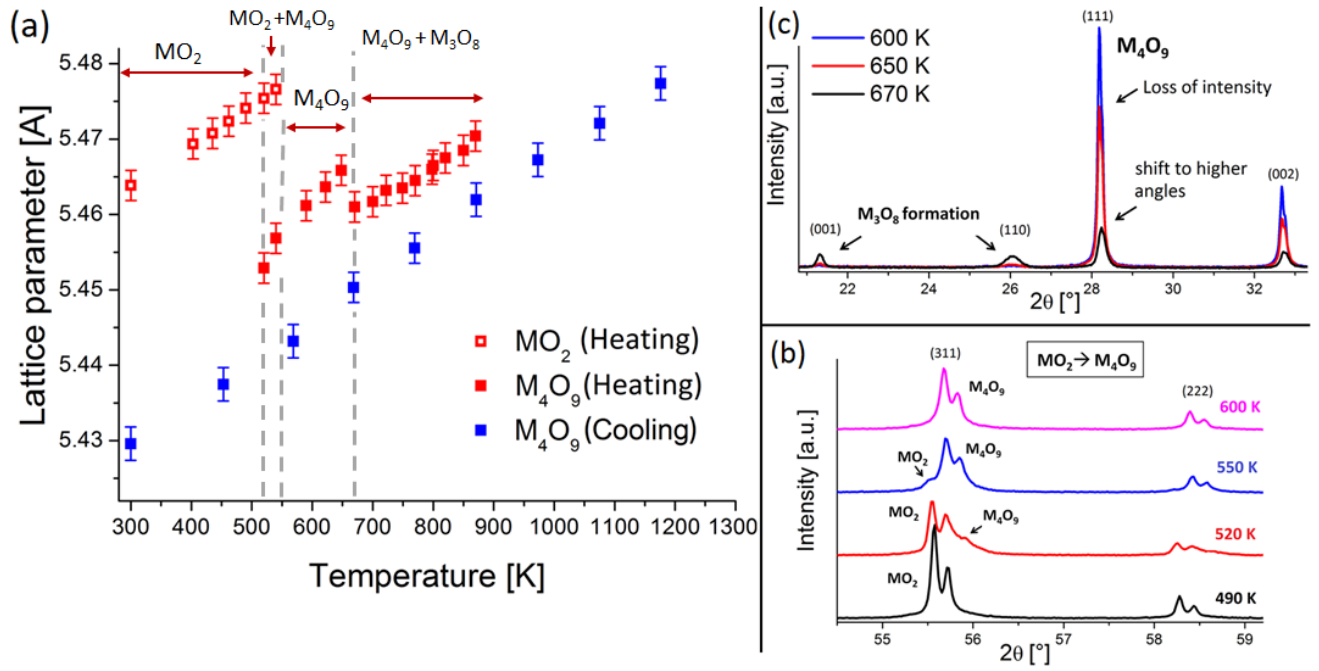
Fig. 5.3: Behaviour of the U$_{0.9}$Am$_{0.1}$O$_2$ sample in air:(a) evolution of the lattice parameter of the cubic structure as a function of the temperature; (b) extracts of the XRD patterns, for selected temperatures, showing the (311) and (222) reflections of the $Fm\bar{3}m$ structure; (c) extracts of the XRD patterns, for selected temperatures, showing the (111), (002) reflections of the $Fm\bar{3}m$ structure and the (001) (110) reflections of the $P\bar{6}2m$ structure.

and U$_3$O$_8$ are represented. It must be stressed that this is a simplified representation since it does not keep into account the effect of americium on the phase equilibria.

For the sample with Am/(Am+U)=0.10, the following evolution was observed:

- at the beginning of the heating, from 300 to 490 K, an approximately linear expansion of the lattice parameter occurred for the MO$_2$ phase, as shown in Fig. 5.3-(a).

- At T = 520 K, a second cubic structure appeared. This is shown in Fig. 5.3-(b), where portions of the XRD pattern are reported. A shoulder at higher angle was presented on the (311) reflection of the MO$_2$ phase (remark: the presence of a double peak for each reflection condition is due to the use of two wavelengths, Cu Kα_1 and Cu Kα_2). The lattice parameter of the second cubic phase was much smaller than the previous one (5.453 vs 5.475 Å at 520 K). The only phenomenon that can explain this difference is a considerable increase of the O/M ratio, since the self-irradiation defects were previously annealed. The second cubic structure can hence be associated to the M$_4$O$_9$ phase. The M$_4$O$_9$ rapidly became the most intense and, at 600 K, the MO$_2$ completely disappeared.

- Subsequently to its formation, a regular thermal dilatation of the M$_4$O$_9$ phase was observed in the $520 \leq$ T ≤ 648 K temperature range.

- At T = 670 K, another discontinuity of the lattice parameter was observed. This corresponded to the appearance of the M$_3$O$_8$ phase, as shown by the portions of XRD patterns

in Fig. 5.3-(c). However, if the loss of intensity of the cubic reflections is clearly explained by the M_3O_8 appearance, their shift to higher angles (XRD pattern at 670 K) and the corresponding decrease in the lattice parameter cannot be simply explained by the formation of the new structure. They indicate a composition change in the cubic phase, likely due to an enrichment in americium of the cubic phase. This implies that the Am/(Am+U) ratios were not equal in the two co-existing phases and that the solubility of americium in the M_3O_8 structure was lower than Am/M=10 mol.% at that temperature.

- Continuing the heating, another approximately regular expansion of the M_4O_9 lattice parameter was observed up to 870 K, meanwhile the intensity of the M_3O_8 reflection was increasing.

- Above 870 K, only the hexagonal phase was observable. This would imply a complete accommodation of americium in this structure, hence a solubility at least equal to Am/(Am+U) =0.10. However, one must be careful before concluding on the complete disappearance of a phase at high temperature. Indeed, the formation of M_3O_8, whose density is lower than MO_2 (ρ_{UO_2}= 10.95 g/cm³, $\rho_{U_3O_8} \simeq$ 8.3 g/cm³ [93]), leads to a swelling of the sample. This causes irregularities in the surface of the powder, hence the X-ray absorption could reduce the intensity of low angle peaks. The presence of a small amount of M_4O_9 is likely.

- The cubic phase was newly visible during the cooling, for T < 1172 K. In this case, the evolution of the lattice parameter was regular till room temperature. This indicates a mostly constant composition during the cooling. The final lattice parameter at room temperature was 5.430(3) Å. The value is considerably smaller than the initial one, confirming the increase of the O/M ratio.

- A phase transition was observed for the M_3O_8 phase during the cooling. As shown in Fig. 5.5, the stable U_3O_8 form at high temperature (T>570 K) is the hexagonal α' ($P\bar{6}2m$). For lower temperatures, the β (*Cmcm*) and α (*C2mm*) polymorphs, both orthorombic, appear. For the Am/(Am+U)=0.10 sample, a structural change from hexagonal to orthorombic was observed at about 570 K, as shown in Fig. 5.4. The XRD patterns can be differentiated through the doubling of the reflection at about 26°.

5.2.1.2   Oxide with Am/(Am+U)=0.15

For the Am/(Am+U)=0.15 composition, the initial lattice parameter at room temperature, equal to 5.476(1) Å, was considerably larger than that of the $U_{0.9}Am_{0.1}O_2$ sample (5.464(1) Å), because of the α self-irradiation. The value represents a swelling of 0.27% relatively to the defect-free lattice parameter, a_0 = 5.461(1)Å, according to Lebreton [106]. This was consistent with the age of the sample of about 220 days.

The evolution of the cubic lattice parameter is shown in Fig. 5.6. A possible composition-temperature path is represented in Fig. 5.5 by the blue path. The behaviour here described was observed during the thermal treatment:
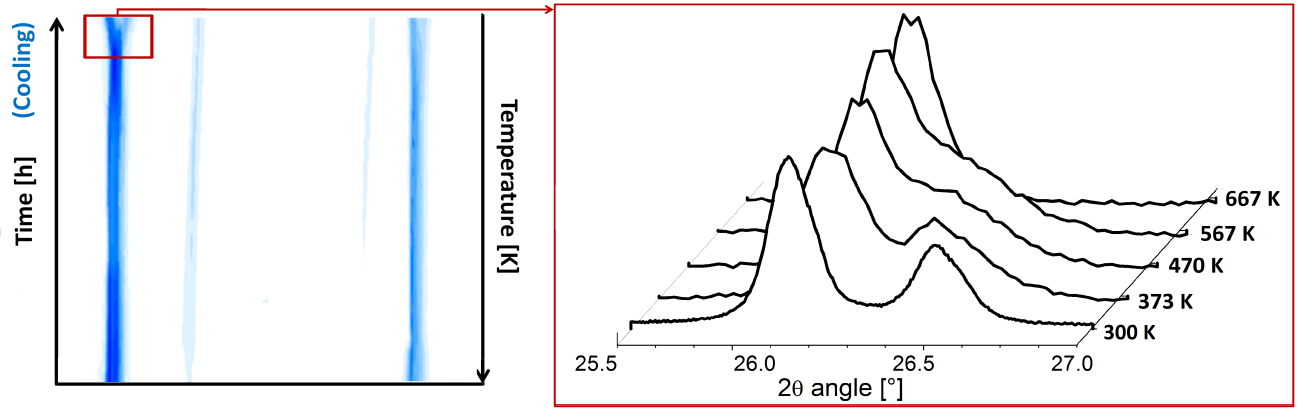
Fig. 5.4: Cooling in air of the Am/(Am+U)=0.10 composition: zoom on the 25.5<2θ<27° range of the XRD patterns. The doubling of the XRD peak indicates the transition from the hexagonal $P\bar{6}2m$ to the orthorombic $C2mm$ structure for M$_3$O$_8$.
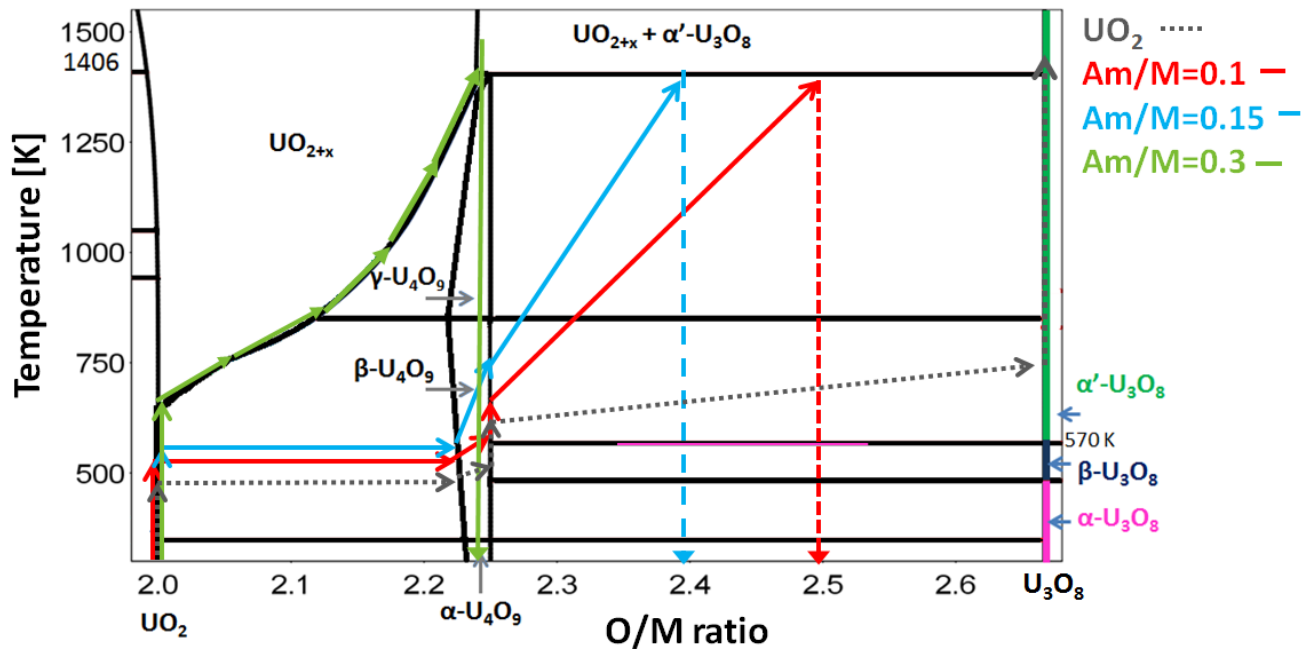
Fig. 5.5: Qualitative representation of the composition-T paths during the heating under air.

- from 300 to 535 K, an almost linear increase of the cubic lattice parameter occurred, as shown in Fig. 5.6-(a).

- A second cubic structure appeared at about 535 K, as shown in Fig. 5.6-(b). As for the Am/(Am+U)=0.10 composition, the lattice parameter of the second cubic phase was considerably smaller than the previous one: 5.472(2) versus 5.490(2) Å, at 535 K. In this case, contrarily to the previous one, the annealing of defects has contributed to the decrease of the lattice parameter. However, the determined contraction is of about 0.33% and hence it cannot be due only to the recovering from self-irradiation (previously determined at 0.27%). The difference can be explained only by an increase of the O/M ratio. As for the previous case, the brief co-existence of two FCC structures with different O/M ratios leads us to the identification of the second cubic structure with the M$_4$O$_9$ phase. This rapidly
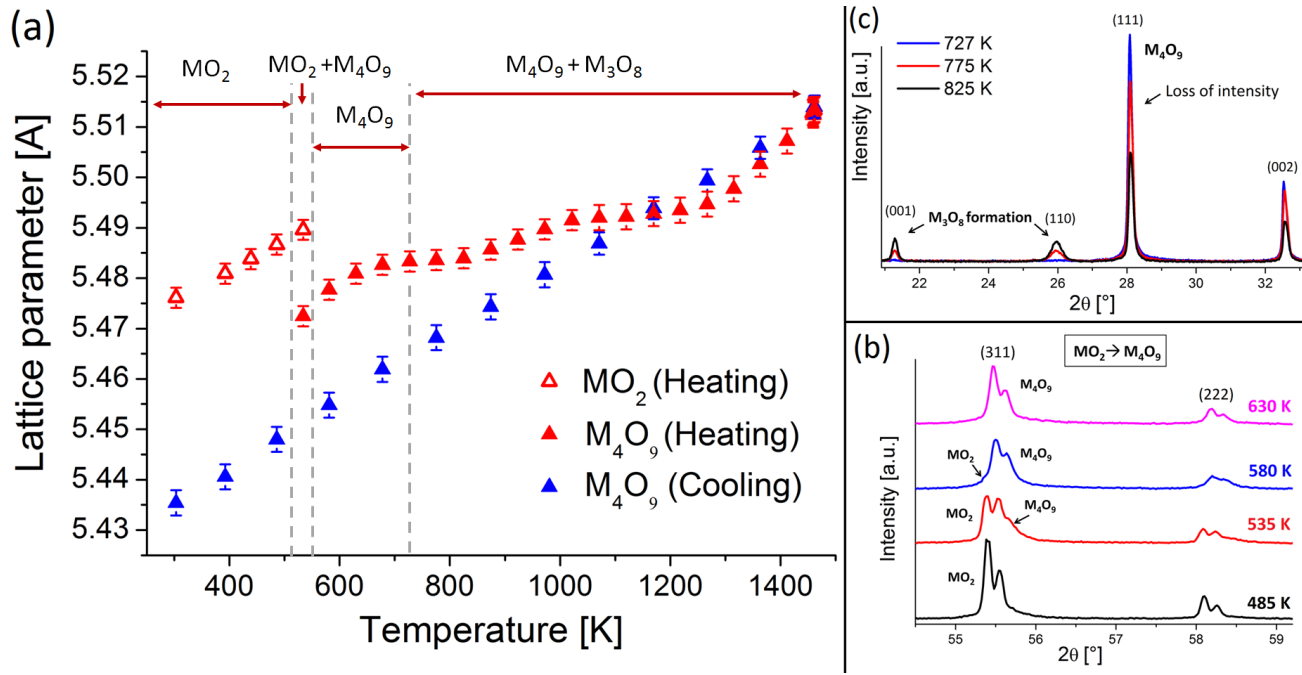
Fig. 5.6: Behaviour of the $U_{0.85}Am_{0.15}O_2$ sample in air:(a) evolution of the lattice parameter of the cubic structure as a function of the temperature; (b) extracts of the XRD patterns, for selected temperatures, showing the (311) and (222) reflections of the $Fm\bar{3}m$ structure; (c) extracts of the XRD patterns, for selected temperatures, showing the (111), (002) reflections of the $Fm\bar{3}m$ structure and the (001) (110) reflections of the $P\bar{6}2m$ structure.

became the most abundant phase and, at 630 K, the MO_2 was completely disappeared.

- An increase of the M_4O_9 lattice parameter was observed for $535 < T < 727$ K. However, this thermal expansion seems slowed down in comparison to the previous one observed for Am/(Am+U)=0.10. This likely indicates the crossing of the oxygen composition domain of the M_4O_9 phase, as shown in the scheme in Fig. 5.5.

- At T=727 K, the M_3O_8 phase appeared, as shown in Fig. 5.6-(c). A corresponding slope break was observed in the evolution of the M_4O_9 lattice parameter (Fig. 5.6-(a)). This indicates a change in its composition; hence, a redistribution of the U and Am species between the two phases can be supposed. This continued up to about 1267 K. Above this temperature, the increase of the M_4O_9 lattice parameter returned linear.

- Contrary to Am/(Am+U)=0.10 composition, the M_4O_9 was clearly visible in the XRD patterns during the entire thermal treatment. At the highest temperature (1470 K), the lattice parameter was constant at 5.513(3) Å during the 4 hours plateau and no evident evolution of the XRD pattern was observed. This indicates that the oxide was likely in thermodynamic equilibrium.

- A regular linear decrease of the M_4O_9 lattice parameter was observed during the cooling, indicating a mostly constant composition for the entire temperature range. The final lattice parameter at room temperature was 5.434(2) Å. The value is considerably smaller than the initial one and also of the defect-free lattice parameter of a $U_{0.85}Am_{0.15}O_2$ oxide

(5.464(1) Å). This confirms the increase of the O/M ratio and, possibly, the enrichment in americium of the cubic phase.

- As for the Am/(Am+U)=0.10 sample, the transition of the M_3O_8 phase from the hexagonal toward the orthorhombic form was observed during the cooling, at about 580 K, as shown in Fig. 5.7.
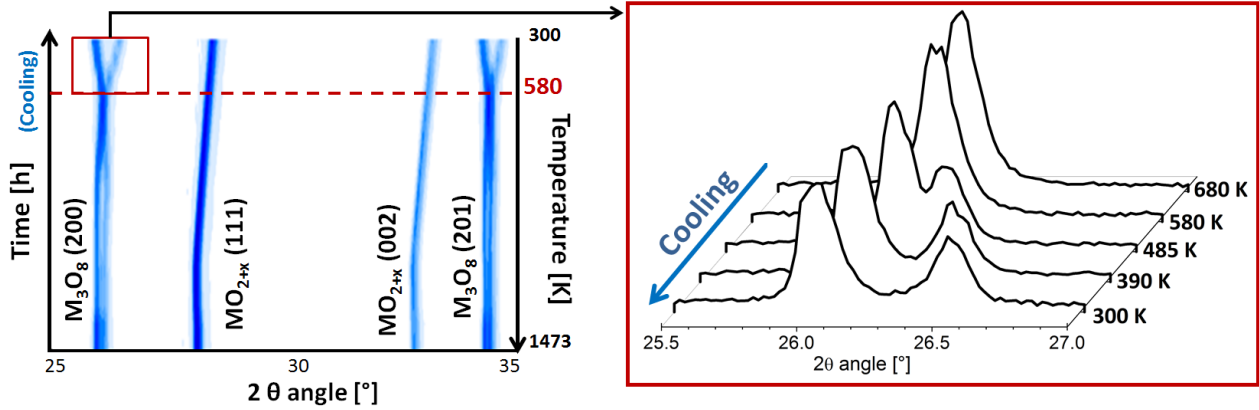
Fig. 5.7: Cooling in air of the Am/(Am+U)=0.15 composition: isointensity map and zoom on the 25.5<2θ<27° range of the XRD patterns. The doubling of the XRD peak indicates the transition from the hexagonal $P\bar{6}2m$ to the orthorombic $C2mm$ structure for M_3O_8.

5.2.1.3   Oxide with Am/(Am+U)=0.30

For the **Am/(Am+U)=0.3** composition, the initial lattice parameter at room temperature was equal to 5.468(1) Å. The value corresponds to a swelling of 0.275% relatively to the defect-free lattice parameter, $a_0 = 5.453(1)$Å, according to Lebreton [106] (section 2.2.4.3). The lattice parameter was consistent with the age of the sample of about 210 days.

The evolution of the cubic lattice parameter as a function of the temperature is shown in Fig. 5.8. A schematic composition-temperature path is represented by the green line in Fig. 5.5.

The following behaviour was observed during the thermal treatment:

- For T≤650 K, an almost linear increase of the lattice parameter with the temperature. In this range, a slight break of the slope is observed at about 464 K, likely due to the annealing of the self-irradiation defects.

- For 650≲ T ≲1000 K, the thermal expansion of the cubic phase was remarkably slowed down and almost constant lattice parameter values were observed. This indicates a continuous increase of the O/M ratio and hence this cubic structure is identified with the MO_{2+x} phase.

- At the end of the MO_{2+x} oxidation, at about 995 K, the first reflections of the M_3O_8 structure were observed, with very low intensity, as shown in Fig. 5.8-(b).
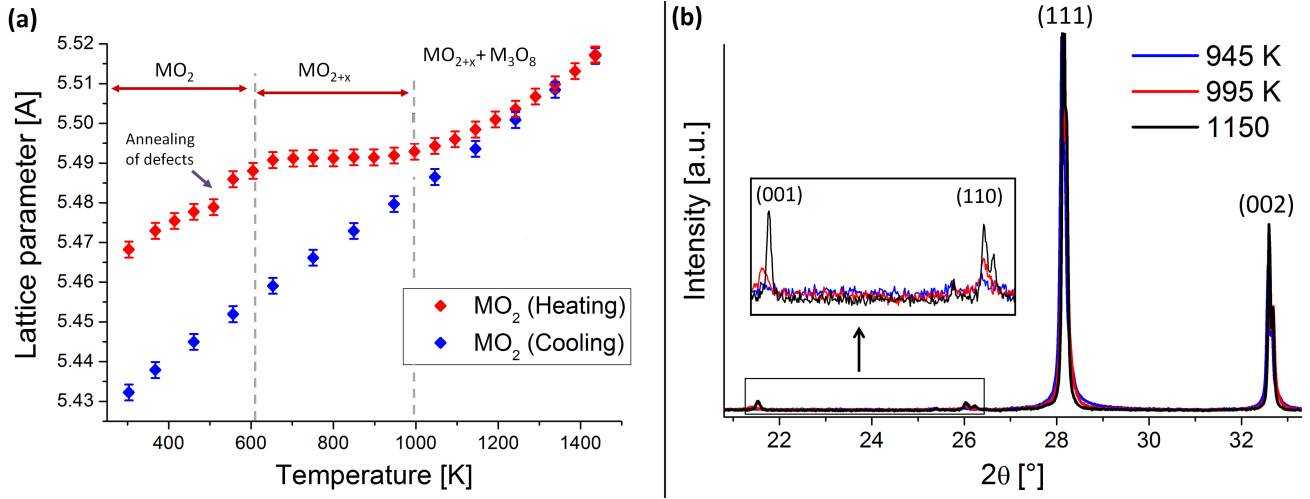
Fig. 5.8: Behaviour of the $U_{0.7}Am_{0.3}O_2$ sample in air:(a) evolution of the lattice parameter of the cubic structure as a function of the temperature; (b) extracts of the XRD patterns, for selected temperatures (heating), showing the (111), (002) reflections of the $Fm\overline{3}m$ structure and the (001) (110) reflections of the $P\overline{6}2m$ structure.

- Above 995 K, a linear increase of the MO_{2+x} lattice parameter with the temperature was observed up to 1473 K. At this temperature, the lattice parameter was constant at 5.517(2) Å during the 4 hours plateau and no evolution of the XRD pattern was observed, indicating that the thermodynamic equilibrium was likely achieved.

- A regular linear decrease of the MO_{2+x} lattice parameter was observed during the entire cooling, indicating a mostly constant composition.

- The transition of the M_3O_8 phase from the hexagonal toward the orthorhombic form was observed during the cooling, for $480 < T < 556$ K, as shown in Fig. 5.9.
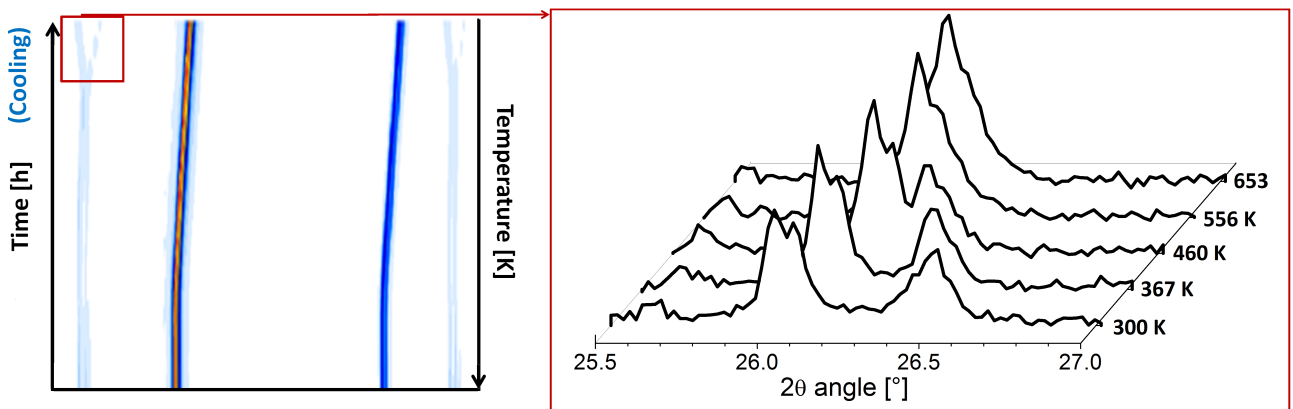
Fig. 5.9: Cooling in air of the Am/(Am+U)=0.30 composition: zoom on the $25.5 < 2\theta < 27°$ range of the XRD patterns. The doubling of the XRD peak indicates the transition from the hexagonal $P\overline{6}2m$ to the orthorombic $C2mm$ structure for M_3O_8.

5.2.1.4 Final room-temperature state

At the end of the thermal treatment in air, the samples with overall Am/(Am+U)=0.10, 0.15, 0.30 were re-ground and then re-prepared for a XRD acquisition, in order to eliminate the errors coming from the swelling of the sample, due to the M$_3$O$_8$ formation. The XRD patterns, shown in Fig. 5.10, were refined according to the Rietveld method [201]. The orthorhombic *C2mm* structure was adopted for the room temperature M$_3$O$_8$ phase. The results are reported in Tab. 5.1.
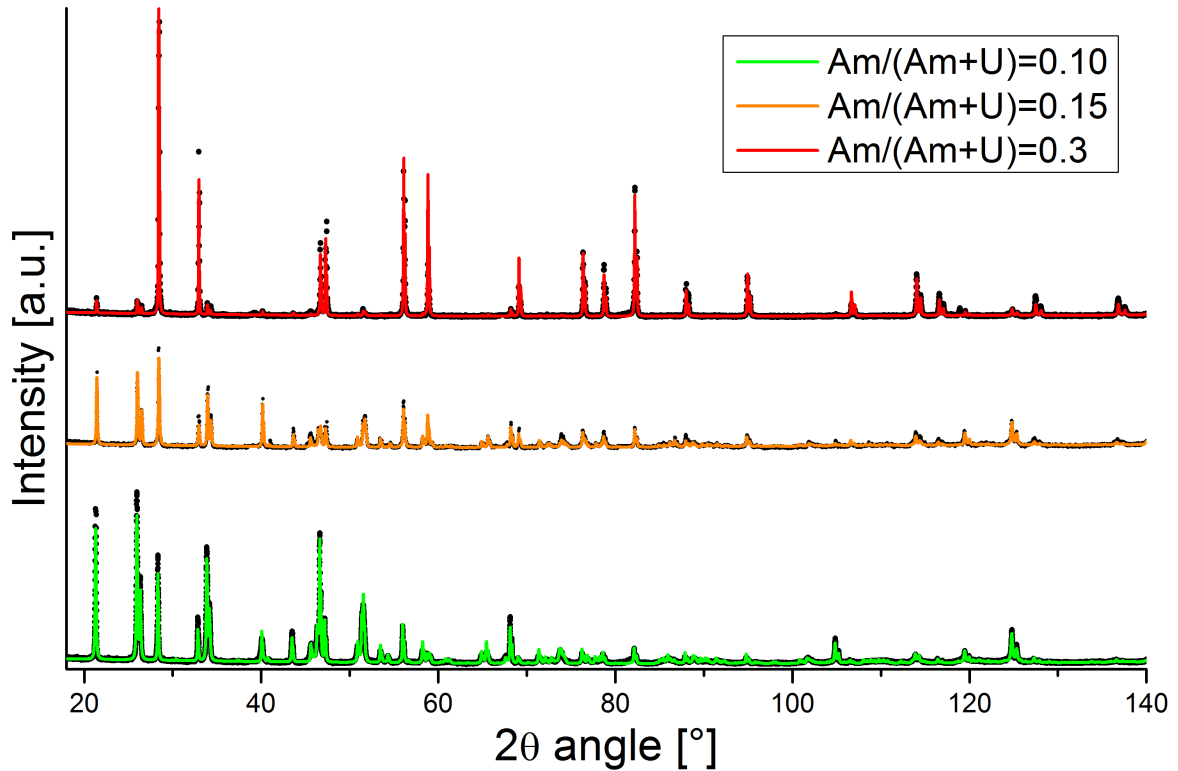
Fig. 5.10: XRD data (black points) acquired at RT and Rietveld fits (colored curves), for the samples with overall Am/(Am+U) = 0.10, 0.15 and 0.30.

Am/(Am+U)	MO$_{2+x}$/M$_4$O$_9$ ($Fm\bar{3}m$)		M$_3$O$_8$ (C2mm)				R$_{wp}$
(mol.%)	wt.%	a (Å)	wt.%	a (Å)	b (Å)	c (Å)	(%)
10	21(5)	5.430(3)	79(5)	6.733(3)	11.938(3)	4.147(3)	9.5
15	43(5)	5.434(2)	57(5)	6.725(3)	11.938(3)	4.145(3)	7.6
30	95(5)	5.432(2)	5(4)	6.726(3)	11.931(3)	4.146(3)	5.3

Table 5.1: Results of the Rietveld refinements at room temperature.

The amount of M$_3$O$_8$ considerably decreases with the overall americium content of the sample, passing from 78(5) wt.% for Am/(Am+U)=0.10, to 47(5) wt.% for Am/(Am+U)=0.15 and only 5(4) wt.% for Am/(Am+U)=0.30. The lattice parameters found for this structure are compared to those of α-U$_3$O$_8$ (see section 2.2) in Fig. 5.11, where the ratios a/a(U$_3$O$_8$), b/b(U$_3$O$_8$), c/c(U$_3$O$_8$) are represented.
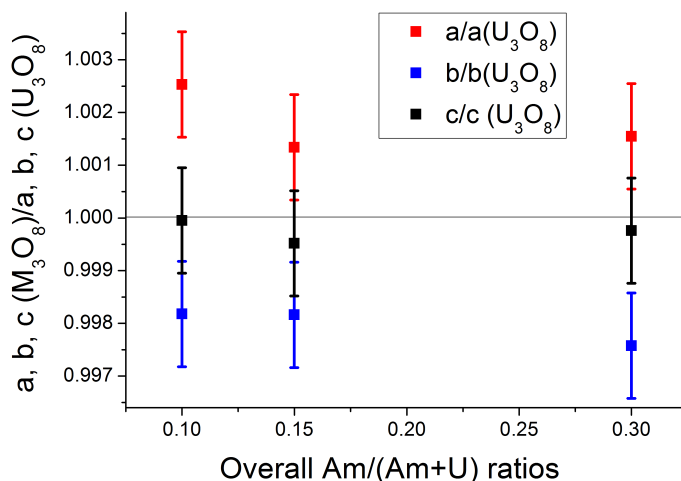
Fig. 5.11: Ratios between the a, b, c lattice parameters of M_3O_8 (this work) and those of α-U_3O_8, for the three samples with overall Am/(Am+U) ratios=0.10, 0.15 and 0.30.

For the three samples, the obtained c lattice parameter is equal to that of U_3O_8 (c=4.147 Å), in the limit of the uncertainty. On the contrary, small but significant differences were found for the a and b parameters, respectively longer and shorter than those of U_3O_8 (a= 6.716 and b= 11.96 Å). On the basis of these systematic variations, the incorporation of slight quantities of americium in the *C2mm* structure can be supposed. Moreover, the a, b, c lattice parameters have very close values for the three samples, within the experimental uncertainty. Under the hypothesis of a oxygen stoichiometric phase (O/M=2.667, as in U_3O_8), this indicates that the M_3O_8 phases of the three samples had a very close Am/(Am+U) ratio. These results at room temperature indicate a maximum solubility of americium in the M_3O_8 structure of about 10 mol.%.

5.2.1.5   Comparison and discussion

Interesting conclusions can be drawn by comparing the behaviours of the three (U, Am)O_2 oxides to the U-O phase equilibria, as in the schematic representation of Fig. 5.5. In this figure, also the evolution of the UO_2 sample, described in section 5.1, is reported.

It can be observed that the UO_2 phase is stoichiometric at room temperature and the hyperstoichiometric domain (O/M>2) exists only for T>600 K. As already discussed in chapter 3, the AmO_2 is the oxide with the highest O/M ratio in the Am-O system. Therefore, the extension of the hyperstoichiometric UO_2 domain to lower temperature with the adding of americium can be excluded. For the three mixed oxides, the MO_2 lattice parameter increased linearly at the beginning of the heating in air, confirming that no O/M increase is possible at low temperature. Subsequently, for Am/(Am+U)=0.10 and 0.15, a rapid oxidation occurred for T $\simeq$ 520 K, with the formation of the M_4O_9 phase, similarly to the UO_2 evolution. On the contrary, the oxidation of the Am/(Am+U)=0.30 started for T$\geq$ 600 K, in a slow way, consistently with the onset of a MO_{2+x} hyperstoichiometric domain.

For Am/(Am+U)=0.10 and 0.15, the oxidation proceeded with the entering of the $M_4O_9+M_3O_8$

biphasic domain, as for UO$_2$. However, the oxidation was slowed down and limited by the addition of americium. In fact, the oxidation transitions were shifted toward higher temperatures and the final O/M ratio was lower and lower with the increasing of the overall Am/(Am+U) ratio.

For Am/(Am+U)=0.30, the oxidation proceeded with the MO$_{2+x}$+M$_3$O$_8$ equilibrium. Remark that this equilibrium could not be correctly represented in the path traced on the U-O phase diagram, in Fig. 5.5. Indeed, in the binary U-O system, the UO$_{2+x}$+U$_3$O$_8$ biphasic domain exists for T>1400 K, whereas for lower temperature the U$_3$O$_8$ appearance must occurs through the U$_4$O$_9$ formation. On the contrary, for the Am/(Am+U)=0.30 composition, the MO$_{2+x}$+M$_3$O$_8$ coexistence started at about 1000 K. This indicates that, for Am/(Am+U)$\simeq$0.3, the MO$_{2+x}$/M$_3$O$_8$ domain is extended at lower temperature, at the expense of the M$_4$O$_9$/M$_3$O$_8$ domain. The extent of the oxidation was however very limited for this composition, with only 5 wt.% of M$_3$O$_8$, confirming the improved resistance toward the oxidation with the increasing americium content.

Finally, it must be remarked that the transformation temperatures observed during the heating are interesting kinetic oxidation data, but they cannot be strictly associated to the phase diagram transition temperatures. The achievement of the thermodynamic equilibrium cannot be assured during the heating. On the contrary, for the three samples analysed, no evolution was observed during the 4-hours isothermal measurement at 1470 K and, hence, it can be concluded that the oxides were at their thermodynamic equilibrium. Moreover, as previously discussed, the lattice parameter evolution during the cooling indicated that the composition was mostly constant. Therefore, the final composition observed at room temperature is here considered representative of the 1470 K equilibrium state. The phase distribution has already been determined by Rietveld refinement of the XRD patterns; further data will be derived by the XAS analysis in section 5.3.

5.2.2 Domain with Am/(Am+)$\geq$0.5

The iso-intensity maps corresponding to the thermal treatment in air of the U$_{0.5}$Am$_{0.5}$O$_{2\pm x}$ and U$_{0.3}$Am$_{0.7}$O$_{2\pm x}$ oxides are reported in Fig. 5.12. These show the presence of one single FCC phase for the entire temperature range.

The XRD patterns were refined according to the Pawely method [200], using the $Fm\overline{3}m$ structure. The resulting lattice parameters of the U$_{0.5}$Am$_{0.5}$O$_{2\pm x}$ and U$_{0.3}$Am$_{0.7}$O$_{2\pm x}$ oxides, for both heating and cooling, are reported in Fig. 5.13.

The initial lattice parameters at room temperature were:

- $a = 5.466(1)$ Å for Am/(Am+U)=0.5. At the time of the measurement, 194 days were passed since the sintering of the sample. This period is longer than that necessary, for this composition, to reach the saturation of the self-irradiation swelling, corresponding to $a = 5.467(1)$ Å (see section 2.2.4.3), consistently with the measured value.

- $a = 5.450(1)$ Å for Am/(Am+U)=0.7. The sample was 190 days old at the time of the measurements and, as in the previous case, the swelling should have reached the saturation.
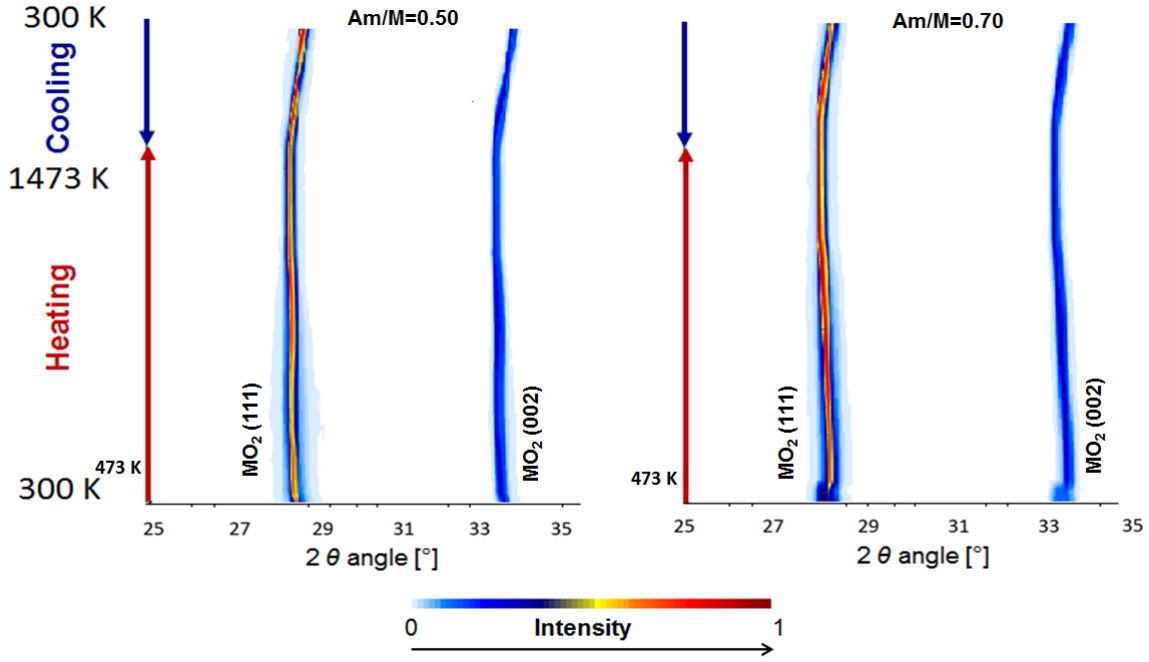
Fig. 5.12: Isointensity maps of HT-XRD measurements in air on $(U,Am)O_2$ with $Am/(Am+U)=0.5$ and 0.7.

The expected value was, according to Lebreton [106], $a = 5.454(1)$ Å. The difference compared to the observed value is very small and it is likely due to slight differences in the $Am/(U+Am)$ and O/M ratios between the sample of Lebreton and that of this work.

Some differences can be remarked between the two compositions at the beginning of the heating. For the sample with $Am/(Am+U)=0.5$, the lattice parameter increased with the temperature, but not in a regular way. More specifically, two changes in the slope are observed: the first for $413 \lesssim T \lesssim 508$ K, the second for $750 \lesssim T \lesssim 950$ K. This evolution can be due to both annealing of defects and increase of the O/M ratio. Above 950 K, a linear increase of the lattice parameter was observed. For the sample with $Am/(Am+U)=0.7$, a decrease of the lattice parameter was surprisingly observed at the beginning of the heating, likely due to the annealing of defects. Subsequently, a mostly linear increase of the lattice parameter was observed during the entire heating.

For both the compositions, the lattices parameters were stable during the 4 hours plateau at 1473 K, at $5.521(2)$ and $5.506(2)$ Å, respectively for $Am/(Am+U)=0.5$ and 0.7.

During the cooling, a regular linear decrease of the lattice parameter was observed for both the samples. Interestingly, for $Am/M=0.5$, the lattice parameters obtained during the cooling overlapped those of the heating in the $1000 \lesssim T \lesssim 1473$ K temperature range. This indicates that the most significant variations of the composition occurred, during the heating, below 1000 K. From the subsequent lattice parameter evolution, one can suppose that the O/M ratio was constant for the rest of the thermal treatment. Similar conclusions can be drawn for $Am/(Am+U)=0.7$, with an overlapping of the heating/cooling lattice parameters for $T \gtrsim 700$ K, indicating that the O/M variations, if any, occurred at even lower temperature for this sample.

The lattice parameters observed at room temperature after the thermal treatment in air were:
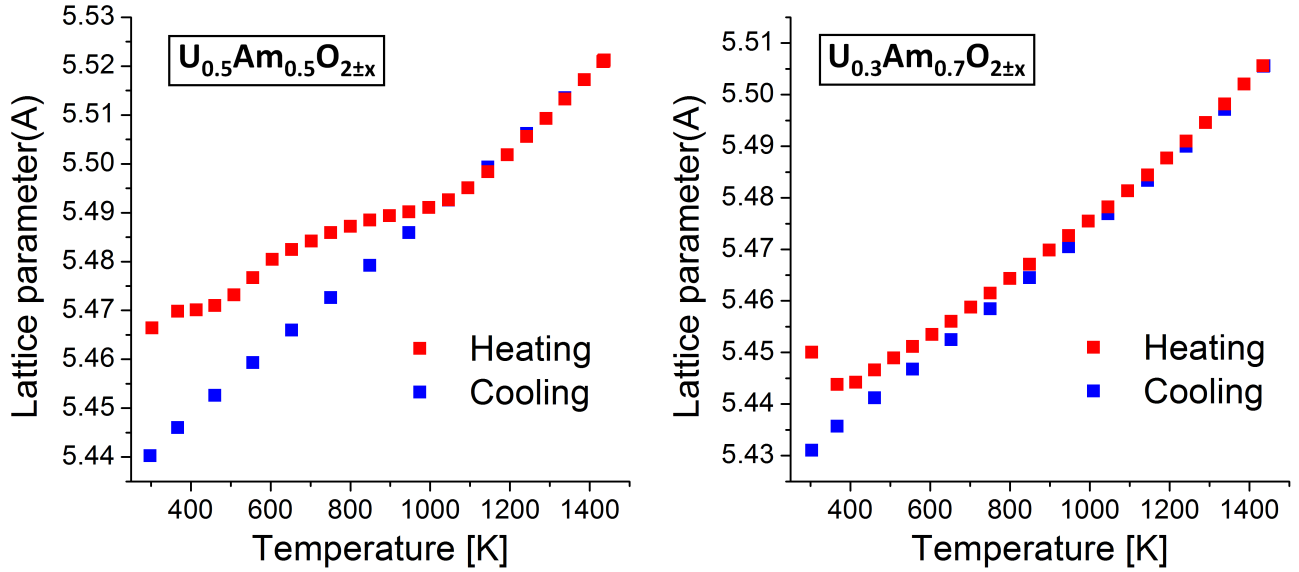
Fig. 5.13: Lattice parameter variation as a function of temperature for U$_{0.5}$Am$_{0.5}$O$_2$ and U$_{0.3}$Am$_{0.7}$O$_2$ oxider in air. (The lattice parameter uncertainty coincides with the symbol size).

- $a = 5.440(1)$ Å for Am/(Am+U)=0.5. This value is considerably smaller than the defect-free lattice parameter estimated by Lebreton for a U$_{0.5}$Am$_{0.5}$O$_{2-x}$ oxide, with measured O/M$\sim$1.93 [106]. This confirms that the O/M ratio of the sample increased with the annealing in air, as expected.

- $a = 5.431(1)$ Å for Am/(Am+U)=0.7. The defect-free lattice parameter proposed by Lebreton is 5.423(1)Å, which is lower than the value here obtained. This is surprising since the difference would indicate that the sample investigated by Lebreton would have been more oxidized (without have been heated in air). However, the O/M of the oxide investigated by Lebreton was unknown. It is also important to remember that the Am/(Am+U) ratio of the oxide here investigated was equal to 0.67 (see section 4.1.2.1), hence lower than the nominal composition and the sample investigated by Lebreton.

5.2.3 Conclusions

The HT-XRD investigation here presented highlighted a complex behaviour of the (U,Am)O$_{2\pm x}$ solid solution in air. The transformations observed in this study and their temperatures, for the five analysed samples, are summarized in Tab. 5.2.

Three major transformations were highlighted during the heating in air:

1. the MO$_2 \rightarrow$M$_4$O$_9$ transition;

2. the slow, continuous oxidation of the MO$_{2+x}$ solid solution;

3. the formation of the M$_3$O$_8$ phase.

Overall	Transformation temperatures [K]			
Am/M	$MO_2 \rightarrow MO_{2+x}$	$MO_{2+x} \rightarrow M_4O_9$	α'-M_3O_8 formation	α'-$M_3O_8 \rightarrow \alpha$-$M_3O_8$
0.10	-	520(20)	650(50)	567(50)
0.15	-	535(20)	775(20)	530(50)
0.30	500-950	-	995(25)	460(50)
0.50	600-900	-	-	-
0.70	-	-	-	-

Table 5.2: Observed phase transitions and corresponding temperatures in air.

The transition toward the M_4O_9 phase occurred for the Am/M=0.10 and 0.15 compositions, at ∼520 and ∼535 K, respectively. This transition was identified by its rapidity (∼ 30 minutes) and the simultaneous presence of two FCC structures (MO_{2+x} and M_4O_9).

Slow oxidations, spread across wide temperature ranges (500-950 and 600-900 K), were instead observed for the Am/M=0.30 and 0.50 compositions. These features indicated a more restrained increase of the O/M ratio for the MO_{2+x} phase. For the Am/(Am+U)=0.70 sample, the evolution of the lattice parameter did not indicate a clear oxidation. In order to clarify these aspects and quantify the final O/M ratios of the oxidized samples, a XAS investigation will be presented in the next section. As already mentioned, the final room temperature composition is considered to be representative of the high temperature state at 1470 K, since no important composition changes occurred during the cooling. Indeed, the lattice parameters of the cubic phases (both MO_{2+x} and M_4O_9) decreased with a regular, linear evolution, for all the samples. They could hence be fitted as a linear function of the temperature:

$$a(T) = a_{RT} + b \cdot (T - 298.15). \tag{5.1}$$

The parameters of Eq. (5.1), for each sample, are reported in Tab. 5.3.

Overall Am/(Am+U)	a_{RT} [Å]	b $\cdot 10^{-5}$ [Å $\cdot K^{-1}$]
0.10	5.430(3)	5.6(8)
0.15	5.434(2)	5.9(8)
0.30	5.432(2)	7.3(5)
0.50	5.440(1)	6.9(4)
0.70	5.431(1)	6.5(4)

Table 5.3: Parameters of Eq. (5.1) for the lattice parameter expansion in air.

The M_3O_8 phase was observed only for the samples with Am/M≤0.30, whereas the Am/M=0.5 and 0.7 compositions remained single-phase cubic. The temperature of the M_3O_8 appearance increased with the americium content, from 650(20) K for Am/M=0.10, up to 995(25) K for Am/M=0.3. The total amount of this phase at room temperature decreased with the overall americium content of the sample, from 79(5) wt.% for Am/M=0.10 to only 5(4) wt.% for Am/M=0.30. These results clearly indicate that the americium increases the resistance toward the oxidation.

Two M_3O_8 polymorphs (identified by the analogies with U_3O_8) were observed: the hexagonal $P\bar{6}2m$ α' phase appeared during the heating and subsequently, during the cooling, it transformed into the α orthorhombic *C2mm* structure. This transition occurred at about 570 K, for the three biphasic samples (Am/M=0.1, 0.15, 0.3). The lattice parameters of the *C2mm* structure, at room temperature, were close for the three compositions and with systematic differences in comparison to the α-U_3O_8. This suggests an incorporation of americium in this structure, similar for the three samples, and hence estimated at Am/(Am+U)$\leq$0.10. This confirms the previous results of Caisso *et al.* [193], who obtained a monophasic $(U_{0.9}Am_{0.1})_3O_8$ oxide through a wet chemical route based on the use of ion-exchange resin microspheres. However, in that study, the authors observed the hexagonal $P\bar{6}2m$ structure at room temperature and they suggested a stabilization of this form through the incorporation of americium. In this work, as already discussed, no effect on the cubic phases (M_4O_9 and MO_{2+x}) was observed during the α'-$M_3O_8 \rightarrow \alpha$-$M_3O_8$ transition. Therefore, the composition of M_3O_8 was necessarily constant during the structural change. It can be concluded that the solubility of americium is equal for both the hexagonal and orthorhombic M_3O_8 polymorphs. Therefore, the results of this work contrast with the stabilization of the hexagonal structure, proposed by Caisso *et al.* No details on the cooling rate used during the manufacture process were provided by these authors [193], but it is possible that the hexagonal structure was maintained because of a fast cooling.

5.3 Room-T XAS study on oxidized samples

In chapter 4, the as-manufactured $(U,Am)O_{2-x}$ oxides were investigated by XAS. This technique has proven to be very useful. XANES allowed determining the cationic oxidation states and hence obtaining the O/M ratios. EXAFS provided insights on the local structure around americium and uranium. Here, the XAS technique is used to investigate the $(U,Am)O_{2+x}$ samples oxidized during the thermal treatment in air, previously detailed. The XAS study was performed at the ROBL beamline of the ESRF, 4 months after the HT-XRD measurements. During that period, the samples were in glove boxes under an inert N_2 atmosphere. The XAS spectra were collected at 15 K and room temperature, in the conditions detailed in Appx. B.

5.3.1 Cationic charges and O/M ratios by XANES

5.3.1.1 Results

The XANES spectra collected at the L_3 edge of Am and U and their corresponding second-derivatives are shown respectively in Fig. 5.14 and Fig. 5.15. The spectra are compared to the reference compounds and to the as-manufactured samples, which were presented in chapter 4. For simplicity, the nomenclature "AmY" and "AmYox", with *Y* equal to the (nominal) overall Am/(Am+U) ratio, is here adopted, respectively for the as-manufactured oxides and the samples treated in air. For *Am70ox*, a problem occurred during the recovery of the powder from the HT-XRD set-up or the preparation for the synchrotron. A high quantity of Pu was found by
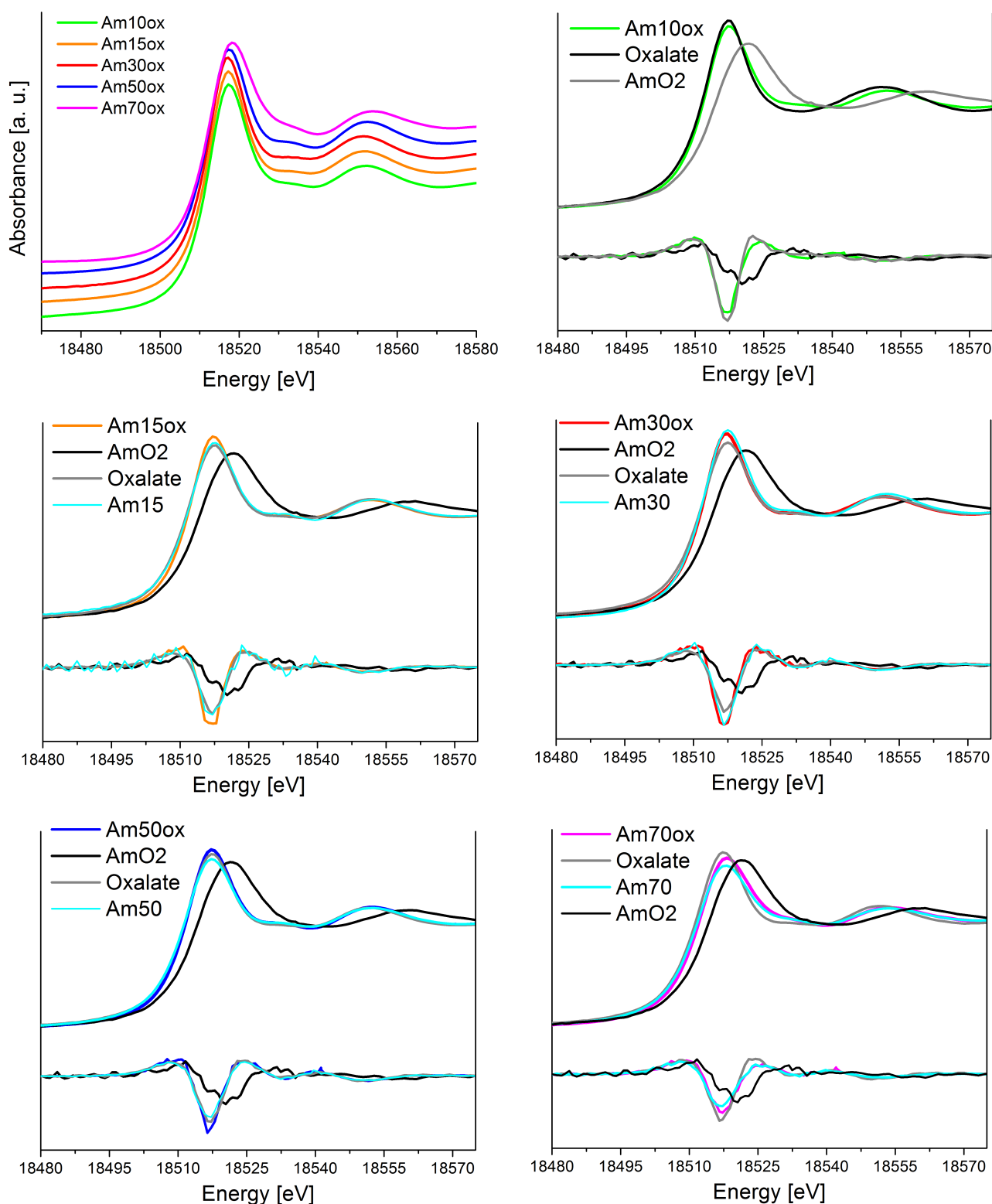
Fig. 5.14: XANES spectra collected at the L_3 edge of Am and their second derivatives for the $(U,Am)O_2$ samples before and after oxidation in air.

XAS in the sample, probably from a contamination with a $(U,Pu)O_2$ oxide (stored in the same glove boxes). As a consequence, the spectra collected at the U edges cannot be considered representative of the oxidized $U_{0.3}Am_{0.7}O_{2\pm x}$ sample and they are not presented. The Am-L_3 edge was reported, in the hypothesis that the MOX contamination did not affect the americium
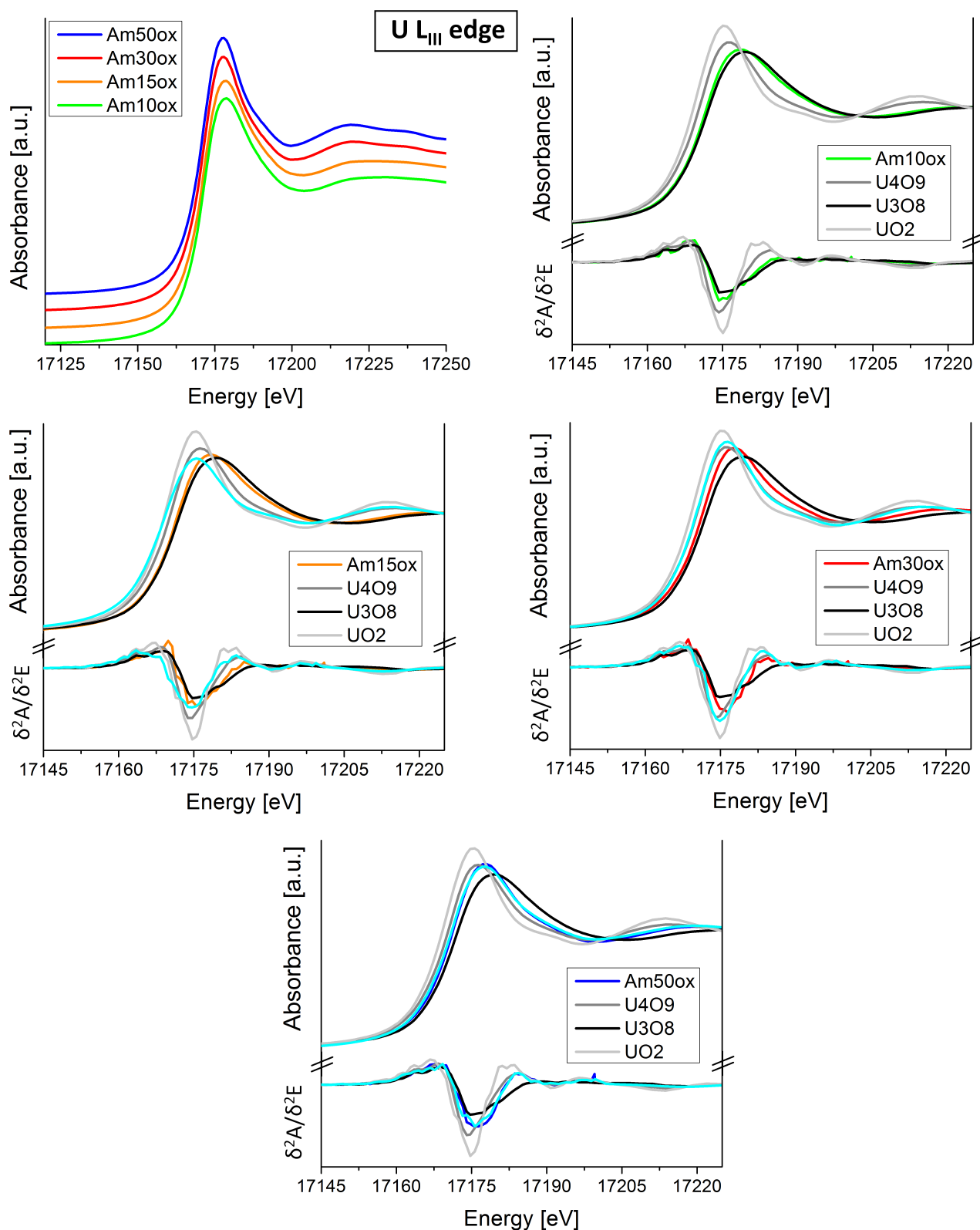
Fig. 5.15: XANES spectra collected at the L$_3$ edge of U and their second derivatives for the (U,Am)O$_2$ samples before and after oxidation in air.

chemical state in the (U,Am)O$_2$ dioxide. The observed energies of the inflection points and the white lines are compared in Tab. 5.4.

Sample	Am L_3 edge [eV]		U L_3 edge [eV]	
	Inflection point	White line	Inflection point	White line
Am10ox	18512.9	18517.4	17171.7	17178.7
Am15	18512.8	18517.3	17169.0	17175.4
Am15ox	18512.5	18517.4	17171.3	17178.4
Am30	18512.7	18517.4	17171.6	17176.4
Am30ox	18512.8	18517.1	17171.7	17177.8
Am50	18512.5	18517.4	17171.6	17177.7
Am50ox	18512.5	18517.4	17171.3	17177.9
Am70	18513.0	18518.0	17171.2	17177.9
Am70ox	18513.1	18518.3	-	-
Oxalate [Am^{3+}]	18513.0	18517.3	-	-
AmO_2	18514.5	18521.5	-	-
UO_2	-	-	17170.2	17175.4
U_4O_9	-	-	17170.9	17176.3
U_3O_8	-	-	17171.9	17179.6

Table 5.4: Energy positions of the inflection points and white lines of the XANES spectra presented in Fig. 5.14 and Fig. 5.15. Values are given with a 0.2 eV uncertainty.

For the Am L_3 edge, the inflection points and the white line positions of all the oxidized samples are identical, within the experimental uncertainty, to the as-manufactured oxides. As discussed in chapter 4, the energies are very close to the Am^{3+}-oxalate reference, indicating the trivalent state of americium. For the sample with Am/(Am+U)=0.7, a slight shift toward higher energies was observed, due to the mixed Am^{3+}/Am^{4+} oxidation state, as discussed in chapter 4. The corresponding oxidized sample presents a very similar white line, only slightly shifted toward higher energies, likely indicating a small increase of the Am^{4+} fraction.

The spectra collected at the U-L_3 edge show remarkable differences between the as-sintered and oxidized samples, being generally shifted toward higher energies. For the *Am10ox*, *Am15ox*, *Am30ox* samples, the white line positions are comprised between those of the U_4O_9 and the U_3O_8 references, indicating a high average oxidation state of uranium. This is consistent with the presence of the cubic and the M_3O_8 phases in these samples, revealed by the XRD results. For the Am/(Am+U)=0.5 composition, the white line position is found at slightly higher energies than the U_4O_9 reference, similarly to the as-sintered oxide.
A quantitative determination of the U and Am oxidation states is performed in the following.

5.3.1.2 Determination of the O/M ratios

The U-L_3 and Am-L_3 XANES spectra were fitted by linear combination of the reference compound spectra, according to the same procedure applied for the as-sintered oxides in chapter 4. The results of the fits are provided in Tab. 5.5. A generally good agreement between the data and the fit was achieved, as indicated by the low R-factor of the fits.

Sample	Am L$_3$ edge				U L$_3$ edge					Overall
	Am^{3+}	AmO$_2$	R-factor	AOS	UO$_2$	U$_4$O$_9$	U$_3$O$_8$	R-factor	AOS	O/M
Am10ox	1	0	0.001	3	0	0.20	0.80	0.001	5.17	2.48(2)
Am15ox	1	0	0.001	3	0	0.25	0.75	0.001	5.13	2.40(2)
Am30ox	1	0	0.002	3	0	0.46	0.54	0.002	4.95	2.20(2)
Am50ox	1	0	0.002	3	0	0.54	0.46	0.002	4.88	1.99(2)
Am70ox	0.68	0.32	0.002	3.32	-	-	-	-	4.89	$\geq$ 1.91

Table 5.5: Results of the linear combination fit of the U-L$_3$ and Am-L$_3$ XANES spectra using the reference compounds: fraction of the combinations, R-factor of the fit, average oxidation state (AOS) and O/M ratio computed from the oxidation states.

For the Am L$_3$ edge, the fit confirmed the presence of americium exclusively in the trivalent state for the oxidized samples with Am/(Am+U)$\leq$0.5. The *Am70ox* sample presents a mixed Am^{3+}/Am^{4+} composition, with an average oxidation state of +3.32(3), slightly higher than that of the as-sintered oxide, equal +3.26(3).

For the U L$_3$ edge, the best fits were obtained using the U$_4$O$_9$ and U$_3$O$_8$ references. For the *Am10ox*, *Am15ox* and *Am30ox* samples, the high average oxidation states, ranging from +4.95 to +5.17, are due to the presence of uranium in both the cubic and the M$_3$O$_8$ phases. For the Am50ox sample, constituted by a single cubic phase, the average oxidation state of uranium was equal to +4.88(3), slightly higher than that of the as-sintered oxide (4.82), but still lower than +5. Therefore, a U^{4+}/U^{5+} mixture can be supposed.

The overall O/M_{tot} ratios of the samples were computed, from the knowledge of the average oxidation states of Am and U. The measured Am/(Am+U) ratios (see section 4.1.2.1) were used for the calculations, instead of the nominal ones. For the biphasic samples, the O/M ratio of the cubic phase (O/M_{cubic}) was hence derived from the mass balance:

$$O/M_{tot} = a \cdot O/M_{cubic} + b \cdot 2.667, \tag{5.2}$$

where a and b are the molar fraction of the cubic and the M$_3$O$_8$ phase, respectively, which were derived by the Rietveld XRD refinements. In Eq. (5.2), the M$_3$O$_8$ is supposed to be a stoichiometric compound (O/M = 2.667). The resulting compositions of the oxidized samples are summarized in Tab. 5.6 and represented in Fig. 5.16. For the U cationic fractions, the presence of U^{6+} was excluded, according to the discussion of chapter 4. For the Am70ox sample, since the XANES spectra could not be collected for uranium, the data of the as-sintered sample were adopted. A reduction of uranium is very unlikely and hence the O/M ratio is expected to be equal to the calculated value of 1.91(2) or higher.

The obtained O/M ratios confirm the identification of the cubic structure of the *Am10ox*, *Am15ox* samples with the M$_4$O$_9$ phase The O/M=2.19 of the *Am30ox* sample is consistent with the oxidation of the MO$_{2+x}$ phase, highlighted by the HT-XRD results. For the monophasic

Sample	Overall composition			Cubic phase composition				
	Cubic[mol.%]	M_3O_8 [mol.%]	O/M_{tot}	Am^{3+}	Am^{4+}	U^{4+}	U^{5+}	O/M
Am10ox	45(5)	55(5)	2.48(2)	0.10	0	0.3	0.6	2.25(3)
Am15ox	0.70(5)	0.30(5)	2.40(3)	0.15	0	0.13	0.72	2.28(3)
Am30ox	0.98(4)	0.02(4)	2.20(2)	0.28	0	0.05	0.67	2.19(2)
Am50ox	1	0	1.99(2)	0.48	0	0.06	0.46	1.99(2)
Am70ox	1	0	1.91(2)	0.46	0.21	0.04^a	0.29^a	$1.91(2)^a$

Table 5.6: Compositions of the cubic phase of the oxidized samples. *a*: not available data, supposed from the as-sintered oxide.
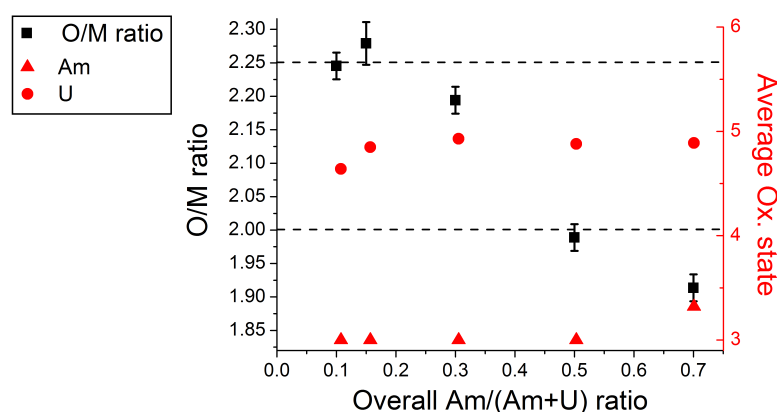
Fig. 5.16: Compositions of the cubic phase of the oxidized samples as a function of the overall O/M ratio of the sample.

Am50ox sample, the O/M ratio is close to the stoichiometric value. This value is consistent with the evolution of the lattice parameter observed during the HT-XRD measurements, which had not indicated a substantial oxidation of the sample. For the Am70ox sample, it is hard to drawn conclusions since the average oxidation of uranium could not be measured after the oxidation. However, considering the HT-XRD data and the americium behaviour (only slightly oxidized), one can suppose that the oxide was still hypo-stoichiometric, even after the thermal treatment in air.

5.3.2   EXAFS results

Am L_{III} and U L_{II} EXAFS spectra were acquired at 15 K on the oxidized samples, according to the procedure detailed in Appx. A. The obtained EXAFS spectra and their Fourier transforms are reported in Fig. 5.17 and Fig. 5.18, respectively for Am and U (the *Am70ox* sample is not reported because of the problems in the preparation).

Remarkable differences can be observed for both the Am L_{III} and U L_{II} EXAFS spectra between the different compositions.

For the monophasic *Am50ox* sample, the EXAFS spectra present features similar to those of the corresponding as-sintered composition, analysed in section 4.2.2. Indeed, the same structural
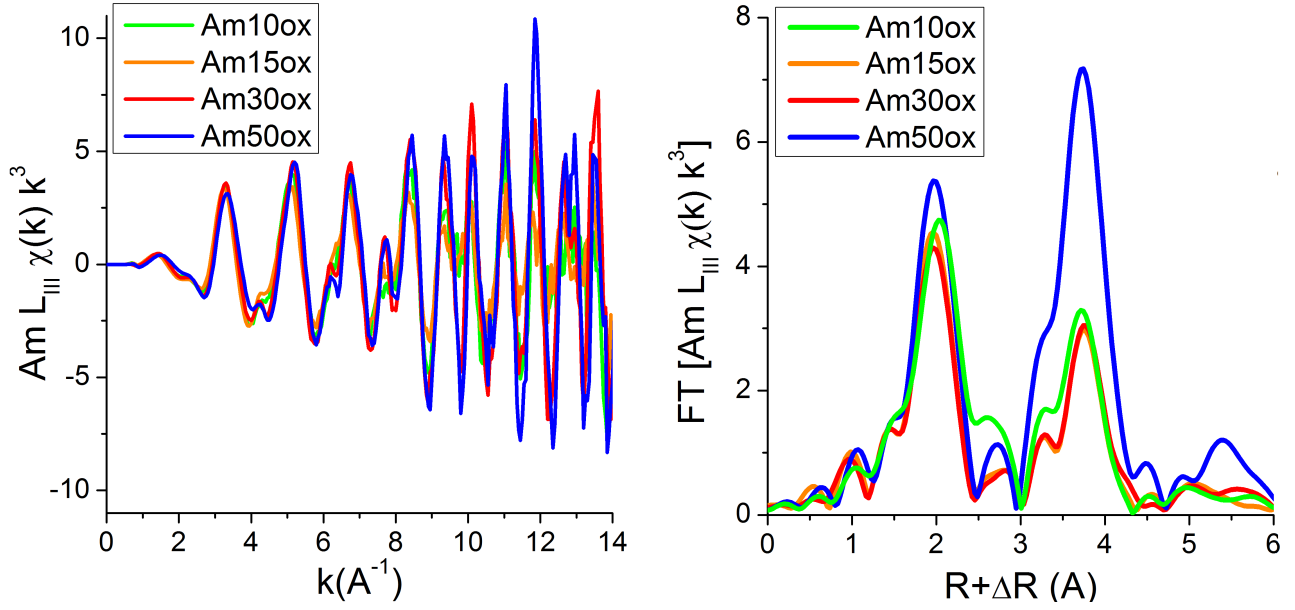
Fig. 5.17: Experimental EXAFS spectra at the L_{III} edge of Am and their Fourier transforms of the oxidized samples. FT boundaries: 3.5-12 Å^{-1}, $dk = 2\text{Å}^{-1}$
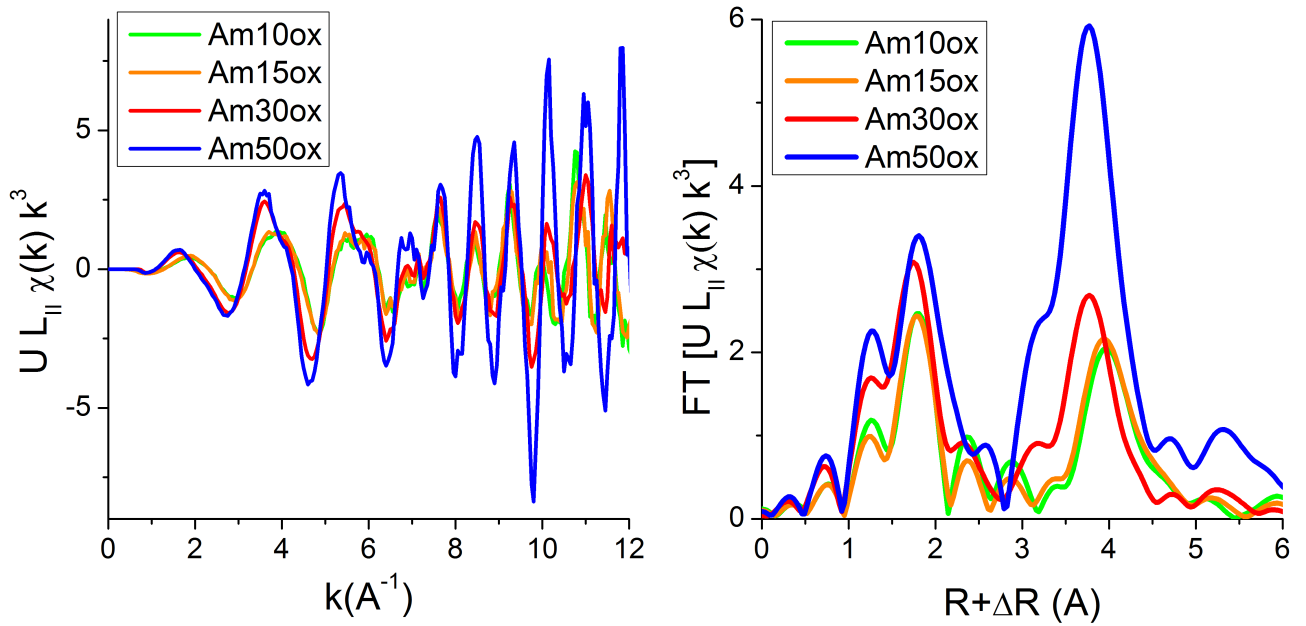
Fig. 5.18: Experimental EXAFS spectra at the L_{II} edge of U and their Fourier transforms of the oxidized samples. FT boundaries: 3.5-11 Å^{-1}, $dk = 2\text{Å}^{-1}$

models were used to refine the EXAFS spectra: a defect-free fluorite model for the Am L_{III} edge and a structural model based on the β-U_4O_9 structure for the U L_{II} edge (see section 4.2.2). In general, a good agreement between the fits and the data was obtained, as shown in Fig. 5.19. The resulting structural parameters, listed in Tab. 5.7, are very similar to those previously obtained for the as-sintered oxide (reported in Tab. 4.10). More specifically, almost identical values, within the uncertainty limits, were obtained for the Am L_3 edge. Few differences were
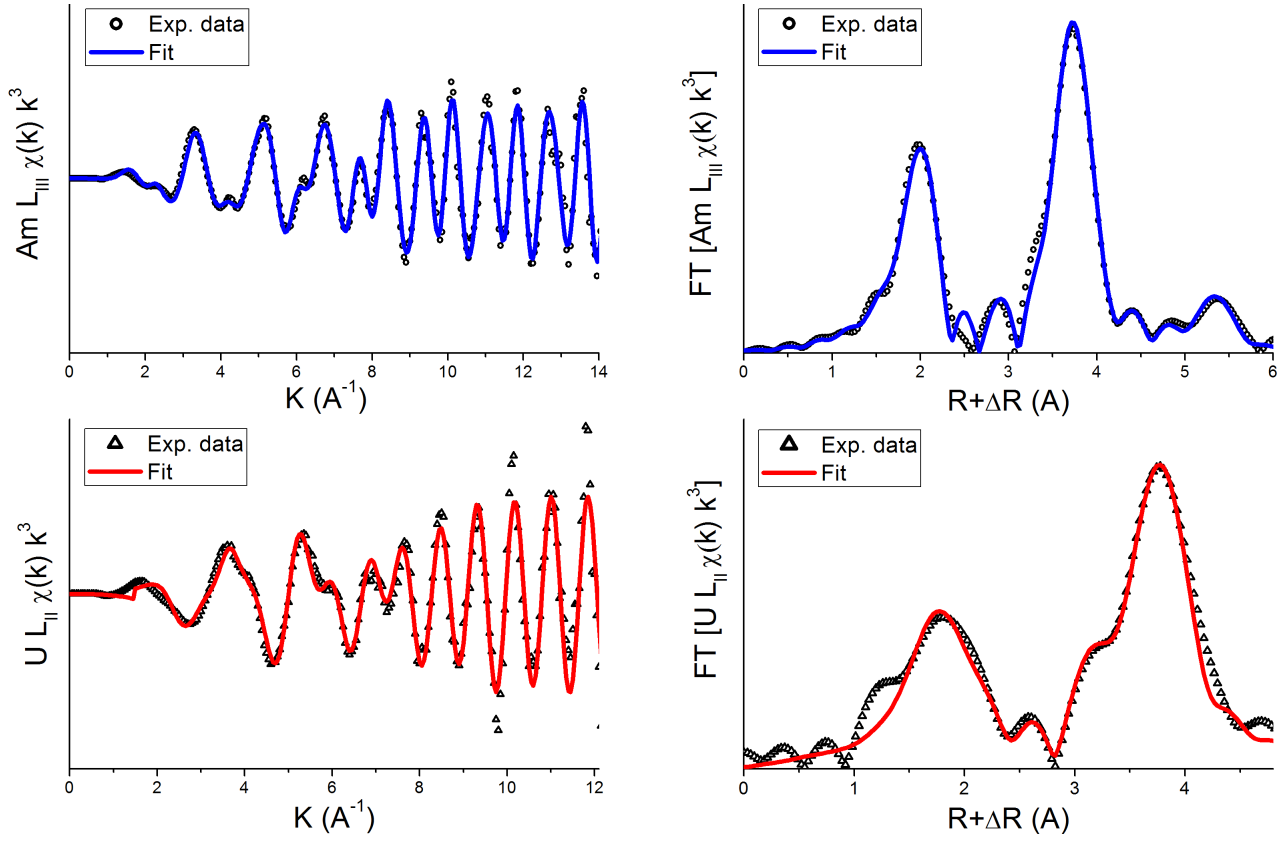
Fig. 5.19: Am L$_3$ and U L$_2$ EXAFS spectra and Fourier transforms of the *Am50ox* sample. FT boundaries: 3.5-13.5 Å^{-1}, $dk = 2$Å^{-1} for Am L$_3$; 3.5-11.2 Å^{-1}, $dk = 2$Å^{-1} for U L$_2$.

Sample	Edge	Shell	R (Å)	N	σ^2(Å^2)	R-factor
	Am-L$_{III}$	O1	2.426(5)	8.1(3)	0.0063(5)	0.009
		Am/U1	3.85(1)	12.1(5)	0.0042(4)	
		O2	4.47(1)	24(3)	0.014(3)	
		Am/U2	5.45(2)	6(2)	0.005(1)	
U$_{0.5}$Am$_{0.5}$O$_2$		Am/U2	5.45(2)	6(2)	0.005(1)	
	U-L$_{II}$	O$_{cubo}$1	2.19(1)	1.7(5)	0.0073(5)	0.011
		O$_{fluo}$1	2.32(1)	5.4(5)	0.011(2)	
		O$_{cubo}$2	2.82(1)	1.7(5)	0.012(2)	
		Am/U1	3.86(1)	12(1)	0.0045(5)	
		O$_{fluo}$2	4.43(1)	25(3)	0.011(1)	

Table 5.7: Parameters resulting from the refinement of the *Am50ox* EXAFS spectra.

observed for the uranium local environment, consisting in slightly shorter U-O distances. These are consistent with the higher average oxidation state of uranium highlighted by the XANES.

The EXAFS spectra of the *Am10ox, Am15ox, Am30ox* could not be fitted to a theoretical model, since the presence of two complex structures (M$_3$O$_8$ and a cubic oxidized phase) would have required the refinement of too many parameters.

The U-L$_{II}$ EXAFS spectra could be fitted by linear combination of the U$_4$O$_9$ and U$_3$O$_8$ references

(previously shown and described in section 4.2.2), achieving a reasonable agreement, as shown in Fig. 5.20. The results of the fits are summarized in Tab. 5.8. The M_4O_9/M_3O_8 phase proportion obtained for *Am10ox* is in very good agreemen with the results obtained by the Rietveld. For the *Am15ox Am30ox* samples, the U_3O_8 contribution to the EXAFS fit is higher than the amount of the M_3O_8 phase determined by XRD. This is probably due to the higher content of Am^{3+} in the cubic structure, which leads to a high oxidation of uranium and hence structural modification in its local environment.
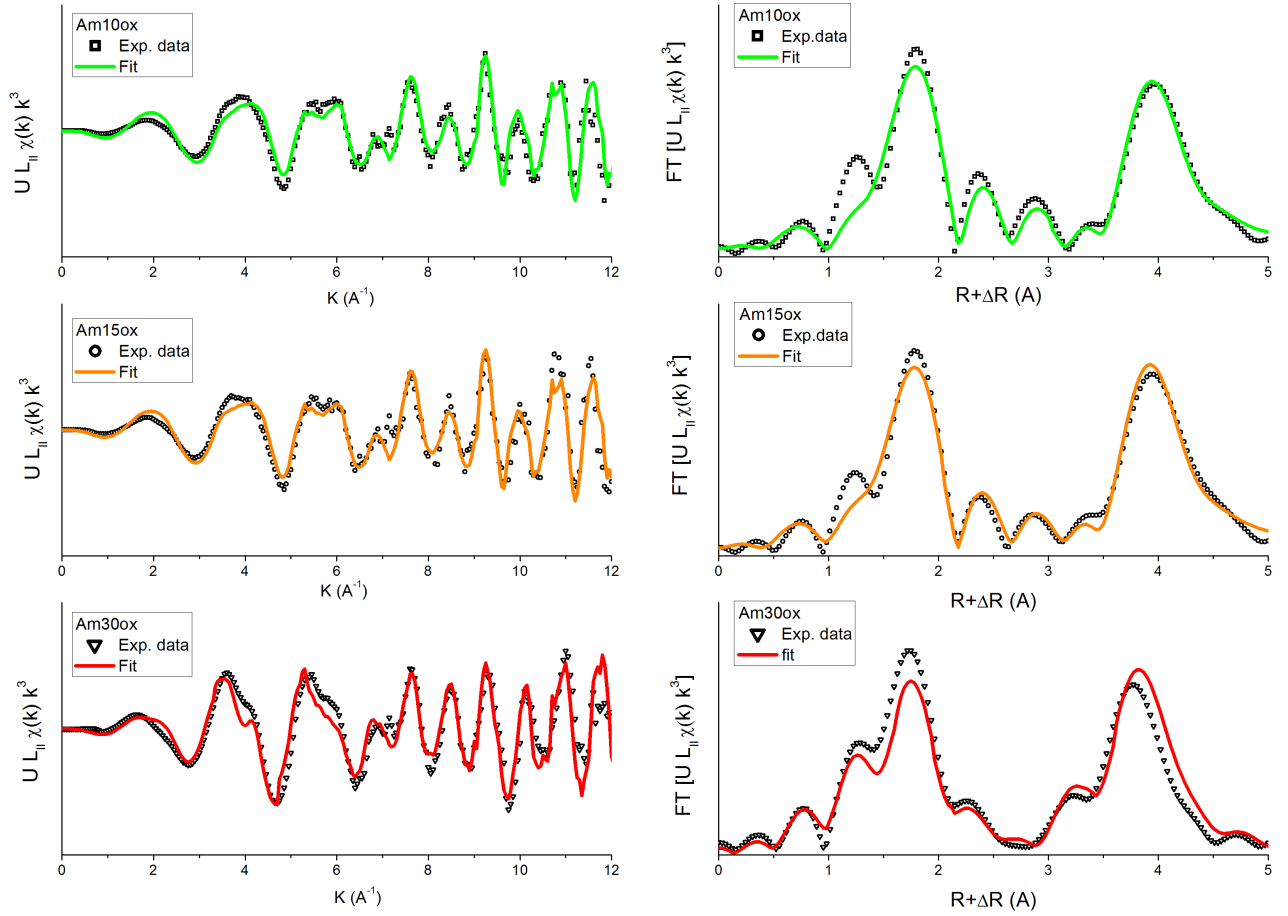
Fig. 5.20: U L_2 EXAFS spectra and Fourier transforms of the *Am10ox*, *Am15ox* and *Am30ox* sample. FT boundaries: 3.5-11.5 Å^{-1}, $dk = 2$Å^{-1}.

| | Linear Combination Fit results | | |
Sample	U_4O_9	U_3O_8	R-factor
Am10ox	0.23	0.77	0.1
Am15ox	0.31	0.69	0.09
Am30ox	0.82	0.3	0.12

Table 5.8: Linear combination fits of the $\chi(k) \cdot k^3$ data.

The Am-L_{III} EXAFS spectra of the *Am10ox*, *Am15ox* and *Am30ox* samples, shown in Fig. 5.17, exhibit significant differences from the defect-free fluorite structure (see for com-

parison the *Am50ox* spectrum). For instance, in the relative k^3-Fourier Transform, a decrease in the intensity of the second main peak (corresponding to the cationic shell) can be remarked. This is due to the loss of the long range order around americium and it indicates a departure from the fluorite structure. The loss of the fluorite-type local environment, observed for the first time in U-Am mixed oxides, is consistent with its solution in the oxygen-rich M_4O_9 and M_3O_8 phases.

5.4   Conclusions

The high temperature behaviour in air of $(U,Am)O_2$ oxides was studied by combining HT-XRD up to 1470 K and XAS at room temperature.

The obtained results showed that the addition of americium to UO_2 improves its resistance against the oxidation. The kinetics of the oxidation was considerably slower for the investigated $(U,Am)O_2$ oxides with $Am/(Am+U)=0.10, 0.15, 0.3$. Indeed, the appearance of the M_3O_8 phase was shifted to higher temperatures with the increasing of the americium content (Tab. 5.2). Furthermore, the mixed oxides were always biphasic during the thermal treatment in air, being constituted by a cubic MO_{2+x}/M_4O_9 phase and M_3O_8. The amount of M_3O_8 decreased with the increasing the americium content, being only 5 wt.% for $Am/(Am+U)=0.30$. On the contrary, UO_2, heated in air, is easily completely transformed in U_3O_8. Moreover, high americium content $(U,Am)O_2$ oxides with $Am/(Am+U)=0.50, 0.7$ were also investigated. These samples remained monophasic during the entire thermal treatment in air, maintaining the fluorite structure. Important structural data were also obtained in this work, as the lattice parameter thermal expansion of the MO_{2+x} and M_4O_9 phases (see Tab. 5.3).

Most importantly for the aim of this work, fundamental data were obtained on the oxygen-rich domain of the U-Am-O phase diagram.

The accommodation of Am^{3+} in the M_4O_9 phase was observed for the first time. A small solubility of Am^{3+} ($Am/M \simeq 0.10$) in the M_3O_8 phase, previously proposed by Caisso *et al.* for the hexagonal α' polymorph, was confirmed and extended also to the orthorombic α structure. This implies that the CALPHAD models of U_4O_9 and U_3O_8 should be respectively extended as:

$$(U^{4+}, U^{5+})_4(O^{2-})_9 \longrightarrow (Am^{3+}, U^{4+}, U^{5+})_4(O^{2-})_9 \tag{5.3}$$

$$(U^{5+}, U^{6+})_3(O^{2-})_8 \longrightarrow (Am^{3+}, U^{5+}, U^{6+})_3(O^{2-})_8 \tag{5.4}$$
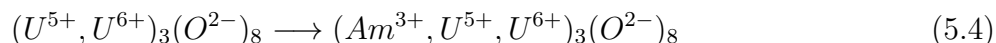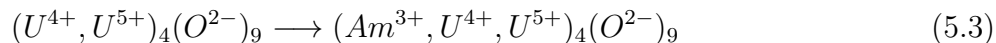
The two models are represented in Fig. 5.21, with the end members at the triangle vertexes and the theoretical stable solid solution represented by a red line.

Furthermore, phase diagram points were obtained in this work. Indeed, as previously discussed, the HT-XRD results did not indicate composition changes during the cooling; hence,

$\boxed{M_4O_9}$ $[(Am^{+3})_4(O^{-2})_9]^{-6}$

$(U_{0.75}, Am_{0.25})_4 O_9$

$[(U^{+4})_4(O^{-2})_9]^{-2}$ U_4O_9 $[(U^{+5})_4(O^{-2})_9]^{+2}$

$\boxed{M_3O_8}$ $[(Am^{+3})_3(O^{-2})_8]^{-7}$

$(U_{0.78}, Am_{0.22})_3 O_8$

$[(U^{+5})_3(O^{-2})_8]^{-1}$ U_3O_8 $[(U^{+6})_3(O^{-2})_8]^{+2}$
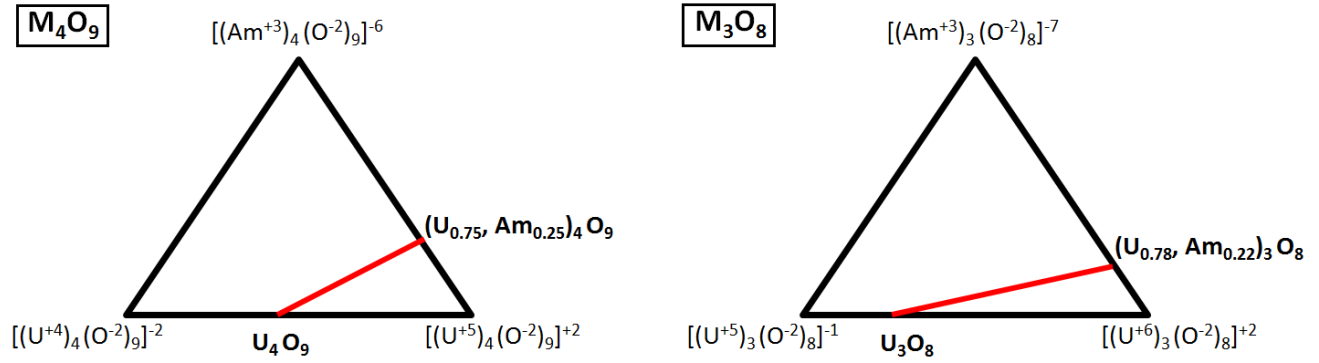
Fig. 5.21: Schematic representation of the M_4O_9 and M_3O_8 CALPHAD models.

the compositions obtained at room temperature (by XRD and XANES) are considered representative of the isothermal measurement performed at 1470 K. These points are summarized in Tab. 5.9. For the M_3O_8 phase of the three biphasic samples (Am10ox, Am15ox, Am30ox), the XRD data indicated a similar Am/M ratio. This was hence fixed to Am/M=0.10. Knowing the overall Am/M in the samples, the corresponding enrichment in americium of the cubic phases (MO_{2+x} and M_4O_9) was calculated by the mass balance. The points are represented in

Overall composition		Chemical formula [mol.%]
Am/M	O/M	
0.1	2.48	$0.45 \cdot (U_{0.9}, Am_{0.1})_4O_9 + 0.55 \cdot (U_{0.9}, Am_{0.1})_3O_8$
0.15	2.37	$0.7 \cdot (U_{0.83}, Am_{0.17})_4O_9 + 0.3 \cdot (U_{0.9}, Am_{0.1})_3O_8$
0.28	2.20	$0.98 \cdot (U_{0.71}, Am_{0.29})O_{2.19} + 0.02 \cdot (U_{0.9}, Am_{0.1})_3O_8$
0.48	1.99	$(U_{0.52}, Am_{0.48})O_{1.99}$
0.67	$\geqslant 1.91$	$(U_{0.33}, Am_{0.67})O_{1.91+x}$

Table 5.9: Obtained phase diagram points at 1473 K.

a 1470 K isothermal section of the U-Am-O phase diagram in Fig. 5.22, where possible, indicative phase boundaries were traced as dotted lines to help the visualisation. The obtained phase diagram data consist of: two points in the single-phase $MO_{2\pm x}$ solid solution, one tie-line in the $MO_{2+x}+M_3O_8$ biphasic domain and two tie-lines in the $M_4O_9+M_3O_8$ biphasic domain.

Finally, the unexpected oxidation behaviour observed for the *Am30ox* sample can be now explained. For Am/M=0.3, the oxidation proceeded by entering the $MO_{2+x}+M_3O_8$ domain for $T \gtrsim 1000$ K, without passing through the formation of M_4O_9, as instead observed for *Am10ox* and *Am15ox* . This was surprising since, in the binary U-O system, the $UO_{2+x}+U_3O_8$ equilibrium is possible only for T>1400 K. This peculiarity is explained by the presence of americium in the trivalent state. Because of this, the maximum **theoretical** Am/M ratios in M_4O_9 and M_3O_8 are 0.25 and 0.22, respectively, as shown by the CALPHAD model in Fig. 5.21. They are likely even lower, especially for M_3O_8, for which the solubility seems limited to Am/M=10 mol%. In any case, the theoretical values are lower than the overall Am/M ratio on the *Am30ox* sample (0.28). This implies that the establishment of the 2-phase $M_4O_9+M_3O_8$ equilibrium

Fig. 5.22: Possible iso-T section at 1470 K of the U-Am-O phase diagram and experimental points here obtained.
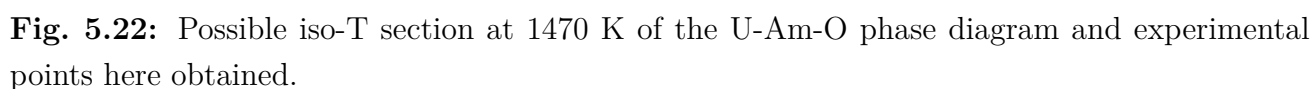
is not possible. Therefore, it is understandable that a high americium content (Am/M$\gtrsim$0.25) induces a stabilization of the MO$_{2+x}$+M$_3$O$_8$ domain in comparison to the U-O system.

Chapter 6

High-temperature thermodynamic properties

In a heterogeneous transmutation scenario, (U,Am)O$_2$ pellets with Am/(Am+U) ratios up to 20 mol.% are placed in the periphery of the reactor core, where temperatures can reach 1470 K [16]. For the homogenous transmutation strategy, lower americium contents are foreseen (maximum 5 mol.%), but the pellets are distributed in the entire reactor core. In this case, during normal operation, the fuel is subject to high temperatures (> 2300 K) and strong gradients.

For both scenarios, the U-Am-O phase diagram needs to be known for the entire temperature range, in order to verify that there are no phase transition that could lead to the formation of secondary phases, in particular during the heating/cooling of the reactor. For instance, in (U,Pu)O$_{2-x}$ oxides, a miscibility gap was highlighted for high plutonium contents. The formation of this biphasic domain needs to be avoided because it would lead to heterogeneities and, hence, a deterioration of the mechanical properties of the pellets. For this reason, it is important to verify the existence of a miscibility gap in the U-Am-O system. Furthermore, in order to guarantee the safety of the fast neutron reactors (FNRs), the knowledge of reliable thermodynamic data, from 300 K up to high temperature, is required for the fuel. For instance, the main guideline for the design of a reactor core is to maintain a safety margin from the melting in the hot spots of the fuel. The melting temperature and the thermal conductivity are hence key parameters. Also the heat capacity C_p plays a crucial rule, since it determines the quantity of heat that can be accumulated in a material. Furthermore, the restructuring of the pellets, induced by the high temperatures and the strong thermal gradients, must be considered. Indeed, mass transports occur, in the fuel, through vaporization/ condensation processes and they lead to radial changes of the O/M and actinide/M ratios. For this reason, determining the solid/gas equilibria over a wide range of composition is essential for the safe assessments of nuclear fuels for FNRs.

This chapter is dedicated to the study of high temperature thermodynamic properties of (U, Am)O$_{2\pm x}$ oxides for a large composition domain, from Am/(Am+U)=0.075 up to 0.70. In section 6.1, the stability of the (U,Am)O$_{2-x}$ solid solution, for high americium contents, is investigated by HT-XRD. In section 6.2, measurements performed by drop calorimetry will be shown. These were performed in collaboration with the PhD students O. Valu and J. Zappey

in JRC-Karlsruhe. The measurements allowed determining the enthalpy and the heat capacity functions in the $300 < T < 1800$ K temperature range. In section 6.3, an investigation of the high temperature vapour pressures by Knudsen Effusion Mass Spectroscopy (KEMS) will be presented. Finally, in section 6.4, a study of the solid-liquid transition of the $(U,Am)O_2$ mixed oxides will be shown. Melting temperatures were measured using a laser-flash technique coupled with fast pyrometry. The post-melting samples were characterized by SEM and XAS, to determine the final compositions.

6.1   Investigation of the $(U,Am)O_{2-x}$ miscibility gap

The existence of this miscibility gap for the $(U,Am)O_2$ solid solution has represented, in the last few years, a small mystery for the thermochemistry of actinide oxides. The question started with the Am-O binary phase diagram. As discussed in Ch. 3, the first representation of the Am-O phase diagram was proposed by Sari and Zamorani [58]. These authors reported a miscibility gap for AmO_{2-x}, in the $1100 < T < 1300$ K range, on the basis of a phase transition indicated by DTA and of comparison with similar actinide and lanthanide oxide systems (Ce-O, Pu-O). Even if no further experimental proves were provided, the miscibility gap was kept in the following phase diagram versions proposed in the literature [60, 62], including the CALPHAD modeling of Gotcu-Freis [64]. If this miscibility existed in the binary Am-O system, it would necessarily lead to the prescence of a miscibility gap in the ternary U-Am-O system. As seen in chapter 3, our investigation on the Am-O system denied the presence of a miscibility gap in AmO_{2-x}, at least for the temperature range indicated by Sari and Zamorani [58]. However, the existence of a miscibility gap cannot be excluded for the ternary system. As mentioned in section 4.1.1, F. Lebreton, who developed the UMACS manufacture process during his PhD [106], observed by XRD two-three fluorite phases, within few hours after the sintering, for oxides with $0.3 \leq$ Am/(Am+U)≤ 0.7. Subsequently, a rapid oxidation was observed and the co-existing structures converged to one single fluorite phase. On the basis of this observation, the presence of a miscibility gap was supposed.

Lebreton tried to experimentally prove the existence of a miscibility gap in the U-Am-O system, during his PhD work [106]. Several *in situ* HT-XRD measurements were performed on $(U,Am)O_2$ oxides with Am/(Am+U)=0.5, 0.6 and 0.70. As already explained in 3, this technique is suitable for the study of phase transition and separations. For instance, the miscibility gap present in the Pu-O and U-Pu-O system has been clearly observed by HT-XRD [153, 155, 158–160, 202]. Precisely on the basis of the results on $(U,Pu)O_{2-x}$ oxides, Lebreton selected very reducing atmospheres for the research of the miscibility gap on $(U,Am)O_2$ oxides. A He-H$_2$(5 mol.%) mixture was used for the experiment, with oxygen partial pressures ranging from 10^{-29} to 10^{-25} atm. Contrary to the $(U,Pu)O_{2-x}$ case, a single fluorite structure was always observed during the measurements of Lebreton, hence no miscibility gap was detected. However, the CALPHAD model of the U-Am-O system proposed in Lebreton's thesis [106] included a miscibility gap for O/M<2, Am/(Am+U)≥ 0.5. This miscibility gap originated in the

U-Am-O model, based on the Am-O binary of Gotcu-Freis [64] and the oxygen potentials of Bartscher and Sari [74]. Thermodynamic calculations based on the model of Lebreton showed that the miscibility gap, in (U,Am)O$_{2\text{-}x}$ oxides, should occur for conditions more oxidizing, in comparison to (U,Pu)O$_{2\text{-}x}$ oxides. The conditions used during the HT-XRD study of Lebreton were too reducing to observe the miscibility gap.

On the basis of these computations, new experimental investigations by *in situ* HT-XRD were performed in this work. The experimental set-up already seen in Ch. 3 and 5, and described in detail in Appx. A, was used. A flowing helium atmosphere was adopted for the experiment. The oxygen partial pressure was regulated, using an oxygen pump at the entrance of the furnace, to $\sim 10^{-20}$ atm. The atmosphere was hence slightly more oxidizing than that used by Lebreton. The (U,Am)O$_2$ oxide with Am/(Am+U)= 0.7 was studied.

The measurements consisted of heating/cooling cycles, between room temperature and 1273 K, according to the methodology explained in section 3.2.1.2. Cooling rates of 100 K·min^{-1} and 50 K·min^{-1} were used. XRD patterns were acquired using a fast detector with a 3° angular window, focusing on the (022) reflection of the fluorite structure. The results were similar for the two cooling rates applied: more than one fluorite structure was clearly observed for T $\lesssim$ 700 K, as shown in 6.1. Moreover, this phase separation was reversible: during the heating, the
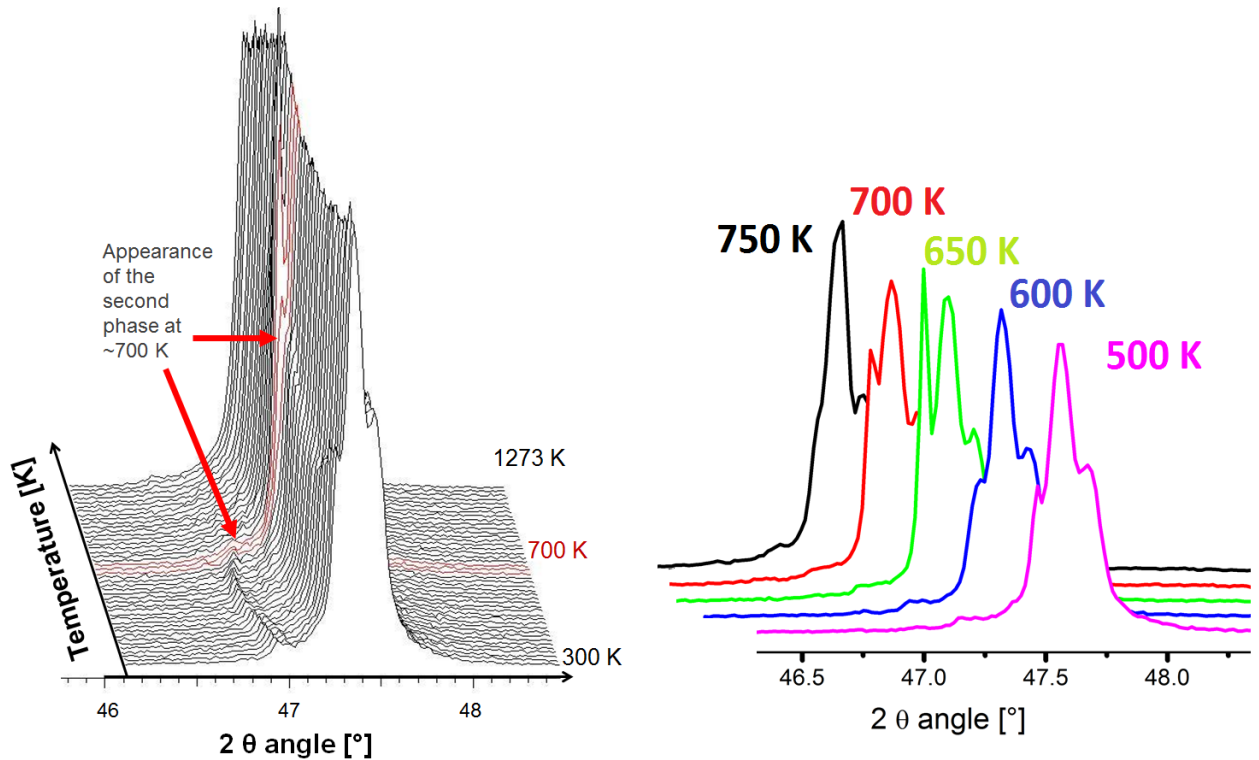
Fig. 6.1: (022) reflection of the fluorite structure collected on a U$_{0.3}$Am$_{0.7}$O$_{2\text{-}x}$ oxide, under a He atmosphere with pO$_2$= 10^{-20} atm. Left: all the XRD patterns, Right: selected temperatures.

secondary phases disappeared and one single (022) reflection was observed for T $\gtrsim$ 700 K. **These results**, very similar to those obtained for the (U,Pu)O$_{2\text{-}x}$ oxides, **confirm the existence of a miscibility gap in the oxygen hypostoichiometric, americium rich domain of the**

$U_{1-y}Am_yO_{2\pm x}$ solid solution. Further measurements would be necessary to better define the limits of this biphasic domain and, in particular, to determine the minimum Am/(Am+U) ratio for which the phase separation can occur.

6.2 High temperature enthalpy and heat capacity

Several studies were reported on the enthalpy increments and the heat capacity of UO_2, from room temperature up to its melting [130–137,141,142], as seen in section 2.4.2. On the contrary, very few experimental data exist for Am binary oxides and U-Am mixed oxides. Measurements of the enthalpy increments from room temperature of AmO_2 were performed by Nishi *et al.* [145], but these were limited to 1080 K (see section 2.4.2). For mixed uranium-americium dioxide, only one set of high temperature enthalpy increments has been reported by Valu *et al.* in the literature [203]. In that work, (U, Am)$O_{2\pm x}$ compounds with Am/(Am+U)=0.09 and 0.19 were investigated by drop calorimetry in the 425-1790 K temperature range. The obtained enthalpy values followed the same trend as the UO_2 and AmO_2 end members and the authors concluded that the Neumann-Kopp additivity rule [204] is valid for these compositions. Here, the investigation of the (U, Am)$O_{2\pm x}$ solid solution is extended to higher americium contents: five compositions with Am/(Am+U) ratio equal to 0.30, 0.40, 0.50, 0.60 and 0.70 were investigated (samples Am30, Am40, Am50, Am60 and Am70).

6.2.1 Experimental conditions and data analysis

The enthalpy increments $H(T) - H(298.15K)$ were measured using a drop calorimetry technique, with the experimental set-up described in Appx. A. Fragments of the pellets presented in chapter 4 were used. The masses of the samples ranged from 15 to 220 mg. The experiments were performed under purified argon atmosphere (oxygen content 1 ppm) for the samples with Am/(Am+U)≤0.5 and under air for the highest americium contents. These choices were made in order to try to maintain an O/M ratio close to 2.0, according to the results of chapter 5. After each measurement, the samples were checked and the mass controlled with a balance of 0.1 mg sensitivity. Even if these controls never revealed changes, a variation of the O/M ratio leading to mass variation inferior to 0.1 mg cannot be excluded. Moreover, since mass changes could not be recorded during the measurement, variations between high temperature and room temperature could not be detected.

    To perform the measurements, the samples were introduced on the top of the experimental chamber, kept at room temperature. The furnace was programmed to reach and keep the target temperature of measurement T_m, at which the heat flow signal was stabilized during 7 hours. After this period, a "cold" sample was dropped into the detector, causing a small thermal shock. In general, the additional heat Q_{meas} provided to the system in order to re-stabilize T_m is equal to the enthalpy increment $H(T) - H(298.15K)$ of the sample (see Appx. A for more details). However, complications appear with samples containing radioactive elements as ^{241}Am because

self-irradiation affects the measurements of their thermophysical properties [205]. Two major phenomena were identified as possibly influencing the drop calorimetry measurements. The first is the accumulation of lattice defects in aged samples. These defects can be annealed with a thermal treatment causing a release of their latent heat, which alters the measured enthalpy values. In order to reduce the effect of this phenomenon, the samples were first thermally treated at the highest measurement temperature in the drop calorimeter. Then, measurements were performed in consecutive days, avoiding the ageing of the samples. The second phenomenon is the heat power generated by the sample itself, which is mostly due to the slowing down of the α particles and the recoil nuclei from decay. Here, the γ-rays contribution is neglected since most of them escape the sample and their energy is relatively low. Hence, to calculate the enthalpy increment, the following relation was applied:

$$H(T) - H(298.5K) = Q_{meas} + Q_\alpha, \tag{6.1}$$

where Q_α is the heat generated from the α deay, that contributes to increase the sample temperature and it is equal to:

$$Q_\alpha = P \cdot m_{Am241} \cdot \Delta t. \tag{6.2}$$

In Eq. (6.2), P is the specific heat power of ^{241}Am, equal to 0.114 mW/mg [206], m_{Am241} is the mass of ^{241}Am in the sample and Δt is the time necessary to restore T_m after the drop. Typical values range from 1 to 3 minutes. The Q_α contribution to Eq. (6.1) is small, but not negligible, ranging from 1% up to 5% for these measurements.

Once the enthalpy as a function of temperature was obtained, the heat capacity C_p was calculated by derivation of the enthalpy function according to:

$$C_P = (\frac{\delta H}{\delta T})_P. \tag{6.3}$$

6.2.2 Experimental results

The enthalpy increments for the five (U, Am)O$_2$ compositions were measured between 470 and 1750 K and the results are reported in Tab. 6.1 and Tab. 6.2, respectively for the measurements in argon and air. For each temperature, the number of measurements n, the mean value of all performed measurements and the corresponding standard deviations are provided.

The data are shown in Fig. 6.2. For clarity of representation, these are divided in two graphs: (a), the literature data for (U, Am)O$_{2\pm x}$ compounds with y=0.09 (Am10) and 0.19 (Am20) [203] and the measurements of this work on Am30 and Am40 samples and (b), the results for Am50, Am60 and Am70. The enthalpy functions of UO$_2$ [25] and AmO$_2$ [145] (the latter extrapolated for T>1080 K) are also reported in the graphs. Fig. 6.2 shows that the two binary dioxides and the mixed compounds share a similar enthalpy trend with temperature. However, in the mixed dioxides with Am/(Am+U)>0.4, the enthalpy increments seem generally higher than those of UO$_2$ and AmO$_2$ for T>1100 K.

Am30			Am40			Am50		
T_m	$H_{T_m} - H(298.15)$	n	T_m	$H_{T_m} - H(298.15)$	n	T_m [K]	$H_{T_m} - H(298.15)$	n
477	12281±751	2	477	13438±338	2	477	13762±598	2
582	20609±2119	2	578	21415±1051	2	582	20278±2576	2
681	29609±598	3	679	28980±1100	2	679	28414±5080	2
780	36372±420	2	785	38572±1200	2	835	40717±5365	4
886	44577±480	2	886	46861±6799	2	981	52547±6029	3
982	55328±4601	2	982	53391±5824	3	1139	68529±2384	2
1088	61781±10415	2	1088	63185±5936	2	1283	81937±6997	2
1189	73538±8477	2	1189	74743±4194	2	1392	94847±8121	2
1289	78513±4887	4	1283	82405±3000	2	1485	102427±14083	3
1392	86720±4108	2	1394	92182±3112	2	1571	112092±8121	2
1425	94500±3520	2	1488	100670±5102	3	1648	127189±7309	2
1486	96587±115	3	1596	116699±15816	3	1739	130926± 5737	3
1550	105563±6000	3	1698	128367±13083	2			
1596	112989±6514	3	1743	135993±4264 2				
1700	116632±9107	3						
1741	118255±10351	3						

Table 6.1: Molar enthalpy increments (in J mol^{-1}) of the Am30, Am40 and Am50 samples measured in argon and their standard deviations. (Temperature in Kelvin).

Am60			Am70		
T_m	$H_{T_m} - H(298.15)$	n	T_m	$H_{T_m} - H(298.15)$	n
480	12790±1145	2	480	13986±394	2
582	20435±284	3	583	20630±1263	4
684	29193±1480	2	685	28316±259	2
785	36576±1313	4	786	37600±949	4
886	47667±1238	4	887	46282±4597	5
987	56020±6885	4	988	57423±4409	5
1088	64363±2753	2	1039	59925±3383	2
1190	70942±7191	6	1089	64011±3299	5
1291	82258±7523	4	1140	72859±3309	4
1393	91273±9510	4	1190	78216±3616	6
1494	102099±4502	4	1241	77709±5856	2
1598	111360±4699	3	1292	85412±4171	5
1648	115171±10373	3	1393	95406±12021	6
			1445	99086±9241	3
			1496	103349±5810	4
			1547	109289±6188	3
			1598	110579±9129	3
			1700	122053±2782	3

Table 6.2: Molar enthalpy increments (in J mol^{-1}) of the Am60 and Am70 samples measured in air and their standard deviations. (Temperature in Kelvin).

The heat capacity functions of the (U, Am)O$_2$ oxides investigated in this work were derived using a linear regression of all the enthalpy data. A Maier-Kelley polynomial relation [207] was
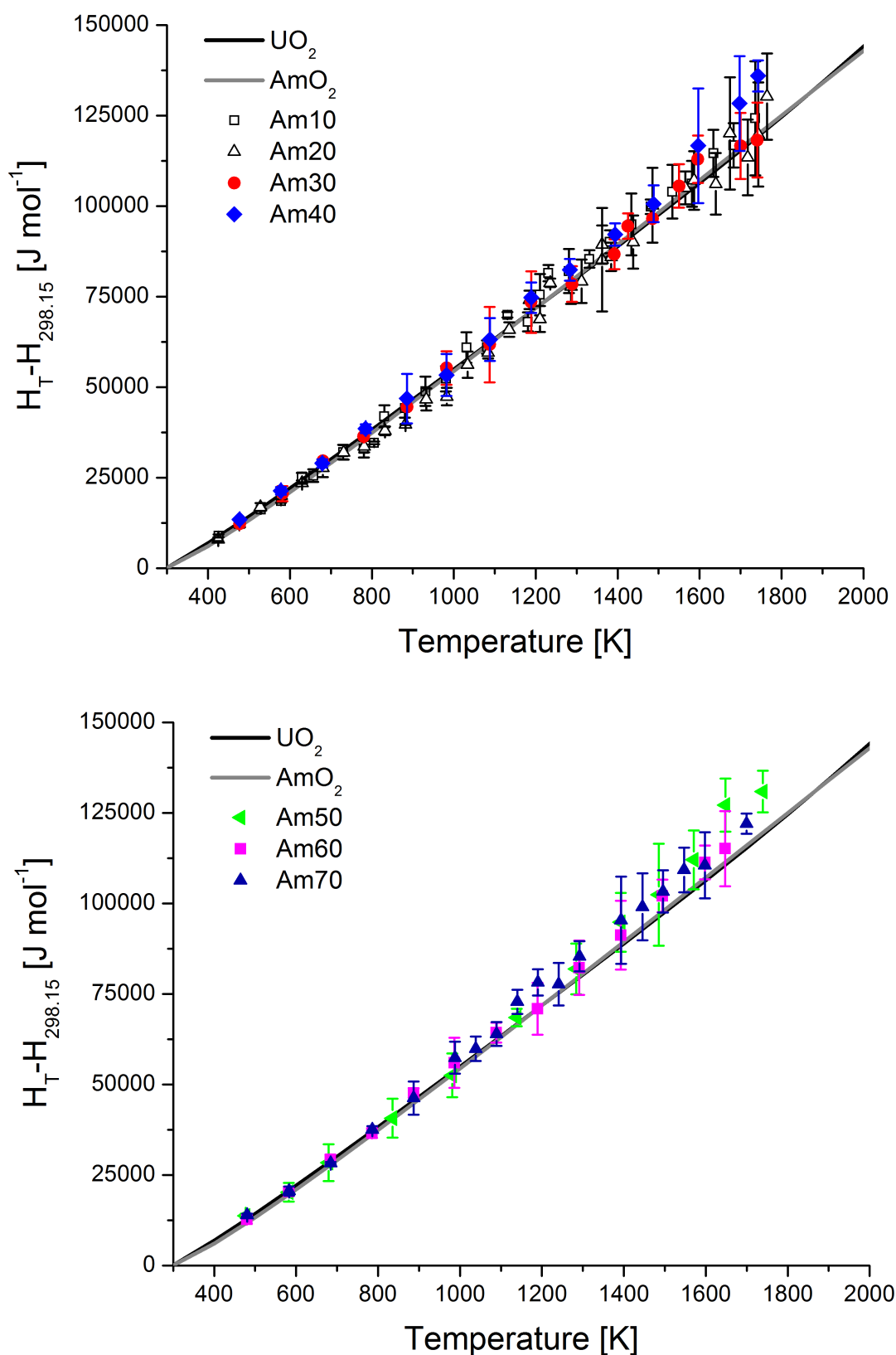
Fig. 6.2: Enthalpy increments of $(U,Am)O_2$ oxides measured in this work: in (a), Am30, Am40; in (b), Am50, Am60, Am70. The data from Valu *et al.* [203] for Am10 and Am20 are reported in (a), whereas the data of UO_2 and AmO_2 (extrapolated for T>1100 K) are represented in both graphs.

used for the fit:

$$C_p = a + b \cdot T + c \cdot T^{-2} \tag{6.4}$$

where T is the temperature in Kelvin and a, b and c are the parameters to optimize.

Since the heat capacity is related to the enthalpy by a differential relation, the assessment is very sensitive to the experimental uncertainties of the enthalpy data. In order to improve the fit, a constraint was applied to the C_p at 298.15 K, by imposing the value obtained with the Neumann-Kopp additivity rule from the C_p of UO_2 (63.6 J·K·mol^{-1}) [25] and AmO_2. For the latter, since no experimental data are available, the heat capacity derived by Konings *et al.* [127] from the trend in the actinide dioxides series was applied (64.3 J·K·mol^{-1}). The Neumann-Kopp rule is generally valid at room temperature for mixed oxides [208] but, for the compositions of this work, one could object that the O/M ratios of the samples were not equal to 2.00. Indeed, the departure from stoichiometry increases the inaccuracy of the additivity rule approximation. However, all the actinides dioxides have close C_p values at room temperature [127] and therefore one can suppose that the error introduced by adopting the UO_2-AmO_2 Neumman-Kopp rule at room temperature is less important than the experimental uncertainties.

For each investigated composition, the applied constraints and the a, b, c parameters of Eq. (6.4) resulting from the fit are listed in Tab. 6.3.

Sample	C_p (298.15) [J·K^{-1}·mol^{-1}]	a[J· K^{-1}· mol^{-1}]	b·10^{-3} [J·K^{-2}· mol^{-1}]	c· 10^6 [J·K·mol^{-1}]
Am30	63.81	79±4	6±4	-1.567±0.280
Am40	63.88	85±9	8±5	-2.122±0.716
Am50	63.95	82±10	11±8	-1.902±1.200
Am60	64.02	74±6	16±7	-1.313±0.323
Am70	64.09	71±8	19±10	-1.137±0.483

Table 6.3: Constraints (Cp (298.15 K)) and parameters for the fit of the high temperature heat capacity according to a Maier-Kelley polynomial.

The obtained heat capacity functions for the five investigated compositions are plotted in Fig. 6.3 (a)-(e), together with their confidence bands. They are also compared with the literature data for the (U,Am)O$_2$ mixed compounds with Am/(Am+U)=0.10, 0.20 and the UO$_2$, AmO$_2$ end members in Fig. 6.3-(f). For the latter, the assessment of Konings based on the enthalpy data by Nishi is adopted here [127]. With the exception of the Am/(Am+U)=0.30 composition, the heat capacity curves obtained in this work are higher than those of UO$_2$ and AmO$_2$, especially for T>800 K. This is consistent with the enthalpy increments with temperature and a possible explanation is provided in the following section.

6.2.3 Discussion

The previous measurements on $U_{0.91}Am_{0.09}O_{2\pm x}$, $U_{0.81}Am_{0.19}O_{2\pm x}$ by Valu *et al.* indicated no substantial deviations from the Neumann-Kopp additivity rule [203]. Here, despite the large uncertainties at high temperatures, the measured enthalpy increments and the derived heat capacities of the (U, Am)O$_{2\pm x}$ compositions with Am/(Am+U)≥0.4 seem to indicate an excess
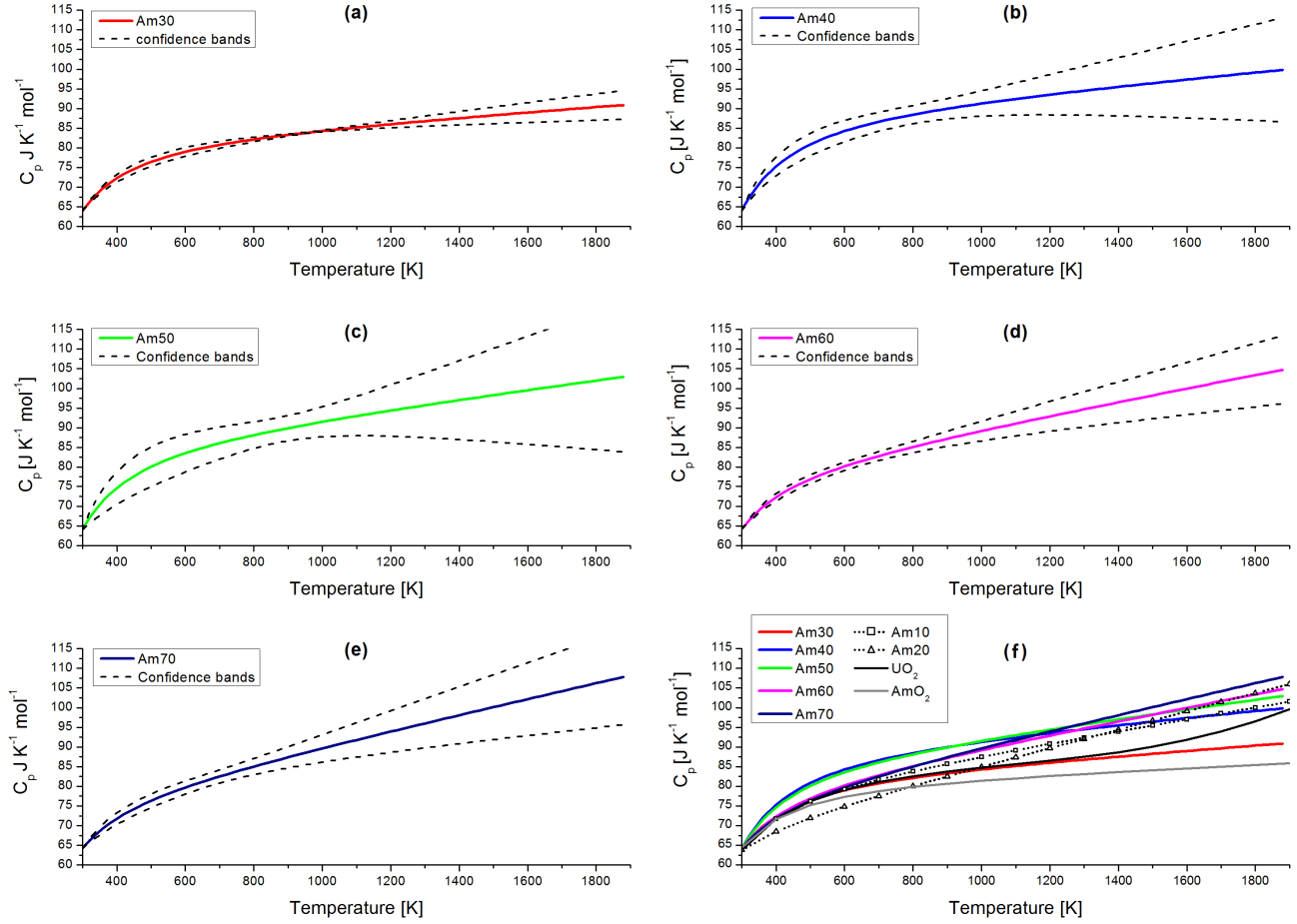
Fig. 6.3: (a)-(e): heat capacity functions of the Am30, Am40, Am50, Am60 and Am70 samples derived from the enthalpy increments obtained by drop calorimetry, plotted together with their confidence bands. (f): comparison of the heat capacities with $U_{0.9}Am_{0.1}O_2$, $U_{0.8}Am_{0.2}O_2$ and the end-members UO_2 and AmO_2.

contribution in comparison to the two end members UO_2 and AmO_2. In order to check this trend, the experimental enthalpies $H_{meas}(T) = H(T) - H(298.15)$ are compared to the theoretical values obtained applying the Neumann-Kopp rule $H_{NK}(T)$. For AmO_2, the extrapolation of the data fit by Nishi is used for T>1100 K [145]. The resulting difference $\Delta(H_{meas} - H_{NK})$ is represented as a function of the temperature for the five investigated compositions in Fig. 6.4. This difference is randomly distributed around the zero-line for the Am30 sample and it can then be neglected. On the contrary, clear shifts toward positive values are observed above 1000 K for the other compositions with Am/(Am+U)$\geq$ 0.40. Moreover, the deviations increases with the temperature.

The systematic nature of the phenomenon indicates the presence of an excess contribution. In general, several factors can contribute to the enthalpy increments of a solid material at high temperature [208], namely the excitations of localized electrons, conduction electrons, lattice dilatation and formation of vacancies. Taking into consideration the structural properties of (U, Am)$O_{2\pm x}$ compounds, the two latter seem the most probable sources of the excess contribution in the enthalpy.
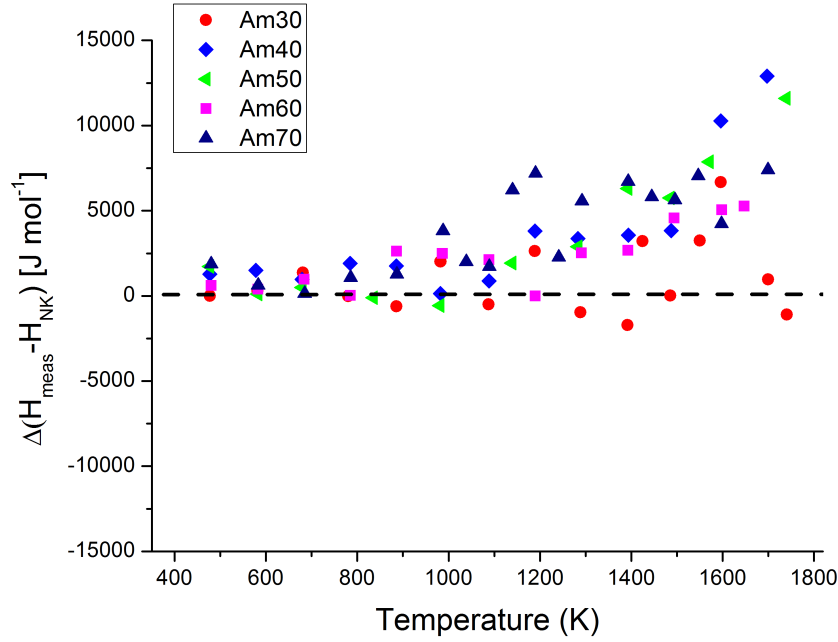
Fig. 6.4: $\Delta(H_{meas} - H_{NK})$ values as a function of temperature obtained for the five compositions analyzed in this work.

Lattice strain can be expected considering the peculiarities highlighted by XAS studies on the $(U, Am)O_{2\pm x}$ solid solution. Indeed, as shown in chapter 4 and 5, XANES results demonstrated the coexistence of various cations (U^{4+}, U^{5+}, Am^{3+} and, only for $Am/(Am+U)>0.5$, Am^{4+}). Even if the fluorite $Fm\bar{3}m$ structure was maintained, direct consequences of the difference in the ionic radii between the cations (U^{4+}, 1.00 Å; U^{5+}, about 0.9 Å in 8-fold coordination; and Am^{3+}, 1.09 Å [109]) were observed by EXAFS, namely the shortening of the average U-O distance and the lengthening of the average Am-O distance. These features result in changes in the lattice vibrations and thus the phonon modes and can cause an excess lattice dilatation contribution to the enthalpy.

However, it can be expected that the main contribution to the additional enthalpy increment comes from oxygen vacancies as changes in the anionic sublattice can considerably affect the enthalpy and the heat capacity. In binary oxides as UO_2, ThO_2 and PuO_2, an unusual C_p increase occurs for T>2000 K because of the oxygen Frenkel pair formation [209, 210]. Smith *et al.* [211] predicted for NpO_{2-x} an anomalous increase of the heat capacity, due to the departure from stoichiometry and formation of oxygen vacancies, occurring for T>1850 K, by using thermodynamic computations based on the CALPHAD method. In Am-containing dioxides a similar effect due to oxygen hypostoichiometry can be expected at even lower temperatures, considering the peculiar instability of americium dioxide at high temperature. Indeed, the oxygen vacancy formation occurs from 1100 K even under pure O_2 (see Ch. 3). Therefore, an excess contribution to the enthalpy can be expressed as:

$$H_{ex} = \Delta H_v \cdot \Delta n(T), \tag{6.5}$$

where ΔH_v is the enthalpy of formation of a vacancy and $\Delta n(T)$ is the molar concentration of oxygen vacancies. The latter depends on the atmosphere (or better, oxygen concentration in the atmosphere), varies with temperature and it can be subject to kinetics effects.

It is important to remember that the AmO_2 enthalpy function adopted in this work does not include the contribution due to the hypo-stoichiometry. The fit of Nishi was extrapolated for T>1080 K for the hypothetical stoichiometric composition, which is not thermodynamically stable above 1100 K, even in one atmosphere of oxygen, as seen in chapter 3. In this context, poor agreement with the Neumann-Kopp rule for T>1100 K for $(U, Am)O_{2-x}$ samples with $Am/(Am+U) \geq 0.38$ is not surprising as these compounds were already hypostoichiometric after the manufacture (see chapter 4). A further high temperature reduction similar to that of AmO_2 can be expected for the Am40 and Am50 samples, which were investigated under argon, as a result of which they were susceptible to oxygen loss. The Am60 and Am70 samples had a hypostoichiometric composition at the end of the manufacture process (O/M= 1.93 and 1.60 respectively). A re-oxidation bringing the O/Am close to 2.00 has likely occurred during the cooling after the first thermal treatment under air (as well as in case of all other high temperature measurements), which, as mentioned, was performed before the drop calorimetry campaign in order to anneal self-irradiation defects. Then, these two compositions will have re-experienced oxygen loss and the concomitant oxygen vacancy formation at the highest measurement temperatures, similarly to AmO_{2-x}, leading to anomalous high enthalpy values. In order to verify the oxygen hypostoichiometry effects on the enthalpy increments of AmO_{2-x}, thermodynamic computations were performed and the results are presented in the next section.

6.2.4 Comparison with thermodynamic computations

Adopting the CALPHAD model presented in chapter 3, the enthalpy increment of AmO_{2-x} was computed as a function of temperature, including in the calculation a gas phase with partial oxygen pressure equal to 0.21 atm, hence simulating air conditions during the measurement. The results are shown in Fig. 6.5-(a), together with the data for Am40, Am50, Am60, Am70, UO_2 and the AmO_2 extrapolated from Nishi [145]. Moreover, in Fig. 6.5-(b), the variation of the composition of the AmO_{2-x} phase with temperature is illustrated: on the left axis, the overall O/Am ratio and on the right axis, the defect fractions of Am^{3+} and vacancies are shown. Fig. 6.5 shows that, under air, the $Am^{4+} \rightarrow Am^{3+}$ reduction and the oxygen vacancy formation start at around 1100 K and, consequently, the O/Am decreases. This causes the departure from the linearity of the enthalpy function, in very good agreement with the previous discussion. Indeed, all the measured enthalpy values for the mixed $(U,Am)O_2$ samples are comprised between the UO_2 and the calculated AmO_{2-x} enthalpy curves, which is consistent with the mixed oxides having an O/M<2.00 at high temperature.

6.2.5 Conclusions

In this part of the study of the high temperature properties, drop calorimetry measurements, performed in the 470<T<1750 K range, were presented. Enthalpy increments data for (U,
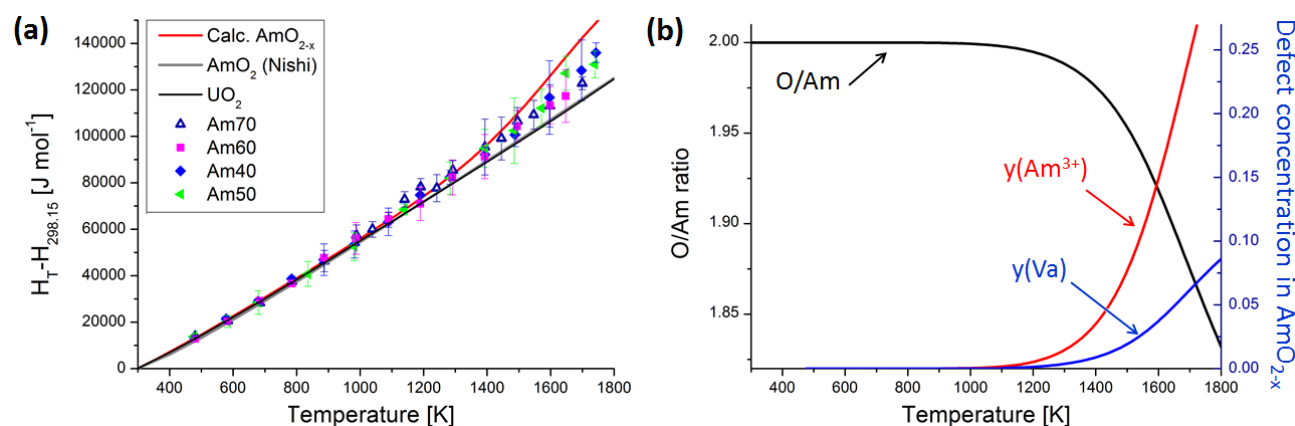
Fig. 6.5: The enthalpy increment function of AmO_{2-x} in air calculated from the CALPHAD model (-) (a) and the corresponding O/Am and defect fractions (b) as a function of temperature. The function is compared to the experimental data obtained in this work and the literature data of UO_2 [25] and stoichiometric AmO_2 [145].

Am)O_2 oxides with Am/(Am+U)=0.30, 0.40, 0.50, 0.60 and 0.70 were reported for the first time. The experimental data were fitted in order to derive the heat capacity functions.

The enthalpy data obtained in this work are higher than those of UO_2 and AmO_2 for T$\geq$1100 K and Am/(Am+U)$\geq$ 0.4. However, the available experimental data for AmO_2 are limited to 1080 K and the enthalpy function was extrapolated above this temperature. This extrapolation is not appropriate for this case because it does not take into account the effect of the oxygen vacancy formation, that occurs in AmO_{2-x} for T>1100 K even under pure O_2 atmosphere. This leads to an increase of the enthalpy values, as confirmed by the thermodynamic computations presented in this work, which are in very good agreement with the experimental trend. Therefore, even if other excess contributions, such as lattice strain or electronic effects, cannot be excluded, the oxygen vacancy formation is likely responsible for the high enthalpy values measured for the compositions with high Am content. In fact, a reduction similar to that of AmO_2 can be supposed at high temperature, even if the O/M-T-pO_2 equilibria of the $(U,Am)O_{2\pm x}$ are still not well known (see section 2.4.3). This kind of data are fundamental in order to draw reliable conclusions on the behavior of the $(U,Am)O_{2\pm x}$ system. For further improvement of the interpretation of the results, the effect of O vacancies on the heat capacity would need to be further quantified.

6.3 High temperature vapour pressures

Various binary and ternary actinide oxide systems were investigated by Knudsen Effusion Mass Spectrometry (KEMS), as U-O [212], Np-O [213], Pu-O [214], Am-O [149], U-Pu-O [215], Pu-Am-O [64]. KEMS is the method of choice for the measurement of vapour pressures, because it allows distinguishing between the numerous molecular species present in the gas. In particular, actinide oxides exhibit complex gas-solid equilibria, with a gaseous phase composed by various molecular species.

In section 3.3.6, the vaporization behaviour of americium oxides was discussed. KEMS experimental data, for 2000 < T <2200 K, were reported by Gotcu-Freis *et al* on AmO_2 [149]. The simultaneous presence of $AmO_2(g)$, $AmO(g)$ and $Am(g)$ in the vapour was observed (oxygen species could not be measured). A stabilization of the vapour pressures was achieved during the measurements, hence the congruent vaporization was likely reached [149]. According to the authors, the congruent vaporization corresponds to an O/Am= 1.5, hence the sesquioxide Am_2O_3. This is consistent with the instability of stoichiometric AmO_2 at high temperature and the CALPHAD Am-O model presented in Ch. 3.

A very accurate study of the gas phase of the U-O system has been presented in the PhD thesis of Pattoret [216]. Fig. 6.6, extracted from this thesis, represents the vapour pressures measured at 2250 K for $UO_{2\pm x}$ oxides, as a function of the O/U ratio. Several molecular gaseous species are shown: U(g), UO(g), $UO_2(g)$, $UO_3(g)$, O(g). For reduced oxides, with O/U < 2, UO(g) and $UO_2(g)$ species have the highest vapour pressure. A sharp decrease is observed moving toward higher O/U ratios. For O/U≃ 1.92, the most abundand species in the gas becomes UO_2. This latter has a vapour pressure mostly flat in the composition domain shown in Fig. 6.6. A minimum of the total pressure is observed for O/U≃ 1.98: this corresponds to the congruent vaporization, where the compositions of the solid and the gas are equal. Any oxide richer or poorer in oxygen will evolve, by matter loss, toward this O/U ratio. Finally, for O/U > 1.98, a sharp increase of the $UO_3(g)$ and O(g) vapour pressure is observed.

KEMS measurements were performed during the PhD work of F. Lebreton on $(U,Am)O_2$ oxides with Am/(Am+U)=0.3, 0.4 and 0.5, as seen in section 2.4.4.2. Moreover, independent measurements on $(U,Am)O_2$ oxides with Am/(Am+U)=0.1, 0.2 were performed at the JRC-Karlsruhe. In this thesis, the experimental investigation was extended to the compositions with Am/(Am+U)= 0.60 and 0.70. KEMS experiments were performed at the JRC-Karlsruhe centre. The results of this study are presented in the following. Moreover, a coherent analysis of all the data available on $(U,Am)O_2$ oxides is proposed.

6.3.1   Principle and experimental conditions

Details on the experimental set-up and procedure are provided in Appx. A, but the basic principles of the KEMS technique are here summarised. The experimental set-up consists of a Knudsen effusion cell, centred in a high-temperature furnace, coupled to a quadrupole mass spectrometer, entirely placed in a shielded glove box. The powdered samples (∼50 mg) are placed in a Knudsen cell (a crucible with a small orifice). A tungsten Knudsen cell was chosen for the measurements of this work, since the tungsten has a high melting point and low reactivity with actinide materials [217].

The entire system is heated under high-vacuum (10^{-7}- 10^{-8} mbar) at the target temperature (generally 2000<T<2400 K for actinide oxides). When the temperature rises, the solid inside the Knudsen cell begins to sublime-vaporise and an equilibrium is established between the vapour and the solid phase. The small orifice of the Knudsen cell allows a small fraction of the vapour leaving, without altering the equilibrium inside the cell. Under the Knudsen condition, the flux
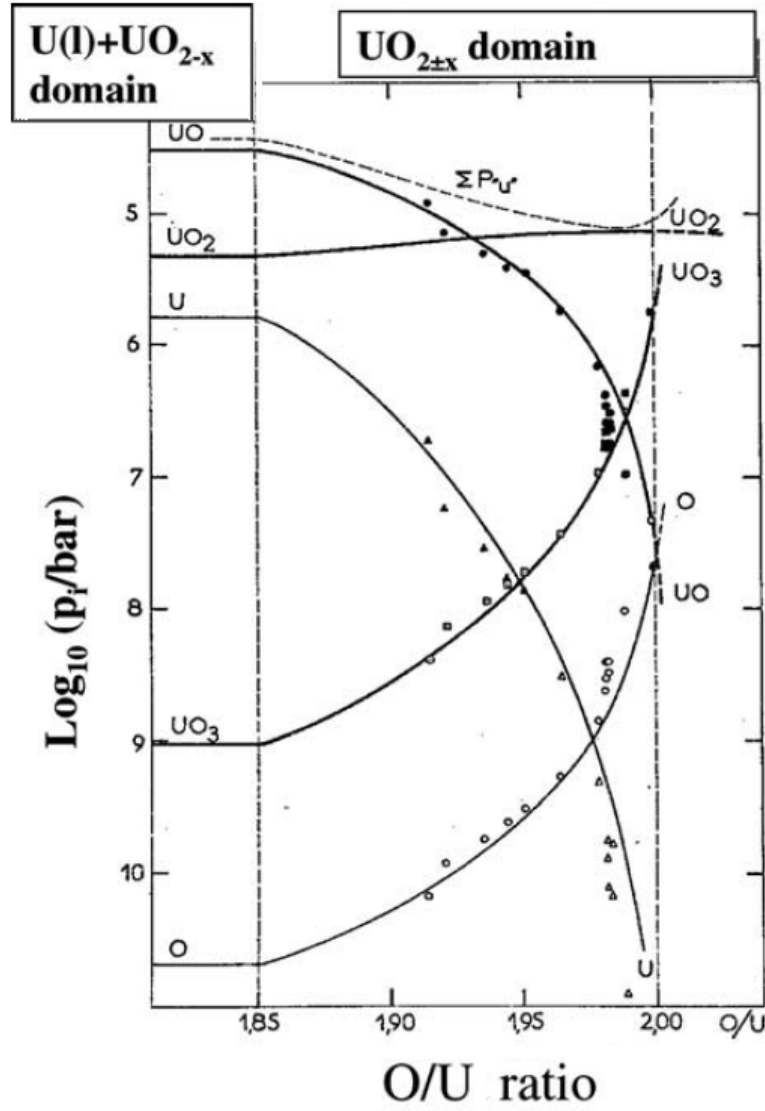
Fig. 6.6: Vapour pressures at 2250 K for $UO_{2\pm x}$ oxides (KEMS study) [216].

of molecules flowing out of the cell is proportional to the partial pressure of the molecular species inside the cell [218]. These effusing molecules are then ionized by bombardment with an electron beam (electron energy = 33 eV). The formed ions are then separated and analysed by the mass spectrometer, using an electrical field. The vapour pressure of the i-species, p_i, can then be calculated from the measured intensity of the corresponding ionic specie I_i^+, as:

$$p_i = I_i^+ \cdot T/K \tag{6.6}$$

where T is the temperature and K is the calibration factor. The K factor depends both on the instrumental features and on the characteristics of the ionic species i. The instrumental factor is obtained by a calibration method based on the vaporization of silver. Details on the determination of the K factor are provided in Appx. A.

The measurements of this work were performed at 2320 K. This temperature was selected because it represents the best compromise between having enough mass spectrometer signal

(detectable vapour pressures) and avoiding the formation of liquid or a too rapid vaporization of the sample. Moreover, KEMS measurements around this temperature were reported for the U-Am-O system [106] and hence the data can be directly compared.

The samples were heated up to 2320 K and the temperature was then kept constant for about 5-6 hours, until the stabilization of the mass signals. As in the previous experiments on (U,Am)O_2 oxides performed at the JRC, the aim was to reach the *congruent vaporization*. For a ternary oxide as (U,Am)O_2, the *total congruent vaporization*, with O/M(solid)= O/M(gas) and Am/M(solid)= Am/M(gas), occurs for one single composition, for a given temperature. For example, KEMS measurements showed that, at 2300 K, the total congruency in (U,Pu)O_{2-x} oxides corresponds to Pu/M slightly below 0.50 [215] and, according to thermodynamic calculations, to Pu/M = 0.42 and O/M = 1.88. [27]. For a ternary oxide with a given Am/M ratio significantly different than the total congruency, the congruency is generally obtained only for the oxygen, thanks to its rapid diffusion, but not for the actinides, as the diffusion of the metals is too slow. In other words, the O/M ratio is equal in the solid and in the gas, but not the Actinide/M ratio (*quasi congruent vaporization*). Small changes in the actinide/metal ratios can anyhow be observed [215], indicating that the composition tends to evolve toward the total congruency. The comparison between the results obtained for different americium contents allows determining the total congruent composition, as shown in the following section.

6.3.2 Ionisation and dissociation

As explained in the previous section, in a KEMS measurement, the vapour pressure of a species i is proportional to the corresponding ionic intensity I_i^+, according to Eq. (6.6). However, in complex systems where several similar species are present in the gas, multiple ionisations and dissociations must be taken into account for the analysis of the data. For this reason, after having reached the stabilization at 2320 K, the ionic intensities were recorded as a function of the energy of the electron beam, to acquire the ionisation efficiency curves for the various gaseous species. The electron energy was varied from 0 to 35 eV, with the aim to detect the dissociations occuring at 33 eV, the energy used for the KEMS measurements.

Similar ionisation efficiency curves were obtained for the two investigated compositions. Those obtained for Am/(Am+U)=0.7 are shown in Fig. 6.7. For the Am species, AmO$^+$ is the most abundant ion, followed by Am$^+$, whereas the AmO$_2^+$ signal is very low. For the U species, (in decreasing order) UO$_2^+$, UO$^+$, UO$_3^+$ and U$^+$ ions are observed.

Some discontinuities are visible in the efficiency curves. These correspond to dissociations process. In order to correctly identify the ionisations and dissociations of the molecular species, the energies reported in the literature for the various reactions [149, 219], schematically shown in Fig. 6.8, were considered.

As an example, the identification of the phenomena contributing to the UO$_2^+$ mass spectrometer signal is shown in Fig. 6.9. The signal starts to be detected at E$\geq$5 eV. This is the minimum energy required to ionize the UO$_2$ molecule and it is named appearance potential. By increasing the electron energy, the UO$_2^+$ regularly increases. A discontinuity occurs at about 11 eV, which
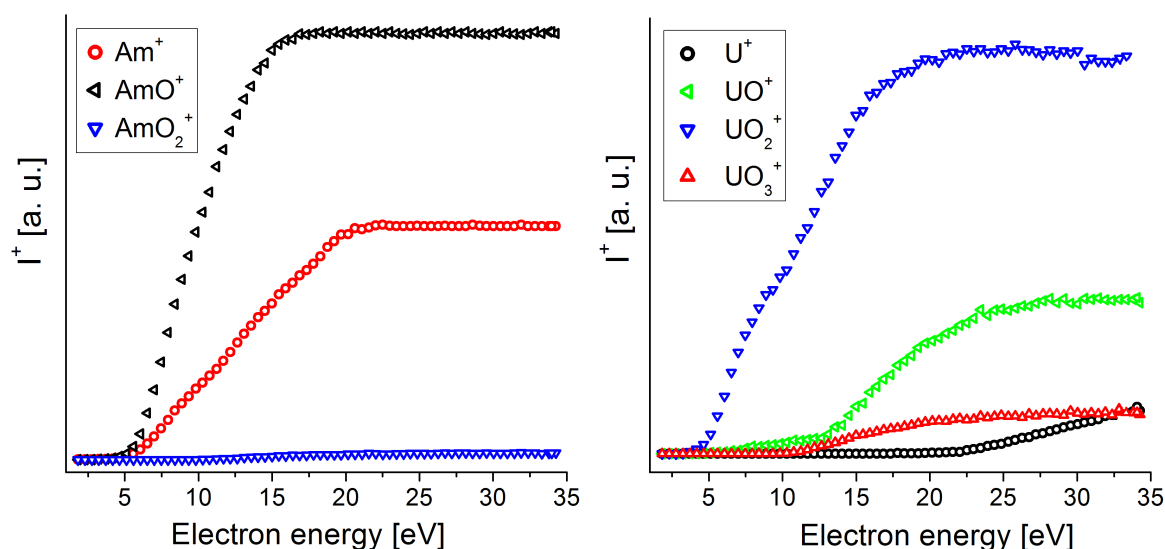
Fig. 6.7: Ionisation efficiency curves for uranium and americium species obtained at 2320 K for the Am70 sample.
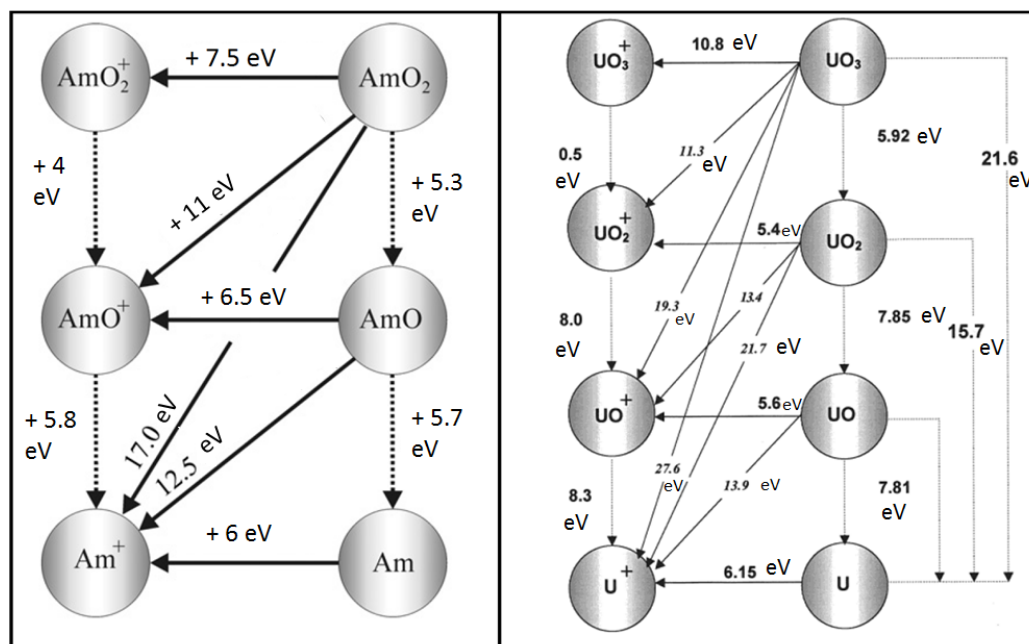
Fig. 6.8: Ionisation and dissociation energies of neutral and positively charged uranium oxides [219] and americium oxides [149] .

is the threshold energy for the $UO_3 \rightarrow UO_2^+ + O + e^-$ reaction. The contribution due to this dissociation increases with the electron energy. Therefore, at 33 eV the UO_2^+ signal is due to two molecular species: $UO_2(g)$ and $UO_3(g)$.

The fragmentation corrections were applied for all the ionic signals and the contribution of each gaseous species in the vapour was calculated. The obtained dissociation factors for the Am60 and Am70 samples are reported in Tab. 6.4. Similar results were obtained for the two compositions. The fragmentation corrections indicated that the U(g) species is negligible; the U^+ intensity comes from the dissociations of the other species. On the contrary, despite the low intensity of the UO_3^+ ions, the $UO_3(g)$ species is not negligible since it is partially dissociated to UO_2^+. For
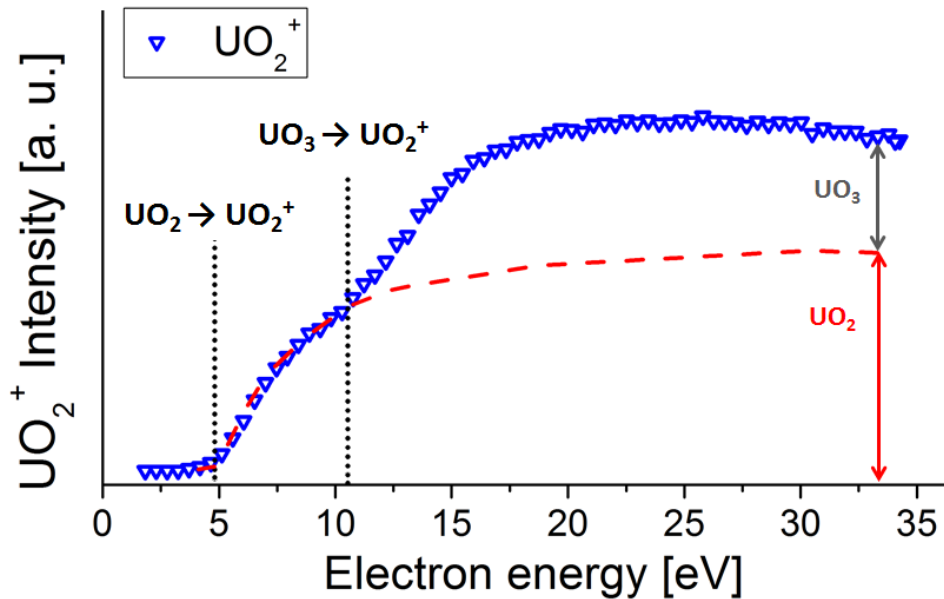
Fig. 6.9: Ionisation efficiency curve for UO_2^+.

the americium species, the fragmentations are less important. Am(g) and AmO(g) are the main species present in the vapour. However, a small dissociation of the AmO_2(g) occurs, contributing in small part to the AmO^+ signal.

| Sample | UO(g) | | | UO_2(g) | | | UO_3(g) | |
	U^+	UO^+		U^+	UO^+	UO_2^+		UO_2^+	UO_3^+
Am60	17%	83%		12%	39%	49%		86%	14%
Am70	6%	94%		9%	32%	59%		79%	21%

| Sample | Am(g) | | AmO(g) | | | AmO_2(g) | |
	Am^+		Am^+	AmO^+		AmO^+	AmO_2^+
Am60	100%		24%	76%		90%	10%
Am70	100%		20%	80%		82%	18%

Table 6.4: Dissociation factors of the U and Am species for a ionization energy of 33 eV.

6.3.3 Vapour pressures at 2320 K

The KEMS data available on (U,Am)O_2 oxides with $0.10 \leq$ Am/(Am+U) ≤ 0.70 are here analysed applying a different methodology than that used by Lebreton in his thesis [106]. More specifically, the ionization cross sections σ were evaluated with a different approach. The ionization cross sections are key parameters for the determination of the K factor of the Eq. (6.6). They are specific to each molecular species and they depend on the energy of the electron beam. The difference of the approach here used concerns the complex molecules as UO, UO_2, UO_3, AmO and AmO_2. For these molecules, no experimental values are available and quantum mechanical calculations are complicated. One simple way to estimate the ionization cross section for a molecule consists in summing those of the constituent atoms. This is called "additivity rule"

and it was applied by Lebreton in his analysis [106]. However, this method does not take into account the molecular bonding. More refined semi-empirical and semi-classical approaches were proposed in the literature [220–222]. The modified additivity rule proposed by Deutsch [222], on the basis of a comprehensive review of experimental data, was here adopted. This takes into account the effect of molecular bonding by introducing weighting factors, which depend on the radii and effective number of electrons of the constituent atoms. Contrary to the additivity rule prediction, the obtained cross sections decrease with the complexity of the molecule: $\sigma(UO_3) < \sigma(UO_2) < \sigma(UO) < \sigma(U)$ and $\sigma(AmO_2) < \sigma(AmO) < \sigma(Am)$. This is due to a screening effect, which has already pointed out in the literature for the gaseous uranium oxides [216]. Differences in the cross section values up to almost a factor of 2 were obtained. This indicates that the ionization cross section is one of the major sources of uncertainty in the determination of the vapour pressures.

The vapour pressures obtained for the various investigated $(U,Am)O_2$ and a UO_2 sample, in the same experimental conditions, are reported in Tab. 6.5 and represented in Fig. 6.10. Considering the uncertainty due the temperature ($\pm$ 20 K), the dissociation process and the ionization cross sections, a relative uncertainty of at least 30% should be considered for the vapour pressure values. These were omitted in Fig. 6.10-(b) for visual clarity.

Initial					Pressure [Pa]					
Am/M	UO_3	UO_2	UO	U	U_{tot}	AmO_2	AmO	Am	Am_{tot}	$\mathbf{p_{tot}}$
UO_2	0.009	3.1	0.67	-	3.78					3.78
10%	0.019	1.37	0.28	0.015	1.68	-	0.06	0.10	0.16	1.84
20%	0.036	1.53	0.17	0.014	1.75	-	0.20	0.192	0.392	2.14
30%	0.27	0.89	0.15	0.011	1.32	0.019	0.33	0.20	0.54	1.86
40%	0.18	0.65	0.11	0.006	0.94	0.012	0.21	0.13	0.35	1.29
50%	0.20	0.42	0.06	0.004	0.68	0.03	0.37	0.17	0.57	1.25
60%	0.11	0.43	0.038	-	0.58	0.065	0.4	0.13	0.60	1.18
70%	0.123	0.25	0.01	-	0.38	0.072	0.613	0.163	0.85	1.23

Table 6.5: Vapour pressures at 2320 K for $(U,Am)O_2$ oxides.

As shown in Fig. 6.10-(a), the total pressure decreases from almost 4 Pa for UO_2 to ~1.2 Pa for the oxides with $0.5 \leq$ Am/(Am+U)≤ 0.7. The value obtained for the Am/(Am+U)=0.10 composition seems too low compared to those of UO_2 and $U_{0.8}Am_{0.2}O_2$, but still within the experimental uncertainty. For $0 \leq$ Am/(Am+U) ≤ 0.4, the major contribution to the total pressure comes from the cumulative uranium pressure (p(U) + p(UO) + p(UO_2) + p(UO_3)). However, this decreases with the americium content, as it would be expected from comparison with other mixed oxide systems as $(U,Pu)O_2$ [215]. The cumulative americium pressure (p(Am)+ p(AmO) + p(AmO_2)) slightly increases, passing from 0.16(5) Pa for Am/(Am+U)=0.10 to 0.85(30) Pa for Am/(Am+U)= 0.7. The cumulative U and Am pressures cross for Am/(Am+U)=0.6 and a minimum of the total pressure seems to be reached for this composition. This indicates that the total congruency occurs for Am/(Am+U) close to this composition.
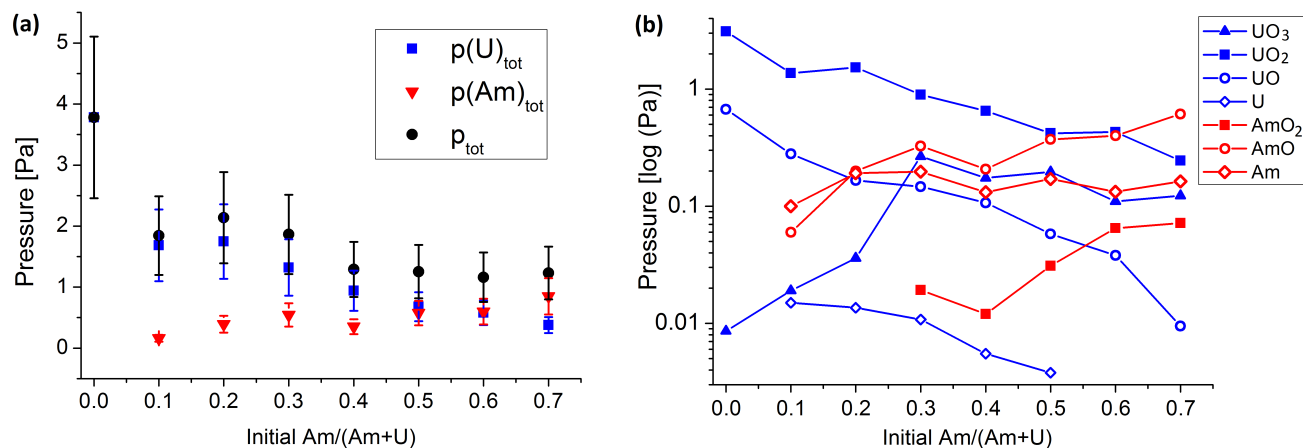
Fig. 6.10: (a) Total pressure and cumulative pressures of the U and Am species as a function of the (initial) Am/(Am+U) ratios of the investigated oxides. (b) Partial vapour pressure of the various U and Am species as a function of the Am/(Am+U) ratio (logarithmic scale).

In Fig. 6.10-(b), the contribution of each species to the vapour pressure is shown. Between the uranium species, UO_2(g) is the most abundant, followed by UO(g) for Am/(Am+U)$\leq$ 0.20 and by UO_3(g) for higher americium contents. UO_2(g) and UO(g) have a regular decreasing trend with the increasing of the americium content. On the contrary, the variation of the UO_3(g) species is peculiar. Firstly, a large increase of this partial pressure is observed passing from the UO_2 sample to the Am/(Am+U)=0.3 composition; subsequently, it slowly decreases for higher americium contents. The high vapour pressure of the UO_3 species is consistent with the mixed U^{4+}/U^{5+} oxidation state of the uranium in the solid phase (see 4). Finally, the U(g) species has the lowest partial pressure and it is not always detectable.

Among the americium species, AmO(g) and Am(g) have the highest partial pressures, with close values. The AmO(g) partial pressure slowly increases with the americium content, whereas the Am(g) is mostly constant. The AmO_2(g) species is not detectable for the oxides with Am/(Am+U) = 0.10, 0.20 and, for the other compositions, it is always lower than the other Am species. However, an increase of the AmO_2(g) pressure of almost one decade occurs with the increasing of the Am/(Am+U) ratio.

6.3.4 Compositions at 2320 K

After the KEMS measurements, the solid phases of the oxide with initial Am/(Am+U)= 0.10, 0.20, 0.60 and 0.70 were analysed by ICPMS (Inductively coupled plasma mass spectrometry), in order to determine the final Am/(Am+U) ratios. The obtained values are (in the order): 0.09(2), 0.19(1), 0.57(1) and 0.73(1). The values are close to the nominal compositions. For the samples with Am/(Am+U) = 0.3, 0.4, 0.5, the analysis could not be performed because not enough material was recovered from the Knudsen cell.

The Am/M, O/U, O/Am and O/M ratios of the gas phase at 2320 K were computed from the vapour pressures. The values are represented as a function of the Am/(Am+U) ratios of the

solid phase (the values measured after the experiment, when available, or the nominal ones) in Fig. 6.11.

The Am/(Am+U) ratio in the gas increases with that of the solid phase (Fig. 6.11-a), as expected. The only exception to the trend is the $U_{0.6}Am_{0.4}O_{2\pm x}$ oxide, whose corresponding Am/M ratio in the gas, equal to 0.27(9), seems too low, but it still consistent considering the uncertainty.
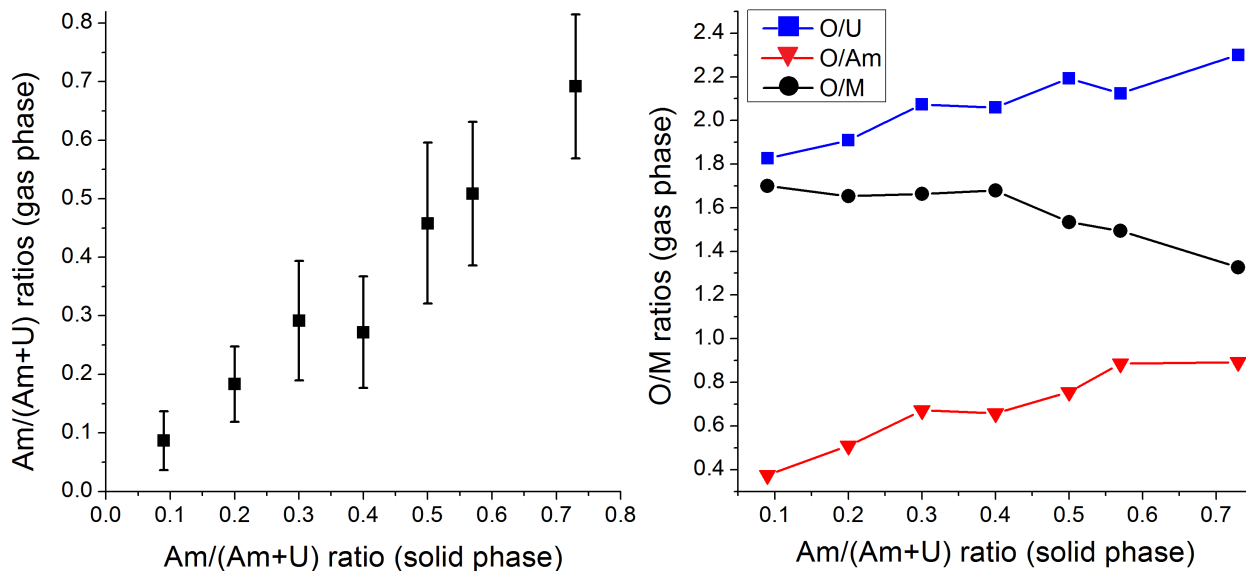
Fig. 6.11: Composition of the gas phase vs the Am/M of the solid phase:(a) Am/(Am+U) ratio; (b) O/U, O/Am and O/M ratio; these data are given with an uncertainty of 0.5, error bars not represented for visual clarity.

The congruent vaporization in the U-O system occurs for O/U $\simeq$ 1.98 (Fig. 6.6). For the Am-O system, the congruent composition is not precisely determined, as discussed in section 3.3.6, but it surely corresponds to an O/Am $\ll$ 2.0, likely close to 1.5. An intermediate O/M between these two values is hence expected for the congruent vaporization of the mixed oxides. Thus, the computed O/M ratios are clearly too low because the oxygen species ($O_2(g)$, $O_3(g)$ and $O(g)$) could not be measured (high background) and hence they are not included in the calculations. The O/U ratio increases from 1.8(5) to 2.3(5) when passing from Am/(Am+U) = 0.10 to 0.70. The increase of the O/U ratio is explained by the high vapour pressure of the UO_3 species for high Am contents. The O/Am ratio increases too with the Am content, but the values are much lower, ranging from 0.4 to 0.9. On the contrary, the computed overall O/M ratio decreases with the americium content in the solid phase. As already said, the obtained values, ranging from 1.7(5) to 1.3(5), are too low because the oxygen species could not be measured. However, the decreasing trend of the overall O/M ratio indicate that the congruent composition for Am/(Am+U) $\simeq$ 0.60 corresponds to an O/M < 2.0. To verify this, the $U_{0.43}Am_{0.57}O_{2-x}$ sample was investigated by XANES, in the same experimental campaign which is described in section 6.4.2. The obtained O/M was 1.90, hence lower than the initial one, equal to 1.94 (see Ch. 4). This result confirms that a reduction occurred, but one cannot trivially conclude on the O/M ratio at 2320 K, since an oxidation likely occurred during the cooling and the storage of the sample (4 months between the KEMS experiment and the XANES measurements). The

O/M ratio corresponding to the total congruency should hence be considered equal or lower than 1.90. This is consistent with the behaviour of the binary oxides.

6.3.5 Conclusions

Vapour pressure measurements were performed by KEMS on $(U,Am)O_2$ oxides with $Am/(Am+U)$ = 0.6 and 0.7. Data from previous works were available on other compositions, ranging from 0.10 $\leq Am/(Am+U) \leq$ 0.5. The focus was here on the variation of the vapour pressures with the $Am/(Am+U)$ ratio of the solid, at one single temperature, 2320$\pm$ 20 K. All the data available were hence analysed with the same approach. Despite the large uncertainties, characteristic of the measurements on gas phases, the results obtained for the various oxides were consistent. Regular decreasing trends with the Am content were observed for the total pressure and the cumulative pressure of the uranium species, whereas a slight increase of the americium species was highlighted. The orders of magnitude of the various uranium (UO, UO_2, UO_3) and americium (Am, AmO, AmO_2) species were coherent between the various oxides investigated. The most abundant uranium species was UO_2 for all the compositions. Between the americium species, AmO is the one with the highest partial pressure.

A cross of the cumulative uranium and americium species occurred for $Am/(Am+U)$=0.6, co-inciding to the minimum of the total pressure. This indicates that the total congruency is close to this composition. Unfortunately, the corresponding O/M ratio could not be determined accurately since the oxygen species in the gas could not be measured (because of the high natural background). However, the O/M ratio of the gas, obtained considering only the actinide species, decreases with the Am content. This indicates that the congruent composition likely occurs in the oxygen hypostoichiometric domain, consistently with the behaviour of the binary oxides. Moreover, the Am60 sample recovered from the Knudsen cell was analysed (4 months after) by XANES and an O/M=1.90(2) was obtained. Since a re-oxidation of the sample cannot be excluded during the cooling from 2320 K to room temperature and the following storage, it can be concluded that the total congruency occurs for $Am/(Am+U)\simeq$0.60 and O/M$\leqslant$1.90(2).

6.4 Melting behavior of U-Am oxides

The melting behaviour of $UO_{2\pm x}$ is well known, as seen in section 2.1. A congruent melting occurs for an O/M$\simeq$2.0 (1.98 according to the assessment of Gueneau [27]), whereas the melting temperature decreases for any departure from the oxygen stoichiometry. On the contrary, the melting behaviour of AmO_2 is not well established. Only one set of measurements is reported in the literature [63] and, in this experiment, largely scattered values were obtained by varying the heating rate. The highest obtained melting temperature- of about 2385 K- was associated to AmO_2, but the O/Am ratio was not determined after the melting. As seen in Ch. 3, according to the CALPHAD assessment here proposed for Am-O, the americium dioxide does not melt congruently, since a reduction occurs at high temperature, leading to an O/Am ratio below 2. Finally, for (U, Am)O_2 oxides, very few data are available for the melting temperature and these are limited to low $Am/(Am+U)$ ratios (see section 2.1.4).

In this part, the melting behaviour of $(U,Am)O_2$ oxides is investigated by a laser-heating technique in a large composition domain, for $0.075 \leq Am/(Am+U) \leq 0.7$. The results of these measurements are discussed in section 6.4.1 and the subsequent post-melting characterizations are presented in section 6.4.2

6.4.1   Melting temperature measurements

6.4.1.1   Experimental procedure

The melting temperature (T_m) measurements were performed at the JRC-Karlsruhe centre, using a laser-heating technique coupled with fast pyrometry.
The experimental set-up and technique were described in detail in previous works [32, 223–226] and a summary is provided in Appx. A. The main advantages of the laser-heating technique are the short measurements duration and the quasi-containerless conditions. During the experiment, the pellets are inside an autoclave, supported in a 3-pin mount by graphite screws, and the laser is focused onto a spot smaller than the sample surface, hence only a limited part is melted. The rest of the pellet can be considered as a "self-crucible" and no contamination with foreign surrounding materials occurs.

The melting-T measurements were performed on the samples with $Am/(Am+U) = 0.075$, 0.10, 0.20, 0.30, 0.5 and 0.7, whose initial characteristics were described in chapter 4. In order to study the effect of the O/M ratio variations, the experiments were performed both under argon and under air for all the compositions, with the exception of the Am70 sample. For this latter, because of the limited quantity of material available, only the measurements under air were performed. To prevent an excessive vaporization of the oxides, a overpressure of about 100 MPa was applied.

A typical result of a melting measurement is reported in Fig. 6.12. The laser-power profile
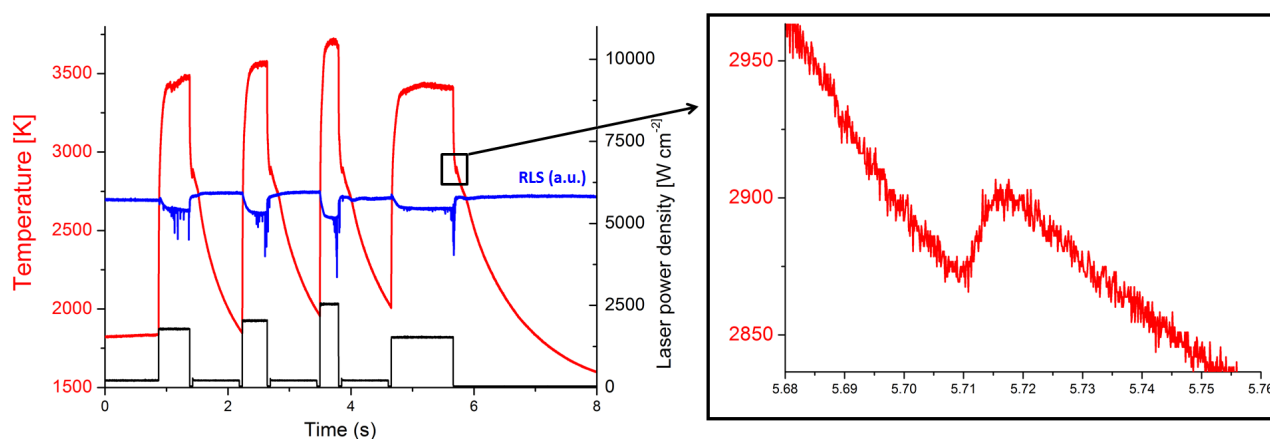
Fig. 6.12: Thermogram (red), laser power profile (black) and reflected light signal (blue) recorded in a laser melting measurement in argon on the Am50 sample.

is represented in black. One measurement was constituted by a pre-heating at about 1500 K, followed by 4 consecutive step-type laser pulses. These were programmed with different duration and intensity, in order to exclude kinetic effects in the measured melting temperature. The red curve in Fig. 6.12 is the thermogram (temperature vs time), acquired with the fast pyrometer (see Appx. A). The melting temperature is determined from the cooling part of the thermogram, by locating the main thermal arrests, which indicates the sample solidification. In addition, a second method was used to facilitate the identification of the melting/freezing transition: the "reflected light signal" (RLS). This relied on a probe *blue* laser, reflected off the sample surface and detected by a pyrometer. Abrupt changes in the reflectivity of the sample indicate the formation of the liquid phase.

At the end of the measurement (4 consecutive laser pulses), the sample was left to cool down to room temperature and checked by visual inspection. The autoclave windows were cleaned (vaporization of the sample) and the gas renewed. Then, the measurement was repeated for the statistic.

6.4.1.2   Experimental results

For the $(U,Am)O_2$ oxides with $0.075 \leq Am/(Am+U) \leq 0.50$, several consecutive measurements of the melting temperature were performed, both under argon and air. For some of the compositions, more than one pellet (from the same batch) were used for the experiments (depending on the material availability). A general overview of all the obtained results is presented in Fig. 6.13. Error bars were omitted for visual clarity, but the uncertainty of each measurement was determined according to the error propagation law, taking into account the standard uncertainty associated to the pyrometer calibration (± 10 K at 3000 K), the sample emissivity ($\pm$ 21 K at 3050 K) and the accuracy in detecting the onset of vibrations in the RLS signal. The estimated cumulative uncertainty is about $\pm 2\%$ of the reported temperature.

Fig. 6.13 shows that the $(U,Am)O_{2\pm x}$ oxides exhibit different behaviours under argon (left) and under air (right). For all the compositions, the T_m measurements under argon were very reproducible. The obtained T_m values generally decrease with the americium content of the sample. A more complicated behaviour was observed under air. For the samples with $0.075 <$ Am/(Am+U) <0.2, the measured T_m decreased during the first laser shots and then it stabilized to 300-400 K lower values. For the Am/(Am+U)= 0.20, three pellets were available for the experiment and this evolution was repeatable for all the samples. For the Am30 and Am50 samples, no clear evolution of the melted temperature was observed during the attempts in air. The obtained values were close to those measured in argon, but slightly lower in any case.

For the $U_{0.3}Am_{0.7}O_{1.90}$, only a small fragment of pellet was available for the experiment. For this reason, only one measurement under air could be performed for this composition.

The average values of the melting temperature measurements are represented as a function
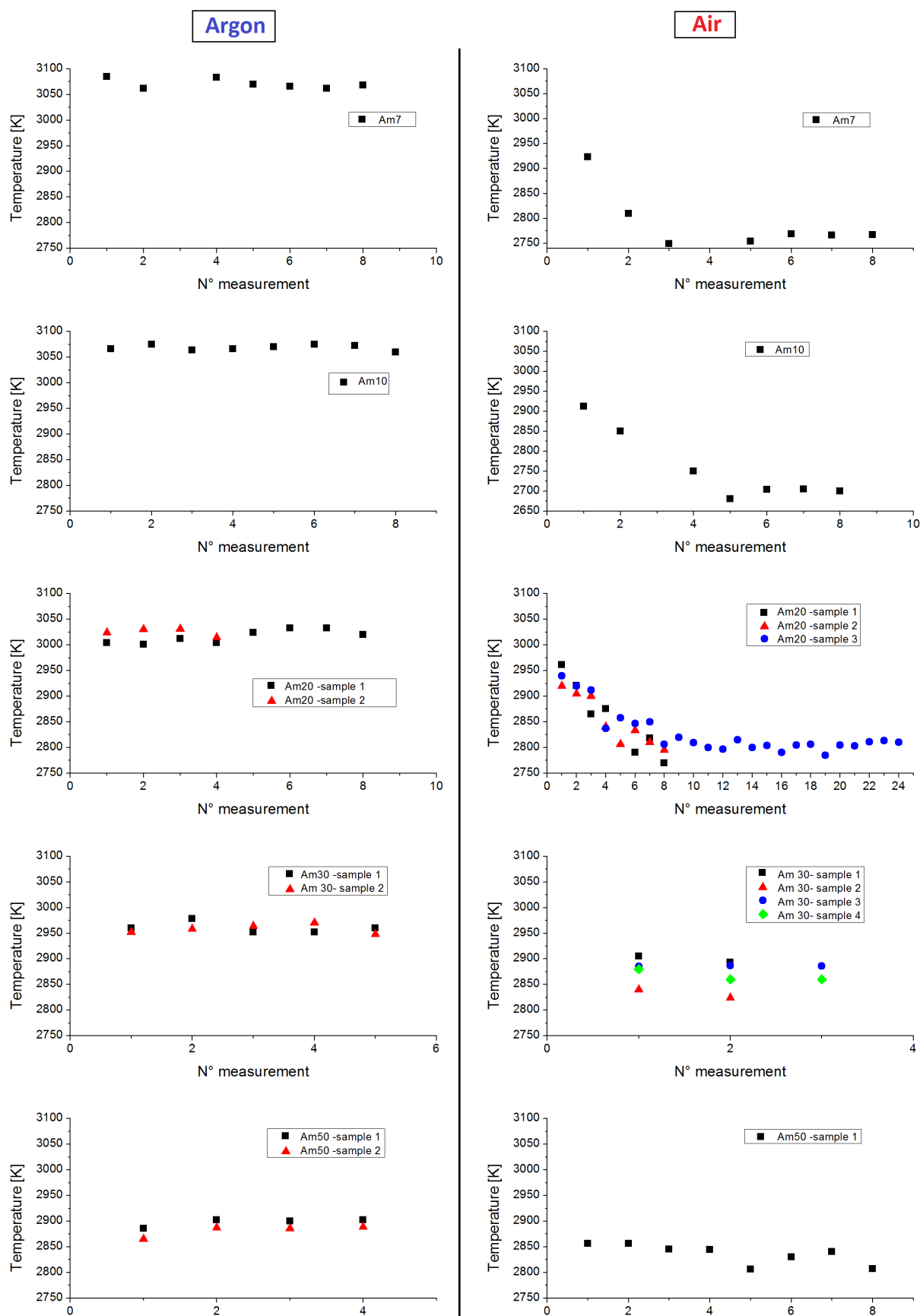
Fig. 6.13: Melting temperature results in consecutive measurements, in Ar and air.

of the initial Am/(Am+U) ratio in Fig. 6.14. For the measurements under air, only the data

obtained after the initial evolution were considered. For comparison, the literature data for UO_2 [32], AmO_{2-x} [63] and $(U, Am)O_{2+x}$ oxides [75] are also reported in Fig. 6.14.
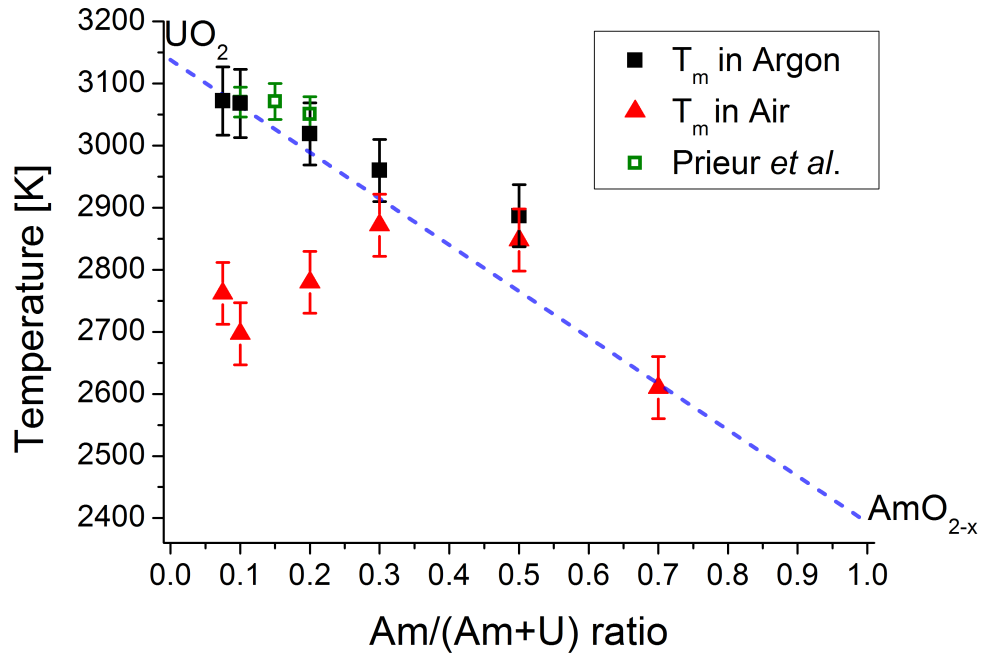
Fig. 6.14: Melting temperatures as a function of the initial Am/(Am+U) ratio of the sample. The results of this work are compared to the data reported in the literature for UO_2, AmO_{2-x} and $(U, Am)O_2$ oxides with Am/(Am+U)=0.10, 0.15, 0.20 [75].

The melting temperatures measured by Prieur *et al.* under argon are in good agreement with the values observed in this work in the same atmosphere. A monotonic, almost linear decrease of the melting temperature with the Am/(Am+U) ratio is observed in this case. It is important to remember that the initial O/M ratio of the samples was not equal to 2.0 for all the compositions (see Ch. 4). Besides, the O/Am ratio corresponding to the melting of AmO_{2-x} is unknown. Therefore, the UO_2-AmO_{2-x} dashed line in 6.14 was drawn as a guide to the eye, but there was no reason to expect this exact trend.

The melting temperatures measured under air are generally lower than those obtained under argon. The variation with the Am/(Am+U) ratio is not monotonic in this case. Close values, around 2700-2760 K, were observed for Am/(Am+U)=0.075 and 0.10. These values are almost 400 K lower than those measured in argon. For $0.10 \leq$ Am/(Am+U)$\leq$0.5, an increase of the melting temperature with the americium content is observed. The highest values are found for the Am30 and Am50 samples. Interestingly, the values obtained for these two compositions under air and under argon are very close. Finally, a large decrease of the melting temperature was observed for Am/(Am+U)= 0.70 in air.

The difference between the results obtained under argon and air clearly indicates a variation of the composition of the investigated samples. For the measurements performed in argon, no evolution of the melting temperature was observed in the consecutive attempts, as previously dis-

cussed and shown in Fig. 6.13. Therefore, no or very limited composition changes occurred under the inert atmosphere. On the contrary, a clear evolution/decrease of the melting temperature was observed for $0.075 \leq$ Am/(Am+U) ≤ 0.2. A similar evolution and generally lower values for the melting temperatures in air were already observed for $(U,Pu)O_{2\pm x}$ oxides [227,228]. These effects can be attributed to the O/M increase and, probably, the formation of hyper-stoichiometric oxides such as M_4O_9 and M_3O_8. Moreover, also changes of the Am/(Am+U) ratios cannot be excluded. Despite the overpressure imposed during the experiment, a partial vaporization of the sample could not be completely avoided. This was clearly observed during the experiments under air: at the end of each measurement series, the windows of the autoclave were covered in powder. As seen in section 6.3, the uranium and americium species have different partial vapour pressures. Therefore, the vaporization of the solid phase could also lead to small variations of the Am/(Am+U) ratio.

In order to obtain reliable phase diagram data, it is necessary to associate a composition to the measured melting temperature. For this reason, post-melting characterization were realized and the results are presented in the next section.

6.4.2 Characterization of the melted sample

As previously mentioned, one of the main advantages of the laser-heating technique is the possibility to obtain containerless conditions, by heating a small fraction of the targeted pellet. In this condition, the sample itself can be considered a self-crucible. This is confirmed by the SEM microscopy images obtained on the melted fragments, as for example shown in Fig. 6.15 for the $U_{0.5}Am_{0.5}O_{2\pm x}$ oxide melted in argon. The more internal part, in respect to the surface targeted with the laser, maintained the initial microstructure observed after the manufacture (see chapter 4). Well-faceted grains of about 10-20 μm are clearly discernible (region 3). Moving toward the surface, an "intermediate region" appears (2), with round-shaped grains that start to connect each other. This part of the sample was at high temperature and it was about to melt. Finally, the surface heated by the laser is clearly discernible in the fragment, because the initial microstructure with well-faceted grains is lost. The melted part seems more dense and compact, without grain boundaries. At higher magnification (region 1), columnar dendrites, typical of the solidification process, can be observed.

Fig. 6.15 shows that the melted part is a small fraction of the sample, with a thickness of about 150-200 μm. Although this characteristic of the laser-heating technique is ideal for the study of high temperature property, the drawback is that the material available for the characterization is very limited. For this reason, the melted samples could only be investigated by XAS, since this technique demands only few mg of materials. The measurements were performed at the INE (Institute for Nuclear Waste Disposal) beamline [229,230] of the ANKA synchrotron facility (Karlsruhe Institute of Technology, Germany), 4 months after the melting temperature experiments. During that time, the samples were stored in a glove box, under an inert nitrogen atmosphere. All the melted oxides were analysed, except the Am/(Am+U)=0.7 composition, for which the sample could not be retrieved after the melting. Besides, also the as-manufactured
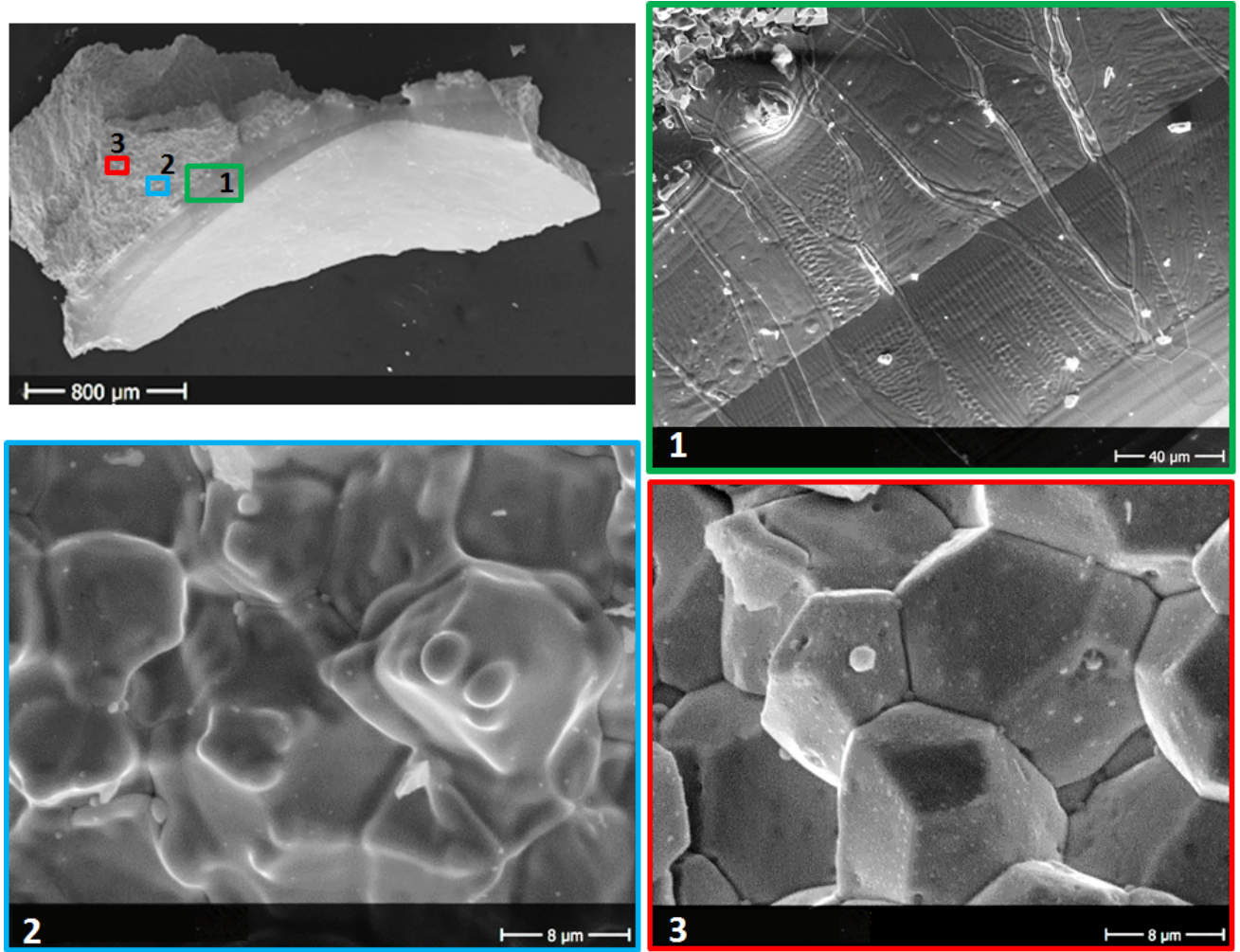
Fig. 6.15: SEM images acquired on the the $U_{0.5}Am_{0.5}O_{2\pm x}$ oxide melted in argon.

samples were characterized at the same time, in order to directly compare the data. In the following, these will be identified as "Amy", with y equal to the nominal Am/(Am+U) ratio. For the melted samples, the suffix "Ar" or "air" is added, according to the atmosphere of the melting measurements.

The conditions of the XAS measurements are detailed in Appx. A. The XAS characterizations were performed with two objectives: the determination of the Am/(Am+U) ratio, through the fluorescence emission; the determination of the O/M ratio by XANES.

6.4.2.1 Determination of the Am/(Am+U) ratio

In this part, the fluorescence emission is used to determine the Am/(Am+U) ratios. This technique was not applied in the previous XAS investigations presented in this work because, for the as-sintered samples, enough material was available for the TIMS analysis (Ch. 4). A description of the method is hence provided.

The basic theory of the XAS spectroscopy is described in Appx. A. The principle of this technique is the photoelectric effect, which leaves the element in an excited state. One of the main mechanisms of disexcitation is the x-ray fluorescence, in which a higher energy core-level elec-

tron fills the deeper core-hole, ejecting an X-ray of well-defined energy. The fluorescence energies emitted in this way are characteristic of the atom, and can be used to identify the elements in a system and also to quantify their concentrations. Indeed, the X-ray fluorescence intensity I_f is proportional to:

$$I_f \propto \mu(E) \cdot I_0, \tag{6.7}$$

where I_0 is the X-ray intensity incident on the sample and $\mu(E)$ is the absorption coefficient. For incident X-ray with energy E sufficiently far from the absorption edge, $\mu(E)$ is a smooth function of the energy and it can be expressed as:

$$\mu(E) \approx \frac{\rho Z^4}{A E^3}, \tag{6.8}$$

where Z and A are respectively the atomic and mass numbers and ρ is the element density. Therefore, considering elements with close atomic numbers as uranium and americium:

$$\frac{I_f(U)}{I_f(Am)} \propto \frac{m(U)}{m(Am)}, \tag{6.9}$$

where m is the mass of the element in the sample. The Am/(Am+U) ratio can hence be obtained by fluorescence spectroscopy.

The method was firstly applied to the as-manufactured samples, whose compositions were previously determined (Ch. 4). X-rays with E = 18.9 keV were used. This energy was chosen because it is beyond the U-L$_3$ ($\sim$ 17166 eV) and Am-L$_3$ ($\sim$ 18510 eV) edges, but below the L$_2$ edges. As an example, one of the X-ray fluorescence spectrum acquired on the Am20 sample is shown in Fig. 6.16-(a). Two characteristic peaks are observed at about 13614 eV and 14620 eV. The first peak corresponds to the fluoresce X-rays emitted by uranium during the Lα_1 (M$_5 \to$ L$_3$) and Lα_2 (M$_4 \to$ L$_3$) electronic transitions. The second peak is due to the emissions from americium, for the same electronic transitions Lα_1 and Lα_2.

For all the as-sintered samples, the ratio between the intensity of the two fluorescence peaks was computed. For the intensity, both the maxima and the area of the peaks were tested. Besides, two different detectors were simultaneously used for recording the fluorescence emission (see Appx. A). For all the cases, the obtained $I_f(Am)/[I_f(Am)+I_f(U)]$ ratios were very similar. The values are represented as a function of the "real" (previously determined by TIMS) composition of the sample in Fig. 6.16-(b). As expected, a linear trend was obtained:

$$\frac{I_f(Am)}{I_f(U) + I_f(Am)} = a \cdot Am/(Am + U) + b. \tag{6.10}$$

The a and b parameters were obtained by fitting the points of Fig. 6.16-(b).

The fluorescence spectra of the melted oxides are compared to the as-sintered samples in Fig. 6.17. Small but clear differences in the $I_f(Am)/I_f(U)$ ratios between the melted and as-sintered samples are observable for the Am20, Am30 and Am50 oxides. A higher Am intensity is observed for all the melted samples, especially for those melted in air. The Am/(Am+U)
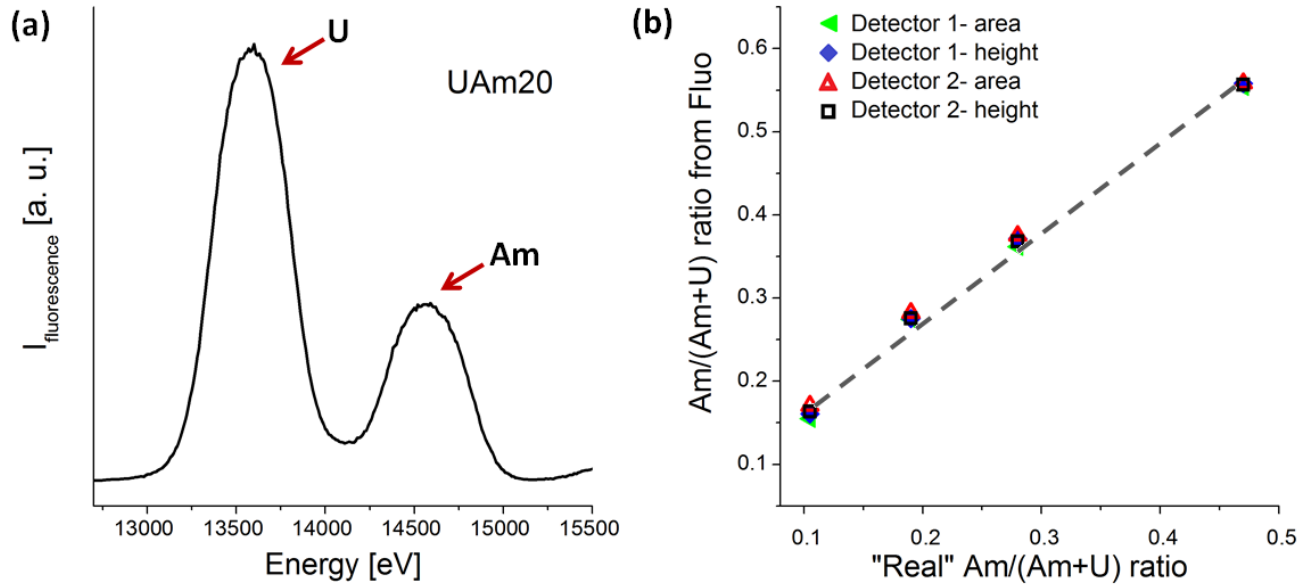
Fig. 6.16: (a) Fluorescence X-ray spectrum of the UAm20 sample for incident X-ray with E = 18.9 keV. (b) Am/(Am+U) ratio obtained by Fluorescence spectroscopy for the as-sintered samples.

ratios were determined by inverting Eq. (6.10) and the results are summarized in Tab. 6.6 and represented in Fig. 6.17 (bottom, right). The obtained Am/(Am+U) ratios of the melted

	Measured Am/(Am+U) ratios [%]		
Sample	As-sintered	Melted Argon	Melted Air
Am7	7.0(2)	7(1)	7(1)
Am10	10.5(8)	10(2)	10(2)
Am20	19(2)	21(3)	23(3)
Am30	28(2)	30(3)	32(3)
Am50	48(1)	47(1)	51(3)

Table 6.6: Am/(Am+U) ratios before and after melting.

samples are very close to the initial ones. This confirms that the rapidity of the laser-heating technique prevents important chemical composition changes. However, for the nominal compositions Am/(Am+U)= 0.2, 0.3 and 0.5, the results systematically show a slightly higher americium content. This indicates that, during the melting measurements, the loss of uranium was larger than that of americium. This is consistent with the vaporization behaviour investigated in the previous section: for Am/(Am+U) < 0.6, the vapour pressures of the uranium species are higher than those of americium, leading to a slight increase of the Am content.

6.4.2.2 Determination of the O/M ratio

For the determination of the O/M ratios, the XANES technique was applied, with the same methodology already used in Ch. 4 and Ch. 5. XANES spectra were collected at the L_3 edge of Am and U. For each composition, the spectra of the as-sintered and melted samples are
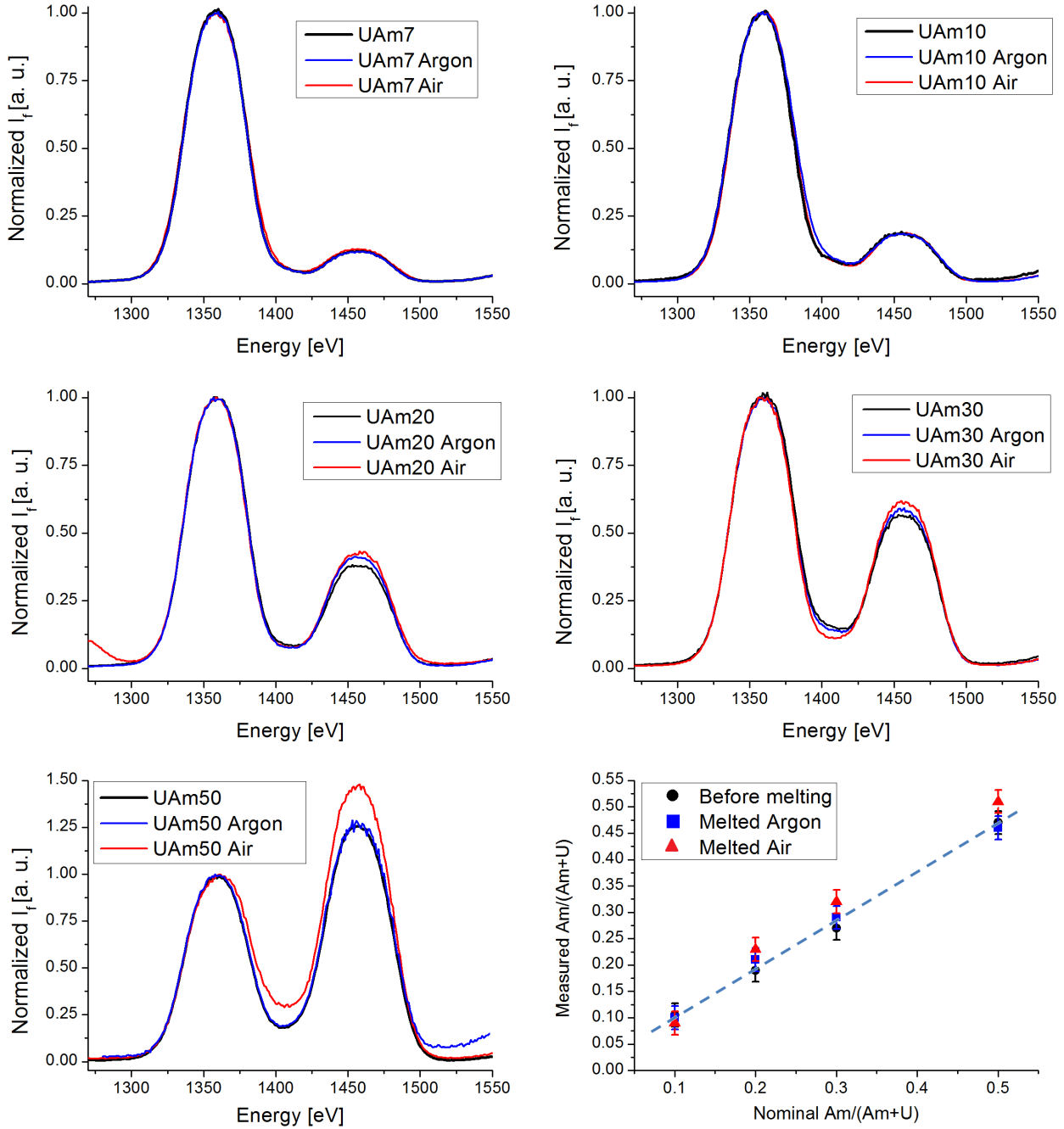
Fig. 6.17: Comparison of the fluorescence spectra obtained on the as-sintered and melted samples of each composition and (bottom-right) resulting Am/M ratio vs the nominal Am/M.

compared in Fig. 6.18 and Fig. 6.19, respectively for the Am-L$_3$ and U-L$_3$ edges. The observed energies of the inflection points and white lines are reported in Tab. 6.7. Besides, the white line positions are compared in Fig. 6.18 and Fig. 6.19 (bottom, right).

For the Am-L$_3$ edge, the inflection point and white line positions of all the melted samples are identical, within the experimental uncertainty, to the as-manufactured oxides. In these latter, as seen in chapter 3, americium is purely trivalent. Only for the *Am50Air* sample (melted in air), a small shift of the inflection point and the white line toward higher energies is observed. This indicates a slight oxidation of americium in this sample.
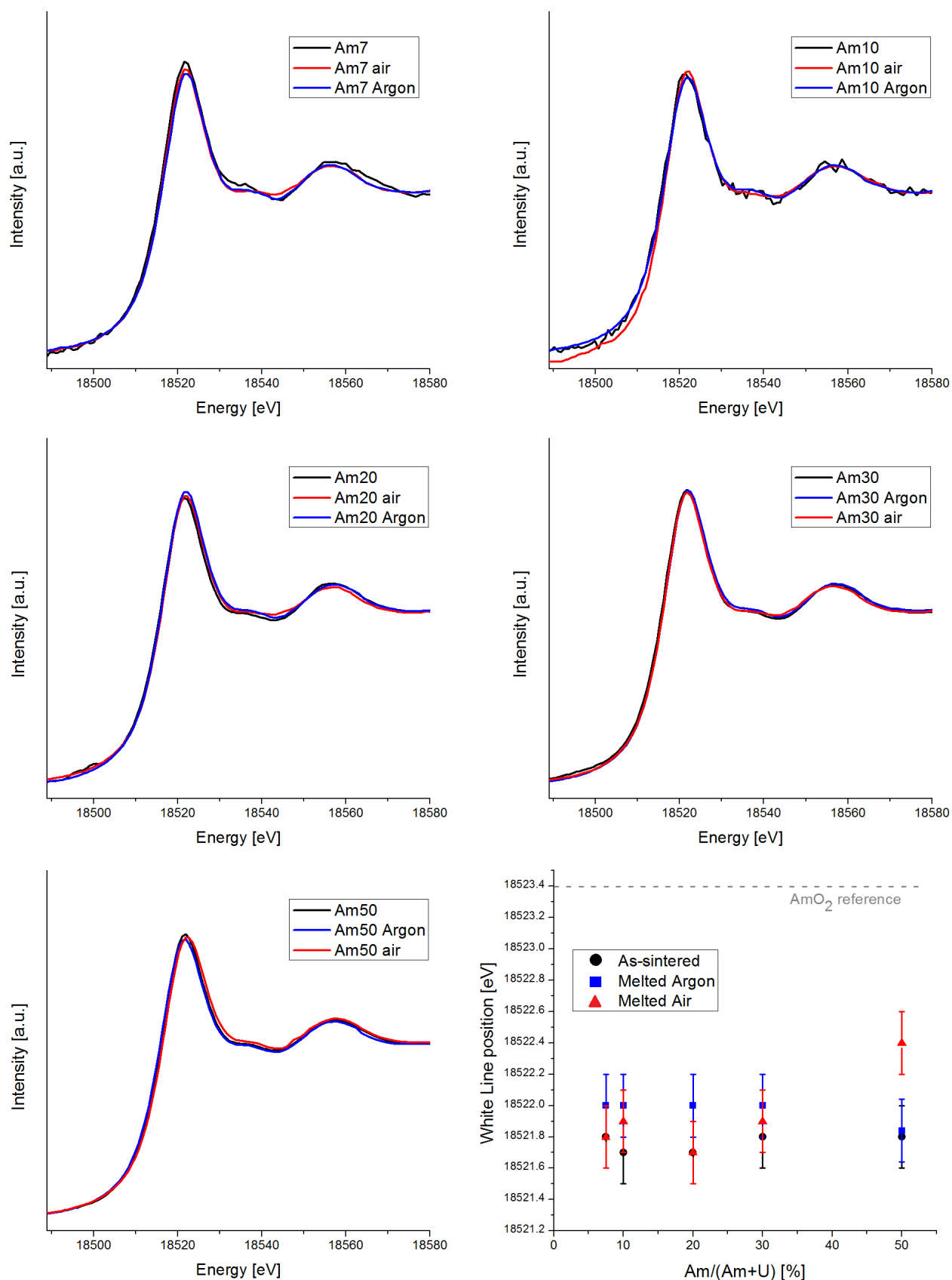
Fig. 6.18: XANES spectra collected at the Am-L$_3$ edge of Am on (U,Am)O$_2$ oxides, before and after melting. Bottom right: observed white lines.

Sample	Am L$_3$ edge [eV]		U L$_3$ edge [eV]	
	Inflection point	White line	Inflection point	White line
Am7	18517.4	18521.8	17170.3	17177
Am7Argon	18517.5	18522	17170	17177.12
Am7Air	18516.9	18521.8	17171	17177.8
Am10	18517.1	18521.7	17170.2	17177.1
Am10Argon	18517.1	18522	17169.8	17177.1
Am10Air	18517.4	18521.9	17172.5	17178.5
Am20	18516.9	18521.6	17171.1	17177.3
Am20Argon	18516.9	18522	17170	17177.4
Am20Air	18517	18522.1	17172.8	17178.7
Am30	18516.9	18521.8	17171.5	17177.5
Am30Argon	18517	18522	17172.4	17178
Am30Air	18517	18521.9	17172.6	17178.9
Am50	18516.9	18521.8	17172.7	17179.5
Am50Argon	18516.7	18521.8	17171.1	17178.6
Am50Air	18517.3	18522.4	17173	17179.7
AmO$_2$	18518.9	18523.4		
UO$_2$			17170.3	17177
U$_3$O$_8$			17173.3	17181.1

Table 6.7: Energy positions of the inflection points and white lines of the XANES spectra presented in Fig. 6.18 and Fig. 6.19. Values are given with a 0.3 eV uncertainty.
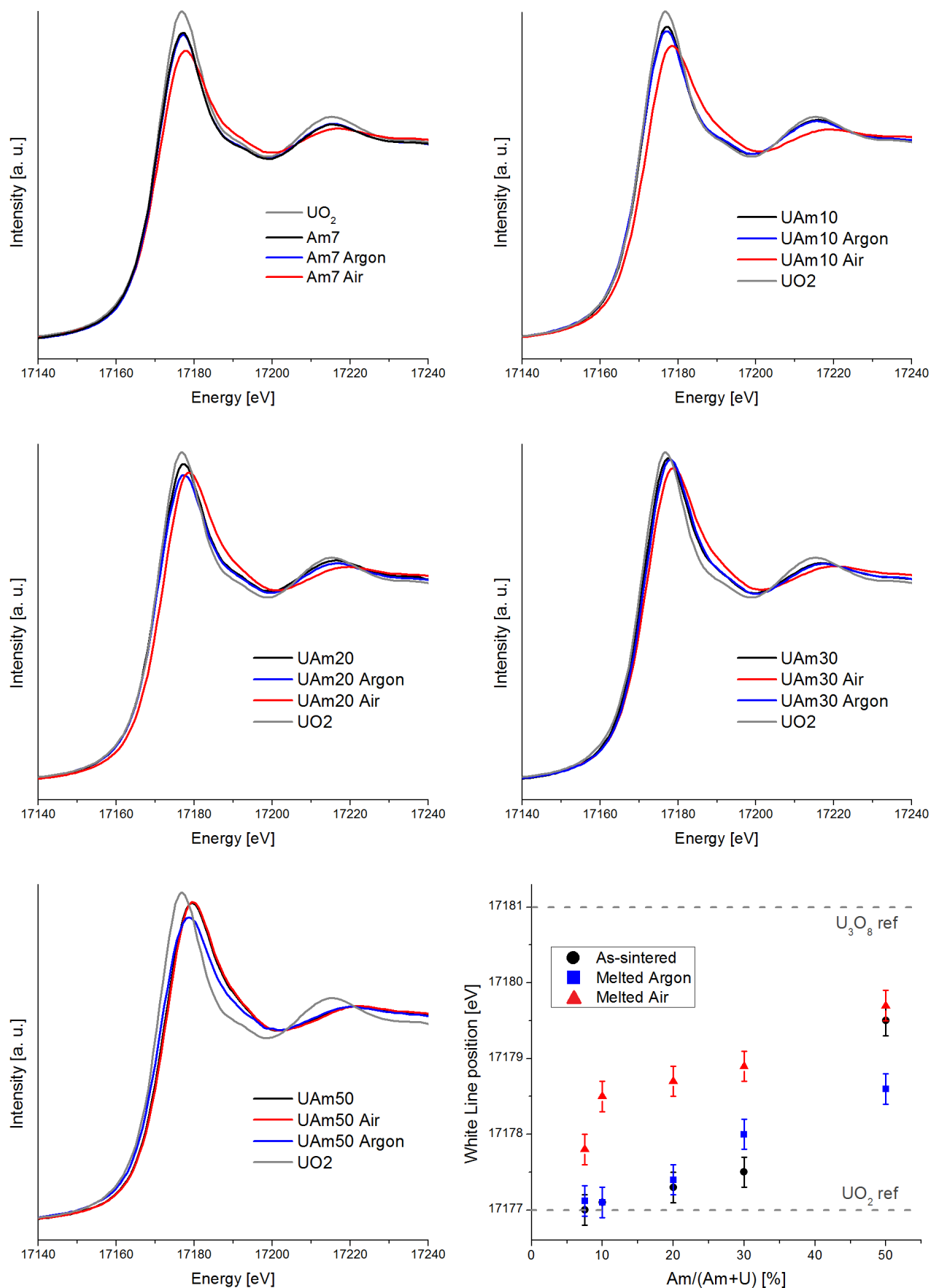
Fig. 6.19: XANES spectra collected at the U-L$_3$ edge of Am on (U,Am)O$_2$ oxides, before and after melting. Bottom right: observed white lines.

A more complicated picture is observed for the U-L_3 edge. For the as-sintered samples, the white line energies generally increase with the americium content, indicating a higher average oxidation state of uranium. This is consistent with the results discussed in Ch. 4.

For the oxides melted under argon, the white lines are very close to the corresponding as-sintered samples, for Am/(Am+U)≤0.20. For *Am30Argon*, the white line is shifted to higher energy, indicating an increased oxidation. On the contrary, for *Am50Argon*, the white line is shifted to lower energy, pointing out a reduction.

Finally, for the samples melted in air, the white lines are always shifted toward higher values, indicating an increase of the oxidation state of uranium.

The average oxidation state of uranium and americium were obtained by linear combination fit of the XANES spectra, according to the procedure explained in Ch. 4. However, the U_4O_9 oxide, previously used as reference, was not available during the experiment (the U_4O_9 spectrum presented in the previous chapter could not be used because of set-up differences between the INE (Anka) and ROBL (ESRF) beamline). For this reason, the as-sintered *Am30* oxide was used as reference. Indeed, as seen in Ch. 4, the uranium average oxidation state in this sample was +4.45, hence very close to that of U_4O_9 (+4.5). The results of the linear combination fits are reported in Tab. 6.8 and the O/M ratios (computed using the measured Am/M values) are represented in Fig. 6.20.

	Am L_3 edge			U L_3 edge				
Sample	(Am^{3+})-ref	AmO_2	AOS	UO_2	Am30	U_3O_8	AOS	O/M
Am7	1	0	3	0.85	0.15	0	4.07	2.00(2)
Am7Argon	1	0	3	0.77	0.23	0	4.10	2.01(2)
Am7Air	1	0	3	0.66	0	0.34	4.45	2.17(2)
Am10	1	0	3	0.74	0.26	0	4.12	2.00(2)
Am10Argon	1	0	3	0.73	0.27	0	4.12	2.00(2)
Am10Air	1	0	3	0.28	0.26	0.46	4.74	2.28(2)
Am20	1	0	3	0.43	0.57	0	4.26	2.01(2)
Am20Argon	1	0	3	0.80	0	0.20	4.27	2.00(2)
Am20Air	1	0	3	0	0.58	0.42	4.82	2.20(2)
Am30Argon	1	0	3	0	0.87	0.13	4.57	2.05(2)
Am30Air	1	0	3	0	0.59	0.41	4.82	2.12(2)
Am50	1	0	3	0	0.69	0.31	4.75	1.96(2)
Am50Argon	1	0	3	0.43	0.14	0.43	4.62	1.93(2)
Am50Air	0.67	0.33	3.33	0	0.54	0.46	4.85	2.04(2)

Table 6.8: Results of the linear combination fit of the U-L_3 and Am-L_3 XANES spectra.

For the as-sintered samples, the O/M values are identical (within the uncertainty) to those obtained in the previous investigation (see Ch. 4). This confirms the validity of using the *Am30*

sample as a reference.
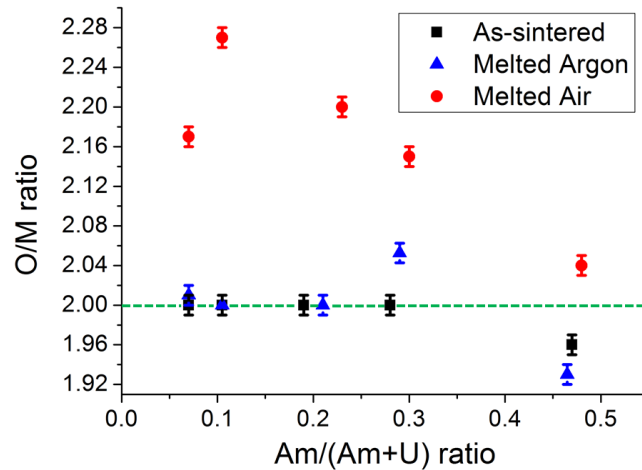
Fig. 6.20: Composition of the melted samples obtained by XAS investigation.

The oxygen stoichiometry of the oxide with Am/(Am+U)≤0.20 was maintained during the melting under argon. For the *Am30Argon* and *Am50Argon* samples, the O/M ratios were respectively higher and lower than the initial ones. A reduction of the Am/(Am+U)=0.5 at high temperature, under argon, is not surprising, considering the results obtained in Ch. 5. Indeed, the addition of americium in the fluorite structure generally stabilizes the hypostoichiometric domain. In this frame, the oxidation of the Am/(Am+U)=0.3 is quite unexpected, especially considering that this had not occurred for the samples with low americium contents. Therefore, this result seems inconsistent with the others and it should be considered with caution, since probably an alteration of the sample occurred during the store or the preparation for the synchrotron.

An increase of the O/M ratio occurred for all the samples melted in air. The oxidation was particularly large for the oxides with low americium content, and especially for the *Am10Air* sample. In this case, an O/M = 2.28(2) was obtained and hence hyperstoichiometric oxide as M_4O_9 and M_3O_8 were surely formed, even if the identification of the phases could not be performed. The increase of the O/M ratio seems less and less important with the increasing of the Am/M ratio. The oxidation was very limited for the *Am50Air* sample, whose final O/M was equal to 2.04(2).

6.4.3   Conclusions

In this part of the work, the melting behaviour of $(U,Am)O_2$ oxides was investigating by a laser-heating technique. Melting temperature measurements were performed on a large composition domain, on samples with $0.07 \leq Am/M \leq 0.70$. Moreover, the experiments were performed under two atmospheres, argon and air, in order to study the effect of O/M ratio variations.

Two different behaviours were observed under argon and under air. In the first case, the measurements were always repeatable and the resulting melting temperature decreased with the americium content of the sample, with a regular trend. On the contrary, under air, the measurements were not reproducible for the oxides with Am/(Am+U)≤0.20. In these cases,

the observed melting temperature decreased during the first attempts and then it stabilized at about 400 K lower values. Based on this behaviour, it was clear that the composition of the oxide varied during the measurements in air, with an increase of the O/M ratio, whereas it was mainly constant during those in argon. This was confirmed by the post-melting characterization. The melted samples were investigated by XAS. The Am/(Am+U) and the O/M ratios were determined by X-ray fluorescence spectroscopy and XANES, respectively.

The variations of the Am/(Am+U) ratios were limited, as expected considering the rapidity of the laser-heating technique. However, slightly higher Am/(Am+U) ratios were systematically observed for the melted samples, especially for those measured in air. This indicates a preferential vaporization of uranium, consistently with the vapour pressures discussed in section 6.3. Considerable increases of the O/M ratio were observed for the samples melted in air, especially for the oxides with Am/(Am+U)≤0.20.

The post-melting characterization allowed to precisely associate the measured melting temperature to a composition, obtaining fundamental phase diagram points of the solidus-liquidus equilibria. These are summarised in Tab. 6.9 and represented in Fig. 6.21.
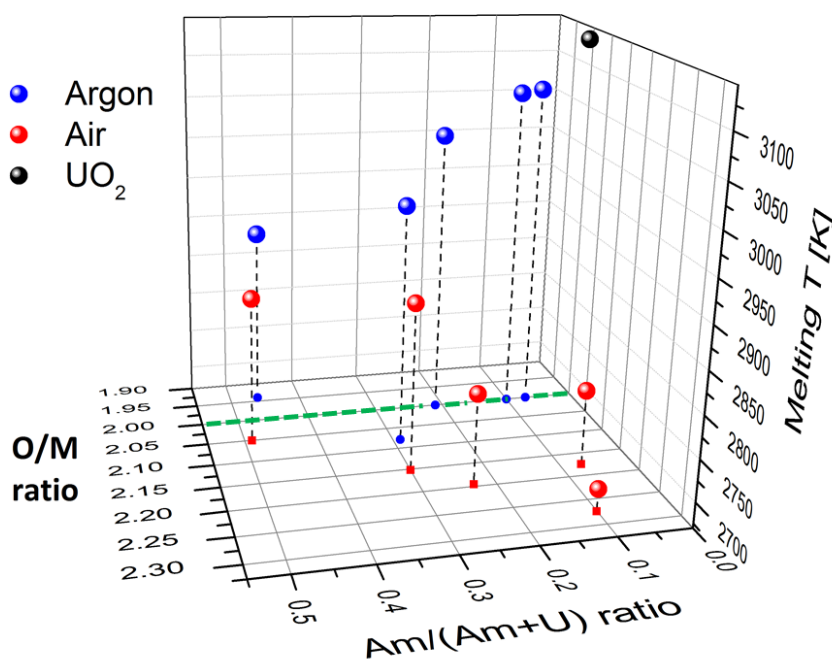
Fig. 6.21: Melting temperature versus the O/M-Am/M composition.

Fig. 6.21 shows a regular decreasing trend with the americium content for O/M ratios close to the stoichiometry. These correspond to the measurements in argon. The melting temperatures measured in air are generally lower, but the trend with the Am/(Am+U) ratio is opposite. Indeed, as already discussed in Ch. 5, the resistance toward the oxidation improves with the increasing americium content. This is confirmed also by this study: a consistent O/M increase was observed for Am/M≤0.2, whereas it was more limited for Am/M=0.3 and 0.5. The increase of the O/M ratio has dramatic effects on the melting temperature, causing a 300-400 K decrease. This is clear looking to the *Am10air* sample: at the highest O/M ratio (2.28(2)) corresponds the

Measurements in Argon		
Am/(Am+U) ratio [%]	O/M ratio	T_m [K]
7(1)	2.01(2)	3072(55)
10(2)	2.00(2)	3068(55)
21(3)	2.00(2)	3019(50)
30(3)	2.05(2)	2960(50)
47(3)	1.93(2)	2887(50)
Measurements in Air		
Am/(Am+U) ratio	O/M ratio	T_m [K]
7(1)	2.17(2)	2762(50)
10(2)	2.28(2)	2697(50)
23(3)	2.20(2)	2780(50)
32(3)	2.12(2)	2872(50)
51(3)	2.04(2)	2848(50)

Table 6.9: Results of the melting temperature measurements and post-melting characterisation.

lowest melting temperature (2697 $\pm$ 35 K). This behaviour is consistent with the other actinide oxides. Indeed, large decreases of the melting temperatures, for O/M > 2.0, were found by Manara *et al.* on UO_{2+x} samples [32] and a similar behaviour, during measurements in air, was observed on $(U,Pu)O_{2+x}$ by Strach *et al* [227, 228].

6.5   Conclusions

In this chapter, some fundamental thermodynamic properties of the $(U,Am)O_2$ oxides were investigated for a wide temperature range. The stability of the $(U,Am)O_{2-x}$ solid solution, for high americium contents, was investigated by HT-XRD. This study revealed the presence of a miscibility gap for an oxide with Am/(Am+U)= 0.70, in the 300 < T < 700 K temperature range. The enthalpy increment was measured in the 470< T< 1750 K temperature range for oxides with 0.30$\leq$ Am/(Am+U) $\leq$0.70, by drop calorimetry. Knudsen effusion cell coupled with mass spectrometry was used to investigate the vaporization behaviour of $(U,Am)O_2$ oxides as a function of the Am/(Am+U) ratio, from Am/M=0.10 to Am/M=0.70. Finally, the melting temperatures of $(U,Am)O_2$ oxides were measured using a laser-heating technique over a wide range of Am/(Am+U) compositions, for both inert (Argon) and oxidizing (Air) atmospheres. The knowledge of these properties is fundamental for the possible use of $(U,Am)O_2$ oxides in a reactor, as transmutation targets.

The results obtained during the melting behaviour investigations represent important phase diagram data. Indeed, thanks to the post-melting characterisation by XAS, it was possible to associate a defined composition (Am/M and O/M) to each measured melting temperature. These data could hence be directly used for the assessment of the solidus-liquidus equilibria of the U-Am-O phase diagram. Contrary to the melting results, the direct use of the HT-XRD,

enthalpy increments and vapour pressures data for the optimisation of the CALPHAD model is not straightforward, because the corresponding compositions are not precisely known. This is due to the difficulty to determine the O/M ratio variations at high temperature. However, these data can be compared with the CALPHAD model. Indeed, thermodynamic computations can be performed to simulate the experimental conditions, by imposing an equilibrium between the solid and the gas phase. This will be seen in the next chapter.

Chapter 7

Thermodynamic modeling of the U-Am-O system

As explained in Ch. 1, the aim of this PhD was to collect experimental structural, phase diagram and thermodynamic data on the U-Am-O system, for developing a CALPHAD thermodynamic model. Actually, as seen in section 2.5, a first CALPHAD assessment was proposed by F. Lebreton in his PhD thesis [106]. Few data were available for the optimization of the $U_{1-y}Am_yO_{2\pm x}$ thermodynamic parameters: i) the oxygen potential data by Bartscher and Sari [74], limited to the Am/(Am+U) = 0.5 composition; ii) the Am^{3+}, U^{4+}, U^{5+} site fractions from the XANES measurements, for Am/(Am+U) $\leq$ 0.50. A good agreement with these data was achieved during the assessment of Lebreton and the existence of the $U_{1-y}Am_yO_{2\pm x}$ solid solution, with a large oxygen composition domain, was reproduced in the computed phase diagrams. However, this model failed to reproduce other experimental results, as for instance the vapour pressure data on the Am/(Am+U) = 0.3, 0.4 and 0.5 compositions. According to Lebreton's model, the total congruency occurs for Am/(Am+U) = 0.49, whereas the experimental results here acquired show that this occurs for Am/(Am+U) $\simeq$0.60 (see Ch. 6). Most importantly, the computed partial pressures of the Am and U species were not in agreement with the experimental data, with differences up to four orders of magnitude.

In this work, the CALPHAD thermodynamic modeling of the Am-O system has been modified, as shown in chapter 3. For the binary U-O and U-Am systems, the assessments from Guéneau *et al.* [27] and Kurata [66] were respectively adopted. In this work, the CALPHAD thermodynamic modeling of the U-Am-O system was started, by assessing the $(U,Am)O_{2\pm x}$ solid solution and the results are herein presented.

7.1 Selection of experimental data

The experimental data selected for the CALPHAD assessment are:

1. The oxygen potential data for the $U_{1-y}Am_yO_{2\pm x}$ reported by Bartscher and Sari [74] on the Am/(Am+U) = 0.50 composition. Oxygen potentials are essential for correctly describing

an oxide solid solution. Unfortunately, even if an experimental campaign by thermogravimetric analysis (TGA) was planned for this work, no new oxygen potential data could have been obtained, because of technical problems.

2. The cationic site fraction obtained by XANES. In comparison to Lebreton's work, more data were used for the assessment. Indeed, during this thesis, data on higher americium contents, up to Am/(Am+U)= 0.70 (Ch. 4), and higher O/M ratios (Ch. 5 and 6) were acquired. These are summarized in Tab. 7.1. From these results, a general behaviour is highlighted:

   - For Am/(Am+U) < 0.50, the result obtained for the *Am30* sample, during the oxidation experiment, indicates that americium remains purely trivalent even for O/M higher the 2.0. Indeed, for O/M = 2.19, no Am^{4+} was observed.

   - The Am/(Am+U) = 0.50 composition seems representing a boundary. Pure trivalent americium is present for O/M $\lesssim$ 2, whereas Am^{4+} starts to be formed in the hyperstoichiometric domain.

   - For Am/(Am+U) > 0.50, the results obtained on the as-manufactured *Am60* and *Am70* samples, indicate that Am^{4+} is present for O/M<2.

It must be noted that, as previously discussed, the O/M ratios determined after the oxidation experiments can be considered representative of the state at 1473 K, since no evolution occurred during the cooling. Thus, the cationic site fractions measured by XANES at room temperature can be associated to 1473 K.

On the contrary, the O/M ratios determined for the as-manufactured oxides (for the present work and the previous ones of Lebreton [106] and Prieur [117]) cannot be associated with a precise temperature. Indeed, as discussed in chapter 4, an evolution of the oxide lattice parameter at room temperature, and hence of the O/M ratio, was observed by Lebreton within the few days after the manufacture. This was due to the experimental conditions: the samples were manufactured as pellets in reducing conditions and then powdered in glove boxes, under air. An oxidation is hence likely to occur. For this reason, the O/M measured by XANES few months after the manufacture cannot be associated to the plateau temperature of the sintering (1873 or 2023 K, depending on the composition). However, the cationic distribution measured on the as-manufactured oxides can be used for the modeling for the corresponding O/M ratio.

The problem is the attribution of a temperature for these data. Nevertheless, it can be supposed that, for a fixed O/M ratio, the charge distribution between U and Am, hence their average oxidation states, is not strongly dependent on the temperature. Indeed, during an in-situ high temperature XANES study reported by Caisso *et al* [231], for 1000 $\leq$ T$\leq$ 1400 K, on a $U_{0.8}Am_{0.2}O_{2-x}$ oxide, it has been shown that americium is still purely trivalent at high temperature. Thus, for the modeling, we assumed that the cationic distribution does not vary strongly with the temperature.

Nominal Am/(Am+U)	Experiment	Temperature	O/M	Am^{3+}	Am^{4+}	U^{4+}	U^{5+}
15 at.%	Manufacture	-	2.02	0.15	0	0.67	0.18
30 at.%	Manufacture	-	2.02	0.28	0	0.40	0.32
50 at.%	Manufacture	-	1.97	0.48	0	0.1	0.42
60 at.%	Manufacture	-	1.93	0.50	0.07	0.08	0.35
60 at.%	Manufacture	-	1.90	0.49	0.18	0.04	0.29
30 at.%	Oxidation exp.	1473 K	2.19	0.28	0	0.05	0.67
50 at.%	Oxidation exp.	1473 K	1.98	0.48	0	0.07	0.45
50 at.%	Melting exp.	2848 K	2.04	0.32	0.17	0.08	0.43

Table 7.1: Site fraction data collected in this work and used for the CALPHAD optimisation.

New thermodynamic data were provided on $U_{1-y}Am_yO_{2\pm x}$ dioxides in this thesis: the high-temperature enthalpy increments and the vapour pressures at 2300 K (Ch. 6). Besides, the existence of a miscibility gap was proven for an $U_{0.3}Am_{0.7}O_{2\pm x}$ oxide (Ch. 6). However, the use of these data for a CALPHAD optimisation is not straightforward because the corresponding compositions are not precisely known, due to the difficulty to control the O/M ratio at high temperature. In a first approach, it was hence preferred to compare these data to the model, after the optimization.

7.2   Model and assessment

In section 2.5.1, the CALPHAD assessment of the U-O system, by Gueneau *et al.* [27], was described. A three sublattice model was used for the $UO_{2\pm x}$ phase. This model is here extended for the ternary system as:

$$(U^{3+}, U^{4+}, U^{5+}, Am^{3+}, Am^{4+})_1(O^{2-}, Va)_2(O^{2-}, Va), \qquad (7.1)$$

where Va represents the vacancies. The first sublattice corresponds to the normal cation positions in the fluorite $Fm\bar{3}m$ structure (Wyckoff site *4a*). According to the experimental results by XANES, the trivalent and tetravalent americium ions were added into this sublattice. The second sublattice corresponds to the normal anion positions in the fluorite structure (Wyckoff site *8c*). Besides the oxygen atoms, vacancies were added into this sublattice in order to describe the hypostoichiometric domain (O/M< 2.0). The third sublattice is included for the oxygen interstitials, for the description of the hyperstoichiometric domain (O/M > 2). By combining the species in the three sublattice, this model can describe compositions ranging from $MO_{1.5}$ to $MO_{2.5}$. The neutral compounds (some of them only theoretical) are represented in Fig. 7.1.

The interaction between some species stabilize or destabilize the fluorite along composition lines between the extreme neutral compositions (red lines in Fig. 7.1). By extrapolation from the binaries, the Am^{4+} species was stable in the fluorite phase, in disagreement with the experimental data. To get the right cationic distributions (co-existence of Am^{3+}, U^{5+}), the introduction of the interaction parameter $L_{(Am^{3+},U^{5+})(*)(*)}$ (where $*$ stands for O^{2-} or Va) between Am^{3+}

and U^{5+} was required. In order to fit both oxygen potential data and to get a wide composition stability domain for the fluorite, it was necessary to introduce additional interaction parameters: $L_{(Am^{3+},U^{4+})(*)(*)}$, $L_{(Am^{4+},U^{5+})(*)(*)}$. These stabilize the co-existence of the indicated cations, for whatever composition of the second and third sublattice, hence for whatever O/M ratio. Moreover, two other interaction parameters were introduced: $L_{(Am^{3+},U^{5+})(O^{2-},Va)(Va)}$ and
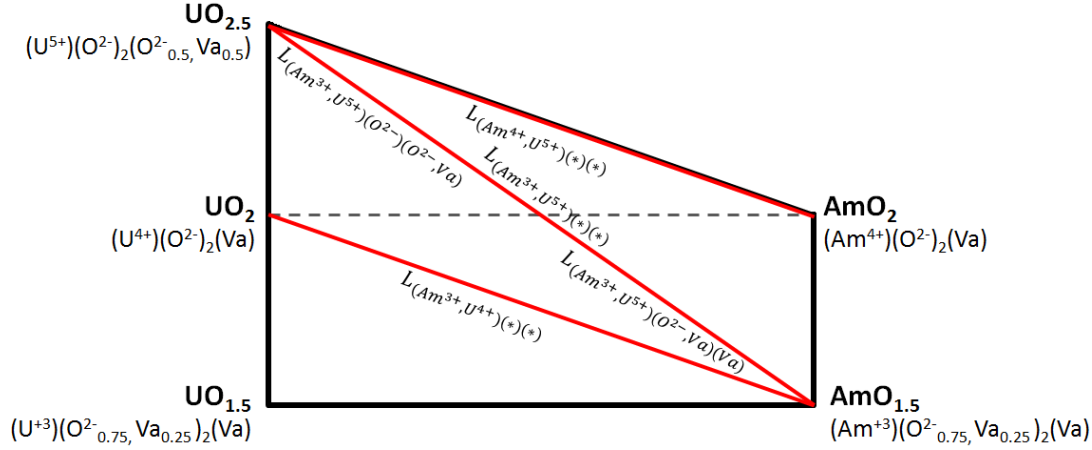
Fig. 7.1: Representation of the neutral compounds of the $(U,Am)O_2$ sublattice model and the optimized ternary interaction parameters .

$L_{(Am^{3+},U^{5+})(O^{2-})(O^{2-},Va)}$, that stabilize the coexistence of trivalent americium and pentavalent uranium, respectively for the hypostoichiometric (O/M < 2) and hyperstoichiometric domain (O/M > 2).

The expression of the Gibbs energy function of the adopted three sublattice model and the optimized parameters are provided in Appx. C.

A good fit of the data selected for the assessment was obtained, as shown in Fig. 7.2. The oxygen potentials (left) calculated for a Am/(Am+U) = 0.50 are in good agreement with the data of Bartscher and Sari [74]. The corresponding site fractions of the species in the three sublattice are reported on the right side of Fig. 7.2. Very similar results are obtained for the different temperatures, confirming that the site fractions do not have a strong direct dependency of the temperature, for a given O/M ratio. In the hypostoichiometric domain, for $1.8 \leq$ O/M < 2.0, americium is purely trivalent. In this range, the reduction proceeds by increasing the oxygen vacancies in the second sublattice and the charge balance is assured by the $U^{5+} \rightarrow U^{4+}$ reduction, in agreement with the experimental data. For O/M $\gtrsim$ 2.0, the uranium is fully pentavalent; the americium starts to be oxidized to the tetravalent state, meanwhile the third sublattice is filled with oxygen.

The site fractions were calculated for Am/(Am+U) ratios higher and lower than 50 %: 70 at.% and 30 at.%. The results, at T= 1473 K, are reported in Fig. 7.3 and compared to the experimental points. For the Am/(Am+U)= 0.70 composition (left side), the coexistence of Am^{3+}, Am^{4+} for O/M<2, beside to the uranium cations, is well described by the model. The computed composition for O/M = 1.90 is in very good agreement with the experimental points. For the
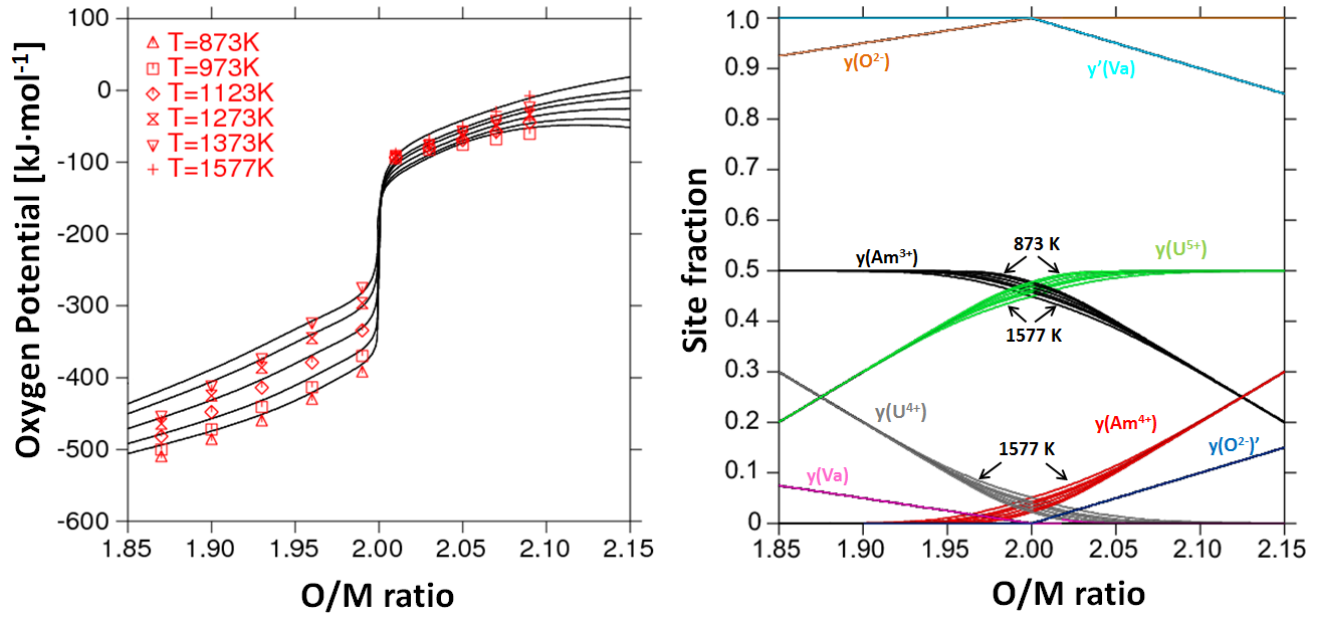
Fig. 7.2: Left: computed (lines) and experimental (red points) oxygen potentials; right: site fractions $y(i)$-where i is a species in the sublattice- in the three sublattices for $U_{0.5}Am_{0.5}O_{2\pm x}$. The third sublattice is identified by a $'$.

.

Am/(Am+U)= 0.30 composition (right side), the presence of americium only in the trivalent state, even for O/M slightly higher than 2.0, is described by the model. However, the Am^{4+} starts to be formed for O/M$\simeq$ 2.14 and the agreement with the experimental data for O/M = 2.19 is less good.
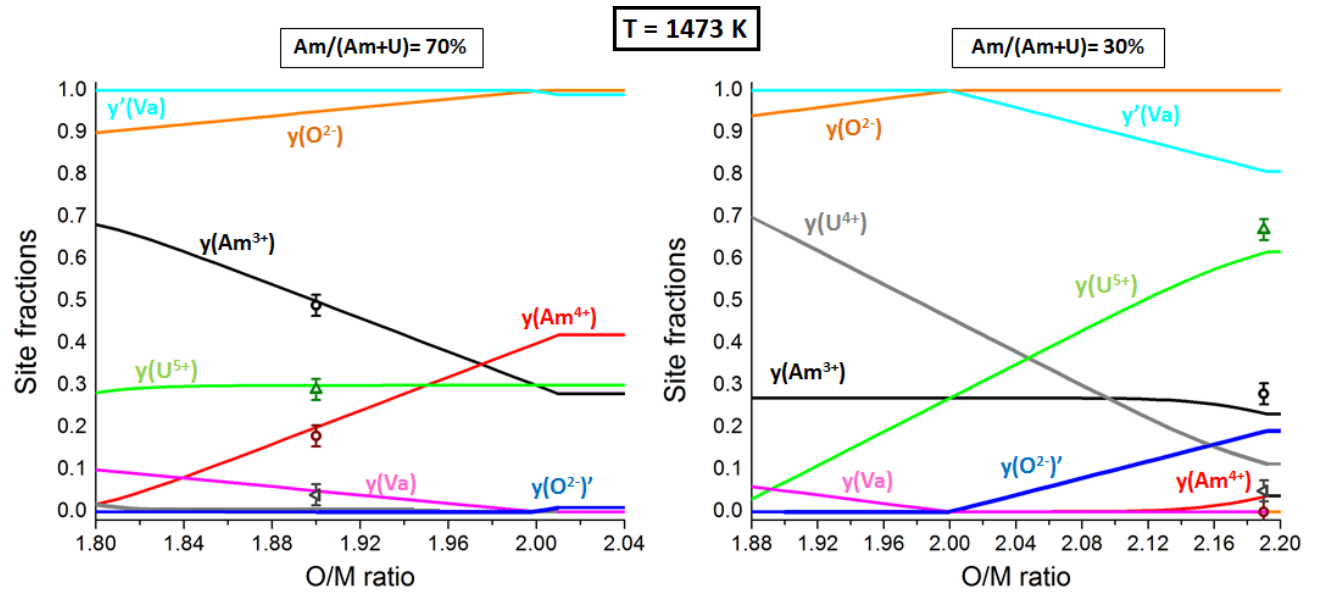
Fig. 7.3: Site fractions calculated at 1473 K for $U_{0.3}Am_{0.7}O_{2\pm x}$ (left) and $U_{0.7}Am_{0.3}O_{2\pm x}$ (right). The third sublattice is identified by a $'$.

In conclusion, a good fit of the experimental data selected for the assessment was achieved. However, it must be stressed that the optimization was performed using only two sets of data:

the cationic site fractions by XANES and the oxygen potentials of Bartscher and Sari [74] for $Am/(Am+U) = 0.5$. This model will be "tested" by comparing thermodynamic calculations with other experimental results in the following section.

7.3   Comparison between calculated and experimental data

In the following, the assessment is used to perform calculations to compare with phase diagram, HT-XRD, KEMS and drop calorimetry data.

7.3.1   Phase diagram

Computed isothermal sections of the U-Am-O ternary phase diagram at 2300, 1500, 1200, 1000, 500 and 300 K are shown in Fig. 7.4 and Fig. 7.5. In Fig. 7.5, zooms on the oxide domain are also reported (right side). Tie-lines in the two-phase domains are represented as green lines and the 3-phase regions are the triangles with a red perimeter. The $U_{1-y}Am_yO_{2\pm x}$ phase is indicated as *C1*.
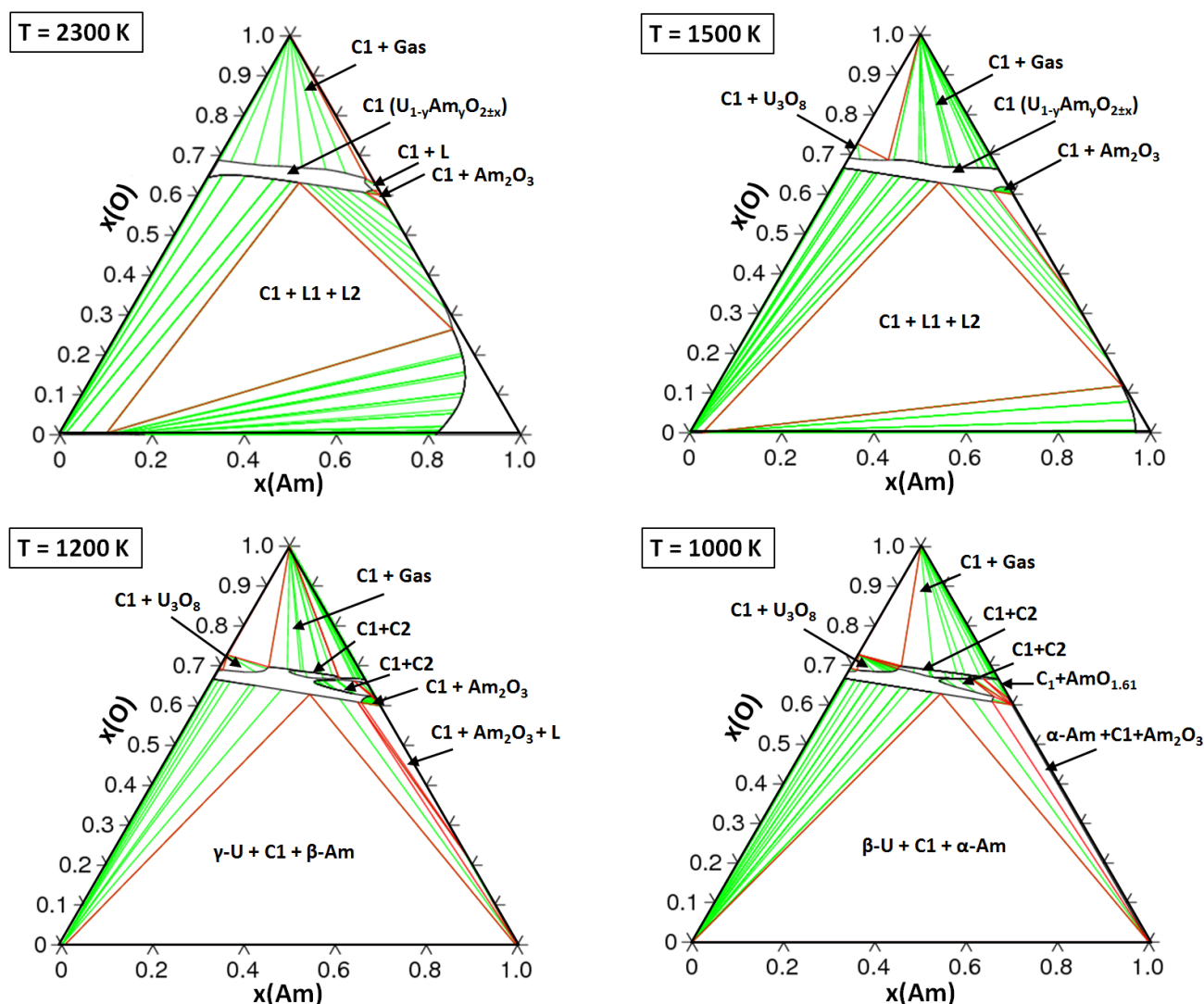
Fig. 7.4: Isothermal sections of the U-Am-O phase diagram for T = 2300, 1500, 1200, 1000 K.
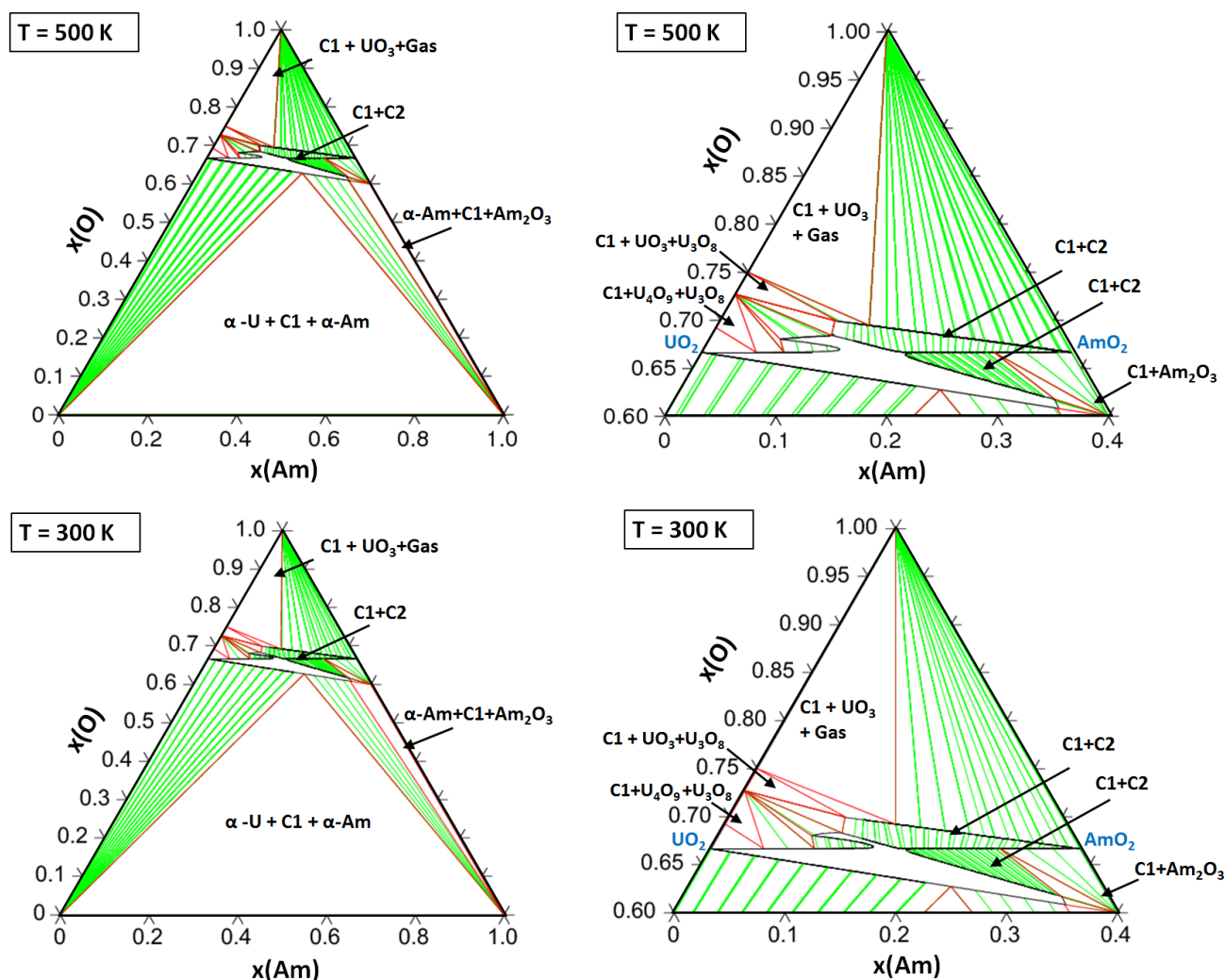
Fig. 7.5: Isothermal sections of the U-Am-O phase diagram for T = 300, 500 K, with zooms on the oxide domain (right).

At 2300 K, the mixed oxide $(U,Am)O_{2\pm x}$ forms a continuous solid solution extending in a wide americium and oxygen composition range. At this temperature, the AmO_{2-x} phase is no more stable in the Am-O binary system. This explains the existence of small two phase regions: [C1 + Liquid (Am,O)] and [C1+ Am_2O_3] in the Am-O rich side of the diagram. For O/M ratio below 2, the mixed oxide $(U,Am)O_{2-x}$ is in equilibrium with an U rich metallic liquid L1 in the U rich corner and with an Am rich metallic liquid L2 in the Am rich corner. This is due to the existence of a miscibility gap in the liquid state in the Am-U system (see Fig. 2.7). In the oxygen rich domain, the mixed oxide $(U,Am)O_{2+x}$ is in equilibrium with the gas (O_2).

At lower temperature, 1500 K, the phase diagram is quite similar. The composition range of the Am rich metallic liquid phase L2 is less extended. In the Am-O side, there is a small two-phase equilibria between the mixed oxide $(U,Am)O_{2-x}$ and the Am_2O_3 sesquioxide. The U-Am mixed oxide extends in the whole composition range between $UO_{2\pm x}$ and AmO_{2-x}. In the oxygen rich region, the mixed oxide $(U,Am)O_{2+x}$ is in equilibrium with U_3O_8.

At 1200 K, in the metallic side, the mixed oxide $(U,Am)O_{2-x}$ is in equilibrium with γ-U (BCC) and β-Am (BCC), due to the existence of a miscibility gap in the BCC phase in U-Am system (see Fig. 2.7). In the oxide domain, several two-phase regions exist:

- For O/M<2, in the Am-O side, the $(U,Am)O_{2-x}$ is in equilibrium with the sesquioxide Am_2O_3 and with $AmO_{1.61}$ phase.

- For O/M < 2, a miscibility gap in the C1 phase exists for Am/(Am+U) contents higher than 0.66.

- For O/M > 2, a miscibility gap is formed for high Am contents. This is likely an artefact of the model, generated by the thermodynamic parameters of the C1 phase (the investigations under air did not highlighted its presence)

- In the UO_2 rich side, the $(U,Am)O_{2+x}$ is in equilibrium with U_3O_8.

At 1000 K, the phase equilibria are similar to those at 1200 K. The liquid is no more present in the metallic domain. In the oxide domain, a very small two-phase region between the mixed oxide $(U,Am)O_{2+x}$ and U_4O_9 exists for high uranium contents. The extent of the miscibility gap in the C1 phase is significantly larger.

At 500 K, only the oxide rich region slightly changes. A second metastable miscibility gap in the UO_2 rich region appears for O/M ratio slightly higher than 2. This is again generated by the parameters of the model. The $(U,Am)O_{2+x}$ is in equilibrium with U_4O_9 and U_3O_8. The mixed oxide is stable for O/M ratio higher than 2 for Am/M contents lower than 0.5, in agreement with the experimental results shown in 4. The "stable" miscibility gap for O/M < 2 exists for Am contents higher than 0.54. The Am rich $(U,Am)O_{2-x}$ is in equilibrium with Am_2O_3. At 300 K, the phase diagram is very similar.

7.3.2 The $U_{1-y}Am_yO_{2\pm x}$ miscibility gap

In Ch.6, a HT-XRD investigation demonstrating the existence of a miscibility gap in the $(U,Am)O_2$ phase, for a sample with Am/(Am+U)= 0.7, was presented. As shown in the previous section, the Calphad model shows the existence of a miscibility gap, in the americium rich domain, for O/M < 2.0. It must be remarked that the existence of this miscibility gap was not imposed during the CALPHAD assessment here performed. Its existence automatically originated from the fitting of the oxygen potential and site fraction data. In order to verify the agreement between the model and the experiment described in Ch. 6, the O/M ratio of a $U_{0.3}Am_{0.7}O_{2-x}$ oxide was computed, as a function of temperature, for a fixed $pO_2= 10^{-20}$ atm. The result is represented on an isopleth section of the U-Am-O phase diagram in Fig. 7.6. According to the calculation, at T = 1273 K, the single-phase $U_{0.3}Am_{0.7}O_{2-x}$ is stable for an atmosphere with $pO_2= 10^{-20}$ atm, consistently with the XRD results. Decreasing the temperature, the O/M increases and the $U_{0.3}Am_{0.7}O_{2-x}$ *moves* toward the miscibility gap. This is entered, according to the model, for T$\approx$ 800 K. The agreement with the HT-XRD measurement (700 K) is hence reasonably good, considering the uncertainty of the model. Moreover, the XRD patterns were
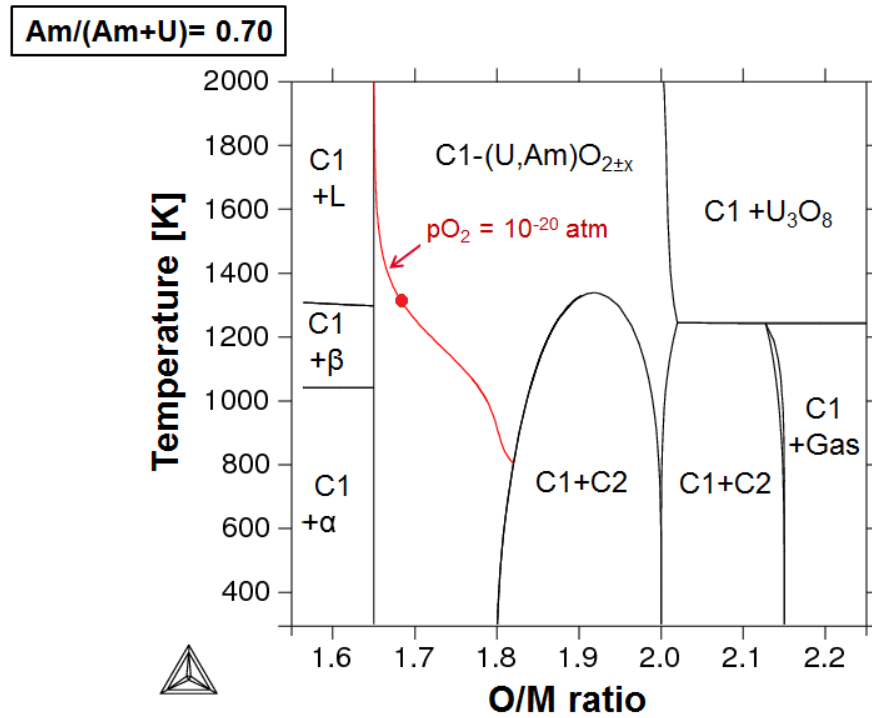
Fig. 7.6: Isopleth section of the U-Am-O phase diagram, for Am/M=0.70 and equilibria points (red line) calculated for $pO_2 = 10^{-20}$ atm.

recorded during a cooling and the oxide could have been out of the thermodynamic equilibrium. Further experiments need to be performed, preferably in isothermal conditions, including also oxides with lower americium contents, in order to define the miscibility gap boundaries.

7.3.3   High temperature vapour pressures

It was previously mentioned that the U-Am-O CALPHAD assessment proposed by Lebreton [106] had a poor agreement with the vapour pressure data available for U-Am oxides with (initial) Am/(Am+U) = 0.3, 0.4 and 0.5. In this part, thermodynamic calculations performed with the two CALPHAD models (this work and Lebreton) are compared to the KEMS experimental data, which were presented in section 6.3, in order to see if the new optimisation improved the description of the gas-solid equilibrium.

7.3.3.1   Comparison with the experimental vapour pressures

Comparing the CALPHAD model to the experimental data is not trivial because the compositions of the oxides can vary at high temperature and it is difficult to control. However, as explained in section 6.3, a stabilization of the mass spectrometric signals was observed during the KEMS measurements, for all the investigated oxides. This likely indicates that the vaporization congruency was achieved, at least for the oxygen. The thermodynamic computations were hence performed by imposing an equal oxygen content in the solid and in the gas phases, at 2320 K.

The total pressure and the cumulative pressures of the uranium and americium species, calculated at 2320 K, are represented as a function of the Am/(Am+U) ratio in the solid phase and compared to the experimental data for all the $(U,Am)O_2$ samples, in Fig. 7.7. Solid and dotted lines are respectively used for the new CALPHAD model and the one from Lebreton. Besides, for three selected compositions Am/(Am+U)= 0.10, 0.30 and 0.70, the vapour pressures calculated with the present model are compared to the experimental data in Tab. 7.2.
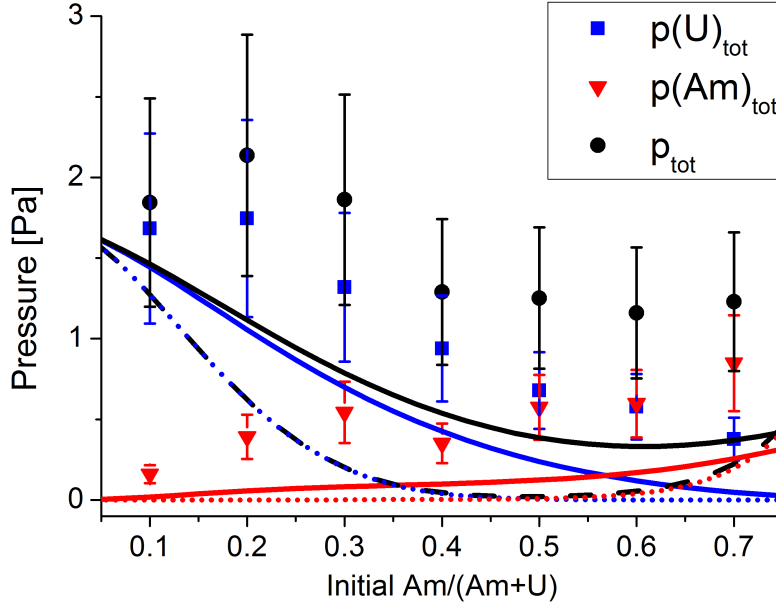
Fig. 7.7: Calculated and measured total pressure and U and Am cumulative pressures at 2320 K, imposing O/M(solid)= O/M(gas). Dotted lines: CALPHAD- Lebreton; solid lines: CALPHAD-this work

	Vapour pressures [Pa]								
	Am10			Am30			Am70		
Species	Exp.	Calc.	**Exp/Calc**	Exp.	Calc.	**Exp/Calc**	Exp.	Calc.	**Exp/Calc**
U(g)	0.015	10^{-5}	1074	0.011	10^{-6}	16128	-	10^{-10}	-
UO(g)	0.28	0.06	4.5	0.15	0.01	15	0.009	$4 \cdot 10^{-5}$	263
UO_2(g)	1.37	1.35	1	0.89	0.64	1.4	0.25	0.03	9
UO_3(g)	0.02	0.03	0.6	0.27	0.05	5.7	0.12	0.02	5.8
U_{tot}(g)	1.68	1.44	1.2	1.3	0.7	1.9	0.378	0.048	7.9
Am(g)	0.1	0.017	6	0.197	0.06	3	0.16	0.03	5
AmO(g) 0.06	0.002	33	0.327	0.021	16	0.61	0.11	5	
AmO_2	-	10^{-5}	-	0.019	0.002	10	0.07	0.11	0.6
Am_{tot}(g)	0.16	0.02	8	0.54	0.08	6.6	0.85	0.26	3
p_{tot}	1.84	1.46	1.3	1.86	0.79	2.37	1.23	0.37	3.3

Table 7.2: Comparison between the calculated (this model) and measured vapour pressures for oxides with Am/(Am+U)= 0.10, 0.30 and 0.70.

The present model shows that the total pressure decreases with the increase of the americium content in the mixed oxides, up to Am/(Am+U)=0.60, where a minimum is predicted,

in agreement with the experimental data. Also the evolution of the calculated total uranium and americium pressures as a function of the Am/(Am+U) ratio is in good agreement with the experiment. On the contrary, the model of Lebreton predicts a minimum of the total pressure for Am/(Am+U)= 0.487. For both the models, the calculated pressures are lower than the experimental data. For the present model, the maximum deviation from the experimental data of the total pressure is $p_{exp}/p_{calc} = 3.3$, for Am/(Am+U)= 0.70 (Tab. 7.2). For this composition, also the deviation of the total uranium pressure, equal to almost 8, is high. However, the improvement in comparison to the previous model is clear, especially for low americium contents.

The differences are more accentuated looking at the partial pressures of all the uranium and americium species, shown in Fig. 7.8.
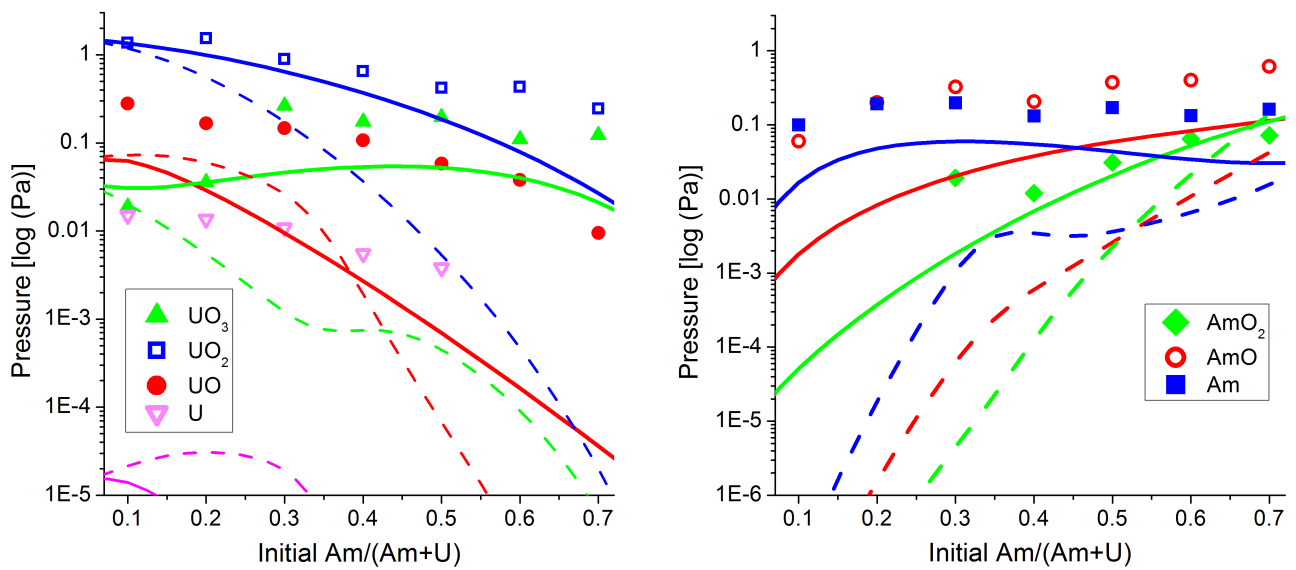
Fig. 7.8: Calculated and measured partial pressures of the U (left) and Am (right) species at 2320 K, imposing O/M(solid)= O/M(gas). Dotted lines: CALPHAD- Lebreton; solid lines: CALPHAD- this work

Concerning the uranium species, the present model well reproduces the vapour pressures measured for $UO_2(g)$, even if the error becomes large for the highest americium contents, passing from p_{exp}/p_{calc}= 1.0, for Am/(Am+U)= 0.10, to 9 for Am/(Am+U)= 0.70. A good agreement is also highlighted for $UO_3(g)$, with a maximum p_{exp}/p_{calc}= 6 for the Am70 sample. On the contrary, the calculations performed with the Lebreton model are very far from the experimental points. For $UO_2(g)$, the agreement with the measured pressure is good only for Am/(Am+U) = 0.10, but then the calculated decrease with the Am/(Am+U) ratio is too sharp and the error becomes huge, almost 10^5 Pa for Am/(Am+U)=0.7. For UO_3, the agreement is also poor, since the model of Lebreton expects a monotonic decrease of the partial pressure with the Am/(Am+U) ratio, contrary to the experiments. Finally, for both the models, a poor agreement is observed for the UO(g) and U(g) species, because the computed pressures are much lower than the measured ones. However, the incapability to correctly reproduce the U(g) species is a common problem in the modeling of the actinide oxides: too low calculated metal vapour pressures are also obtained for UO_2 [50] and $(U,Pu)O_2$ [27] [215].

For the americium species, the calculations performed with the present model are consistent with the experimental data: the magnitude orders between the Am(g), AmO(g) and AmO$_2$(g) is respected. The computed values are generally lower than the experimental ones, but the differences are limited, with a maximum deviation $p_{exp}/p_{calc}= 6$, for the Am(g) of the Am10 sample. A very good agreement is obtained for the AmO$_2$(g) partial pressure: the increase with the Am/(Am+U) is perfectly reproduced. A difference of a factor 10 is observed for the Am30 sample, but the experimental value seems a little out of the trend. For the other compositions, the p_{exp}/p_{calc} ratios are very close to 1. On the contrary, the calculations performed with the previous model show too low pressures, with errors even higher than 10^5 Pa for the oxides with low americium content.

In conclusion, the new CALPHAD model here proposed achieved a better description of the U$_{1-y}$Am$_y$O$_2$ vaporization behaviour in comparison to the previous assessment. The only large disagreement between the calculations and the experimental data was observed for UO(g) and U(g). However, the calculated vapour pressure of the main species are in good agreement with the experimental data. Therefore, in the following, further calculations with the new CALPHAD model will be presented, in order to try to better understand the vaporization behaviour of the U$_{1-y}$Am$_y$O$_2$ oxide and especially the contribution of the oxygen species (not measured during the KEMS experiment).

7.3.3.2 Congruent vaporization at 2320 K

The partial vapour pressures of all the gaseous species, calculated at 2320 K in the hypothesis of oxygen congruency, are represented in Fig. 7.9, for the entire composition range $0 \le$ Am/(Am+U) ≤ 1 (of the solid phase). Beside the actinide species already discussed, the model allowed also computing the partial pressures of O(g) and O$_2$(g), not measured by KEMS. Interestingly, the O(g) pressure (light grey curve) is low for the uranium rich side, but it continuously increases with the Am/(Am+U) ratio. According to the model, this species becomes comparable with the main ones for Am/(Am+U) $\gtrsim 0.5$. This implies that the determination of the gas composition considering only the actinide species, performed in Fig. 7.8, was very imprecise. Indeed, as previously remarked, the obtained O/M ratios of the gaseous phase were too low, being lower than 1.5 for Am/(Am+U) > 0.5 (see Fig. 6.11).

In Fig. 7.10, the vapour pressures are calculated as a function of the O/M ratio, for the metal congruent composition Am/(Am+U) = 0.60. A minimum in the total pressure is observed for O/M ≈ 1.76, which corresponds to the oxygen congruent composition. The total congruent vaporization at 2320 K occurs hence for Am/M ≈ 0.60 and O/M ≈ 1.76. This is consistent with the behaviour of the binaries U-O and Am-O, for which the congruent composition is, respectively O/U $\simeq 1.98$ and O/Am $\simeq 1.5$. For O/M < 1.76, the Am(g), AmO(g) and UO$_2$(g) are the major species. For O/M > 1.76, a continuous increase of AmO$_2$(g), UO$_3$(g) and O(g) is observed. Besides, a more sharp increase of the O$_2$ partial pressure is shown. The O(g) and O$_2$(g) species have the highest partial pressure for O/M $\gtrsim 1.80$, with values that reach 10^5 Pa
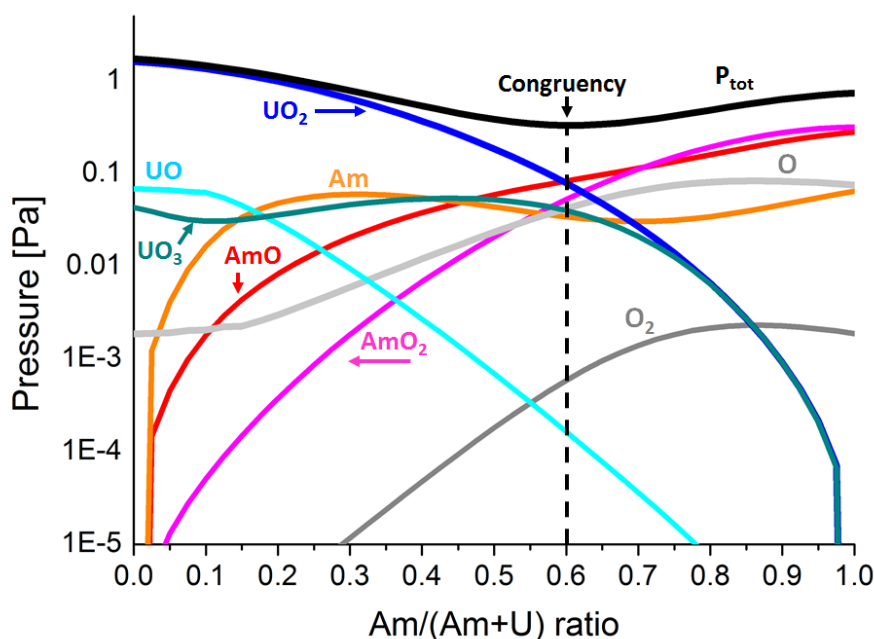
Fig. 7.9: Calculated pressures as a function of the Am/(Am+U) ratio at 2320 K, imposing O/M(solid)= O/M(gas).
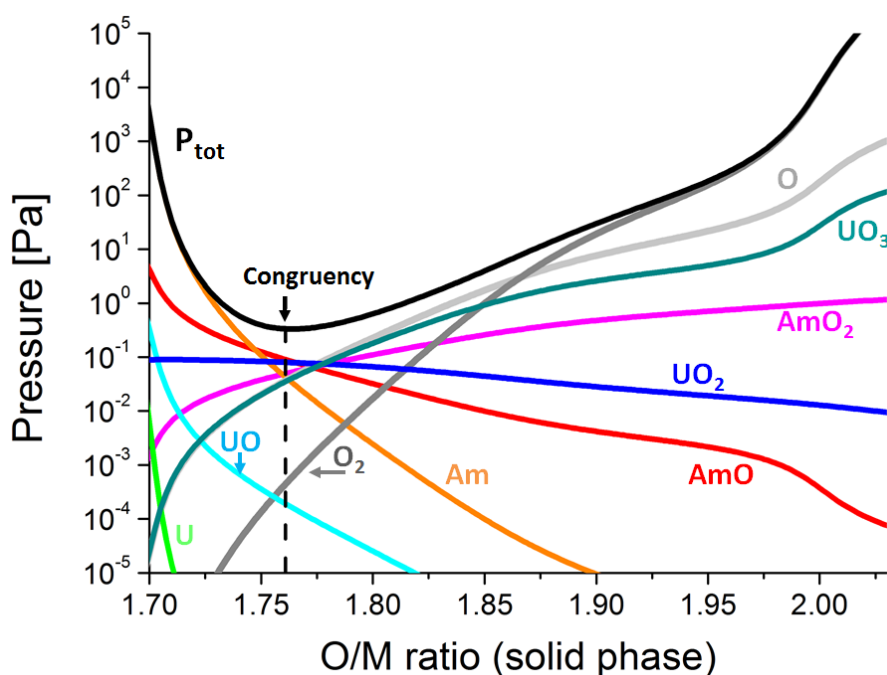
Fig. 7.10: Calculated pressures as a function of the O/M ratio at 2320 K, for an Am/(Am+U) ratio equal to 0.60.

for O/M close to 2.0. This confirms once again the importance of the oxygen species in the determination of the gas composition.

The calculated composition of the gas at 2320 K, as a function of the Am/(Am+U) ratio in the solid, is shown in Fig. 7.11: on the left, the O/M(gas); on the right, the Am/(M)(gas). A decreasing of the O/M ratio with the increase of the Am/(Am+U) ratio in the solid is expected
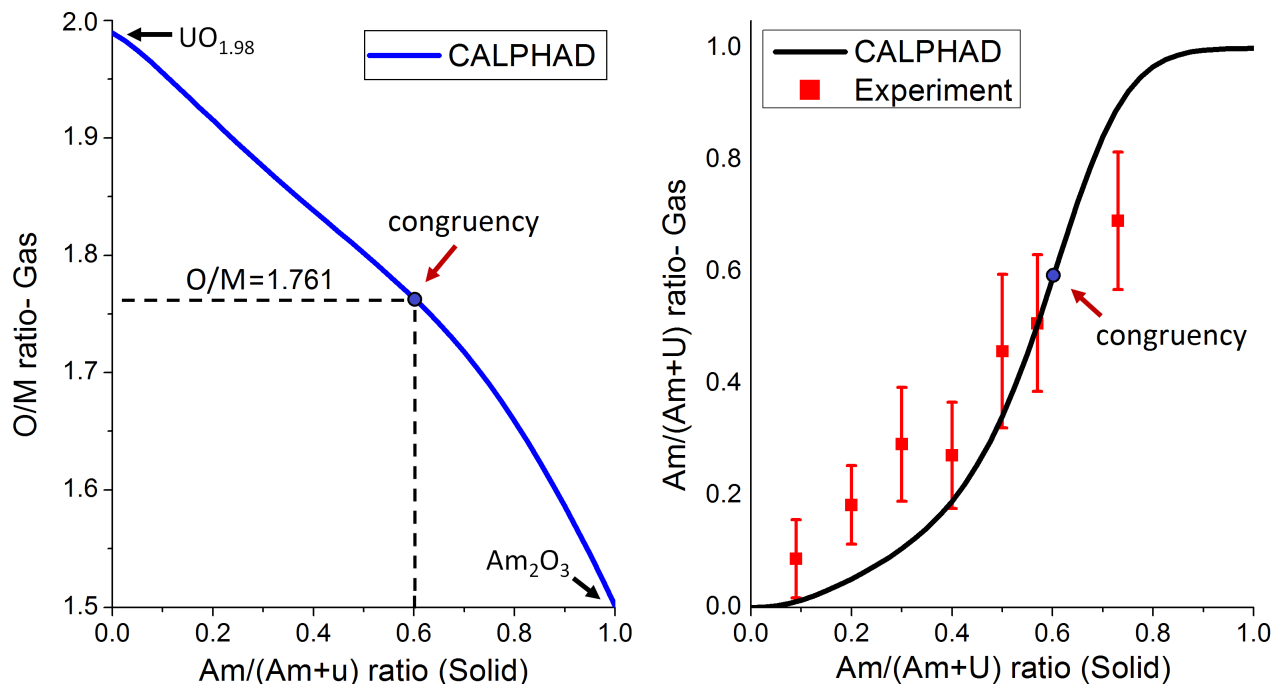
Fig. 7.11: Calculated composition of the gas phase at 2320 K.

by the model, consistently with the behaviour of the two binary oxides discussed in section 6.3. As already said, according to the model, the total congruency occurs for an $Am/(Am+U) \approx 0.60$ and an $O/M \approx 1.76$.

The computed $Am/(Am+U)$ ratios of the gas as a function of the $Am/(Am+U)$ ratio in the solid (right side of Fig. 7.11) are consistent with the experimental data. A very good agreement is obtained for the oxide with $Am/(Am+U) = 0.57$, hence the composition close to the total congruency, according to the model.

7.3.4 Enthalpy functions

Measurements of the enthalpy increments at high temperature, $H(T)-H(298.15)$, were presented in section 6.2 for $(U,Am)O_2$ oxides with $0.30 \leq Am/(Am+U) \leq 0.70$. In addition, values for the $Am/(Am+U) = 0.10$ and 0.20 compositions were reported in the literature [203]. The measurements were performed under a purified argon atmosphere ($pO_2 \approx 1$ ppm) for $Am/(Am+U) \leq 0.50$ and under air for the highest americium contents (0.60 and 0.70). Comparing the results to the UO_2 and AmO_2, an excess contribution to the enthalpy was highlighted for $Am/(Am+U) \geqslant 0.4$ and $T > 1200$ K. Thermodynamic computations performed using the Am-O CALPHAD model indicated that this excess contribution could come from the formation of oxygen vacancies ($O/M < 2$) at high temperature.

Calculation on ternary oxides are here presented in order to verify if the enthalpy functions are correctly reproduced by the new assessment. Three compositions were selected:

- $Am/(Am+U) = 0.10$; the enthalpy function was calculated for an $O/M = 2$;

- $Am/(Am+U) = 0.50$. For this composition, the enthalpy function was calculated in two

ways: first, for an oxide with fixed O/M = 2.0; second, by imposing, for $T \geqslant 1200$ K, an equilibrium between the $U_{0.5}Am_{0.5}O_{2\pm x}$ and a gas with $pO_2 \approx 1$ ppm (simulating argon).

- Am/(Am+U) = 0.70. As for the previous case, the enthalpy function was calculated in two ways: first, for an oxide with fixed O/M = 2.0; second, by imposing, for $T \geqslant 1200$ K, an equilibrium between the $U_{0.3}Am_{0.7}O_{2\pm x}$ and a gas with $pO_2 \approx 0.21$ atm (simulating air).

The results of the calculations are compared to the experimental data in Fig. 7.12.
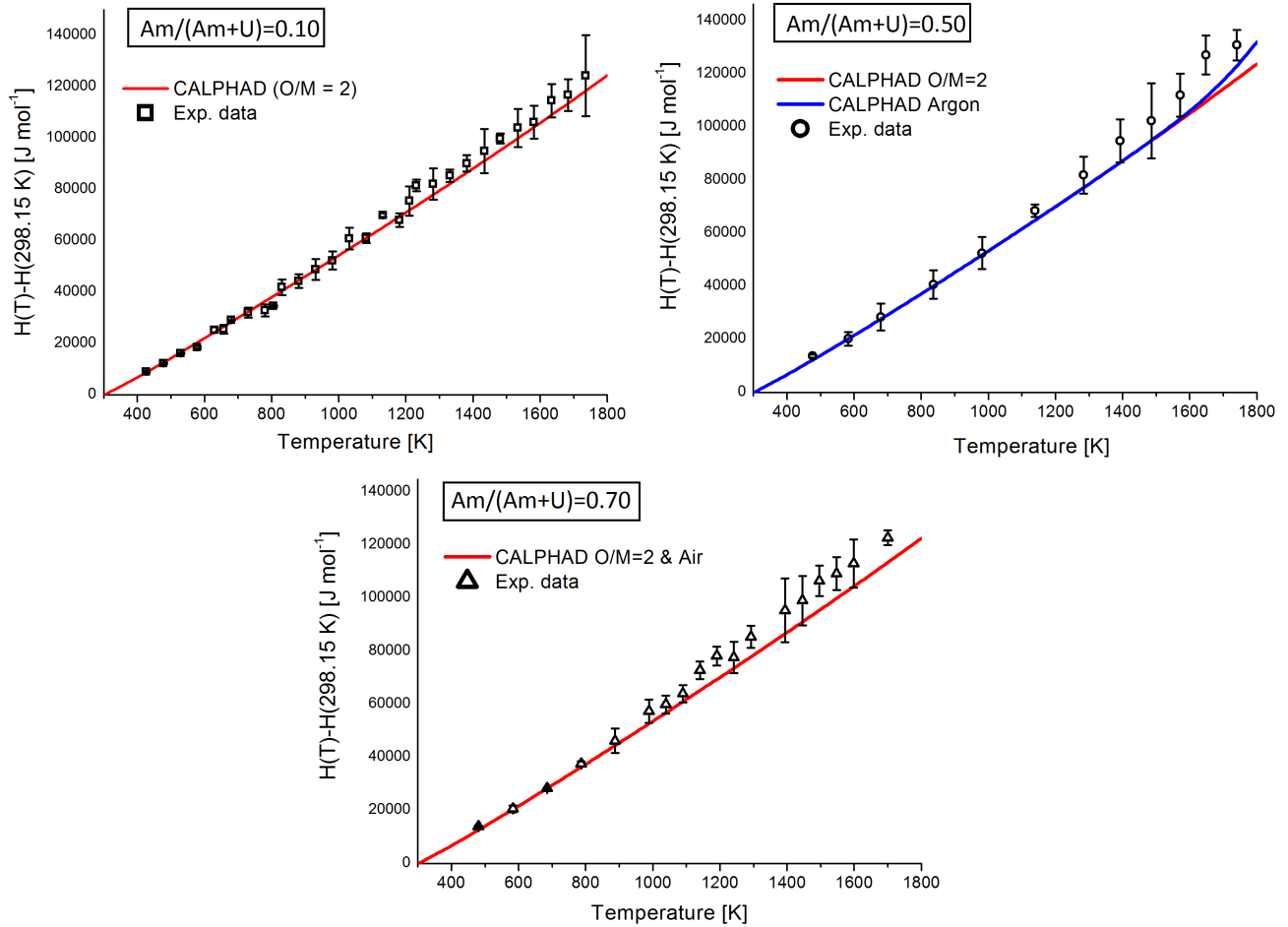
Fig. 7.12: Calculated enthalpy functions compare to experimental data for Am/(Am+U)=0.10, 0.50 and 0.70.

The calculated enthalpy function of the $U_{0.9}Am_{0.1}O_2$ oxide is in good agreement with the experimental data.

For Am/(Am+U) = 0.50, the two calculated enthalpy functions, with fixed O/M and in equilibrium with an inert gas, are almost identical up to 1600 K. Above this temperature, a small departure toward higher values is observed for the enthalpy calculated in equilibrium with the gas. As previously said, this excess contribution is due to a reduction of the oxide: the corresponding calculated O/M ratio decreases from 2.0 at 1200 K, to 1.965 at 1800 K. However, the agreement with the experimental data is not good: the measured enthalpy increments are systematically higher than the calculated curve. This likely indicates that the reduction of the

oxide is underestimated by the model. This could be due to the metastable miscibility gap predicted for hyperstoichiometric oxides.

The agreement is not very good for the Am/(Am+U) = 0.70 either. In this case, the curves calculated for O/M = 2.0 and for the oxide in equilibrium with a gas of pO_2 = 0.21 atm (air) are identical (the two are overlapping in Fig. 7.12). Indeed, according to the model, no reduction occurs for the oxide under this atmosphere: the computed O/M ratio at 1800 K is 2.001. Therefore, the model does not reproduce well the higher enthalpy values experimentally observed for T $\gtrsim$ 1200 K.

7.4   Conclusions

In this last part of the work, the CALPHAD assessment of the U-Am-O system has been started, focusing on the $U_{1-y}Am_yO_{2\pm x}$ solid solution. The thermodynamic parameters of this phase were optimized using the oxygen potentials by Bartscher and Sari [74] for $U_{0.5}Am_{0.5}O_{2\pm x}$ and the cationic site fractions, obtained in this work and in the previous PhD of Lebreton [106] and Prieur [117]. It must be underlined that the available data are not sufficient to obtain a reliable CALPHAD model. Indeed, more thermodynamic data on mixed oxides with precisely known composition (O/M ratio) would be necessary. In particular, oxygen potentials data are fundamental to correctly describe an oxide solid solution. Unfortunately, a TGA experimental campaign, planned for this PhD work, could not be performed because of technical problems.

Nevertheless, the preliminary U-Am-O CALPHAD assessment here presented succeeded in explaining and reproducing various experiments.

In section 7.3.2, it was shown that a miscibility gap in the $U_{1-y}Am_yO_{2\pm x}$ solid solution is expected by the model, in the oxygen hypostoichiometric domain and for Am/(Am+U) > 0.50. This is in agreement with an *in situ* HT-XRD experiment performed in this work, which proved the existence of this miscibility gap for an oxide with Am/(Am+U) = 0.70 and T $\lesssim$ 700 K. Moreover, thermodynamic calculations performed with the CALPHAD model, simulating the HT-XRD conditions, reproduced well the experimental results, showing the entering of the miscibility gap for T ≤ 800 K (assuming thermodynamic equilibrium).

The results of the KEMS measurements were also reproduced in a fair way. The improvement of the vapour pressure calculations comes from the change of the AmO(g) and AmO_2(g) thermodynamic functions (see Ch. 3), that lead to a better description in both the binary and the ternary systems. The computed total congruent composition at 2320 K coincides with an Am/(Am+U) ratio equal to 0.60, in agreement with the experimental data. The general trends of the total pressure and the partial pressures of the main gaseous species (UO_2, UO_3, AmO, Am, AmO_2) were in reasonable agreement with the data, but the calculated values were systematically lower. Moreover, the agreement for the uranium species became poorer for the oxides with high americium content (Am/M = 0.60 and 0.70). Similarly, for the calculations of the enthalpy function presented in section 7.3.4, the consistency between the model and the experimental data was good for oxides with low Am content and poorer for Am/(Am+U) $\gtrsim$ 0.50. Finally, as

shown in section 7.3.1, the model expects also a second miscibility gap, in the americium-rich domain, for hyperstoichiometric $U_{1-y}Am_yO_{2+x}$ oxides. Contrary to the hypostoichiometric one, this miscibility gap is an artefact of the model. Indeed, several HT-XRD measurements in oxidizing conditions were presented in Ch. 5 and a $U_{1-y}Am_yO_{2+x}$ phase separation was not highlighted.

In conclusion, the CALPHAD optimization here performed for the $U_{1-y}Am_yO_{2+x}$ phase needs to be improved, especially for the americium rich domain, with $Am/(Am+U) > 0.5$ and $O/M \gtrsim 2.0$. New thermodynamic experimental data for oxides with high americium contents would be necessary. Moreover, for the perspectives, the CALPHAD optimization should be extended to the other phases. Indeed, the solubility of americium in oxygen rich oxides as M_4O_9 and M_3O_8 was experimentally observed in this work and it should be hence included in the model. Finally, also the thermodynamic parameters of the liquid phase should be assessed, using the melting results here reported.

Chapter 8

General conclusions and perspectives

Americium isotopes are produced in the nuclear reactor core through neutron captures on uranium nuclei and subsequent radioactive decays. After plutonium, americium is the major contributor to the long-term radiotoxicity of the spent nuclear fuel. In order to reduce the ecological footprint of the geological disposals, the partition and transmutation (P&T) strategy has been proposed. Various possibilities have been considered. A promising way is the transmutation of americium in Fast Neutron Reactors (FNRs). In this frame, two scenarios are possibles, respectively named homogeneous and heterogeneous transmutation. In the first case, americium is diluted in low quantity (up to 5%) in the nuclear fuel; in the second scenario, americium is concentrated (15%) in specific assemblies, named MABBs (Minor Actinide Bearing Blankets), located at the periphery of the reactor core. In the frame of the P&T research, uranium and americium mixed oxides, $(U_{1-y}Am_y)O_{2\pm x}$ are under investigation as promising transmutation targets. A thorough knowledge of the thermodynamic properties of such compounds is essential for the safety of the FNRs. For this reason, this PhD work has been dedicated to the experimental investigation of these properties, with the aim to develop a thermodynamic database for the U-Am-O system. The semi-empirical CALPHAD method has been selected for this purpose. Three types of data can be used for a CALPHAD assessment: structural, phase diagram and thermodynamic data. The experimental work of this thesis has hence been articulated according to these three guidelines.

The first step for the thermodynamic investigation of a ternary system is the study of the associated binaries. For the U-O system, a reliable CALPHAD model was obtained by Guéneau *et al.* [27], thanks to the numerous experimental data available in the literature. For the Am-O system, a CALPHAD model was proposed by Gotcu-Freis *et al* [64]. However, this was affected by several uncertainties because of the lack, and in some cases inconsistency, of experimental data on americium oxides. Thus, it has been necessary to investigate and re-assess the Am-O system. An *in situ* HT-XRD investigation was hence performed on AmO_{2-x}, under controlled oxygen partial pressure. The analysis of the new acquired data led to establish the lattice parameter variation of AmO_{2-x} as a function of the temperature and the O/Am ratio. For reducing conditions, the results highlighted the existence of a composition range for the BCC $AmO_{1.61+x}$ phase. The miscibility gap in the AmO_{2-x} fluorite phase, proposed in the literature by Sari and

Zamorani [58], was not detected. The O/Am ratio of the AmO_{2-x}/Am_2O_3 phase boundary at 1500 K was determined. Adopting these new phase diagram data and recently reviewed Gibbs energy functions for the Am-O gaseous species [127], the CALPHAD thermodynamic assessment of Gotcu-Freis could be modified. The new assessment led to an enhanced description of the oxide phase equilibria and of the Am_2O_3 vaporization behaviour, compared to the previous model.

The U-Am-O ternary system was then investigated. $(U,Am)O_{2\pm x}$ pellets, with $Am/(Am+U)$ ratio ranging from 0.075 to 0.70, were manufactured during this work. Structural investigations were then performed on the as-sintered oxides, by coupling XRD with XAS and Raman spectroscopy. The formation of a single-phase fluorite structure was always confirmed by the XRD results. The XAS revealed that the $(U,Am)O_{2\pm x}$ solid solution presents the co-existence of three/four cationic species, namely Am^{3+}, U^{4+}, U^{5+} and, for $Am/(Am+U)$ ratios higher than 0.5, also Am^{4+}. This cation charge distribution is unique among the actinide dioxides. For $Am/(Am+U) \leq 0.30$, the sintered oxides presented O/M ratios close to 2.0. For these compositions, the purely trivalent state of americium was compensated by a similar fraction of the pentavalent uranium. For higher americium contents, this compensation mechanism was not sufficient to preserve the oxygen stoichiometry and the oxides had an O/M < 2. Moreover, the maximum observed fraction of Am^{3+} is ~ 0.50: for higher $Am/(Am+U)$, tetravalent americium was present. As already mentioned, this complicated charge distribution does not alter the fluorite symmetry of the cationic sublattice. On the contrary, the presence of complex oxygen defects in the anionic sublattice was highlighted by Raman spectroscopy and EXAFS, in particularly for $Am/(Am+U) \geq 0.50$. In these high-americium content oxides, the data suggest the formation of oxygen defect clusters localized around the uranium cations, similar to those present in the U_4O_9 and U_3O_7 fluorite-superstructures.

Despite these effects on the oxygen sublattice even for O/M < 2, the addition of americium to the $UO_{2\pm x}$ solid solution improves the stability against the oxidation. This was shown by a HT-XRD investigation in air coupled with a XAS characterization of the obtained oxidized samples, with $0.10 \leq Am/(Am+U) \leq 0.70$. Whereas UO_2 is rapidly oxidized during heating under air, for T > 600 K, to U_4O_9+ U_3O_7 and then U_3O_8 phases, the oxidation was slower and less important for the $(U,Am)O_2$ mixed oxides. For $Am/(Am+U) = 0.10$ and 0.15, the dioxide phase MO_2 disappeared during the heating in air, meanwhile M_4O_9 and M_3O_8 were formed. For $Am/(Am+U) = 0.30$, the MO_{2+x} phase was observed together with M_3O_8. For the three mixed oxides, the formation of M_3O_8 was shifted to higher temperature with the increasing of the $Am/(Am+U)$ ratio, whereas the formed fraction of this phase decreased. This is not surprising, since a similar behaviour was observed in other mixed oxides, as $(U,Pu)O_2$ [202] and $(U,Np)O_2$ [199]. However, in these studies, the formation of M_3O_8 was always observed even for high contents of neptunium (Np/M = 0.70) and plutonium (Pu/M = 0.66). On the contrary, the oxides with $Am/(Am+U) = 0.50$, 0.70 remained monophasic during the thermal treatment in air, no hyperstoichiometric oxides were observed. The improvement against the oxidation is hence even more accentuated with the addition of americium to the solid solution. In addition, this investigation provided phase diagram data, at 1473 K, on the MO_{2+x}-M_4O_9-M_3O_8 domain.

The accommodation of americium in M_4O_9, up to Am/(U+Am)=0.15, was observed for the first time. The solubility of americium in M_3O_8 was estimated as Am/(Am+U)$\simeq$ 0.10, in agreement with a previous study in the literature [193]. Tie-lines at 1473 K were determined in the M_4O_9-M_3O_8 and MO_{2+x}-M_3O_8 domains.

The study of the U-Am-O ternary phase diagram continued with the investigation of the solid-liquid equilibria. Measurements of the melting temperature, by laser-heating techniques, were performed on oxides with $0.07 \leq$ Am/(Am+U) ≤ 0.50. In order to investigate the effects of the O/M ratio, argon and air were used for the measurements. Two very different behaviours were observed. The oxides melted in argon kept an O/M ratio close to 2.0 (confirmed by post-melting characterization), with the exception of the $U_{0.5}Am_{0.5}O_{1.93}$ sample, which was slightly reduced. A linear decrease of the melting temperature with the Am/(Am+U) was observed, passing from $T_m = 3130(31)$ K for UO_2 [32] to $T_m = 2887(30)$ for $U_{0.5}Am_{0.5}O_{1.93}$. Under air, a large increase of the O/M ratio (up to 2.28) was observed for the oxides with Am/(Am+U) ≤ 0.20. The oxidation caused a dramatic decrease of the melting temperature, of almost 400 K. On the contrary, the oxides with Am/(Am+U) = 0.30 and 0.50 were less oxidized (O/M = 2.10 and 2.04, respectively) and the corresponding melting temperature were very close to those measured in argon. Therefore, the highest melting temperatures in air were observed for the americium-rich oxides. These results are hence consistent with the previous study on the oxidation in air.

The experimental campaign of $(U,Am)O_2$ proceeded with the investigation of high temperature thermodynamic properties. Enthalpy increments, H(T)-H(298.15 K), were measured by drop calorimetry in the $400 < T < 1800$ K temperature range, on oxides with $0.30 \leq$ Am/(Am+U) ≤ 0.70. The results were compared to the literature values for Am/(Am+U) = 0.10 and 0.20 [203]. For all the compositions, a regular, almost linear increase of the enthalpy with the temperature was observed. The trends were very similar to those reported in the literature for UO_2 and AmO_2, in the second case limited to 1100 K. However, a slight but systematic departure of the enthalpy curves, toward higher values, was observed for $T > 1200$ K, for the oxides with Am/(Am+U) > 0.40. Thermodynamic computations performed with the Am-O CALPHAD model suggested that this excess contribution is due to the reduction of the oxides, hence the formation of oxygen vacancies, for $T > 1200$ K. Unfortunately, this hypothesis could not be experimentally verified because of the impossibility to measure the O/M ratio during the calorimetric measurements.

Knudsen effusion cells coupled with mass spectrometry (KEMS) was used to investigate the vaporization behaviour of $(U,Am)O_2$ with Am/(Am+U) = 0.6 and 0.70 at 2320 K. This is a method of choice for the measurements of the vapour pressures in such complex systems, where the gas is constituted of many species, such as U(g), UO(g), UO_2(g), UO_3(g), Am(g), AmO(g) and AmO_2(g). A systematic analysis of the data collected for a large composition domain, $0.10 \leq$ Am/(Am+U) ≤ 0.70., was performed in this thesis. A regular decreasing trend with the Am/(Am+U) ratio is highlighted for the cumulative pressure of the uranium species, along with

a slight increase of the americium species. A minimum of the total pressure is observed for $Am/(Am+U) \simeq 0.60$, corresponding to the congruent vaporization composition. Among the americium species, $Am(g)$ and $AmO(g)$ exhibit the highest vapour pressures, with close value. The $AmO_2(g)$ pressure is below the detection limit ($< 10^{-2}$ Pa) for the oxides with $Am/(Am+U)$ < 0.20, but a regular increase is then observed for the oxides richer in Am. Among the uranium species, the highest partial pressure is shown by $UO_2(g)$, consistently with the UO_2 vaporization behaviour. In comparison to congruent UO_{2-x} oxide, a higher UO_3 vapour pressure is observed. The presence of this species is consistent with the high oxidation state of uranium (U^{4+}/U^{5+}) in $(U,Am)O_2$, due to the compensation of the trivalent state of americium.

Finally, the CALPHAD thermodynamic modeling of the U-Am-O system was started, focusing on the $(U,Am)O_2$ solid solution. However, this assessment is affected by the lack of thermodynamic data associated to precise compositions (O/M ratios). In particular, oxygen potentials data would be necessary for correctly describing the oxygen domain of the solid solution, but only one set of data for $U_{0.5}Am_{0.5}O_{2\pm x}$ is available in the literature [74]. An experimental campaign by TGA was planned for this PhD work, but unfortunately it could not be performed because of technical problems. Nevertheless, during the CALPHAD assessment, a good agreement with the oxygen potential data for $U_{0.5}Am_{0.5}O_{2\pm x}$ and the cation site fraction by XAS was achieved. The obtained model is able to fairly reproduce the enthalpy functions for $(U,Am)O_2$ oxides with $Am/(Am+U) \lesssim 0.40$. The calculated vapour pressures were in reasonable agreement with the KEMS data, hence the equilibrium between the dioxide and gas phase is better reproduced, thanks to the new thermodynamic functions introduced for the americium gas species. Moreover, a miscibility gap in the americium-rich domain ($Am/M > 0.50$) of the $(U,Am)O_2$ is expected by the model for $O/M < 2.0$. The existence of this miscibility gap, longly debated [106], was confirmed in this PhD by a HT-XRD investigation for an $Am/(Am+U) = 0.70$, for $T \leq 700$ K, in good agreement with the CALPHAD model.

In conclusion, the consistent results obtained by different experimental techniques (XRD, XAS, Raman spectroscopy, KEMS, drop calorimetry, laser-melting) have highlighted the peculiarity of the U-Am mixed oxides, induced by the high stability of trivalent americium, compensated by the partial oxidation of U^{4+} to U^{5+}. Indeed, this explains the high oxygen potential values of $(U,Am)O_2$, thus their improved resistance against the oxidation and their easier reduction at high temperature.

On the basis of the knowledge of the thermodynamic properties of the $(U,Am)O_2$ oxides achieved in the present work, some conclusions can be drawn in view of their use as transmutation targets. As mentioned at the beginning, the envisaged $Am/(Am+U)$ ratio of the transmutation targets is 0.15, but a maximum value of 0.20 was also considered. The stability of the solid solution was here confirmed for americium contents much higher than this value. Moreover, no dramatic effects on the thermodynamic properties, in comparison to UO_2, were highlighted for $Am/(Am+U) \leq 0.20$. The enthalpy increment measurements showed values very close to those of UO_2. The decrease of the melting temperature with the americium content,

for O/M close to 2.0, should not have consequences on the reactor behaviour during normal conditions (the maximum temperature for MABBs is 1480 K). However, the high temperature data here provided should be considered for predicting the evolution of the mixed oxides in case of accidental conditions. Finally, fundamental thermodynamic properties for the oxide fuels are the oxygen potentials, which determine the O/M evolution during irradiation and the interaction with the cladding. No new data could be provided in this work. On the basis of the oxygen potential available in the literature for AmO_{2-x} and $U_{0.5}Am_{0.5}O_{2\pm x}$, the Am addition surely causes an increase of the oxygen potentials, which is not positive for the behaviour in the reactor. However, similar increase of the oxygen potentials are observed with the $(U,Pu)O_2$ fuel. These can be managed, for instance by decreasing the initial O/M ratio of the fuel, but a better knowledge of the oxygen potentials remains essential.

This work has pointed out that further investigations on the thermodynamics of the U-Am-O system, and also of the Am-O system, are necessary. As already said, measuring the oxygen potentials of the $(U,Am)O_2$ oxides is essential. At first, these measurements should be performed on $(U,Am)O_2$ oxides with Am/(Am+U) = 0.50, in order to verify the agreement with the only available data in the literature [74]. The investigations should then be extended to other compositions, with both lower and higher americium contents. Besides, oxygen potentials measurements should also be performed on binary americium oxides. For AmO_{2-x}, three series of oxygen potentials measurements have been reported in the literature [57, 59, 60], but large discrepancies exist between these data. Therefore, new measurements are needed to understand the sources of these differences. In this frame, in order to improve the reliability of the data, conventional techniques, as the thermogravimetric analysis (TGA), should be coupled with XANES characterizations, to verify the compositions of the samples before and after the TGA experiments. This work has indeed proved the utility of this technique for the determination of the O/M ratio and data on the cationic oxidation distributions, very useful for the CALPHAD modeling. Moreover, efforts should be directed to improve the applicability of *in situ* high-temperature XAS techniques also to radioactive samples, in order to measure the variations of the O/M ratio as a function of temperature.

The miscibility gap of the U-Am-O phase diagram needs further investigations. HT-XRD measurements should be performed on oxides with Am/(Am+U) lower and higher than 0.70, possibly in isothermal conditions, in order to precisely determine the boundaries of the biphasic domain. KEMS measurements on $(U,Am)O_2$ should be extended to a wide temperature range in order to investigate the variation of the vapour pressures as a function of the temperature. Moreover, also the vaporization behaviour of AmO_2 needs to be re-investigated. KEMS experiments under O_2 are hence necessary, in order to stabilized the fluorite oxide against its reduction into Am_2O_3. These measurements would also allow the determination of fundamental thermodynamic properties as the enthalpy of formation of $AmO_2(g)$.

The thermodynamic modeling of the U-Am-O system, started in this work, needs to be continued. In the three sublattice model, the relations between the numerous parameters have to be improved in order to avoid the formation of metastable miscibility gaps, predicted by the present

model. Moreover, the solidus/liquidus data and the phase diagram data in the MO_2-M_4O_9-M_3O_8 domain have to be taken into account to improve the description of the phase equilibria. For future research, the coupling of the experimental investigations with thermodynamic calculations is mandatory, as proven in the present. Finally, considered the peculiarities of americium oxides, the next step of this research should be the investigation of the U-Pu-Am-O quaternary system, to better understand and predict the behaviour of the nuclear oxide fuels.

Appendix A

Experimental techniques

A.1   Room Temperature XRD

The XRD characterizations at room temperature were performed in the L7 laboratory of the Atalante facility, at CEA Marcoule. The diffractometer is a Bruker D8 Advance diffractometer in $\theta - \theta$ Bragg-Brentano geometry, equipped with a copper source [λ(Kα_1 and Kα_2) = 1.5406 and 1.5444 Å] and a Bruker LYNXEYE linear detector, with a 3° opening angle. The set-up has been especially modified for radioactive materials. The sample holder is inside a sealed stage, which is connected to a glove box for the preparation and loading of the sample. This latter is a powder, which is mixed with a grease, to avoid its dispersion during the connection from the glove box to the XRD set-up. The sealed stage has a beryllium window, to minimise the X-ray absorption.

Diffraction patterns were recorded in the $25 \leq 2\theta \leq 120°$ range, with a step of 0.01°, for a total recording duration of about 3 hours. For peak position correction, Au powder was added as a 2θ standard.

Analysis and refinement of the X-ray diffraction patterns were performed using the Fullprof Suite software [232] by applying the Le Bail method [171] and a Thompson-Cox-Hastings function [233] for peak profile description.

A.2   High Temperature XRD

In situ HT-XRD measurements were performed at the LEFCA facility of CEA Cadarache. The experimental set-up and procedure and the data analysis method are here described.

A.2.1   Experimental set-up

In situ HT-XRD measurements were performed using a Bragg-Brentano θ-θ Bruker D8 Advance X-ray diffractometer using copper radiation from a conventional tube source (Kα_1 + Kα_2 radiation: λ = 1.5406 and 1.5444 Å). The device is completely implemented in a nitrogen-filled glovebox dedicated to handling nuclear materials, as shown in Fig. A.1 (a). An MRI-Hightemp hot stage, shown in Fig. A.1 (b) and (c), was used for heating the sample. This consists of a

closed cylindrical metallic chamber, of about 0.5 l, whose windows are covered with Kapton, which allows to incident and reflected beams to enter and exit the chamber. The furnace allows heating the sample up to 2273 K using a metallic strip and a radiant heater, both made of Mo or a rhenium-platinum alloy, depending on the used atmosphere. For all the measurements presented in this work, since inert and oxidizing atmospheres were used, the PtRh strip was preferred. The controlling thermocouple was welded to the bottom of the metal strip. Before the measurements, a temperature calibration was carried out in steps of 100 K, from room temperature up to 1973 K, using MgO powder as reference. According to previous experiments, a constant uncertainty of ± 15 K is estimated on the temperature range considered.
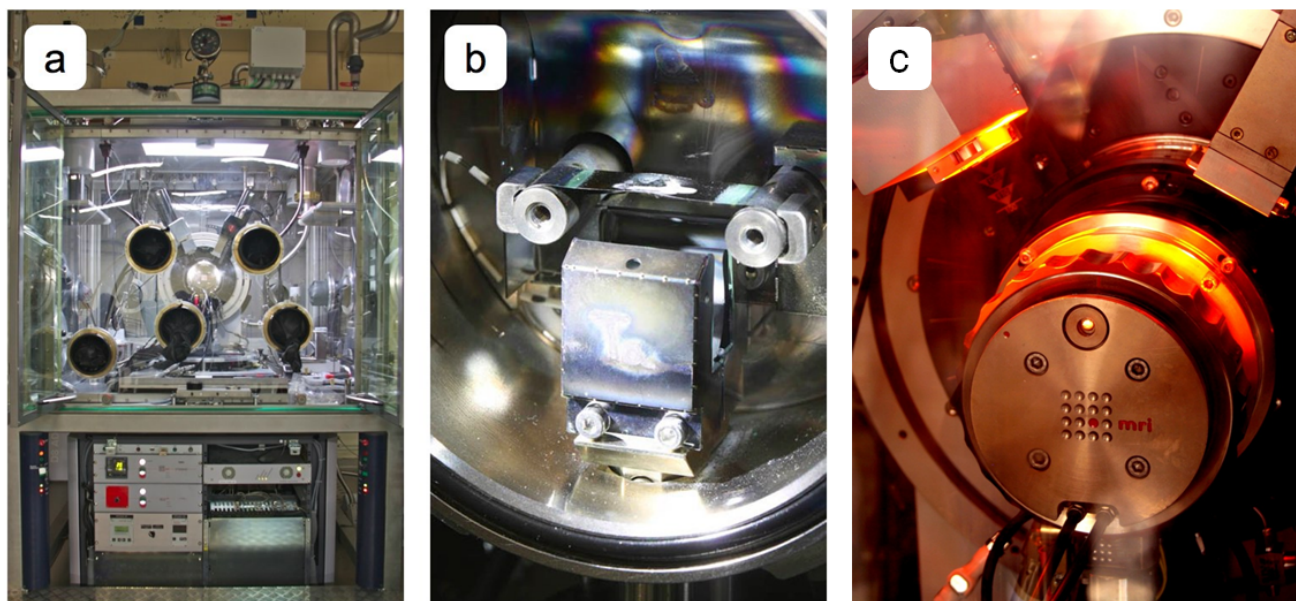
Fig. A.1: (a) Glovebox with the XRD set-up. (b) Insides of the furnace, heating stage and the omega heating element. (c) Furnace during operation.

The atmosphere inside the hot stage was controlled through a constantly flowing gas. Air and He/O_2 mixtures were used during the measurements presented in this thesis. Oxygen partial pressures (pO_2) between 0.21 and 10^{-20} atm were imposed at the inlet of the gas circuit by using a Gen-Air oxygen pump-gauge (developed by the Setnag company [234]), based on a zirconia electrolyte operating at 1100 K. The device can measure pO_2 from 10^{-35} to 0.25 atm and the provider indicates a relative uncertainty of 3% for this entire range; however, according to the repeatability of our experiences, higher uncertainties up to 25% should be considered for $pO_2 < 10^{-6}$ atm.

A.2.2　Data analysis

XRD patterns refinement was performed according to the Pawley method [200] using the TOPAS 4.0 software [235]. Instrumental contributions coming from the geometry, tube type and slits were included in the fitting according to the fundamental parameter approach [236]. Contributions from the microstructure were simulated by a physical broadening function. The uncertainty on the lattice parameters determined from the XRD patterns refinement is between ± 0.001 and

± 0.003 Å, depending on the quality of the XRD pattern and the fit goodness. When more than one phase was detected, a Rietveld refinement [201] was performed to retrieve the fraction of each phase.

A.3 X-ray absorption spectroscopy

The X-ray absorption (XAS) techniques used in this work will be briefly described. These techniques refer to the details of how x-rays are absorbed by an atom at energies near and above the core-level binding energies of that atom. Specifically, the **XAS studies the modulation of an atom's x-ray absorption probability due to the local environment of the atom** [237]. XAS spectra are especially sensitive to the oxidation state, the coordination chemistry of the probed element and to the distances, coordination number and species of the atoms immediately surrounding the selected element (distances ~ 8 Å).

A.3.1 Principle

The principle of the X-ray absorption spectroscopy (XAS) is the photoelectric effect, which is the predominant interaction mechanism between matter and X-rays (energy between 500 eV and 500 keV). The absorption coefficient μ of a material gives the probability that x-rays will be absorbed according to Lambert-Beer's law:

$$I = I_0 e^{-\mu t}, \tag{A.1}$$

where I_0 is the incident X-ray intensity, t is the thickness of the sample, and I is the intensity transmitted through the sample. In general, $\mu(E)$ is a smooth, decreasing function of the energy and it can be expressed as:

$$\mu(E) \approx \frac{\rho Z^4}{A E^3}, \tag{A.2}$$

where Z and A are respectively the atomic and mass numbers and ρ is the element density. However, when the incident X-ray energy equals the binding energy of a core electron of a particular element in the sample, a sharp rise in the absorption is observed: this is called **absorption edge** and it corresponds to the promotion of the core electron to empty valence levels and to the continuum. This can occurs, for example, to electron in the $1s$ orbitals corresponding to the K shell, $2s$, $2p_{1/2}$, $2p_{3/2}$ orbitals corresponding to the L_1, L_2, and L_3 shells. In the present work, the uranium was probed at the L_3 (~ 17166 eV) and L_2 (~ 20948 eV) edges and the americium was probed at the L_3 (~ 18510 eV) edge. Following an absorption event, the atom is in an excited state, with one empty core level. One of the main mechanisms of disexcitation for heavy elements is the x-ray fluorescence, in which a higher energy core-level electron fills the deeper core-hole, ejecting an X-ray of well-defined energy. The intensity of the X-ray fluorescence emission I_f is proportional to the absorption coefficient of the material $\mu(E)$. The $\mu(E)$ function can hence be measured in transmition geometry, according to Eq. (A.1), or

in fluorescence geometry, according to:

$$\mu(E) \propto \frac{I_f}{I_0}. \tag{A.3}$$

The representation of the absorption coefficient as a function of the incident energy $\mu(E)$ is called the X-ray absorption spectrum. As an example, spectra collected at the Am-L_3 absorption edge on reference compounds are shown in Fig. A.2.
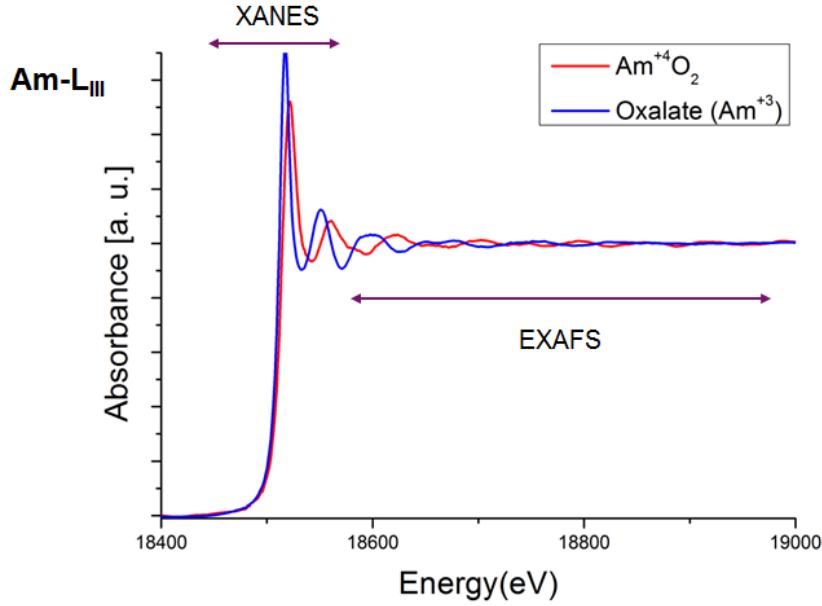
Fig. A.2: Example of XAS spectra collected in this work.

The following features can be identified in a spectrum:

- The **absorption edge**, its position is identified as the the first zero crossing of the second derivative of the $\mu(E)$ function.

- The **white line** is defined as the zero crossing of the first derivative of the $\mu(E)$ function.

The X-ray absorption spectrum is typically divided into two regimes: X-ray Absorption Near-Edge Spectroscopy (**XANES**, -30/+30 eV relative to the absorption edge) and Extended X-ray Absorption Fine-structure Spectroscopy (**EXAFS**). XANES is strongly sensitive to formal oxidation state and coordination chemistry (e.g., octahedral, tetrahedral coordination) of the absorbing atom, while the EXAFS is used to determine the distances, coordination number, and species of the neighbours of the absorbing atom. The EXAFS region corresponds to electrons which are emitted with high kinetic energy. Their interaction with the first neighbour atoms originates a modulation of the $\mu(E)$, due to the local environment. Since the EXAFS is best understood in terms of wave behaviour of the electrons, it is usual to convert the energy (E) dependence to the wave number k of the electrons:

$$k = \frac{\sqrt{2m(E - E_0)}}{\hbar} \tag{A.4}$$

where E_0 is the adsorption edge and m is the electron mass. The EXAFS equation, describing the modulation, is:

$$\chi(k) = \sum_j \frac{N_j f_j(k) e^{-2k^2\sigma_j^2}}{kR_j^2} sin[2kR_j + \delta_j(k)] \tag{A.5}$$

where $f(k)$ and $\delta(k)$ are scattering properties of the neighbour atoms, N is the number of neighbour atoms, R is the distance of the neighbour atoms and σ^2 is called Debye-Waller factor. This latter is a measure of the disorder in the neighbour distance and it is due both to the thermal agitation and the structural disorder.

A.3.2 Experimental set-up and conditions at the ROBL beamline

Small amounts (1-2 mg) of powdered sample were mixed with boron nitride were prepared (in a glove box) at CEA and pressed into pellets. These were doubly confined in polyethylene/teflon sample holders and shipped to the ESRF/Grenoble, for measurement at the ROBL beamline, under dedicated operating conditions (6 GeV, 180 mA). Spectra were collected at the U L_3, Am L_3, and U L_2 edges (17166, 18510, and 20948 eV), in both transmission and fluorescence modes, using ionization chambers filled with N_2/Ar and a Canberra energy-dispersive 13-element germanium solid-state detector. The beam size and distance between the sample and detector were adapted to remain in the linear range of the fluorescence detector. A double Si(111) crystal monochromator was used for energy selection, and the calibration was performed using metallic foils whose K edges are close to the edges of interest, i.e., yttrium (17038 eV), zirconium (17998 eV), and molybdenum (20000 eV). The references were measured at the same time of the samples, in transmission mode, using a second ionization chamber behind the foil. The spectra acquisitions were performed at room temperature and at 20 K (to reduce the thermal disorder for the EXAFS spectra), using a closed-cycle helium cryostat.

A.3.3 Experimental set-up and conditions at the INE beamline

Small amounts (1-2 mg) of powdered sample were mixed with boron nitride and pressed into pellets. These were putted in polyethylene sample holders and confined in a double sealed vinyl bag, for measurement at the INE beamline of the ANKA facility (Germany), under dedicated operating conditions (2.5 GeV, 120-150 mA). Spectra were collected at the U L_3, Am L_3, and U L_2 edges (17166, 18510, and 20948 eV), at room temperatures. Spectra were acquired both in transmission and fluorescence modes, using argon-filled ionization chambers and a Canberra LEGe five pixel fluorescence detector. A Ge(422) double crystal monochromator coupled with collimating and focusing Rh-coated mirrors were used for energy selection. The calibration was performed using metallic foils whose K edges are close to the edges of interest: yttrium (17038 eV), zirconium (17998 eV), and molybdenum (20000 eV). The references were measured at the same time of the samples, in transmission mode.

A.3.4   Data analysys

The XANES spectra were normalized using a linear function for pre- and postedge, using the Athena software [238]. The normalized spectra were fitted by linear combination of reference compound spectra, in order to determine the average oxidation states.

For EXAFS, The ATHENA software [238] was used for extracting EXAFS oscillations. Experimental EXAFS spectra were Fourier-transformed using a Hanning window. The ARTEMIS software was used for the curve fitting in k^3. Both interatomic scattering path phases and amplitudes were calculated using the FEFF8.40 ab initio code [239].

A.4   Raman spectroscopy

Micro-Raman spectroscopy was performed at JRC-Karlsruhe, using the experimental set-up described in [184]. A α-radiation and atmospheric tight Raman sample holder, shown in Fig. A.3, was adopted for the radioactive samples investigated in this work.
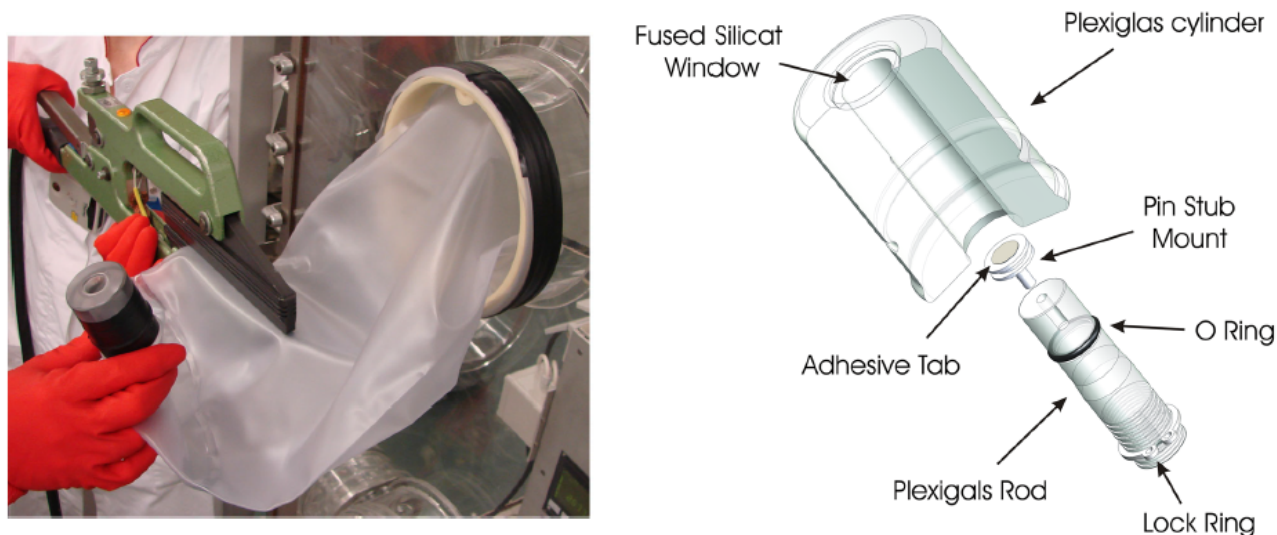
Fig. A.3: α-tight sample holder for Raman spectroscopy (figure extracted from [184]).

The Raman microscope is equipped with a long working distance (10.6 mm) objective which offers a 0.5 numerical aperture with a X50 magnification. The Raman spectroscope is a Jobin Yvon T 64000 equipped with a 1800 grooves per mm grating, a low noise LN2 cooled CCD detector an edge filter blocking the laser elastic scattering coming from the sample. The excitation source is a Kr^+ Coherent CW laser with main wavelengths at 647 nm or 752 nm, with a controllable nominal power, (up to few watts depending on the wavelength). The power impinging the sample surface is lower by a factor 5 approximately. Using the long focal x50 objective and the single spectrometer mode permits a good spectral resolution of ±1 cm^{-1} independently of the surface shape, with a spatial resolution of 2 μm X 2 μm on the sample surface. The spectrograph is calibrated with the T_{2g} excitation of a silicon single crystal, set at 520.5 cm^{-1}. The instrument was calibrated on a daily basis prior to measurements.

A.5 Drop calorimetry

The principle of the drop calorimetry is to measure the change in heat (enthalpy) in a sample between its initial and final temperature.

A.5.1 Experimental set-up

The enthalpy increment measurements were performed using a Setaram Multi Detector High Temperature Calorimeter (MDHTC 96 type) operating in drop mode. A schematic representation of the drop calorimeter is provided in Fig. A.4-a. The graphite furnace is separated from the experimental chamber by an alumina tube. The furnace is programmed to maintain a constant temperature inside the experimental chamber, which is measured by thermocouples arranged at different heights of the chamber surface. The arrangement provides good integration of the heat exchanges. The calorimeter has been nuclearized in the JRC-Karlsruhe laboratories in order to work with radioactive materials. More details about this design are provided in [240].

A.5.2 Experimental procedure

A schematic representation of the drop calorimeter is provided in Fig. A.4-a. To perform the measurements, the samples were introduced on the top of the experimental chamber, which is at room temperature. The furnace was programmed to reach and keep the target temperature of measurement T_m, at which the heat flow signal was stabilized during 7 hours. After this period, a *cold* sample was dropped into the detector, causing a small thermal shock. The additional heat provided to the system in order to re-stabilize T_m is proportional to the enthalpy increment of the sample. Drops were repeated every 25 minutes, which were sufficient to restore the temperature and the heat flow.

Fig. A.4-b shows a result of one measurement performed at 1600 K on two Am30 samples. Before and after each sample, small ingots of high purity Pt (99.9%) were dropped to be used as reference materials. These allowed determining the sensitivity S of the calorimeter, according to the following equation:

$$S = \frac{\int \Phi_r dt}{\int_{Ta}^{Tm} C_{P,R}(T)dt} \cdot \frac{M_R}{m_R} \tag{A.6}$$

Where $\int \Phi_r dt$ is the heat flow integrated in the time, Ta is the ambient temperature, $C_{P,R}(T)$ is the heat capacity function of the standard material [31] and m_r and M_r are respectively its mass and molar mass. The molar enthalpy increment of the sample ΔH_m from T_a to T_m can be calculated as:

$$\Delta_{Ta}^{Tm} H_m = \frac{\int \Phi_s d\tau}{S} \cdot \frac{M_S}{m_s} \tag{A.7}$$

in which $\int \Phi_s d\tau$ represents the heat provided by the furnace to bring the sample at T_m, M_s and m_s are the molar mass and the mass and S is computed as an average value of the two references dropped before and after the sample.
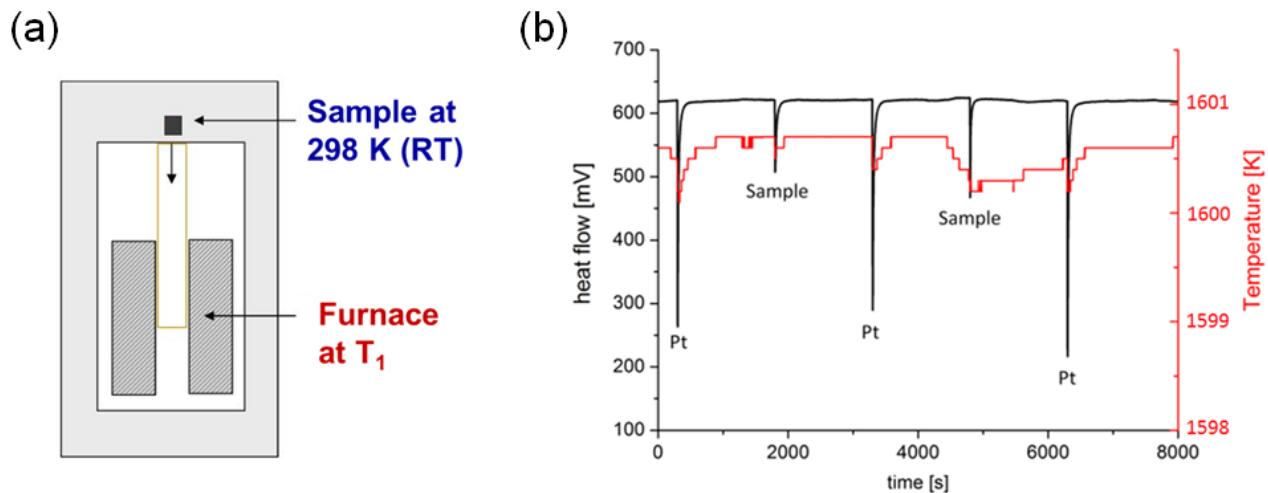
Fig. A.4: (a) Schematic representation of the drop calorimeter. (b) Example of a measurement result.

A.6 Knudsen effusion cells mass spectrometry

The vapour pressure measurements were performed at the JRC-Karlsruhe laboratory, using a Knudsen effusion cell coupled with mass spectrometry (KEMS), installed in a shielded glove box. The experimental set-up, schematically represented in Fig. A.5, is detailly described in the literature [241, 242]. Powdered samples of about 30-40 mg are placed in tungsten Knudsen cell, centred in a high-temperature tungsten furnace. The whole system was placed in a ultra-high vacuum chamber (10^{-6}-10^{-4} Pa).

When the sample is heated at temperature T, it begins to vaporise and equilibrium is established in the cell between the vapour and the condensed phase. This is the total equilibrium vapour pressure of the sample at T. The cell is equipped with a small orifice at its top. This allows a small part of the vapour to leave, without altering the equilibrium vapour pressure in the cell. The diameter of the orifice is dimensioned in order to respect the Knudsen condition. This is valid when there are no collisions between the gaseous species inside the cell, i. e. when the mean free path of the molecules is large compared to the diameter of the orifice. Under the Knudsen condition, the flux of molecules flowing out of the cell is proportional to the partial pressure of this molecular species inside the cell [218].

The vapour species leaving the cell travel in a molecular flow, toward the quadrupole mass spectrometer, where they cross an electronic beam. A small fraction of the gaseous molecules (0.001%) is ionised by electron impact and then the masses are separated by an electrical field. The vapour pressure of the i-species p_i can then be calculated from the measured intensity of the corresponding ionic specie I_i^+, as:

$$p_i = I_i^+ \cdot T/K \tag{A.8}$$
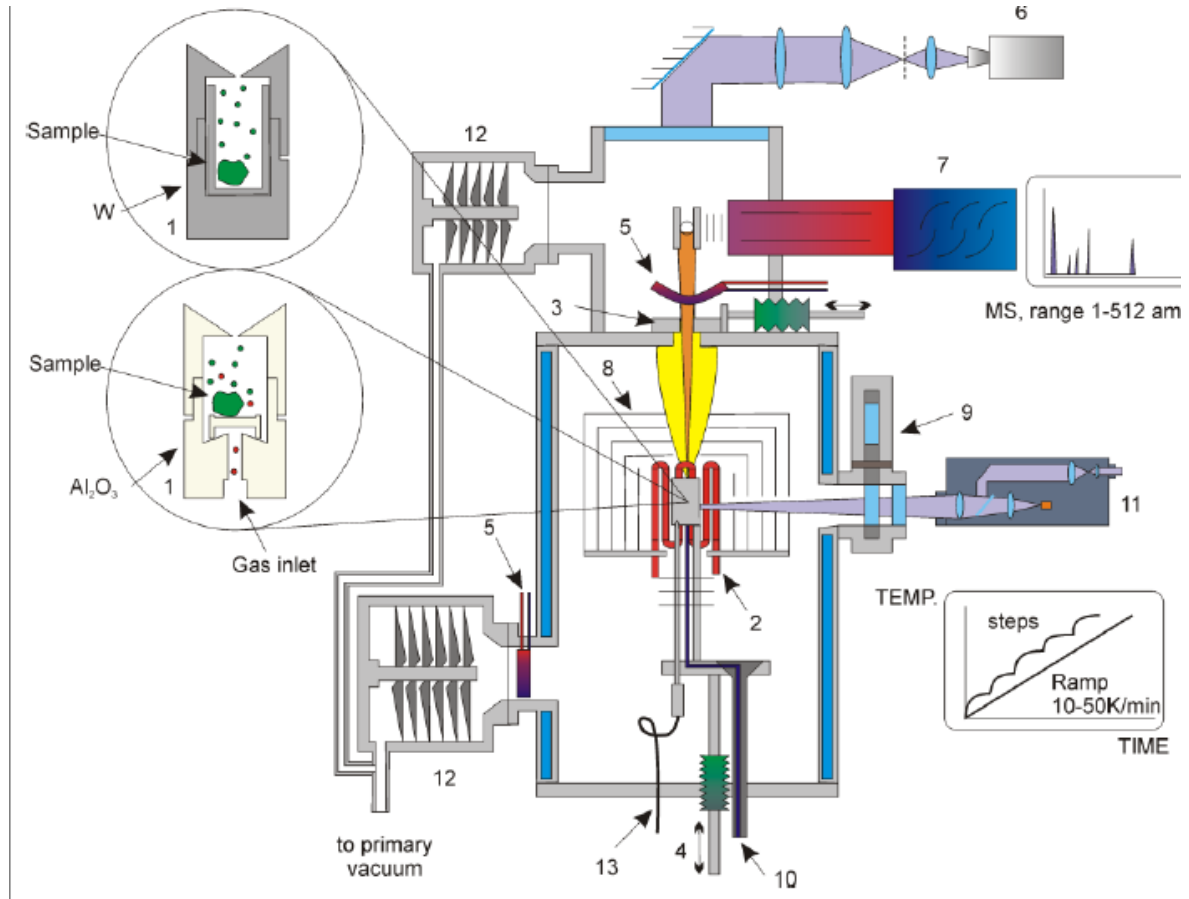
Fig. A.5: Representation of the KEMS set-up [241].

where T is the temperature and K is the calibration factor. This latter can be expressed as:

$$K = k_g \cdot k_i, \tag{A.9}$$

where k_g is an instrumental factor, independent of the i-species, whereas k_i depends on the gaseous species i. k_i can be expressed as:

$$k_i = \sigma_i \cdot \gamma_i \cdot f_i, \tag{A.10}$$

where σ_i is the ionisation cross section of the species i, γ_i is the efficiency of the secondary ion multiplier and f_i is the isotopic abundance of i. The ionisation cross sections of the various U and Am species were evaluated using the modified additivity rule proposed by Deutsh [222]. The secondary ion multiplier is calculated, for species with mass number higher than 50, with the approximation:

$$\gamma_i = \delta/\sqrt{M_i}, \tag{A.11}$$

where δ is a constant of the instrument and M_i is the mass of the species [218].

The instrumental k_g factor of the KEMS systems is determined by vaporizing a reference material together with the sample. In this work, silver was adopted as a reference [243], because it does not interact with the actinide oxides. Moreover, silver vaporized completely up to 1500

K, generally before the actinide oxide vaporization started. The overall calibration factor K of silver is derived from:

$$p_{Ag} = I_{Ag}^+ \cdot T_{Ag}/K_{Ag} = I_{Ag}^+ \cdot T_{Ag}/(k_g \cdot \sigma_{Ag} \cdot \gamma_{Ag} \cdot f_{Ag}). \tag{A.12}$$

Combining Eq. (A.8) with Eq. (A.12), it is possible to determine the vapour pressure of any species:

$$p_i = p_{Ag} \cdot \frac{I_i \cdot T_i}{I_{Ag}^+ \cdot T_{Ag}} \cdot \frac{\sigma_{Ag} \cdot \gamma_{Ag} \cdot f_{Ag}}{\sigma_i \cdot \gamma_i \cdot f_i}. \tag{A.13}$$

Finally, substituting Eq. (A.11) in Eq. (A.13), one finally obtains:

$$p_i = p_{Ag} \cdot \frac{I_i \cdot T_i}{I_{Ag}^+ \cdot T_{Ag}} \cdot \frac{\sqrt{M_i}}{\sqrt{M_{Ag}}} \cdot \frac{\sigma_{Ag} \cdot f_{Ag}}{\sigma_i \cdot f_i}. \tag{A.14}$$

A.7 Laser-heating

The melting temperature measurements were performed by laser heating and fast multi-channel pyrometry, an experimental method developed at JRC-Karlsruhe [32,223]. The experimental set-up, schematically shown in Fig. A.6, was detailed in previous publications [32,223,224,224,226].

During the experiment, the mixed oxide pellet is held in a sealed autoclave under a controlled atmosphere of pressurized argon or air. A typical 200 Pa overpressure is used in order to avoid a too important vaporization. A short pulse ($\sim$ ms) from a 4.5 kW Nd:YAG continuous wave laser operating at 1064 nm is used to locally heat and melt a circular spot of approximately 2-3 mm in diameter on the surface of the samples. Before the next pulse, the sample is let to cool down naturally. The sample surface temperature is detected by means of a fast pyrometer operating near 650 nm, with a nominal measurement spot size of 0.5 mm in diameter. The normal spectral emissivities (NSE) of U-Am dioxides, necessary for the determination of the sample temperature, was estimated using a multichannel (256 channels) pyrometer, according to the procedure detailed in [223].

According to previous experiences, an uncertainty of ± 50 K is estimated for the recorded temperature [226]. This takes into account the uncertainty in the sample emissivity. The melting temperature is determined analysing the thermogram, by identification of the main thermal arrest during the cooling. Simultaneously, a second method is used for detecting the melting: the so-called Reflected Light Signal (RLS) technique. This involves the detection of the variations in the effective reflectivity of the sample surface that accompanies the formation of the liquid phase. Such an analysis is carried out by means of a 0.75 W, 488 nm Ar$^+$ laser beam, that is reflected by the sample surface and then detected by a second channel (tuned to this laser wavelength) of the same pyrometer used for the temperature measurement.
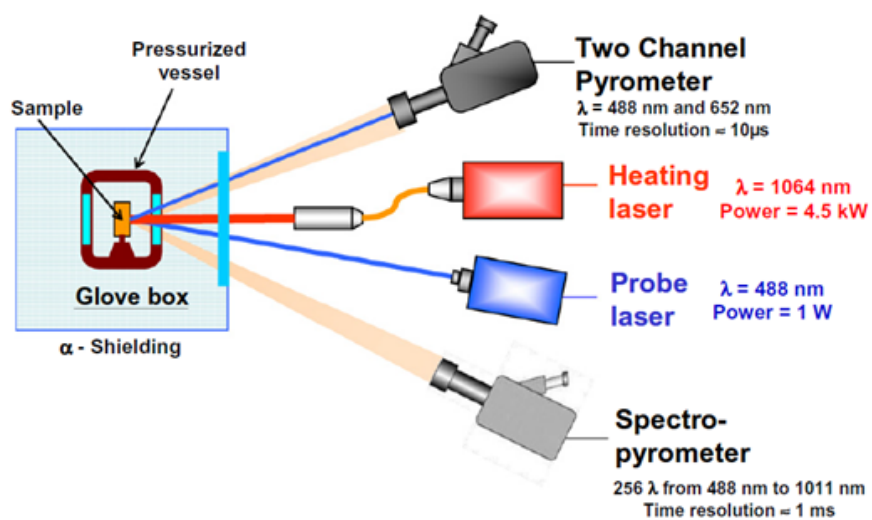
Fig. A.6: Representation of the experimental set-up used for the melting measurements.

Appendix B

Materials

B.1   AmO$_2$ powders

Composition		Am C9		Am TCH	
		Technique	Value	Technique	Value
Isotopic (at.%)	^{241}Am	TIMS	98.74(1)	TIMS	100.0(3)
	^{242}Am	TIMS	<0.02 (LOD)	TIMS	<0.02(LOD)
	^{243}Am	TIMS	1.25(1)	TIMS	<0.02(LOD)
Chemical (mol.%)	Am	α spectrometry	83(8)	α spectrometry	81(2)
	Pu	-	-	TIMS	2.7(1)
	Np	Calculated	0.21	Spectrophotometry	1.2(2)
	U	ICP-QMS	-	ICP-QMS	0.09(1)
	Na	ICP-AES	0.6(2)	ICP-QMS	<0.03 (LOD)
	Si	ICP-AES	<0.2	ICP-QMS	0.07(1)
	Fe	ICP-AES	0.4(1)	ICP-QMS	<0.03 (LOD)
	Ce	ICP-AES	1.7(5)	-	-
	Nd	ICP-AES	0.5(1)	-	-

Table B.1: Chemical compositions of the AmO$_2$ samples.

TIMS: Thermal Ionization mass spectrometry

ICP-QMS: Inductively coupled plasma-quadrupole mass spectrometry

ICP-AES: Inductively coupled plasma- atomic emission spectroscopy

ICP-SFMS: Inductively coupled plasma- sector field mass spectrometry

LOD: limit of detection

B.2   UO$_2$ powders

TIMS: Thermal Ionization mass spectrometry

ICP-QMS: Inductively coupled plasma-quadrupole mass spectrometry

NC: Not communicated

Composition		Natural UO$_2$		UO$_2$-CAD	
		Technique	Value	Technique	Value
Isotopic (at.%)	^{234}U	TIMS	0.0060(6)	N.C.	0.001(6)
	^{235}U	TIMS	0.722(7)	N.C.	0.258(1)
	^{236}U	TIMS	<0.005(1)	N.C.	<0.0003
	^{238}U	TIMS	99.27(3)	N.C.	99.741(2)
Chemical (mol.%)	U	-	-	N.C.	87.80(2)
	Th	ICP-QMS	0.011(1)	N.C.	<0.0001
	C	N.C.	0.0077	N.C.	0.0018

Table B.2: Chemical compositions of the UO$_2$ samples.

Appendix C

Thermodynamic models

The Gibbs energy functions of all the phases refer to the Stable Element Reference (SER) state, the stable state for the element at 298 K and 10^5 Pa [21].

C.1   Am-O system

As seen in Ch. 3, the Am-O CALPHAD model of Gotcu-Freis [64] has been modified in this work. The modifications concern: the $AmO_{1.61}$, the AmO_2 solid phases and the $AmO(g)$ and $AmO_2(g)$ species of the gas phase.

For the $AmO_{1.61}$, a new sublattice model has been introduced. This is presented in Ch. 3. The thermodynamic parameters are reported in Tab. C.1. For the solid AmO_2 and gas species, the same model as in [64] has been maintained, but some of the parameters were re-assessed. These are reported in Tab. C.1. We refer to the work of Gotcu *et al.* [64] for the $O2GAS, GAMO2, GAMO15$ functions and the Gibbs energies of the other phases.

C.2   The U-Am-O system

The Calphad assessment of the U-Am-O system has been presented in Ch. 7. The optimization concerned only the $(U,Am)O_2$ phase. As seen in Ch. 7, the three sublattice model used for the $(U,Am)O_{2\pm x}$ phase is:

$$(U^{3+}, U^{4+}, U^{5+}, Am^{3+}, Am^{4+})_1 (O^{2-}, Va)_2 (O^{2-}, Va). \tag{C.1}$$

The general Gibbs energy function associated to this model is:

$$G^{(U,Am)O_2} = \sum_i \sum_j \sum_k G^{(U,Am)O_2}_{i:j:k} + R \cdot T \sum_i y_i \cdot ln y_i + 2 \cdot R \cdot T \sum_j y_j \cdot ln y_j$$

$$+ R \cdot T \sum_k y_k \cdot ln y_k + \sum_{i_1} \sum_{i_2} \sum_j \sum_k y_{i_2} \cdot y_{i_1} \cdot y_j \cdot y_k \cdot [^0 L^{(U,Am)O_2}_{i_1,i_2:j:k} + (y_{i_1} - y_{i_2}) \cdot ^1 L^{(U,Am)O_2}_{i_1,i_2:j:k}]$$

$$+ \sum_{i_1} \sum_{i_2} \sum_{j_1} \sum_{j_2} \sum_k y_{i_1} \cdot y_{i_2} \cdot y_{j_1} \cdot y_{j_2} \cdot [^0 L^{(U,Am)O_2}_{i_1,i_2:j_1,j_2:k}] + \sum_{i_1} \sum_{i_2} \sum_j \sum_{k_1} \sum_{k_2} y_{i_1} \cdot y_{i_2} \cdot y_{k_1} \cdot y_{k_2} \cdot [^0 L^{(U,Am)O_2}_{i_1,i_2:j:k_1,k_2}]$$

$$\text{(C.2)}$$

where y_i represents the fraction of the species i in the first sublattice (j and k, second and third sublattices respectively), $G^{(U,Am)O_2}_{i:j:k}$ are the Gibbs energies of the different compounds formed by considering the species i in the first sublattice, j and k in the second and the third sublattices, respectively. $^n L^{(U,Am)O_2}$ are the interaction parameters between species in the different sublattices.

The optimized parameters for this phase are listed in Tab. C.2.

Thermodynamic parameters	Reference
AmO$_{2\text{-x}}$ phase	

$$G^{AmO_2}_{(Am^{4+})(O^{2-})(Va)} - H^{SER}_{Am} - 2H^{SER}_O = GAMO2 \qquad \text{[64]}$$

$$G^{AmO_2}_{(Am^{4+})(Va)(Va)} - H^{SER}_{Am} = GAMO2 - O2GAS \qquad \text{[64]}$$

$$G^{AmO_2}_{(Am^{4+})(O^{2-})(O^{2-})} - H^{SER}_{Am} - 3H^{SER}_O = GAMO2 + \tfrac{1}{2}O2GAS + 124307 \qquad \text{[64], this work}$$

$$G^{AmO_2}_{(Am^{4+})(Va)(O^{2-})} - H^{SER}_{Am} - H^{SER}_O = GAMO2 - \tfrac{1}{2}O2GAS + 124307 \qquad \text{[64], this work}$$

$$G^{AmO_2}_{(Am^{3+})(Va)(Va)} - H^{SER}_{Am} = GAMO15 - \tfrac{3}{4}O2GAS + 1.1247 \cdot RT \qquad \text{[64]}$$

$$G^{AmO_2}_{(Am^{3+})(Va)(O^{2-})} - H^{SER}_{Am} - H^{SER}_O = GAMO15 - \tfrac{1}{4}O2GAS + 1.1247 \cdot RT + 321092 \qquad \text{[64], this work}$$

$$G^{AmO_2}_{(Am^{3+})(O^{2-})(O^{2-})} - H^{SER}_{Am} - 3H^{SER}_O = GAMO15 + \tfrac{3}{4}O2GAS + 1.1247 \cdot RT + 321092 \qquad \text{[64], this work}$$

$$G^{AmO_2}_{(Am^{3+})(O^{2-})(Va)} - H^{SER}_{Am} - 2H^{SER}_O = GAMO15 + \tfrac{1}{4}O2GAS + 1.1247 \cdot RT \qquad \text{[64]}$$

$$^0L^{AmO_2}_{(Am^{3+},Am^{4+})(*)(*)} = 30010 - 4.608 \cdot T \qquad \text{this work}$$

$$^1L^{AmO_2}_{(Am^{3+},Am^{4+})(*)(*)} = -24182 + 15.28 \cdot T \qquad \text{this work}$$

| AmO$_{1.61\text{+x}}$ phase | |

$$G^{AmO_{(1.61)}}_{(Am^{3+})(O^{2-})(O^{2-})} - 2H^{SER}_{Am} - 4H^{SER}_O = 2 \cdot GAMO15 + \tfrac{1}{2}O2GAS - 5306 + 6.527 \cdot T \qquad \text{this work}$$

$$G^{AmO_{(1.61)}}_{(Am^{4+})(O^{2-})(O^{2-})} - 2H^{SER}_{Am} - 4H^{SER}_O = 2 \cdot GAMO2 + 5170 + 21.31 \cdot T \qquad \text{this work}$$

$$G^{AmO_{(1.61)}}_{(Am^{3+})(O^{2-})(Va)} - 2H^{SER}_{Am} - 3H^{SER}_O = 2 \cdot GAMO15 - 5306 + 6.527 \cdot T \qquad \text{this work}$$

$$G^{AmO_{(1.61)}}_{(Am^{4+})(O^{2-})(Va)} - 2H^{SER}_{Am} - 3H^{SER}_O = 2 \cdot GAMO2 - \tfrac{1}{2}O2GAS + 5170 + 21.31 \cdot T \qquad \text{this work}$$

$$^0L^{AmO_{(1.61)}}_{(Am^{3+},Am^{4+})(O^{2-})(O^{2-})} = {}^0L^{AmO_{(1.61)}}_{(Am^{3+},Am^{4+})(O^{2-})(Va)} = +11305 - 4.4928 \cdot T \qquad \text{this work}$$

| Gas | |

$$G^{gas}_{AmO} - H^{SER}_{Am} - H^{SER}_O = -15158.18 - 26.15 \cdot T - 34.32 \cdot T \cdot ln(T) - 0.003065 \cdot T^2$$
$$+1.068 \cdot 10^{-6} \cdot T^3 - 3.337 \cdot 10^{-10} \cdot T^4 + 134461 \cdot T^{-1}; 298 < T < 1500K \qquad \text{[127], this work}$$
$$= +103714.5 - 903.37 \cdot T + 85.67 \cdot T \cdot ln(T) - 0.0558 \cdot T^2$$
$$+5.043 \cdot 10^{-6} \cdot T^3 - 2.357 \cdot 10^{-10} \cdot T^4 - 21759000 \cdot T^{(-1)}; 1500 < T < 4000K$$

$$G^{gas}_{AmO_2} - H^{SER}_{Am} - 2H^{SER}_O = -367811.05 + 82.66 \cdot T - 52.79 \cdot T \cdot ln(T) - 0.013038 \cdot T^2$$
$$+4.5275 \cdot 10^{-6} \cdot T^3 - 8.5244 \cdot 10^{-10} \cdot T^4 + 168795 \cdot T^{-1}; 298 < T < 1000K \qquad \text{[127], this work}$$
$$= -364504.84 + 85.89 \cdot T - 54.49 \cdot T \cdot ln(T) - 0.003587 \cdot T^2$$
$$+2.438 \cdot 10^{-7} \cdot T^3 - 1.09558 \cdot 10^{-11} \cdot T^4 - 630200 \cdot T^{(-1)}; 1000 < T < 4000K$$

Table C.1: Thermodynamic parameters for the AmO$_{1.6}$, AmO$_2$ and gas phases, assessed in this work.

Thermodynamic parameters of the $(U,Am)O_2$ phase	Reference
$G^{(U,Am)O_2}_{(U^{3+})(O^{2-})(Va)}$	
$G^{(U,Am)O_2}_{(U^{4+})(O^{2-})(Va)}$	
$G^{(U,Am)O_2}_{(U^{5+})(O^{2-})(Va)}$	
$G^{(U,Am)O_2}_{(U^{3+})(Va)(Va)}$	
$G^{(U,Am)O_2}_{(U^{4+})(Va)(Va)}$	
$G^{(U,Am)O_2}_{(U^{5+})(Va)(Va)}$	
$G^{(U,Am)O_2}_{(U^{3+})(O^{2-})(O^{2-})}$	
$G^{(U,Am)O_2}_{(U^{4+})(O^{2-})(O^{2-})}$	[27]
$G^{(U,Am)O_2}_{(U^{5+})(O^{2-})(O^{2-})}$	
$G^{(U,Am)O_2}_{(U^{3+})(Va)(O^{2-})}$	
$G^{(U,Am)O_2}_{(U^{4+})(Va)(O^{2-})}$	
$G^{(U,Am)O_2}_{(U^{5+})(Va)(O^{2-})}$	
$L^{(U,Am)O_2}_{(U^{4+},U^{5+})(O^{2-})(Va)}$	
$L^{(U,Am)O_2}_{(U^{3+},U^{5+})(O^{2-})(Va)}$	
$G^{(U,Am)O_2}_{(Am^{4+})(O^{2-})(Va)} - H^{SER}_{Am} - 2H^{SER}_O = GAMO2$	[64]
$G^{(U,Am)O_2}_{(Am^{4+})(Va)(Va)} - H^{SER}_{Am} = GAMO2 - O2GAS$	[64]
$G^{(U,Am)O_2}_{(Am^{4+})(O^{2-})(O^{2-})} - H^{SER}_{Am} - 3H^{SER}_O = GAMO2 + \frac{1}{2}O2GAS + 124307$	[64], this work
$G^{(U,Am)O_2}_{(Am^{4+})(Va)(O^{2-})} - H^{SER}_{Am} - H^{SER}_O = GAMO2 - \frac{1}{2}O2GAS + 124307$	[64], this work
$G^{(U,Am)O_2}_{(Am^{3+})(Va)(Va)} - H^{SER}_{Am} = GAMO15 - \frac{3}{4}O2GAS + 1.12467 \cdot RT$	[64]
$G^{(U,Am)O_2}_{(Am^{3+})(Va)(O^{2-})} - H^{SER}_{Am} - H^{SER}_O = GAMO15 - \frac{1}{4}O2GAS + 1.12467 \cdot RT + 321092$	[64], this work
$G^{(U,Am)O_2}_{(Am^{3+})(O^{2-})(O^{2-})} - H^{SER}_{Am} - 3H^{SER}_O = GAMO15 + \frac{3}{4}O2GAS + 1.125 \cdot RT + 321092$	[64], this work
$G^{(U,Am)O_2}_{(Am^{3+})(O^{2-})(Va)} - H^{SER}_{Am} - 2H^{SER}_O = GAMO15 + \frac{1}{4}O2GAS + 1.125 \cdot RT$	[64]
$^0L^{(U,Am)O_2}_{(Am^{3+},Am^{4+})(*)(*)} = 30010 - 4.608 \cdot T$	this work
$^1L^{(U,Am)O_2}_{(Am^{3+},Am^{4+})(*)(*)} = -24182 + 15.28 \cdot T$	this work
$^0L^{(U,Am)O_2}_{(Am^{3+},U^{5+})(*)(*)} = -369140$	
$^0L^{(U,Am)O_2}_{(Am^{3+},U^{4+})(*)(*)} = -310395 + 35.8 \cdot T$	
$^0L^{(U,Am)O_2}_{(Am^{4+},U^{5+})(*)(*)} = -340000$	this work
$^0L^{(U,Am)O_2}_{(Am^{3+},U^{5+})(O^{2-},Va)(Va)} = -346283$	
$^0L^{(U,Am)O_2}_{(Am^{3+},U^{5+})(O^{2-})(O^{2-},Va)} = -386170$	

Table C.2: Thermodynamic parameters for the $(U,Am)O_2$ phase assessed in this work.

Bibliography

[1] "Key world energy statistics 2014 - India Environment Portal | News, reports, documents, blogs, data, analysis on environment & development | India, South Asia."

[2] P. Wersin, M. Kiczka, and K. Koskinen, "Porewater chemistry in compacted bentonite: Application to the engineered buffer barrier at the Olkiluoto site," *Applied Geochemistry*, vol. 74, pp. 165–175, 2016.

[3] "LOI n° 91-1381 du 30 décembre 1991 relative aux recherches sur la gestion des déchets radioactifs," 1991.

[4] M. Salvatores and G. Palmiotti, "Radioactive waste partitioning and transmutation within advanced fuel cycles: Achievements and challenges," *Progress in Particle and Nuclear Physics*, vol. 66, no. 1, pp. 144–166, 2011.

[5] M. Salvatores, "Nuclear fuel cycle strategies including Partitioning and Transmutation," *Nuclear Engineering and Design*, vol. 235, no. 7, pp. 805–816, 2005.

[6] R. S. Herbst, P. Baron, and M. Nilsson, "6 - Standard and advanced separation: PUREX processes for nuclear fuel reprocessing," in *Advanced Separation Techniques for Nuclear Fuel Reprocessing and Radioactive Waste Treatment*, Woodhead Publishing Series in Energy, pp. 141–175, Woodhead Publishing, 2011.

[7] C. Rostaing, C. Poinssot, D. Warin, P. Baron, and B. Lorraina, "Development and Validation of the EXAm Separation Process for Single Am Recycling," *Procedia Chemistry*, vol. 7, pp. 367–373, 2012.

[8] W. Maschek, X. Chen, F. Delage, A. Fernandez-Carretero, D. Haas, C. Matzerath Boccaccini, A. Rineiski, P. Smith, V. Sobolev, R. Thetford, and J. Wallenius, "Accelerator driven systems for transmutation: Fuel development, design and safety," *Progress in Nuclear Energy*, vol. 50, no. 2, pp. 333–340, 2008.

[9] T. Abram and S. Ion, "Generation-IV nuclear power: A review of the state of the science," *Energy Policy*, vol. 36, no. 12, pp. 4323–4330, 2008.

[10] "GIF Portal - Home - Public." `https://www.gen-4.org/gif/jcms/c_9260/public`. Accessed: 2017-09-11.

[11] R. J. M. Konings and D. Haas, "Fuels and targets for transmutation," *Comptes Rendus Physique*, vol. 3, no. 7–8, pp. 1013–1022, 2002.

[12] J. Somers, "Minor Actinide Bearing Fuels: Fabrication and Irradiation Experience in Europe," *Energy Procedia*, vol. 7, pp. 169–176, 2011.

[13] T. Takeda, "Minor actinides transmutation performance in a fast reactor," *Annals of Nuclear Energy*, vol. 95, pp. 48–53, 2016.

[14] C. T. Walker and G. Nicolaou, "Transmutation of neptunium and americium in a fast neutron flux: EPMA results and KORIGEN predictions for the superfact fuels," *Journal of Nuclear Materials*, vol. 218, no. 2, pp. 129–138, 1995.

[15] S. Pillon, "3.05 - Actinide-Bearing Fuels and Transmutation Targets," in *Comprehensive Nuclear Materials* (R. J. M. Konings, ed.), pp. 109–141, Oxford: Elsevier, 2012.

[16] E. D'Agata, P. R. Hania, S. Bejaoui, C. Sciolla, T. Wyatt, M. H. C. Hannink, N. Herlet, A. Jankowiak, F. C. Klaassen, and J. M. Bonnerot, "MARIOS: Irradiation of UO2 containing 15% americium at well defined temperature," *Nuclear Engineering and Design*, vol. 242, pp. 413–419, 2012.

[17] E. D'Agata, P. R. Hania, S. Bejaoui, C. Sciolla, T. Wyatt, M. H. C. Hannink, N. Herlet, A. Jankowiak, F. C. Klaassen, J. M. Lapetite, D. A. Boomstra, M. Phelip, and F. Delage, "The results of the irradiation experiment MARIOS on americium transmutation," *Annals of Nuclear Energy*, vol. 62, pp. 40–49, 2013.

[18] D. Horlait, F. Lebreton, T. Delahaye, N. Herlet, and P. Dehaudt, "U1-xAmxO2pmδ MABB Fabrication in the Frame of the DIAMINO Irradiation Experiment," *Procedia Chemistry*, vol. 7, pp. 485–492, 2012.

[19] G. L. Hofman, J. H. Bottcher, J. A. Buzzell, and G. M. Schwartzenberger, "Thermal conductivity and thermal expansion of hot-pressed trisodium uranate (Na3uo4)," *Journal of Nuclear Materials*, vol. 139, no. 2, pp. 151–155, 1986.

[20] "OECD NEA/NSC: Thermodynamics of Advanced Fuels – International Database (TAF-ID)." `https://www.oecd-nea.org/science/taf-id/`. Accessed: 2017-01-22.

[21] B. S. H. Lukas, S. G. Fries, *Computational Thermodynamics The Calphad Method \ Materials science.* 2007.

[22] A. Kroupa, "Modelling of phase diagrams and thermodynamic properties using Calphad method – Development of thermodynamic databases," *Computational Materials Science*, vol. 66, pp. 3–13, 2013.

[23] M. Baichi, C. Chatillon, G. Ducros, and K. Froment, "Thermodynamics of the O–U system: III – Critical assessment of phase diagram data in the U–UO2+x composition range," *Journal of Nuclear Materials*, vol. 349, no. 1–2, pp. 57–82, 2006.

[24] D. Labroche, "PhD thesis, Etude thermodynamique du ternaire U Fe O," 2000.

[25] J. K. Fink, "Thermophysical properties of uranium dioxide," *Journal of Nuclear Materials*, vol. 279, no. 1, pp. 1–18, 2000.

[26] C. Guéneau, M. Baichi, D. Labroche, C. Chatillon, and B. Sundman, "Thermodynamic assessment of the uranium–oxygen system," *Journal of Nuclear Materials*, vol. 304, no. 2–3, pp. 161–175, 2002.

[27] C. Guéneau, N. Dupin, B. Sundman, C. Martial, J.-C. Dumas, S. Gossé, S. Chatain, F. D. Bruycker, D. Manara, and R. J. M. Konings, "Thermodynamic modelling of advanced oxide and carbide nuclear fuels: Description of the U–Pu–O–C systems," *Journal of Nuclear Materials*, vol. 419, no. 1–3, pp. 145–167, 2011.

[28] L. R. Morss, N. M. Edelstein, J. Fuger, "The Chemistry of the Actinide and Transactinide Elements- Third Edition," 2006.

[29] C. Guéneau, V. Dauvois, P. Pérodeaud, C. Gonella, and O. Dugne, "Liquid immiscibility in a (O,U,Zr) model corium," *Journal of Nuclear Materials*, vol. 254, no. 2–3, pp. 158–174, 1998.

[30] R. E. Latta and R. E. Fryxell, "Determination of solidus-liquidus temperatures in the UO2+x system (-0.50<x<0.20)," *Journal of Nuclear Materials*, vol. 35, no. 2, pp. 195–210, 1970.

[31] R. K. Edwards, A. E. Martin, *Thermodynamics, Proc. Symp., vol. 2.* International Atomic Energy Agency, 1966.

[32] D. Manara, C. Ronchi, M. Sheindlin, M. Lewis, and M. Brykin, "Melting of stoichiometric and hyperstoichiometric uranium dioxide," *Journal of Nuclear Materials*, vol. 342, no. 1–3, pp. 148–163, 2005.

[33] B. E. Schaner, "Metallographic determination of the UO2-U4O9 phase diagram," *Journal of Nuclear Materials*, vol. 2, no. 2, pp. 110–120, 1960.

[34] P. E. Blackburn, "Oxygen Dissociation Pressures over Uranium Oxides," *J. Phys. Chem.*, vol. 62, no. 8, pp. 897–902, 1958.

[35] L. E. J. Roberts and A. J. Walter, "Equilibrium pressures and phase relations in the uranium oxide system," *Journal of Inorganic and Nuclear Chemistry*, vol. 22, no. 3–4, pp. 213–229, 1961.

[36] C. Picard and P. Gerdanian, "Etude thermodynamique du systeme uranium-oxygene a 1050 °C," *Journal of Nuclear Materials*, vol. 99, no. 2–3, pp. 184–189, 1981.

[37] A. Kotlar, P. Gerdanian, M. Dodé, "J. Chim. Phys. Phys. Chim. Biol," p. 687, 1968.

[38] A. Kotlar, P. Gerdanian, M. Dodé, "J. Chim. Phys. Phys. Chim. Biol," p. 862, 1967.

[39] P. O. Perron, *Report AECL-3072.* 1968.

[40] E.F. Westrum, Jr., Y. Takahashi, F. Gronvold, "J. Am. Chem. Soc.," p. 529, 1965.

[41] F. Grønvold, N. J. Kveseth, A. Sveen, and J. Tichý, "Thermodynamics of the UO2+x phase I. Heat capacities of UO2.017 and UO2.254 from 300 to 1000 K and electronic contributions," *The Journal of Chemical Thermodynamics*, vol. 2, no. 5, pp. 665–679, 1970.

[42] K. Gotoo and K. Naito, "Study on U4O9—part I. An anomaly of the heat capacity near the room temperature," *Journal of Physics and Chemistry of Solids*, vol. 26, no. 11, pp. 1673–1677, 1965.

[43] K. Naito, T. Tsuji, and T. Matsui, "An electrical conductivity and X-ray study of a high-temperature transition in U4O9," *Journal of Nuclear Materials*, vol. 48, no. 1, pp. 58–66, 1973.

[44] N. Keiji, "Phase transitions of U4O9," *Journal of Nuclear Materials*, vol. 51, no. 1, pp. 126–135, 1974.

[45] A. M. George and M. D. Karkhanavala, "Studies of the electrical properties of uranium oxides—I: Electrical conductivity of α-U3O8," *Journal of Physics and Chemistry of Solids*, vol. 24, no. 10, pp. 1207–1212, 1963.

[46] F. Grønvold, "High-temperature X-ray study of uranium oxides in the UO2-U3O8 region," *Journal of Inorganic and Nuclear Chemistry*, vol. 1, no. 6, pp. 357–370, 1955.

[47] R. J. Ackermann, A. T. Chang, and C. A. Sorrell, "Thermal expansion and phase transformations of the U3O8-z phase in air," *Journal of Inorganic and Nuclear Chemistry*, vol. 39, no. 1, pp. 75–85, 1977.

[48] H. R. Hoekstra and S. Siegel, "The uranium-oxygen system: U3O8-UO3," *Journal of Inorganic and Nuclear Chemistry*, vol. 18, pp. 154–165, 1961.

[49] M. D. Karkhanavala and A. M. George, "δ-U3O8, A high temperature modification: Part I: Preparation and characterization," *Journal of Nuclear Materials*, vol. 19, no. 3, pp. 267–273, 1966.

[50] C. Guéneau, S. Chatain, S. Gossé, C. Rado, O. Rapaud, J. Lechelle, J. C. Dumas, and C. Chatillon, "A thermodynamic approach for advanced fuels of gas-cooled reactors," *Journal of Nuclear Materials*, vol. 344, no. 1–3, pp. 191–197, 2005.

[51] R. E. Rundle, N. C. Baezinger, A. S. Wilson, R. A. McDonald, "J. Am. Chem. Soc.," *70*, p. 99, 1948.

[52] L. Nowicki, F. Garrido, A. Turos, and L. Thomé, "Polytypic arrangements of cuboctahedral oxygen clusters in U3O7," *Journal of Physics and Chemistry of Solids*, vol. 61, no. 11, pp. 1789–1804, 2000.

[53] I. Grenthe, J. Fuger, R. J. M. Konings, R. J. Lemire, A. B. Muller, C. Nguyen-Trung, H. Wanner, *Chemical thermodynamic 1- Chemical Thermodynamics of Uranium.* H. Wanner and I. Forest, OECS, North Holland, Amsterdam, 1992.

[54] W. H. Zachariasen, "Crystal chemical studies of the 5f-series of elements. XII. New compounds representing known structure types," *Acta Cryst.*, vol. 2, no. 6, pp. 388–390, 1949.

[55] D. H. Templeton and C. H. Dauben, "Crystal Structures of Americium Compounds 1," *J. Am. Chem. Soc.*, vol. 75, no. 18, pp. 4560–4562, 1953.

[56] T. D. Chikalla and L. Eyring, "Phase relationships in the americium-oxygen system," *Journal of Inorganic and Nuclear Chemistry*, vol. 30, no. 1, pp. 133–145, 1968.

[57] T. D. Chikalla and L. Eyring, "Dissociation pressures and partial thermodynamic quantities for americium oxides," *Journal of Inorganic and Nuclear Chemistry*, vol. 29, no. 9, pp. 2281–2293, 1967.

[58] C. Sari and E. Zamorani, "An investigation in the americium oxide system," *Journal of Nuclear Materials*, vol. 37, no. 3, pp. 324–330, 1970.

[59] S. Casalta, *Etude des propriétés du système Am-O en vue de la transmutation de l'Americium 241 en réacteur à neutrons rapides.* PhD thesis, 1996.

[60] H. Otobe, M. Akabori, and K. Minato, "Oxygen Potential Measurement of Americium Oxide by Electromotive Force Method," *Journal of the American Ceramic Society*, vol. 91, no. 6, pp. 1981–1985, 2008.

[61] F. Lebreton, R. C. Belin, T. Delahaye, and P. Blanchart, "In-situ X-ray diffraction study of phase transformations in the Am–O system," *Journal of Solid State Chemistry*, vol. 196, pp. 217–224, 2012.

[62] C. Thiriet and R. J. M. Konings, "Chemical thermodynamic representation of AmO2-x," *Journal of Nuclear Materials*, vol. 320, no. 3, pp. 292–298, 2003.

[63] R. E. McHenry, "Melting Points of Curium and Americium Oxides," *Trans. Am. Nucl. Soc. 8*, p. 75, 1965.

[64] P. Gotcu-Freis, J. Y. Colle, C. Guéneau, N. Dupin, B. Sundman, and R. J. M. Konings, "A thermodynamic study of the Pu–Am–O system," *Journal of Nuclear Materials*, vol. 414, no. 3, pp. 408–421, 2011.

[65] R. J. Silva, G. Bidoglio, P. B. Robouch, I. Puigdomenech, H. Wanner, and M. H. Rand, *Chemical Thermodynamics of Americium.* Newnes, 2012.

[66] M. Kurata, "Thermodynamic database on U-Pu-Zr-Np-Am-Fe alloy system II — Evaluation of Np, Am, and Fe containing systems-," *IOP Conf. Ser.: Mater. Sci. Eng.*, vol. 9, no. 1, p. 012023, 2010.

[67] T. Ogawa, "Alloying behaviour among U, Np, Pu and Am predicted with the Brewer valence bond model," *Journal of Alloys and Compounds*, vol. 194, no. 1, pp. 1–7, 1993.

[68] F. Lebreton, "Phd thesis- synthèse et caractérisation d'oxydes mixtes d'uranium et d'américium."

[69] D. Prieur, P. M. Martin, A. Jankowiak, E. Gavilan, A. C. Scheinost, N. Herlet, P. Dehaudt, and P. Blanchart, "Local Structure and Charge Distribution in Mixed Uranium–Americium Oxides: Effects of Oxygen Potential and Am Content," *Inorg. Chem.*, vol. 50, no. 24, pp. 12437–12445, 2011.

[70] D. Prieur, F. Lebreton, P. M. Martin, A. Jankowiak, T. Delahaye, P. Dehaudt, and P. Blanchart, "Reactive sintering of U1-yAmyO2 in overstoichiometric conditions," *Journal of the European Ceramic Society*, vol. 32, no. 8, pp. 1585–1591, 2012.

[71] D. Prieur, P. Martin, F. Lebreton, T. Delahaye, D. Banerjee, A. C. Scheinost, and A. Jankowiak, "Accommodation of multivalent cations in fluorite-type solid solutions: Case of Am-bearing UO2," *Journal of Nuclear Materials*, vol. 434, no. 1–3, pp. 7–16, 2013.

[72] F. Lebreton, D. Horlait, T. Delahaye, and P. Blanchart, "Fabrication and characterization of U1-xAmxO2±δ compounds with high americium contents (x = 0.3, 0.4 and 0.5)," *Journal of Nuclear Materials*, vol. 439, no. 1–3, pp. 99–102, 2013.

[73] F. Lebreton, D. Horlait, R. Caraballo, P. M. Martin, A. C. Scheinost, A. Rossberg, C. Jégou, and T. Delahaye, "Peculiar Behavior of (U,Am)O2-δ Compounds for High Americium Contents Evidenced by XRD, XAS, and Raman Spectroscopy," *Inorg. Chem.*, vol. 54, no. 20, pp. 9749–9760, 2015.

[74] W. Bartscher and C. Sari, "A thermodynamic study of the uranium-americium oxide U0.5Am0.5O2±x," *Journal of Nuclear Materials*, vol. 118, no. 2–3, pp. 220–223, 1983.

[75] D. Prieur, F. Lebreton, M. Caisso, P. M. Martin, A. C. Scheinost, T. Delahaye, and D. Manara, "Melting behaviour of americium-doped uranium dioxide," *The Journal of Chemical Thermodynamics*, vol. 97, pp. 244–252, 2016.

[76] D. R. Olander, "Fundamental Aspects of Nuclear Reactor Fuel Elements: Solutions to Problems," Tech. Rep. TID-26711-P2, California Univ., Berkeley (USA). Dept. of Nuclear Engineering, 1976.

[77] M. Freyss, T. Petit, and J.-P. Crocombette, "Point defects in uranium dioxide: Ab initio pseudopotential approach in the generalized gradient approximation," *Journal of Nuclear Materials*, vol. 347, no. 1–2, pp. 44–51, 2005.

[78] A. D. Murray and B. T. M. Willis, "A neutron diffraction study of anion clusters in nonstoichiometric uranium dioxide," *Journal of Solid State Chemistry*, vol. 84, no. 1, pp. 52–57, 1990.

[79] B. T. M. Willis, "Positions of the Oxygen Atoms in UO2.13," *Nature*, vol. 197, no. 4869, pp. 755–756, 1963.

[80] B. T. M. Willis, "Crystallographic studies of anion-excess uranium oxides," *J. Chem. Soc., Faraday Trans. 2*, vol. 83, no. 7, pp. 1073–1081, 1987.

[81] K. O. Kvashnina, S. M. Butorin, P. Martin, and P. Glatzel, "Chemical State of Complex Uranium Oxides," *Phys. Rev. Lett.*, vol. 111, no. 25, p. 253002, 2013.

[82] S. D. Conradson, D. Manara, F. Wastin, D. L. Clark, G. H. Lander, L. A. Morales, J. Rebizant, and V. V. Rondinella, "Local Structure and Charge Distribution in the UO2-U4O9 System," *Inorg. Chem.*, vol. 43, no. 22, pp. 6922–6935, 2004.

[83] R. Ngayam-Happy, M. Krack, and A. Pautz, "Effects of stoichiometry on the defect clustering in uranium dioxide," *Journal of Physics: Condensed Matter*, vol. 27, no. 45, p. 455401, 2015.

[84] D. J. M. Bevan, I. E. Grey, and B. T. M. Willis, "The crystal structure of β-U4O9-y," *Journal of Solid State Chemistry*, vol. 61, no. 1, pp. 1–7, 1986.

[85] F. Garrido, R. M. Ibberson, L. Nowicki, and B. T. M. Willis, "Cuboctahedral oxygen clusters in U3O7," *Journal of Nuclear Materials*, vol. 322, no. 1, pp. 87–89, 2003.

[86] F. Garrido, A. C. Hannon, R. M. Ibberson, L. Nowicki, and B. T. M. Willis, "Neutron Diffraction Studies of U4O9: Comparison with EXAFS Results," *Inorg. Chem.*, vol. 45, no. 20, pp. 8408–8413, 2006.

[87] L. Desgranges, G. Baldinozzi, G. Rousseau, J.-C. Nièpce, and G. Calvarin, "Neutron Diffraction Study of the in Situ Oxidation of UO2," *Inorg. Chem.*, vol. 48, no. 16, pp. 7585–7592, 2009.

[88] L. R. Morss, N. M. Edelstein, J. Fuger, *The Chemistry of the Actinide and Transactinide Elements- Third Edition.* Springer, 2006.

[89] B. Belbeoch, J. C. Boivineau, and P. Perio, "Changements de structure de l'oxyde U4O9," *Journal of Physics and Chemistry of Solids*, vol. 28, no. 7, pp. 1267–1275, 1967.

[90] L. Desgranges, G. Baldinozzi, D. Siméone, and H. E. Fischer, "Refinement of the α-U4O9 Crystalline Structure: New Insight into the U4O9 U3O8 Transformation," *Inorg. Chem.*, vol. 50, no. 13, pp. 6146–6151, 2011.

[91] H. R. Hoekstra, S. Siegel, and F. X. Gallagher, "The uranium-oxygen system at high pressure," *Journal of Inorganic and Nuclear Chemistry*, vol. 32, no. 10, pp. 3237–3248, 1970.

[92] B. O. Loopstra, "Neutron diffraction investigation of U3O8," *Acta Cryst.*, vol. 17, no. 6, pp. 651–654, 1964.

[93] B. O. Loopstra, "The structure of β-U3O8," *Acta Crystallographica Section B Structural Crystallography and Crystal Chemistry*, vol. 26, no. 5, pp. 656–657, 1970.

[94] B. O. Loopstra, "The phase transition in α-U3O8 at 210°C," *J. Appl. Cryst.*, vol. 3, no. 2, pp. 94–96, 1970.

[95] S. Siegel, "The crystal structure of trigonal U3O8," *Acta Cryst.*, vol. 8, no. 10, pp. 617–619, 1955.

[96] V. Amirthalingam, "δ-U3O8: A high temperature modification: Part II. single crystal studies," *Journal of Nuclear Materials*, vol. 20, no. 2, pp. 193–194, 1966.

[97] B. O. Loopstra, "On the existence of δ-U3O8; a comment on papers by Karkhanavalla and George, and by Amirthalingam," *Journal of Nuclear Materials*, vol. 29, no. 3, pp. 354–355, 1969.

[98] J. X. Boucherle and J. Schweizer, "Refinement of the Nd2o3 structure and determination of the neutron scattering length of neodymium," *Acta Cryst. B*, vol. 31, no. 11, pp. 2745–2746, 1975.

[99] D. T. Cromer, "The Crystal Structure of Monoclinic Sm2O3," *J. Phys. Chem.*, vol. 61, no. 6, pp. 753–755, 1957.

[100] V. Grover, A. Banerji, P. Sengupta, and A. K. Tyagi, "Raman, XRD and microscopic investigations on CeO2–Lu2O3 and CeO2–Sc2O3 systems: A sub-solidus phase evolution study," *Journal of Solid State Chemistry*, vol. 181, no. 8, pp. 1930–1935, 2008.

[101] D. Horlait, L. Claparède, N. Clavier, S. Szenknect, N. Dacheux, J. Ravaux, and R. Podor, "Stability and Structural Evolution of Ce1–xLnxO2–x/2 Solid Solutions: A Coupled μ-Raman/XRD Approach," *Inorg. Chem.*, vol. 50, no. 15, pp. 7150–7161, 2011.

[102] K. Teske, H. Ullmann, and D. Rettig, "Investigation of the oxygen activity of oxide fuels and fuel-fission product systems by solid electrolyte techniques. Part I: Qualification and limitations of the method," *Journal of Nuclear Materials*, vol. 116, no. 2–3, pp. 260–266, 1983.

[103] B. Belbeoch, C. Piekarski, P. Pério no. 8, pp. 837–843, 1961., "Structure de U4O9," *Acta Crystallographica*, vol. 14, no. 8, pp. 837–843, 1961.

[104] C. Hurtgen and J. Fuger, "Self-irradiation effects in americium oxides," *Inorganic and Nuclear Chemistry Letters*, vol. 13, no. 3–4, pp. 179–188, 1977.

[105] M. Vespa, M. Rini, J. Spino, T. Vitova, and J. Somers, "Fabrication and characterization of (U, Am)O2-x transmutation targets," *Journal of Nuclear Materials*, vol. 421, no. 1–3, pp. 80–88, 2012.

[106] F. Lebreton, *Synthèse et caractérisation d'oxydes mixtes d'uranium et d'américium.* Limoges, 2014.

[107] K. Mayer, B. Kanellakopoulos, J. Naegele, and L. Koch, "On the valency state of americium in (U0.5Am0.5)O2-x," *Journal of Alloys and Compounds*, vol. 213–214, pp. 456–459, 1994.

[108] T. Nishi, M. Nakada, C. Suzuki, H. Shibata, Y. Okamoto, M. Akabori, and M. Hirata, "Valence state of Am in (U0.95Am0.05)O2.0," *Journal of Nuclear Materials*, vol. 418, no. 1–3, pp. 311–312, 2011.

[109] R. D. Shannon, "Revised effective ionic radii and systematic studies of interatomic distances in halides and chalcogenides," *Acta Crystallographica Section A*, vol. 32, no. 5, pp. 751–767, 1976.

[110] T. L. Markin and R. S. Street, "The uranium-plutonium-oxygen ternary phase diagram," *Journal of Inorganic and Nuclear Chemistry*, vol. 29, no. 9, pp. 2265–2280, 1967.

[111] J. A. Fahey, R. P. Turcotte, and T. D. Chikalla, "Thermal expansion of the actinide dioxides," *Inorganic and Nuclear Chemistry Letters*, vol. 10, no. 6, pp. 459–465, 1974.

[112] D. G. Martin, "The thermal expansion of solid UO2 and (U, Pu) mixed oxides — a review and recommendations," *Journal of Nuclear Materials*, vol. 152, no. 2–3, pp. 94–101, 1988.

[113] K. Minato, M. Takano, H. Otobe, T. Nishi, M. Akabori, and Y. Arai, "Thermochemical and thermophysical properties of minor actinide compounds," *Journal of Nuclear Materials*, vol. 389, no. 1, pp. 23–28, 2009.

[114] K. Minato, Tanako, T. Nishi, A. Itoh, Y. Arai, "Properties of Minor Actinide compounds relevant to nuclear fuel technology," 2006.

[115] H. Matzke, A. Turos, and G. Linker, "Polygonization of single crystals of the fluorite-type oxide UO2 due to high dose ion implantation +," *Nuclear Instruments and Methods in Physics Research Section B: Beam Interactions with Materials and Atoms*, vol. 91, no. 1, pp. 294–300, 1994.

[116] D. Prieur, J.-F. Vigier, T. Wiss, A. Janssen, J. Rothe, A. Cambriani, and J. Somers, "Structural investigation of self-irradiation damaged AmO2," *Journal of Solid State Chemistry*, vol. 212, pp. 7–12, 2014.

[117] D. Prieur, A. Jankowiak, T. Delahaye, N. Herlet, P. Dehaudt, and P. Blanchart, "Fabrication and characterisation of U0.85Am0.15O2-x discs for MARIOS irradiation program," *Journal of Nuclear Materials*, vol. 414, no. 3, pp. 503–507, 2011.

[118] D. Horlait, R. Caraballo, F. Lebreton, C. Jégou, P. Roussel, and T. Delahaye, "Self-irradiation and oxidation effects on americium sesquioxide and Raman spectroscopy studies of americium oxides," *Journal of Solid State Chemistry*, vol. 217, pp. 159–168, 2014.

[119] D. Horlait, F. Lebreton, P. Roussel, and T. Delahaye, "XRD Monitoring of α Self-Irradiation in Uranium–Americium Mixed Oxides," *Inorg. Chem.*, vol. 52, no. 24, pp. 14196–14204, 2013.

[120] P. Martin, S. Grandjean, M. Ripert, M. Freyss, P. Blanc, and T. Petit, "Oxidation of plutonium dioxide: an X-ray absorption spectroscopy study," *Journal of Nuclear Materials*, vol. 320, no. 1–2, pp. 138–141, 2003.

[121] P. Martin, S. Grandjean, C. Valot, G. Carlot, M. Ripert, P. Blanc, and C. Hennig, "XAS study of (U1-yPuy)O2 solid solutions," *Journal of Alloys and Compounds*, vol. 444–445, pp. 410–414, 2007.

[122] P. Martin, M. Ripert, G. Carlot, P. Parent, and C. Laffon, "A study of molybdenum behaviour in UO2 by X-ray absorption spectroscopy," *Journal of Nuclear Materials*, vol. 326, no. 2–3, pp. 132–143, 2004.

[123] T. Nishi, M. Nakada, C. Suzuki, H. Shibata, A. Itoh, M. Akabori, and M. Hirata, "Local and electronic structure of Am2O3 and AmO2 with XAFS spectroscopy," *Journal of Nuclear Materials*, vol. 401, no. 1–3, pp. 138–142, 2010.

[124] S. D. Conradson, B. D. Begg, D. L. Clark, C. den Auwer, M. Ding, P. K. Dorhout, F. J. Espinosa-Faller, P. L. Gordon, R. G. Haire, N. J. Hess, R. F. Hess, D. Webster Keogh, G. H. Lander, D. Manara, L. A. Morales, M. P. Neu, P. Paviet-Hartmann, J. Rebizant, V. V. Rondinella, W. Runde, C. Drew Tait, D. Kirk Veirs, P. M. Villella, and F. Wastin, "Charge distribution and local structure and speciation in the UO2+x and PuO2+x binary oxides for x<0.25," *Journal of Solid State Chemistry*, vol. 178, no. 2, pp. 521–535, 2005.

[125] E. A. Hudson, J. J. Rehr, and J. J. Bucher, "Multiple-scattering calculations of the uranium l3-edge x-ray-absorption near-edge structure," *Phys. Rev. B*, vol. 52, no. 19, pp. 13815–13826, 1995.

[126] T. Nishi, M. Nakada, A. Itoh, C. Suzuki, M. Hirata, and M. Akabori, "EXAFS and XANES studies of americium dioxide with fluorite structure," *Journal of Nuclear Materials*, vol. 374, no. 3, pp. 339–343, 2008.

[127] R. J. M. Konings, O. Beneš, A. Kovács, D. Manara, D. Sedmidubský, L. Gorokhov, V. S. Iorish, V. Yungman, E. Shenyavskaya, and E. Osina, "The Thermodynamic Properties of the f-Elements and their Compounds. Part 2. The Lanthanide and Actinide Oxides," *Journal of Physical and Chemical Reference Data*, vol. 43, no. 1, p. 013101, 2014.

[128] L. R. Morss and J. Fuger, "Enthalpy formation of americium dioxide and a thermochemical estimate of the electrode potential Am4+/Am3+," *Journal of Inorganic and Nuclear Chemistry*, vol. 43, no. 9, pp. 2059–2064, 1981.

[129] L. R. Morss and D. C. Sonnenberger, "Enthalpy of formation of americium sesquioxide; systematics of actinide sesquioxide thermochemistry," *Journal of Nuclear Materials*, vol. 130, pp. 266–272, 1985.

[130] G. E. Moore and K. K. Kelley, "High-Temperature Heat Contents of Uranium, Uranium Dioxide and Uranium Trioxide 1," *J. Am. Chem. Soc.*, vol. 69, no. 9, pp. 2105–2107, 1947.

[131] R. A. Hein, L. H. Sjodahl, and R. Szwarc, "Heat content of uranium dioxide from 1200 to 3100 K," *Journal of Nuclear Materials*, vol. 25, no. 1, pp. 99–102, 1968.

[132] R. A. Hein, P. N. Flagella, and J. B. Conway, "High-Temperature Enthalpy and Heat of Fusion of UO2," *Journal of the American Ceramic Society*, vol. 51, no. 5, pp. 291–292, 1968.

[133] Y. Takahashi and M. Asou, "High-temperature heat-capacity measurements on (U, Gd)O2 by drop calorimetry and DSC," *Journal of Nuclear Materials*, vol. 201, pp. 108–114, 1993.

[134] J.B. Conway, R. A. Hein *J. Nucl. Mater. 15*, p. 149, 1965.

[135] A. E. Ogard, J. A. Leary *Thermodyn. Nucl. Mater., Vienna 651*, 1967.

[136] L. Leibowitz, L. W. Mishler, and M. G. Chasanov, "Enthalpy of solid uranium dioxide from 2500 °K to its melting point," *Journal of Nuclear Materials*, vol. 29, no. 3, pp. 356–358, 1969.

[137] D. R. Fredrickson and M. G. Chasanov, "Enthalpy of uranium dioxide and sapphire to 1500 K by drop calorimetry," *The Journal of Chemical Thermodynamics*, vol. 2, no. 5, pp. 623–629, 1970.

[138] K. C. Mills, F. H. Ponsford, M. J. Richardson, N. Zaghini, and P. Fassina, "Heat capacity and enthalpy of UO2 and gadolinia-doped UO2," *Thermochimica Acta*, vol. 139, pp. 107–120, 1989.

[139] J. P. Hiernaut, G. J. Hyland, and C. Ronchi, "Premelting transition in uranium dioxide," *Int J Thermophys*, vol. 14, no. 2, pp. 259–283, 1993.

[140] C. Ronchi, M. Sheindlin, M. Musella, and G. J. Hyland, "Thermal conductivity of uranium dioxide up to 2900 K from simultaneous measurement of the heat capacity and thermal diffusivity," *Journal of Applied Physics*, vol. 85, no. 2, pp. 776–789, 1999.

[141] C. Ronchi, J. P. Hiernaut, R. Selfslag, and G. J. Hyland, "Laboratory Measurement of the Heat Capacity of Urania up to 8000 K: I. Experiment," *NSE*, vol. 113, no. 1, pp. 1–19, 1993.

[142] M. Amaya, K. Une, and K. Minato, "Heat capacity measurements on unirradiated and irradiated fuel pellets," *Journal of Nuclear Materials*, vol. 294, no. 1–2, pp. 1–7, 2001.

[143] C. Ronchi and G. J. Hyland, "International Conference on Actinides Analysis of recent measurements of the heat capacity of uranium dioxide," *Journal of Alloys and Compounds*, vol. 213, pp. 159–168, 1994.

[144] M. T. Hutchings, "High-temperature studies of UO2 and ThO2 using neutron scattering techniques," *J. Chem. Soc., Faraday Trans. 2*, vol. 83, no. 7, pp. 1083–1103, 1987.

[145] T. Nishi, A. Itoh, K. Ichise, and Y. Arai, "Heat capacities and thermal conductivities of AmO2 and AmO1.5," *Journal of Nuclear Materials*, vol. 414, no. 2, pp. 109–113, 2011.

[146] O. S. Vălu, D. Staicu, O. Beneš, R. J. M. Konings, and P. Lajarge, "Heat capacity, thermal conductivity and thermal diffusivity of uranium–americium mixed oxides," *Journal of Alloys and Compounds*, vol. 614, pp. 144–150, 2014.

[147] D. Labroche, O. Dugne, and C. Chatillon, "Thermodynamic properties of the O–U system. II – Critical assessment of the stability and composition range of the oxides UO2+x, U4O9-y and U3O8-z," *Journal of Nuclear Materials*, vol. 312, no. 1, pp. 50–66, 2003.

[148] M. Baichi, C. Chatillon, G. Ducros, and K. Froment, "Thermodynamics of the O–U system. IV – Critical assessment of chemical potentials in the U–UO2.01 composition range," *Journal of Nuclear Materials*, vol. 349, no. 1–2, pp. 17–56, 2006.

[149] P. Gotcu-Freis, J. Y. Colle, J. P. Hiernaut, and R. J. M. Konings, "The vaporisation behaviour of americium dioxide by use of mass spectrometry," *Journal of Nuclear Materials*, vol. 409, no. 3, pp. 194–198, 2011.

[150] T. B. Lindemer, *CALPHAD 10.* 1986.

[151] T. B. Lindemer and T. M. Besmann, "Chemical thermodynamic representation of UO2 pm x," *Journal of Nuclear Materials*, vol. 130, pp. 473–488, 1985.

[152] T. M. Besmann, "Modeling the thermochemical behavior of AmO2-x," *Journal of Nuclear Materials*, vol. 402, no. 1, pp. 25–29, 2010.

[153] R. Vauchy, R. C. Belin, A.-C. Robisson, and F. Hodaj, "High temperature X-ray diffraction study of the kinetics of phase separation in hypostoichiometric uranium–plutonium mixed oxides," *Journal of the European Ceramic Society*, vol. 34, no. 10, pp. 2543–2551, 2014.

[154] R. Vauchy, A.-C. Robisson, P. M. Martin, R. C. Belin, L. Aufore, A. C. Scheinost, and F. Hodaj, "Impact of the cation distribution homogeneity on the americium oxidation state in the U0.54Pu0.45Am0.01O2-x mixed oxide," *Journal of Nuclear Materials*, vol. 456, pp. 115–119, 2015.

[155] R. C. Belin, M. Strach, T. Truphémus, C. Guéneau, J.-C. Richaud, and J. Rogez, "In situ high temperature X-Ray diffraction study of the phase equilibria in the UO2–PuO2–Pu2O3 system," *Journal of Nuclear Materials*, vol. 465, pp. 407–417, 2015.

[156] M. Chollet, R. C. Belin, J.-C. Richaud, and M. Reynaud, "Phase Relationships in the U – Np – O System," *Procedia Chemistry*, vol. 7, pp. 472–476, 2012.

[157] M. Strach, R. C. Belin, J.-C. Richaud, and J. Rogez, "Biphasic MO2+x–M3O8–z Domain of the U–Pu–O Phase Diagram," *Inorg. Chem.*, vol. 54, no. 18, pp. 9105–9114, 2015.

[158] T. Truphémus, R. C. Belin, J. C. Richaud, and J. Rogez, "Phase Equilibria in the Uranium-Plutonium-Oxygen Ternary Phase Diagram at (U0.55,Pu0.45)O2-x and (U0.45,Pu0.55)O2-x," *Procedia Chemistry*, vol. 7, pp. 521–527, 2012.

[159] T. Truphémus, R. C. Belin, J.-C. Richaud, M. Reynaud, M.-A. Martinez, I. Félines, A. Arredondo, A. Miard, T. Dubois, F. Adenot, and J. Rogez, "Structural studies of the phase separation in the UO2–PuO2–Pu2O3 ternary system," *Journal of Nuclear Materials*, vol. 432, no. 1–3, pp. 378–387, 2013.

[160] R. Vauchy, R. C. Belin, A.-C. Robisson, and F. Hodaj, "Effect of cooling rate on achieving thermodynamic equilibrium in uranium–plutonium mixed oxides," *Journal of Nuclear Materials*, vol. 469, pp. 125–132, 2016.

[161] M. Zinkevich, D. Djurovic, and F. Aldinger, "Thermodynamic modelling of the cerium–oxygen system," *Solid State Ionics*, vol. 177, no. 11–12, pp. 989–1001, 2006.

[162] C. Guéneau, C. Chatillon, and B. Sundman, "Thermodynamic modelling of the plutonium–oxygen system," *Journal of Nuclear Materials*, vol. 378, no. 3, pp. 257–272, 2008.

[163] N. Trautmann, "Accurate determination of the first ionization potential of actinides by laser spectroscopy," *Journal of Alloys and Compounds*, vol. 213, pp. 28–32, 1994.

[164] S. Köhler, R. Deißenberger, K. Eberhardt, N. Erdmann, G. Herrmann, G. Huber, J. V. Kratz, M. Nunnemann, G. Passler, P. M. Rao, J. Riegel, N. Trautmann, and K. Wendt, "Determination of the first ionization potential of actinide elements by resonance ionization mass spectroscopy," *Spectrochimica Acta Part B: Atomic Spectroscopy*, vol. 52, no. 6, pp. 717–726, 1997.

[165] J. K. Gibson, R. G. Haire, J. Marçalo, M. Santos, A. Pires de Matos, and J. P. Leal, "Determination of the ionization energy of NpO2 and comparative ionization energies of actinide oxides," *Journal of Nuclear Materials*, vol. 344, no. 1, pp. 24–29, 2005.

[166] P. Gotcu-Freis, J. P. Hiernaut, J. Y. Colle, C. Nästrén, A. F. Carretero, and R. J. M. Konings, "Vaporisation of candidate nuclear fuels and targets for transmutation of minor actinides," *Journal of Nuclear Materials*, vol. 411, no. 1–3, pp. 119–125, 2011.

[167] D. Horlait, A. Feledziak, F. Lebreton, N. Clavier, D. Prieur, N. Dacheux, and T. Delahaye, "Dilatometric study of U1-xAmxO2±δ and U1-xCexO2±δ reactive sintering," *Journal of Nuclear Materials*, vol. 441, no. 1–3, pp. 40–46, 2013.

[168] T. Delahaye, F. Lebreton, D. Horlait, N. Herlet, and P. Dehaudt, "Application of the UMACS process to highly dense U1-xAmxO2±δ MABB fuel fabrication for the DIAMINO irradiation," *Journal of Nuclear Materials*, vol. 432, no. 1–3, pp. 305–312, 2013.

[169] V. J. Wheeler and I. G. Jones, "Thermodynamic and composition changes in UO2±x (x< 0.005) at 1950 K," *Journal of Nuclear Materials*, vol. 42, no. 2, pp. 117–121, 1972.

[170] F. Lebreton, D. Prieur, A. Jankowiak, M. Tribet, C. Leorier, T. Delahaye, L. Donnet, and P. Dehaudt, "Fabrication and characterization of americium, neptunium and curium bearing MOX fuels obtained by powder metallurgy process," *Journal of Nuclear Materials*, vol. 420, no. 1–3, pp. 213–217, 2012.

[171] A. L. Bail, "Whole powder pattern decomposition methods and applications: A retrospection," *Powder Diffraction*, vol. 20, no. 4, pp. 316–326, 2005.

[172] R. I. Cooper and B. T. M. Willis, "Refinement of the structure of β-U4O9," *Acta Cryst A, Acta Cryst Sect A, Acta Crystallogr A, Acta Crystallogr Sect A, Acta Crystallogr A Found Crystallogr, Acta Crystallogr Sect A Found Crystallogr*, vol. 60, no. 4, pp. 322–325, 2004.

[173] C. Hennig, "Evidence for double-electron excitations in the L_3-edge x-ray absorption spectra of actinides," *Phys. Rev. B*, vol. 75, p. 035120, 2007.

[174] C. Hennig, S. Skanthakumar, and L. Soderholm, "Double photoexcitation of 2p and 4f electrons in curium," *Journal of Electron Spectroscopy and Related Phenomena*, vol. 180, no. 1, pp. 17 – 20, 2010.

[175] J. Chaboy, A. Marcelli, and T. A. Tyson, "Influence of double-electron transitions on the exafs l edges of rare-earth systems," *Phys. Rev. B*, vol. 49, pp. 11652–11661, 1994.

[176] T. Shimanouchi, M. Tsuboi, and T. miyazawa, "Optically Active Lattice Vibrations as Treated by the GF-Matrix Method," *The Journal of Chemical Physics*, vol. 35, no. 5, pp. 1597–1612, 1961.

[177] V. G. Keramidas and W. B. White, "Raman spectra of oxides with the fluorite structure," *The Journal of Chemical Physics*, vol. 59, no. 3, pp. 1561–1562, 1973.

[178] G. M. Begun, R. G. Haire, W. R. Wilmarth, and J. R. Peterson, "Raman spectra of some actinide dioxides and of EuF2," *Journal of the Less Common Metals*, vol. 162, no. 1, pp. 129–133, 1990.

[179] D. Manara and B. Renker, "Raman spectra of stoichiometric and hyperstoichiometric uranium dioxide," *Journal of Nuclear Materials*, vol. 321, no. 2, pp. 233–237, 2003.

[180] T. Livneh and E. Sterer, "Effect of pressure on the resonant multiphonon Raman scattering in UO2," *Phys. Rev. B*, vol. 73, no. 8, p. 085118, 2006.

[181] L. Desgranges, G. Baldinozzi, P. Simon, G. Guimbretière, and A. Canizares, "Raman spectrum of U4O9: a new interpretation of damage lines in UO2," *J. Raman Spectrosc.*, vol. 43, no. 3, pp. 455–458, 2012.

[182] L. Desgranges, Y. Pontillon, P. Matheron, M. Marcet, P. Simon, G. Guimbretière, and F. Porcher, "Miscibility Gap in the U–Nd–O Phase Diagram: a New Approach of Nuclear Oxides in the Environment?," *Inorg. Chem.*, vol. 51, no. 17, pp. 9147–9149, 2012.

[183] G. Guimbretière, L. Desgranges, A. Canizarès, R. Caraballo, F. Duval, N. Raimboux, R. Omnée, M. R. Ammar, C. Jégou, and P. Simon, "In situ Raman monitoring of He2+ irradiation induced damage in a UO2 ceramic," *Appl. Phys. Lett.*, vol. 103, no. 4, p. 041904, 2013.

[184] M. Naji, J.-Y. Colle, O. Beneš, M. Sierig, J. Rautio, P. Lajarge, and D. Manara, "An original approach for Raman spectroscopy analysis of radioactive materials and its application to americium-containing samples," *J. Raman Spectrosc.*, vol. 46, no. 9, pp. 750–756, 2015.

[185] L. Desgranges, P. Simon, P. Martin, G. Guimbretiere, and G. Baldinozzi, "What Can We Learn From Raman Spectroscopy on Irradiation-Induced Defects in UO2?," *JOM*, vol. 66, no. 12, pp. 2546–2552, 2014.

[186] Z. Talip, T. Wiss, P. E. Raison, J. Paillier, D. Manara, J. Somers, and R. J. Konings, "Raman and X-ray Studies of Uranium–Lanthanum-Mixed Oxides Before and After Air Oxidation," *J. Am. Ceram. Soc.*, vol. 98, no. 7, pp. 2278–2285, 2015.

[187] M. J. Sarsfield, R. J. Taylor, C. Puxley, and H. M. Steele, "Raman spectroscopy of plutonium dioxide and related materials," *Journal of Nuclear Materials*, vol. 427, no. 1–3, pp. 333–342, 2012.

[188] J. Schoenes, "Optical properties and electronic structure of UO2," *Journal of Applied Physics*, vol. 49, no. 3, pp. 1463–1465, 1978.

[189] J. Schoenes, "Electronic transitions, crystal field effects and phonons in UO2," *Physics Reports*, vol. 63, no. 6, pp. 301–336, 1980.

[190] T. T. Meek, B. von Roedern, P. G. Clem, and R. J. Hanrahan, "Some optical properties of intrinsic and doped UO2 thin films," *Materials Letters*, vol. 59, no. 8, pp. 1085–1088, 2005.

[191] S.-W. Yu, J. G. Tobin, J. C. Crowhurst, S. Sharma, J. K. Dewhurst, P. Olalde-Velasco, W. L. Yang, and W. J. Siekhaus, "f-f origin of the insulating state in uranium dioxide: X-ray absorption experiments and first-principles calculations," *Phys. Rev. B*, vol. 83, no. 16, p. 165102, 2011.

[192] C. Suzuki, T. Nishi, M. Nakada, M. Akabori, M. Hirata, and Y. Kaji, "Core-hole effect on XANES and electronic structure of minor actinide dioxides with fluorite structure," *Journal of Physics and Chemistry of Solids*, vol. 73, no. 2, pp. 209–216, 2012.

[193] M. Caisso, P. Roussel, C. Den Auwer, S. Picart, C. Hennig, A. C. Scheinost, T. Delahaye, and A. Ayral, "Evidence of Trivalent Am Substitution into U3O8," *Inorg. Chem.*, vol. 55, no. 20, pp. 10438–10444, 2016.

[194] G. C. Allen and N. R. Holmes, "A mechanism for the UO2 to α-U3o8 phase transformation," *Journal of Nuclear Materials*, vol. 223, no. 3, pp. 231–237, 1995.

[195] R. J. McEachern, J. W. Choi, M. Kolár, W. Long, P. Taylor, and D. D. Wood, "Determination of the activation energy for the formation of U3O8 on UO2," *Journal of Nuclear Materials*, vol. 249, no. 1, pp. 58–69, 1997.

[196] R. J. McEachern and P. Taylor, "A review of the oxidation of uranium dioxide at temperatures below 400°C," *Journal of Nuclear Materials*, vol. 254, no. 2, pp. 87–121, 1998.

[197] P. Taylor, R. J. McEachern, D. C. Doern, and D. D. Wood, "The influence of specimen roughness on the rate of formation of U3O8 on UO2 in air at 250°C," *Journal of Nuclear Materials*, vol. 256, no. 2, pp. 213–217, 1998.

[198] G. Rousseau, L. Desgranges, F. Charlot, N. Millot, J. C. Nièpce, M. Pijolat, F. Valdivieso, G. Baldinozzi, and J. F. Bérar, "A detailed study of UO2 to U3O8 oxidation phases and the associated rate-limiting steps," *Journal of Nuclear Materials*, vol. 355, no. 1–3, pp. 10–20, 2006.

[199] M. Chollet, R. C. Belin, J.-C. Richaud, M. Reynaud, and F. Adenot, "High-Temperature X-ray Diffraction Study of Uranium–Neptunium Mixed Oxides," *Inorg. Chem.*, vol. 52, no. 5, pp. 2519–2525, 2013.

[200] G. S. Pawley, "Unit-cell refinement from powder diffraction scans," *J Appl Crystallogr*, vol. 14, no. 6, pp. 357–361, 1981.

[201] H. M. Rietveld, "A profile refinement method for nuclear and magnetic structures," *J Appl Crystallogr*, vol. 2, no. 2, pp. 65–71, 1969.

[202] M. Strach, R. C. Belin, J.-C. Richaud, and J. Rogez, "In-Situ High Temperature XRD on U0.54Pu0.46O2-x: A Study of the Miscibility Gap," *MRS Online Proceedings Library Archive*, vol. 1743, 2015.

[203] O. S. Vălu, O. Beneš, R. J. M. Konings, and H. Hein, "The high temperature heat capacity of the (Th, Pu)O2 system," *The Journal of Chemical Thermodynamics*, vol. 68, pp. 122–127, 2014.

[204] H. Kopp, "Investigations of the Specific Heat of Solid Bodies," *Phil. Trans. R. Soc. Lond.*, vol. 155, pp. 71–202, 1865.

[205] D. Staicu, T. Wiss, M. Sheindlin, V. Rondinella, J.-P. Hiernaut, and C. Ronchi, "Impact of Auto-irradiation on the Thermophysical Properties of Oxide Nuclear Reactor Fuels," in *Proceedings of the ECTP 2005*, Springer, 2005.

[206] D. W. Osborne and H. E. Flotow, "Half-life of 242Pu from precise low-temperature heat capacity measurements," *Phys. Rev. C*, vol. 14, no. 3, pp. 1174–1178, 1976.

[207] C. G. Maier and K. K. Kelley, "An Equation For The Representation Of High-Temperature Heat Content Data," *J. Am. Chem. Soc.*, vol. 54, no. 8, pp. 3243–3246, 1932.

[208] J. Leitner, P. Voňka, D. Sedmidubský, and P. Svoboda, "Application of Neumann–Kopp rule for the estimation of heat capacity of mixed oxides," *Thermochimica Acta*, vol. 497, no. 1–2, pp. 7–13, 2010.

[209] R. Szwarc, "The defect contribution to the excess enthalpy of uranium dioxide-calculation of the frenkel energy," *Journal of Physics and Chemistry of Solids*, vol. 30, no. 3, pp. 705–711, 1969.

[210] R. J. M. Konings and O. Beneš, "The heat capacity of NpO2 at high temperatures: The effect of oxygen Frenkel pair formation," *Journal of Physics and Chemistry of Solids*, vol. 74, no. 5, pp. 653–655, 2013.

[211] A. L. Smith, J. Y. Colle, O. Beneš, R. J. M. Konings, B. Sundman, and C. Guéneau, "Thermodynamic assessment of the neptunium–oxygen system: Mass spectrometric studies and thermodynamic modelling," *The Journal of Chemical Thermodynamics*, vol. 103, pp. 257–275, 2016.

[212] K. Nakajima and Y. Arai, "Investigation of vaporization behavior of hyper-stoichiometric uranium dioxide by Knudsen effusion mass spectrometry," *Journal of Nuclear Materials*, vol. 317, no. 2–3, pp. 243–251, 2003.

[213] P. Gotcu-Freis, J. Y. Colle, J. P. Hiernaut, and R. J. M. Konings, "(Solid+gas) equilibrium studies for neptunium dioxide," *The Journal of Chemical Thermodynamics*, vol. 43, no. 3, pp. 492–498, 2011.

[214] P. Gotcu-Freis, J. Y. Colle, J. P. Hiernaut, F. Naisse, C. Guéneau, and R. J. M. Konings, "Mass spectrometric studies of the vapour phase in the (Pu+O) system," *The Journal of Chemical Thermodynamics*, vol. 43, no. 8, pp. 1164–1173, 2011.

[215] P. Gotcu-Freis, J.-Y. Colle, J.-P. Hiernaut, O. Beneš, C. Guéneau, and R. J. M. Konings, "A mass spectrometric investigation of the vaporisation behaviour in the (U+Pu+O) system," *The Journal of Chemical Thermodynamics*, vol. 71, pp. 212–220, 2014.

[216] A. Pattoret, *Etude thermodynamiques par spectrometrie de masse sur les systemes uranium oxygen et uranium carbone.* PhD thesis, 1969.

[217] M. Miller and K. Armatys, "Twenty Years of Knudsen Effusion Mass Spectrometry: Studies Performed in the Period 1990-2010," *The Open Thermodynamics Journal*, vol. 7, no. 1, 2013.

[218] J. Drowart, C. Chatillon, J. Hastie, and D. Bonnell, "High-temperature mass spectrometry: Instrumental techniques, ionization cross-sections, pressure measurements, and thermodynamic data (IUPAC Technical Report)," *Pure Appl. Chem., PAC*, vol. 77, no. 4, pp. 683–737, 2005.

[219] F. Capone, Y. Colle, J. P. Hiernaut, and C. Ronchi, "Mass Spectrometric Measurement Of the Ionization Energies and Cross Sections Of Uranium and Plutonium Oxide Vapors," *J. Phys. Chem. A*, vol. 103, no. 50, pp. 10899–10906, 1999.

[220] H. Deutsch, T. D. Märk, V. Tarnovsky, K. Becker, C. Cornelissen, L. Cespiva, and V. Bonacic-Koutecky, "Measured and calculated absolute total cross-sections for the single ionization of CFx and NFx by electron impact," *International Journal of Mass Spectrometry and Ion Processes*, vol. 137, pp. 77–91, 1994.

[221] H. Deutsch, C. Cornelissen, L. Cespiva, V. Bonacic-Koutecky, D. Margreiter, and T. D. Märk, "Total electron impact ionization cross sections of free molecular radicals: the failure of the additivity rule revisited," *International Journal of Mass Spectrometry and Ion Processes*, vol. 129, pp. 43–48, 1993.

[222] H. Deutsch, K. Becker, and T. D. Märk, "A modified additivity rule for the calculation of electron impact ionization cross-section of molecules ABn," *International Journal of Mass Spectrometry and Ion Processes*, vol. 167, pp. 503–517, 1997.

[223] D. Manara, M. Sheindlin, W. Heinz, and C. Ronchi, "New techniques for high-temperature melting measurements in volatile refractory materials via laser surface heating," *Review of Scientific Instruments*, vol. 79, no. 11, p. 113901, 2008.

[224] F. De Bruycker, K. Boboridis, R. J. M. Konings, M. Rini, R. Eloirdi, C. Guéneau, N. Dupin, and D. Manara, "On the melting behaviour of uranium/plutonium mixed dioxides with high-Pu content: A laser heating study," *Journal of Nuclear Materials*, vol. 419, no. 1–3, pp. 186–193, 2011.

[225] F. De Bruycker, K. Boboridis, P. Pöml, R. Eloirdi, R. J. M. Konings, and D. Manara, "The melting behaviour of plutonium dioxide: A laser-heating study," *Journal of Nuclear Materials*, vol. 416, no. 1–2, pp. 166–172, 2011.

[226] R. Böhler, M. J. Welland, D. Prieur, P. Cakir, T. Vitova, T. Pruessmann, I. Pidchenko, C. Hennig, C. Guéneau, R. J. M. Konings, and D. Manara, "Recent advances in the study of the UO2–PuO2 phase diagram at high temperatures," *Journal of Nuclear Materials*, vol. 448, no. 1, pp. 330–339, 2014.

[227] M. Strach, *In situ studies of uranium-plutonium mixed oxides : Influence of composition on phase equilibria and thermodynamic properties.* Aix-Marseille, 2015.

[228] M. Strach, D. Manara, R. C. Belin, and J. Rogez, "Melting behavior of mixed U–Pu oxides under oxidizing conditions," *Nuclear Instruments and Methods in Physics Research Section B: Beam Interactions with Materials and Atoms*, vol. 374, no. Supplement C, pp. 125–128, 2016.

[229] Jörg Rothe, Melissa A. Denecke, K. Dardenne, Thomas Fanghänel, "The INE-Beamline for actinide research at ANKA : Radiochimica Acta," vol. 94, pp. 691–696, 2006.

[230] K. Dardenne, B. Brendebach, M. A. Denecke, X. Liu, J. Rothe, and T. Vitova, "New developments at the INE-Beamline for actinide research at ANKA," *J. Phys.: Conf. Ser.*, vol. 190, no. 1, p. 012037, 2009.

[231] M. Caisso, S. Picart, R. C. Belin, F. Lebreton, P. M. Martin, K. Dardenne, J. Rothe, D. R. Neuville, T. Delahaye, and A. Ayral, "In situ characterization of uranium and americium oxide solid solution formation for CRMP process: first combination of in situ XRD and XANES measurements," *Dalton Trans.*, vol. 44, no. 14, pp. 6391–6399, 2015.

[232] J. Rodríguez-Carvajal, "Introduction to the Program FULLPROF: Refinement of Crystal and Magnetic Structures from Powder and Single Crystal Data," *Commission on Powder Diffraction (IUCr) Newsletter*, vol. 26, pp. 12–19, 2001.

[233] P. Thompson, D. E. Cox, and J. B. Hastings, "Rietveld refinement of Debye–Scherrer synchrotron X-ray data from Al2O3," *J Appl Crystallogr*, vol. 20, no. 2, pp. 79–83, 1987.

[234] "Product : GEN'AIR oxygen pump gauge - SETNAG." `http://www.setnag.com/en/produit/oxygen-pump-gauge/gen-air-oxygen-pump-gauge/11`. Accessed: 2017-01-22.

[235] Bruker AXS: Madison, WI, "TOPAS V4: General Profile and Structure Analysis Software for Powder Diffraction Data. User's Manual.," 2005.

[236] R. W. Cheary and A. Coelho, "A fundamental parameters approach to X-ray line-profile fitting," *J Appl Crystallogr*, vol. 25, no. 2, pp. 109–121, 1992.

[237] G. Bunker, *Introduction to XAFS.* Illinois Institute of technology, 2010.

[238] B. Ravel and M. Newville, "ATHENA, ARTEMIS, HEPHAESTUS: data analysis for X-ray absorption spectroscopy using IFEFFIT," *J Synchrotron Radiat*, vol. 12, no. 4, pp. 537–541, 2005.

[239] J. J. Rehr, A. Ankudinov, and S. I. Zabinsky, "New developments in NEXAFS/EXAFS theory," *Catalysis Today*, vol. 39, no. 4, pp. 263–269, 1998.

[240] O. Beneš, P. Gotcu-Freis, F. Schwörer, R. J. M. Konings, and T. Fanghänel, "The high temperature heat capacity of NpO2," *The Journal of Chemical Thermodynamics*, vol. 43, no. 5, pp. 651–655, 2011.

[241] J.-Y. Colle, D. Freis, O. Benes, R. J. M. Konings, "Knudsen Effusion Mass Spectrometry of Nuclear Materials: Applications and developments," *ECS Trans.*, vol. 46, no. 1, pp. 23–28, 2013.

[242] J. P. Hiernaut, J. Y. Colle, R. Pflieger-Cuvellier, J. Jonnet, J. Somers, and C. Ronchi, "A Knudsen cell-mass spectrometer facility to investigate oxidation and vaporisation processes in nuclear fuel," *Journal of Nuclear Materials*, vol. 344, no. 1–3, pp. 246–253, 2005.

[243] K. O. Anderson, Hultgren, *Selected Values of Thermodynamic Properties of Metals and Alloys.* John Wiley and Sons.

Etude du diagramme de de phase ternaire U-Am-O : résumé

Cette thèse de doctorat s'inscrit dans le cadre de la gestion des actinides mineurs qui est un des défis majeurs pour l'industrie du nucléaire. En effet, lors de l'irradiation en réacteur, en parallèle à la formation des produits de fission, des captures neutroniques par les noyaux de l'uranium (U) et du plutonium (Pu) conduisent à la production d'atomes lourds appelés Actinides Mineurs (AMs) tels que le neptunium (Np), l'américium (Am) et le curium (Cm). Ces éléments très radioactifs ont un fort impact sur la radiotoxicité des colis de déchets ultimes. Le plus pénalisant des AMs est l'américium dont le retraitement permettrait de diminuer substantiellement l'empreinte écologique des sites d'enfouissement géologique. Son extraction sélective du combustible usé suivie de sa dilution dans une matrice UO_2 pour obtenir des pastilles d'oxydes mixtes d'uranium-américium $U_{1-y}Am_yO_{2\pm x}$, permettraient sa transmutation dans des réacteurs à neutrons rapides. Cependant, l'ajout de ces matériaux ne doit pas impacter la sûreté du fonctionnement des réacteurs. Afin de s'en assurer, une connaissance approfondie des propriétés des oxydes mixtes $U_{1-y}Am_yO_{2\pm x}$ est nécessaire afin de prévoir leur comportement en réacteur aussi bien en conditions nominales qu'accidentelles. Dans ce contexte, ces travaux de thèse ont été consacrés à l'étude des propriétés thermodynamiques de ces composés dans une large gamme de compositions (7,5 %mol ≤ Am/(U+Am) ≤ 70 %mol).

L'objectif principal de cette thèse était le développement d'un modèle thermodynamique du système ternaire U-Am-O en utilisant la méthode CALPHAD (CALculation of PHAse Diagrams), une technique semi-empirique permettant de calculer des diagrammes de phase en utilisant les propriétés structurales (phases, cristallographie, degrés d'oxydation…) et thermodynamiques (température de transition, enthalpies de formation, capacité thermique, potentiels chimiques...) disponibles sur le système étudié.

Cependant, la modélisation d'un système ternaire repose sur les modèles des sous-systèmes binaires. Le système U-O a été longuement étudié expérimentalement, ce qui a permis le développement d'un modèle très fiable. Au contraire, peu de données sont disponibles pour le système Am-O. Afin de répondre aux questions soulevées sur le premier modèle disponible dans la littérature, la première étape a consisté à acquérir de nouvelles données expérimentales sur le système Am-O. Pour cela, des campagnes de mesure de Diffraction des Rayons-X (DRX) in situ à haute température ont été réalisées afin d'acquérir de nouvelles données de transition de phases ainsi que les coefficients d'expansion thermique et l'évolution des paramètres de maille en fonction du rapport O/Am. Ces résultats ont permis de clarifier la nature des équilibres du diagramme de phase dans le domaine AmO_{2-x}-$AmO_{1.61+x}$-Am_2O_3 et d'améliorer le modèle CALPHAD existant et le diagramme de phase du système Am-O.

Pour le système ternaire U-Am-O, les données expérimentales sont très limitées. Donc, une part très importante de cette thèse a été consacrée à l'étude expérimentale du système ternaire U-Am-O en combinant de nombreuses techniques expérimentales.

Dans un premier temps, des pastilles d'$U_{1-y}Am_yO_{2\pm x}$ ont été synthétisées par un procédé de métallurgie de poudres. Ces pastilles ont ensuite été caractérisées par diffraction des rayons-X (DRX) et microscopie électronique à balayage (MEB). Ces mêmes composés ont également été caractérisés à l'aide du rayonnement synchrotron à l'ESRF (Grenoble). Les expériences de spectroscopie d'absorption-X (SAX) ont permis de déterminer à la fois les degrés d'oxydations de l'Am et de l'U

mais aussi leurs environnements locaux permettant ainsi d'obtenir une description structurale complète des composés (U, Am)$O_{2\pm x}$. Ces résultats ont permis de mettre en évidence les spécificité structurales de cette solution solide par comparaison avec les autres oxydes mixtes d'actinides (U,Pu)O_2, (U,Np)O_2.

Dans une deuxième phase, une étude du domaine riche en oxygène du diagramme de phase MO_{2+x}-M_3O_8 (avec M= metal= Am+U) a été réalisée par DRX à haute température (jusqu'à 1700 K) et par SAX à l'ESRF. L'ensemble des résultats démontrent une stabilisation de la phase MO_{2+x} et donc une résistance à la suroxydation qui augmente avec la teneur en Am. De plus, le couplage de la DRX et de la SAX a permis d'obtenir des informations quantitatives sur les fractions des phases M_3O_8 et MO_{2+x}, ainsi que sur le rapport O/M (oxygène/métal), qui représentent des données indispensables à la modélisation CALPHAD.

En outre, grâce à un financement européen dans le cadre du programme GENTLE, des mesures de propriétés thermodynamiques ont été réalisées dans l'institut de recherche JRC-Karlsruhe (Allemagne) de la commission européenne. Des mesures de capacité thermique par calorimétrie à chute et de température de fusion par chauffage laser (autour de 3000 K), ainsi que des mesures de pressions de vapeur à haute température (2300 K), grâce à des cellules de Knudsen couplées avec un spectromètre de masse, ont été effectuées.

Enfin, sur la base de ces différentes mesures expérimentales, un premier modèle Calphad est proposé pour décrire les propriétés thermodynamiques et le diagramme de phase U-Am-O.

Titre : Etude du diagramme de phase ternaire Uranium-Américium-Oxygène

Mots clés : Uranium, Américium, Oxydes, Thermodynamique, Calphad, Non stœchiométrie

Résumé : La connaissance des propriétés thermodynamiques du système U-Am-O est essentielle pour prédire le comportement en réacteur des pastilles $(U,Am)O_2$ à haute température. Dans ce travail, des mesures expérimentales de propriétés structurales et thermodynamiques des oxydes mixtes $(U,Am)O_2$ ont été effectuées pour fournir des données d'entrée à la modélisation thermodynamique du système U-Am-O par la méthode Calphad. Le diagramme de phase Am-O a été révisé sur la base de données de diffraction des rayons X à haute température montrant: l'existence d'un domaine de composition pour la phase $AmO_{1.61+x}$ et l'absence de lacune de miscibilité dans la fluorine. L'étude des oxydes mixtes par XANES et EXAFS a montré la stabilité de l'Am^{3+} dans ces oxydes, compensée par l'oxydation partielle de l'U^{4+} en U^{5+}.

L'étude de l'oxydation par DRX HT a permis de montrer la stabilisation des oxydes $(U,Am)O_2$ en phase fluorine par rapport à l'UO_2 vis-à-vis de la formation d'oxydes plus riches en oxygène. Des données de diagramme de phase ont été déterminées. Les incréments enthalpiques ont été mesurés par calorimétrie de chute. Une contribution d'excès de la capacité calorifique pourrait être due à la réduction des oxydes à haute température. Les pressions de vapeur des espèces gazeuses ont été mesurées par effusion de Knudsen couplée à la spectrométrie de masse. La congruence de vaporisation a été déduite de ces données. Enfin, sur la base de toutes ces mesures expérimentales, un modèle Calphad est proposé pour décrire les propriétés thermodynamiques et le diagramme de phase U-Am-O à l'état solide.

Title : Study of the Uranium-Americium-Oxygen ternary phase diagram

Keywords : Uranium, Americium, Oxides, Thermodynamics, Calphad, Non-stoichiometry

Abstract : A good knowledge of the thermodynamic properties of the U-Am-O system is required to predict the high temperature in-reactor behavior of the $(U,Am)O_2$ pellets. In this work, experimental measurements of structural and thermodynamic properties of $(U,Am)O_2$ mixed oxides were performed to provide input data for the thermodynamic modeling of the U-Am-O system with the Calphad method. The Am-O phase diagram was revised on the basis of high temperature XRD measurements showing: the existence of a composition range for the $AmO_{1.61+x}$ phase and the absence of a miscibility gap in the fluorite phase. The investigation of the mixed oxides using XANES and EXAFS has highlighted the stability of the Am^{3+} in these oxides, compensated by the partial oxidation of U^{4+} into U^{5+}. The investigation of the oxidation under air by HT XRD showed the stabilization of the fluorite structure against the formation of oxygen richer oxides, found for UO_2. Phase diagram data were determined. Enthalpy increments were measured by drop calorimetry. An excess contribution for the heat capacity could be related to the reduction of the oxides at high temperature. The vapor pressures were measured by KEMS. The congruency of the ternary system was deduced from these data. Finally, on the basis of these experimental data, a Calphad model was proposed describing the thermodyanmic properties of the mixed oxides and the phase diagram in the solid state of the U-Am-O system.